FOSSIL ENERGY

DOE/BC/14126-14
(DE90000214)

MODIFICATION OF CHEMICAL AND PHYSICAL FACTORS IN STEAMFLOOD TO INCREASE HEAVY OIL RECOVERY

Annual Report for the Period
October 1, 1988 -- September 30, 1989

By
Y.C. Yortsos

February 1990

University of Southern California
Los Angeles, California

Bartlesville Project Office
U. S. DEPARTMENT OF ENERGY
Bartlesville, Oklahoma

DOE/BC/14126-14
Distribution Category UC-122

MODIFICATION OF CHEMICAL AND PHYSICAL FACTORS IN STEAMFLOOD TO INCREASE HEAVY OIL RECOVERY

Annual Report for the Period
October 1, 1988 - September 30, 1989

By
Y.C. Yortsos

February 1990

Work Performed Under Contract No. FG19-87BC14126

Prepared for
U.S. Department of Energy
Assistant Secretary for Fossil Energy

Thomas B. Reid, Project Manager
Bartlesville Project Office
P.O. Box 1398
Bartlesville, OK 74005

Prepared by
University of Southern California
Department of Petroleum Engineering
Los Angeles, CA 90089-1211

Contents

List of Figures

List of Tables

ACKNOWLEDGEMENTS

The research reported in this volume was supported by the U.S. Department of Energy under Contract FG19-87BC14126, subcontracted from Stanford University. We would like to express our gratitude to Tom Reid, our DOE Project Manager, for his steady support and commitment. Thanks are also due to Prof. Bill Brigham and Dr. Louis Castanier of SUPRI for their continuing interest and their invaluable help in administering the subcontract. Part of the work on reservoir heterogeneity was also supported by the USC Center for Oil Recovery Research, sponsored by the donor companies Conoco, Elf-Aquitaine, Pallwell, Phillips Petroleum, Shell, Sun, Texaco, and Unocal. All these sources of support are gratefully acknowledged.

ABSTRACT

This report summarizes research progress made during the period October 1, 1988-September 30, 1989. We report advances in the following general areas:

1. Chemical-Steam Simulation Model
2. Vapor-Liquid Flow in Porous Media
3. Foam Flow in Porous Media
4. Caustic Flooding at Elevated Temperatures
5. Reservoir Heterogeneity

Additional efforts have been devoted in the last quarter of the past year in upgrading and debugging the simulator. New features were added in three-phase relative permeabilities, the vertical equilibrium and the phase behavior subroutines.

The study of vapor-liquid flow in porous media continued. Three aspects were addressed: (i) The onset (nucleation) of phase change (evaporation-condensation); (ii) The subsequent growth of the gas phase; and (iii) The macroscopic description of various processes involving simultaneous steam-water flow.

We used percolation models previously developed to study nucleation during the liquid-to-vapor phase change (evaporation, desorption) in porous media. A cavity model to describe the geometry of nucleation sites was proposed and the stability of vapor-liquid interfaces in porous media was examined. Effects of general pore size distibutions were also incorporated in the percolation approach. Analytical expressions for Bethe lattice representations of the porous media were obtained based on which the effect of nucleation was assessed.

The subsequent to nucleation growth of the gas phase was analysed in two different contexts, one in which the driving force is the pressure decline (typical of gas in solution), and another driven by temperature difference (typical of boiling). The latter study is still in progress, thus we report only on the solution gas process. We examined the growth of a gas "bubble" in porous media by studying in detail the roles played by diffusion, interfacial forces, pressure decline rates and the imposed supersaturation.

It was found that under conditions of slow pressure decline rate the process is quasi-static and can be approximated by an (invasion) percolation approach. The models previously developed may be used to quantify the critical gas saturation and the relative permeabilities. Under the

same conditions but with negligible capillarity, on the other hand, the growth is described by Diffusion-Limited-Aggregation (DLA), for which critical gas saturation and relative permeabilities are undefined.

The knowledge gained from our previous pore level studies was subsequently used to model vapor-liquid processes at the macroscopic level for two flow configurations, one involving counter-current flow and the other concurrent flow. The latter is typical of steady-state experiments for steam-water relative permeabilities and it is still in progress. A unified description was developed. Specific emphasis is placed on effects of heat conduction, capillarity and vapor pressure lowering (Kelvin effect), which have been either neglected or misrepresented in previous studies. We examined saturation profiles and the dependence of the critical heat flux on the system parameters, notably the permeability.

The experimental study of the parameters that affect foam generation and propagation in porous media continued. The effect of flow rate of gas and the surfactant phases on foam generation were investigated. The results point out to the existence of a minimum pressure gradient for foam formation and flow. Within experimental accuracy, a discontinuity was observed in the dependence of the pressure drop on the flow rate. Effects of the use of a foam generator were also evaluated. Experiments are under way that employ continuous pressure monitoring along the core, in order to study foam incubation.

On the theoretical side, we examined the modification of the classical Buckley-Leverett and Johnson-Bossler-Newmann methods when one (or both) of the flowing phases is non-Newtonian of a power-law rheology. The appropriate approach was formulated, and sensitivity studies were performed. The effects of fluid rheology (shear thickening or shear-thinning) and flow rate on the displacement features were investigated. A modification of the JBN method was also suggested.

To critically evaluate the suitability of caustic solutions as steam additives, experimental studies were conducted using long cores. It was found that for temperatures exceeding the 120°C, caustic consumption increases significantly and results into a large drop in the solution pH. This sharp pH decline is due to an irreversible reaction involving silica, caustic and clay, previously unnoticed due to short residence times and/or low temperatures. This interaction is likely to impose substantial requirements on the volume of the caustic injected. It was concluded that caustic injection at elevated temperatures in reservoirs with moderate clay content would not be economically feasible.

Necessary requirement for the understanding of vapor-liquid flow in heterogeneous media (e.g. steam injection in naturally fractured systems) is the elucidation of capillary effects at the regions of heterogeneity. Previous works have been restricted to either static conditions or outflow end-effects. We have undertaken a study to analyse capillary heterogeneity effects under general flow conditions. The saturation response to various forms of heterogeneity was examined both analytically and numerically, and the effects of process parameters, such as mobility ratio, flow rate, and scale and correlation of heterogeneity were investigated.

1 INTRODUCTION

This report covers part of the work performed in the area related to physicochemical factors for the improvement of oil recovery efficiency in steamfloods. Specific goals of the original subcontract were the further development of a chemical-steam simulator, the study of the mechanisms of vapor-liquid flow, the effect of foaming agents on oil displacement and the effect of caustic solutions at elevated temperatures. Upon renewal of the subcontract on October 1, 1988, additional objectives were added involving studies of heterogeneity and non-Newtonian flow.

A chemical-steam simulator has been partly developed over a period of several years with the support of previous DOE contracts to USC. Activity on this subject has slowed down in the last two years. A renewed effort started in the last quarter of the past year to further debug and upgrade the simulator. New features were added in three-phase relative permeabilities, the vertical equilibrium and the phase behavior subroutines. The simulator consists of several thousand Fortran statements in 13 files, each containing several subroutines. At present, we are in the process of debugging and upgrading the energy balance section. We shall provide a complete report upon the completion of the task.

The study of vapor-liquid flow in porous media continued in an effort to understand the basic mechanisms involved in vapor- liquid flow, phase change and transport. Three aspects were addressed: (i) The onset (nucleation) of phase change (evaporation-condensation); (ii) The subsequent growth of the gas phase; and (iii) The macroscopic description of various processes involving simultaneous steam-water flow.

Particular emphasis was placed on nucleation phenomena in phase change in porous media. For this, the percolation models previously developed need to be modified. Appropriate heterogeneous nucleation (cavity) models to describe the geometry of nucleation sites are also necessary. Finally, the stability of vapor-liquid interfaces in porous media must be analysed. This effort is described in Section 2. For completion, effects of general pore size distibutions are included, to circumvent the limitations of previous models. For quantitative assessment, analytical expressions for Bethe lattice representations of the porous media are developed.

The growth of the gas phase subsequent to nucleation occurs by different mechanisms depending on the process. In one case the driving force is the pressure decline (typical of gas in solution), while in another application the growth is driven by temperature difference (typical of boiling).

The latter study is still in progress, thus we report only on the solution gas process. The growth of a gas "bubble" in porous media is examined by studying in detail the roles played by diffusion, interfacial forces, pressure decline rates and the imposed supersaturation. This effort is reported in Section 3. Particular attention is placed on the effect of pressure decline rate on both nucleation and buuble growth. The conditions for quasi-static growth, required for the applicability of a percolation approach, are delineated. Corresponding implications to relative permeabilities are investigated.

In parallel, a detailed modeling of vapor-liquid processes at the macroscopic level was initiated for two flow configurations, one involving countercurrent flow and the other concurrent flow. The latter is typical of steady-state experiments for steam-water relative permeabilities, it is still in progress and will be reported in the future. For the case of vapor-liquid steady-state counterflow, a unified description is attempted, valid for both heat pipes and geothermal applications. Specific emphasis is placed on the effects of heat conduction, capillarity and vapor pressure lowering (Kelvin effect), which have been either neglected or misrepresented in previous studies. This effort is reported in Section 4. We examined saturation profiles and the dependence of the critical heat flux on the system parameters, notably the permeability.

The experimental study of the parameters that affect foam generation and propagation in porous media also continued. The effect of flow rate of gas and the surfactant phases on foam generation were investigated. Specific objective was the investigation of a minimum pressure gradient for foam formation and flow. Effects of the use of a foam generator were also evaluated. Experiments are under way that employ continuous pressure monitoring along the core, in order to study foam incubation. We report on this activity in Section 5.

On the theoretical side, the methods for determination of relative permeabilities in non-Newtonian flow were examined. It is required that the classical Buckley-Leverett and Johnson- Bossler-Newmann methods must be modified, when one (or both) of the flowing phases is non-Newtonian of a power-law rheology. The appropriate approach is formulated and sensitivity studies are performed in Section 6. Effects of fluid rheology (shear thickening or shear-thinning) and flow rate on the displacement features are investigated. The proper modification of the JBN method is also suggested.

To critically evaluate the suitability of caustic solutions as steam additives, the extent of the

caustic/rock interaction and the rate of propagation of pH fronts at elevated temperatures must be determined. Specifically, the state of equilibrium at higher temperatures, an issue of importance to the models developed, must be investigated. To this end, experimental studies were conducted using long cores. Temperatures as high as 180° C and flow rates in the range 0.2-4.8 ft/day were the parameters varied. This effort is reported in Section 7.

Finally, in an effort to assess effects of heterogeneity on the process performance, the elucidation of capillary effects is necessary. This is particularly needed in the modeling of steamfloods in naturally fractured systems, a topic of future interest in this work. Unfortunately, previous works even for the standard, immiscible flow have been restricted to either static conditions or outflow end-effects. We have undertaken a study to analyse capillary heterogeneity effects under general flow conditions. The saturation response to various forms of heterogeneity is examined both analytically and numerically, and the effects of process parameters, such as mobility ratio, flow rate, and scale and correlation of heterogeneity are investigated. This effort is reported in Section 8.

2 NUCLEATION AND PORE GEOMETRY EFFECTS ON CAPILLARY DESORPTION

M. Parlar and Y.C. Yortsos

2.1 INTRODUCTION

Experimental vapor sorption isotherms are indispensable means for the characterization of the texture of porous solids [2, 39, 51, 52]. The commonly used approach relies on Kelvin's equation for the description of capillary condensation and evaporation, and on a model representation of the actual pore geometry and topology. Owing to its obvious significance, the latter has attracted considerable attention.

Early works made use of the simplified model of a bundle of parallel capillaries. Such models have limited success, since they neglect connectivity and topological issues by emphasizing only local (single pore) phenomena [41, 40]. It is now accepted that capillary evaporation in a pore depends, in addition, on its accessibility to other vapor-occupied pores or to the bulk phase outside. The resulting hysteresis cannot be captured by local effects alone, and, as pointed out by Everett [39], requires the interplay of pore space topology.

Network models incorporating percolation concepts have emerged as useful alternatives and have been successfully used to predict several characteristics of primary [71, 76, 109] and secondary [70, 72] sorption processes. A comprehensive approach outlining the relevance of percolation theory in the description of primary and secondary sorption processes was developed in [80]. Although regular lattices were also examined, Bethe lattices were exploited to obtain exact solutions. Results in [80] generalized previous expressions derived by Fisher and Essam [44] and Flory [45] to arbitrary (non-zero) fraction of initial source sites. In a concurrent study, Mason [72] revised his previous model [71], likewise pursuing a percolation approach that led to results similar, although not identical, to those in [80].

All previous network and percolation models for capillary sorption rely on two important premises: the neglect of nucleation phenomena in the liquid-to-vapor transition, and the postulate of some form of relationship between site and bond size distributions.

Lack of nucleation attributes percolation-like features to primary desorption. It appears to have been partly justified in some experiments on porous glass [14, 36, 55, 89], and for a variety of

adsorptives (including xenon [14], nitrogen [36], n-decane [89], carbon tetrachloride, benzene, and water [55]). The experimental results of Barrett et al. [6] on the silica-gel/nitrogen system also reveal a similar behavior. On the other hand, deviations from a percolation behavior have also been noted and variously attributed to nucleation, finite size, vapor compressibility, or other effects. At present, a quantitative assessment of the importance of nucleation during desorption is lacking.

A similar uncertainty exists in the interrelation between pore body and pore throat sizes. This issue is common to any model of porous media, and of particular interest to processes involving two phases, where occupied throats determine phase conductivity, while occupied bodies determine the phase volume. To be sure, any such relationship would be material-specific, reflecting the particular history (diagenetic, etc.) of the porous medium. With few exceptions, most studies bypass the issue by considering site-only or bond-only processes. In the mixed bond-site problem considered in Chapter [80], use was made of an algebraic relationship proposed in [71] to relate site and bond size distributions. This relationship is the lower limit of a general inequality reflecting the constraint that a pore body has size greater than its associated pore throats. The model developed in [80] relies exclusively on this limiting condition, thus unduly prohibiting the consideration of largely arbitrary site and bond distributions.

In this section, these two issues are explored in some detail. Conditions to estimate nucleation effects in desorption are outlined, and simple models for nucleation during desorption are presented. The previous expressions are also generalized to account for arbitrary site and bond size distributions. The approach taken entails the special case of Zhdanov et al. [123], where all bonds have the size of the associated site reduced by a constant factor. The local hysteresis in the adsorption-desorption cycle of cylindrical elements is also briefly discussed.

Capillary sorption, by virtue of the phase change involved, may be the prototypical process, among many others involving immiscible phases (e.g., mercury porosimetry), for the direct application of percolation theory to porous media. This process is further coupled here with a nucleation mechanism that leads to accessibility-controlled growth from internal sources. Besides its direct physical relevance, the ensuing analysis may thus be useful to other percolation processes as well. Phase change in porous media is common to many applied processes (e.g., vapor-liquid flow in oil and geothermal reservoirs [75, 79]), which stand to benefit directly from the present investigation.

2.2 EFFECTS OF NUCLEATION

Before proceeding, we briefly summarize the postulates of the present model. The porous medium is represented by a network of bonds and sites (throats and bodies) of size distributions $\alpha_b(r)$ and $\alpha_s(r)$, and of coordination number Z. Sites and bonds have approximately spherical and cylindrical shapes, respectively, although nucleation pits on rough surfaces are also allowed (see below). Aside from this, other issues of roughness, notably those of fractal structure of the surface [104, 4], are not considered. Additional assumptions are that each pore unit (body or throat) is occupied by a single phase only, vapor or liquid, and that volumetric contributions are obtained from sites only, unless otherwise noted. Stability considerations [41] require that, if a throat is occupied by vapor (as in desorption), the adjacent two bodies are also occupied by vapor, while if a body is occupied by liquid (as in adsorption), all emanating throats are also occupied by liquid. For convenience, surface adsorption effects [15, 29, 33] are ignored.

Given a pore element (site or bond) of size r, there is a corresponding value of the relative pressure (P_v/P_{vo}) given by Kelvin's equation:

$$r = -\frac{r_{ch}}{\ln(P_v/P_{vo})}, \tag{1}$$

with the characteristic radius r_{ch} defined by

$$r_{ch} = \frac{2s\sigma_{LV}V_L}{RT}. \tag{2}$$

Here, σ_{LV} is the surface tension, V_L the liquid molar volume, R the gas constant and T the absolute temperature, while P_v and P_{vo} are equilibrium and saturation vapor pressures, respectively. The parameter s is geometry dependent: In sites, for both adsorption and desorption, it takes the value 1. By contrast, in the cylindrical geometry bonds, s changes from 1 for desorption to 1/2 for adsorption. This difference reflects local hysteresis for elements of cylindrical geometry, and it is tacitly assumed negligible [70, 71, 72, 76, 109, 123]. In the case of a single pore (infinite connectivity), the above define the relative pressure for phase change in the element of size r. One may then parameterize the process (adsorption, desorption) by a variable radius, denoted hereafter for consistency [56, 57, 80, 79] by r_d, and obtained from (1) and (2) by taking $s = 1$.

Capillary adsorption (whether primary or secondary) is independent of accessibility or nucleation effects, although it may be subject to local hysteresis. At any stage r_d, vapor in all sites with

$r < r_d$ and all bonds with $r < r_d/2$ is allowed to (and will actually) condense. However, all bonds emanating from a liquid-occupied site (size $r < r_d$) would also condense in view of the stability considerations outlined above. Thus, a substantially larger fraction of bonds would be occupied by liquid, and the effect of geometry during adsorption would be greatly minimized. In fact, if the volumetric contribution of bonds is taken to be negligible (possibly more appropriate for uniform sphere packs), as in the analysis below, local geometry has no effect on the primary hysteresis loop. By contrast, local hysteresis would affect secondary desorption, where bond statistics are of primary concern. We shall postpone further discussion of this interesting case to a future study.

Desorption, on the other hand, depends strongly on accessibility, and possibly, on nucleation (heterogeneous being the most likely mechanism). In the absence of the latter, vapor occupancy during primary desorption occurs solely through access to the outside bulk vapor, first established at the percolation threshold. In secondary desorption, the liquid-to-vapor transition originates also from preexisting vapor sites. Furthermore, when nucleation is in effect, vapor occupancy will also take place in liquid-occupied pores that are not necessarily connected to a vapor site. In the general case, therefore, the following two conditions must simultaneously hold, for an element to be occupied by vapor:

1. The pore (site or bond) is *allowed* to desorb, $r > r_d$.

2. The pore (site or bond) has *access* to:

(a) the bulk vapor outside (e.g. in primary desorption in the absence of nucleation), and/or to

(b) vapor-occupied pore elements acting as internal sources. The latter either may have been present initially (e.g. in secondary desorption) or may be generated through nucleation during the process (whether primary or secondary).

Clearly, if nucleation is allowed, the formation of an infinite cluster is not required for a primary desorption process to initiate and proceed. In fact, percolation characteristics could very well be erased from the desorption isotherms. To assess their importance, the two nucleation mechanisms are discussed separately.

2.2.1 Homogeneous Nucleation

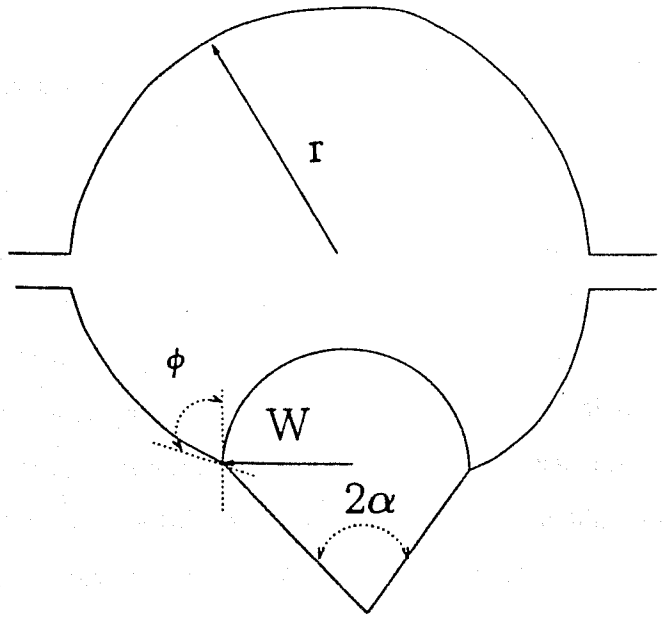

Figure 1: Schematic of a nucleation site in a pore body.

Existing models for nucleation rates in single-component systems make use of kinetic expressions of the form [2, 43, 112, 122]

$$J = K \exp[-\frac{4\pi\sigma r_c^2}{3k_B T} f], \tag{3}$$

where k_B is the Boltzmann constant, K is a kinetic parameter [43], and r_c is the radius of critical size nuclei related to pressure via Kelvin's equation. The dimensionless function f represents effects of wettability and nucleation site geometry. Its value lies between 0 and 1, to cover the range between perfectly heterogeneous to homogeneous nucleation. For example, for conical cavities in spherical pore bodies, as in Fig. 1, as long as the liquid-vapor meniscus is inside the pit,

$$f = \frac{2\sin\alpha[1 - \sin(\theta - \alpha)] + \cos\theta\cos^2(\theta - \alpha)}{4\sin\alpha}, \tag{4}$$

where θ is the contact angle and α the half pit angle. When the interface is at the pit mouth, f is given by

$$f = \frac{2\sin\alpha[1 + \cos(\phi + \psi)] + \sin^2(\phi + \psi)[3\cos\theta - 2\sin(\phi + \psi + \alpha)]}{4\sin\alpha}, \tag{5}$$

where ϕ is the angle between the tangent drawn to the meniscus (assumed spherical) at the pit mouth and the tangent to the spherical pore body at the same point (see Fig. 1), and varies between $(\pi/2 + \theta - \alpha - \psi)$ (when the meniscus first arrives to the pit mouth) and 0 (when the

meniscus radius r_m equals the pore body radius r). The angle ψ depends on the ratio of pit to pore size,

$$\psi = \sin^{-1}(\frac{W}{r}), \tag{6}$$

while the meniscus radius depends on geometrical parameters through

$$r = \frac{W}{\sin(\phi + \psi)}. \tag{7}$$

Usually, the onset of nucleation is arbitrarily defined at the rate $J = 1$ *nucleus* per *sec-cc*. The precise definition is immaterial, since both the critical size and the corresponding supersaturation are insensitive to large variations in J. For example, for xenon at 151 ^oK, an increase in J by eight orders of magnitude (from 10^{-4} to 10^4) reduces the nucleation radius

$$r_N = [-\frac{3k_BT\ln(J/K)}{4\pi\sigma f}]^{1/2}, \tag{8}$$

from 15.4 to 13.8 Å, for $f = 1$, clearly a negligible change. It follows that a quite sharp and fixed threshold for the onset of nucleation can be identified.

When $r_d > r_N$ (vapor pressure greater than nucleation pressure), no phase change occurs via homogeneous nucleation, while when $r_d < r_N$, there is vapor occupancy via homogeneous nucleation in all pore elements (bonds and sites) of radius $r > r_d$. We recall that in the absence of nucleation, the onset of primary desorption is at the percolation threshold, defined in terms of a radius r_{pt}

$$\int_{r_{pt}}^{\infty} \alpha_b(r)dr = \frac{1}{Z-1}, \tag{9}$$

for a Bethe lattice. Note that the bond size distribution is used, since desorption is controlled by pore throats, in view of the stability premises outlined above. Thus, whether nucleation is a significant factor in a desorption experiment or not largely depends on the ratio r_N/r_{pt}. Nucleation would be clearly negligible if the latter is significantly smaller than 1.

Quantitative estimates are possible if $\alpha_b(r)$ is relatively smooth. For Z not too large, it can be easily shown that r_{pt} is of the same order as the mean throat size λ_b. For example, for the size distribution

$$\alpha_b(r) = \frac{\pi r}{2\lambda_b^2}\exp[-\frac{\pi r^2}{4\lambda_b^2}], \tag{10}$$

we have

$$\frac{r_{pt}}{\lambda_b} = [\frac{4\ln(Z-1)}{\pi}]^{1/2}, \tag{11}$$

the RHS of which is close to 1 for typical values of Z. Thus, for all practical purposes, the ratio

$$\frac{r_N}{\lambda_b} = \frac{[3k_BT \ln K/4\pi\sigma]^{1/2}}{\lambda_b}, \tag{12}$$

may serve to measure the importance of homogeneous nucleation. An insignificant contribution is expected for media of larger mean size, a likely occurrence in many applications.

On the other hand, sorption experiments are of utility insofar as the corresponding isotherms are not too steep, so that reasonable resolutions are possible. In turn, this requires smaller pore sizes. For instance, the slope of the sorption isotherm in a (liquid volume) vs. (relative pressure) plot is roughly equal to

$$\frac{dS_L}{d(P_v/P_{vo})} \approx \frac{r^2}{r_{ch}}\alpha_s(r)\exp(\frac{r_{ch}}{r}), \tag{13}$$

if equal volume sites are assumed. For a distribution of the type (10) with an average site radius λ_s, the slope has an estimate of order λ_s/r_{ch}, near the onset of desorption. Similar conclusions are reached if it is required that the relative pressure at the onset of desorption be not too close to 1. For example, a value equal to 0.8 requires λ_b/r_{ch} ($\approx r_{pt}/r_{ch}$) $\approx$ 4.48.

It follows that successful sorption experiments ought to be conducted under conditions such that simultaneously, λ_b/r_{ch} is not too large, and λ_b/r_N is not too small. The two requirements are favored at higher values of σ and lower values of T, conditions commonly practiced in sorption experiments. Percolation-type theories that do not account for homogeneous nucleation, may then be successfully used for the determination of the size distributions. It can be shown that this is likely the case in typical experiments. For example, for the conditions in [14] and [55], the relative pressure for homogeneous nucleation of xenon (water) is 0.406 (0.385), while experimentally observed desorption thresholds are approximately at 0.525 (0.670). These data clearly suggest that at the onset of nucleation, most of the pore elements are already vapor-occupied via percolation mechanisms, free of homogeneous nucleation.

2.2.2 Heterogeneous Nucleation

While homogeneous nucleation can be adequately estimated, this is hardly the case for the heterogeneous case, due to the uncertainty in the state of wettability and the geometry of the nucleation sites. Specific models or a probabilistic approach may then be necessary. Typically, the surface roughness is approximated by conical pits of the type studied by Ward et al. [112] and Forest [46].

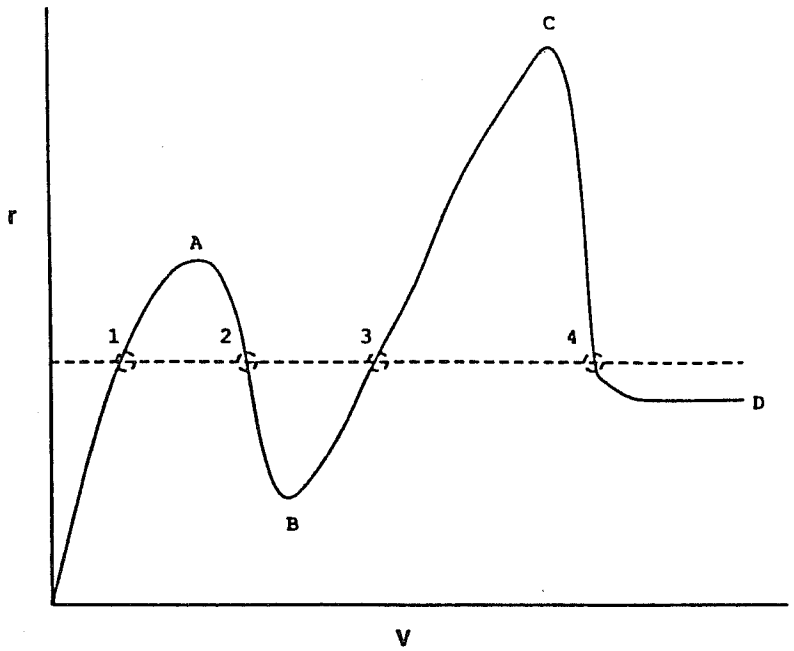

Figure 2: Schematic of meniscus radius-volume relationship for bubble growth in a hydrophilic conical cavity.

Geometric and interfacial properties of the latter may further be assigned a probability distribution function. To be specific, consider a nucleation site of conical pit geometry in a pore element (pore body) of size r (Figure 1). The pit would be characterized by a half-width W, an angle α, and a contact angle θ. Clearly, we must require that the conical pit be considerably smaller than the pore element itself, thus we take the ratio

$$\beta = \frac{W}{r} \tag{14}$$

to be constant and small (e.g., $\beta = 0.1$), for α not too small. One is then interested in determining the relative pressure (radius) at which the pore element becomes fully occupied by vapor via heterogeneous nucleation, and the corresponding effects on the desorption curve.

Closely paralleling the analysis in [46, 111, 112], it can be shown that under favorable wettability conditions (high contact angle), vapor bubbles do indeed form in the pits. However, as long as the radius r_d associated with the prevailing vapor pressure is greater than the half-width W, such bubbles are restricted near the pit mouth and would grow to a generally small size with the meniscus located near the pit mouth. Figure 2 shows a qualitative schematic of the relationship

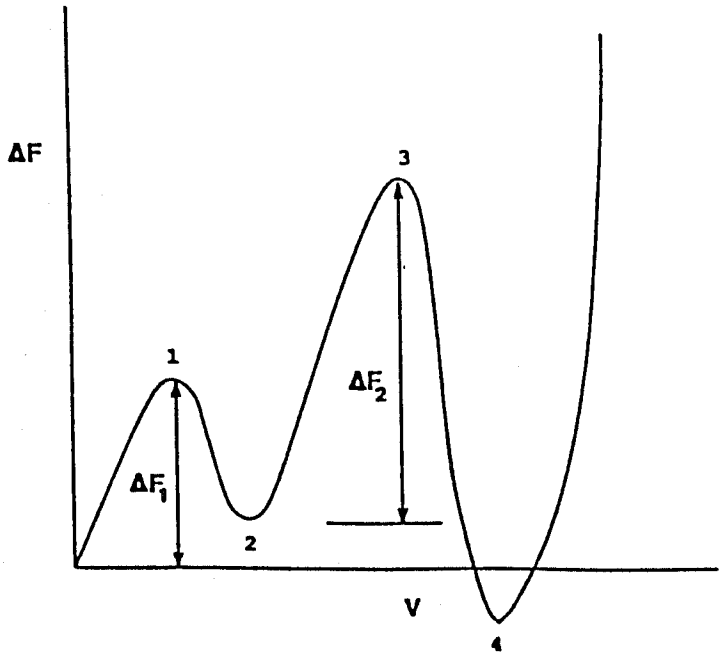

Figure 3: Schematic of change in Helmholtz free energy-volume relationship.

between vapor-liquid meniscus radius (r) and bubble volume (V) for a *hydrophilic* conical cavity ($\theta - \alpha < \pi/2$) satisfying the inequality $\beta < \cos(\theta - \alpha)$. The meniscus exhibits successively a local maximum ($W/\cos(\theta - \alpha)$, point A), a local minimum (W, point B), and a global maximum (r_s = site radius, point C), where the entire site becomes occupied by vapor, to be followed by an eventual reduction in radius to that of the associated bonds (point D). From such diagrams, the stability of the equilibrium states may be readily identified. As with the case of homogeneous nucleation, however, and for all practical purposes, kinetic considerations would prevail in determining the occurence of vapor occupancy.

The corresponding relationship between the change in the Helmholtz free energy ΔF and the bubble volume V is qualitatively shown in Figure 3, for the most interesting case $W/\cos(\theta - \alpha) > r_d > W$. Two energy barriers exist. If a bubble forms with volume greater than that corresponding to the first barrier (ΔF_1), it would grow to a metastable state at the pit mouth. However, for the occupancy of the host pore element by such a bubble, a second energy barrier (ΔF_2) must be overcome, the kinetics of which are favorable only if $r_d < W$. Thus, the pore may become vapor-occupied via heterogeneous nucleation, although at a relative pressure P_v^*/P_{vo}, which is considerably

smaller than that of the pore element itself, P_v/P_{vo},

$$\frac{P_v^*}{P_{vo}} = (\frac{P_v}{P_{vo}})^{1/\beta}. \tag{15}$$

Identical conclusions can be reached for the hydrophobic case [46]. Since β is assumed to be small, heterogeneous nucleation is, thus, likely to be important only in larger pore sizes, hence in porous media with wide size distributions and long tails (such that P_v/P_{vo} can be close to unity). It is worth noting that, at least for such model porous media, heterogeneous nucleation is pore size-hence relative pressure-dependent, in contrast to the homogeneous case.

The simplest model to be considered contains pits in each site with a constant β (half-width W is a fixed fraction of the site radius), all such pits having the same contact angle θ and half-angle α. A precise nucleation radius r_N can then be defined from (8). Note that $r_N = \infty$ if $f = 0$, as tacitly assumed later. If $r_d > r_N$, there will be no heterogeneous nucleation. If $r_d < r_N$, heterogeneous nucleation will take place in all pores with radius $r_p > [\cos(\theta - \alpha)/\beta]r_d$. However, while in most pores growth will be limited to the pit mouths (with negligible effect on volume considerations), occupancy of the entire pore elements will occur in those with radius $r_p > r_d/\beta$. With this type of simple, but instructive, model it is possible to make a quantitative assessment of nucleation, as discussed in later sections.

One concludes that the relative contribution of heterogeneous nucleation to primary desorption can be measured by the ratio of the maximum pit width to the percolation radius, $\beta r_{s,max}/r_{pt}$ or $\beta r_{s,max}/\lambda_b$, in view of (11). The use of the maximum site size should be noted. When this ratio is substantially less than unity, for instance in relatively narrow size distributions, we anticipate that nucleation-free percolation dominates the process. Several practical applications are likely to satisfy this condition. In the opposite case, vapor occupancy of pore elements would also occur from internal sources (nucleation sites). While the likelihood of the latter is less, a quantitative assessment of its importance would be desirable and is explored below.

2.2.3 Accessibility Functions

The uncertainty of nucleation effects necessitates the use of a probabilistic approach. We shall postulate that at any pressure level, parametrized by r_d, a fraction f_q of the sites (or f_p of bonds) with radius $r > r_d$ is also allowed to undergo a liquid-to-vapor transition via (*heterogeneous*) nucleation. The resulting vapor-liquid menisci advance and occupy adjacent pores until a pore throat

with radius smaller than r_d is encountered. In the absence of a specific model, the nucleation probability fraction f_q (in general, variable with r_d or pressure) is unknown. Therefore, the accessibility functions derived below are general and apply to any functional f_q (or f_p). Note that for the simple model introduced in the previous section, the nucleation fraction (f_q or f_p) at any r_d can be simply obtained:

$$f_k = \frac{1}{p_j}\int_{r_d/\beta}^{\infty} \alpha_j(r)dr, \quad (j = s, k = q; j = b, k = p). \tag{16}$$

$$p_s = q = \int_{r_d}^{\infty} \alpha_s(r)dr,$$
$$p_b = p = \int_{r_d}^{\infty} \alpha_b(r)dr,$$

represent the number fraction of sites and bonds, respectively, in the allowed interval $[r_d, \infty]$. For simplicity, the two fractions will be related by the expression [71]

$$(1-q) = (1-p)^Z. \tag{17}$$

A generalization to arbitrary sizes is presented in the next section. As previously pointed out, the analysis for secondary desorption does not include local hysteresis.

It is recalled that, in the absence of nucleation, primary desorption is an ordinary percolation process [71, 72, 76, 80, 109, 123], while secondary desorption requires the solution to a growth problem from a fixed number of sources as discussed in [80]. In the presence of nucleation, the desorption process (primary or secondary) is neither of the above. Here, in addition, sources (sites or bonds) are constantly generated during the process. three cases are distinguished, pertaining to bond percolation (no site participation), site percolation (no bond participation), and a mixed site-bond problem. The analysis is for a Bethe lattice, although appropriate algorithms for regular lattices may be readily constructed.

Bond Percolation

At the initiation of secondary desorption, a fraction p_i of bonds are vapor-occupied (*initial sources*). At any stage $p > p_i$, the fraction of bonds *allowed* for vapor occupancy is p. Some allowed pores will be connected to initial sources, some will be connected to *generated sources* in the newly allowed

interval, $p - p_i$, and some will be *isolated* without access to either type of source. Denoting the actually *occupied fraction* by $P_b(p; p_i, f_p)$ and the *isolated fraction* by I_b, we obtain

$$P_b(p; p_i, f_p) = p - I_b(p; p_i, f_p). \tag{18}$$

The fraction I_b consists of isolated clusters of bonds of various sizes. A bond in any such cluster has size in $[r_d, r_i]$ (probability $p - p_i$) and may not be a source bond (probability $1 - f_p$). Furthermore, all perimeter bonds have sizes in the interval $[0, r_d]$ (probability $1 - p$). Therefore, the total isolated fraction at any stage is

$$I_b(p; p_i, f_p) = \sum_{n=1}^{\infty} B_n (p - p_i)^n (1 - f_p)^n (1 - p)^{t_n}, \tag{19}$$

where B_n is the configuration coefficient [44]

$$B_n = \frac{2(Z-1)[(n+1)(Z-1)-1]!}{(n-1)!t_n!}, \tag{20}$$

and t_n is the perimeter,

$$t_n = (Z-2)n + Z. \tag{21}$$

The infinite series in 19 can be evaluated [44, 80]

$$P_b(p; p_i, f_p) = p - (1 - f_p)(p - p_i)[\frac{1-p}{1-x}]^{2(Z-1)}, \tag{22}$$

where x is the solution in the interval $[0, 1/(Z-1)]$ of

$$x(1-x)^{Z-2} = (1 - f_p)(p - p_i)(1 - p)^{Z-2}. \tag{23}$$

Equations 22 and 23 give the accessible fraction for bond percolation and a nonzero nucleation probability fraction f_p. The latter can vary with p as desired. The agreement with the expressions in [80] in the absence of nucleation ($f_p = 0$) is noted. Figures 4 and 5 depict the accessibility functions obtained for $p_i = 0$ (primary desorption) and $p_i = 0.05$ (secondary desorption), respectively, for $Z = 4$ and various values of the constant f_p. It is apparent that, in the presence of nucleation, the sharpness of the primary desorption curve is greatly reduced as the nucleation probability increases.

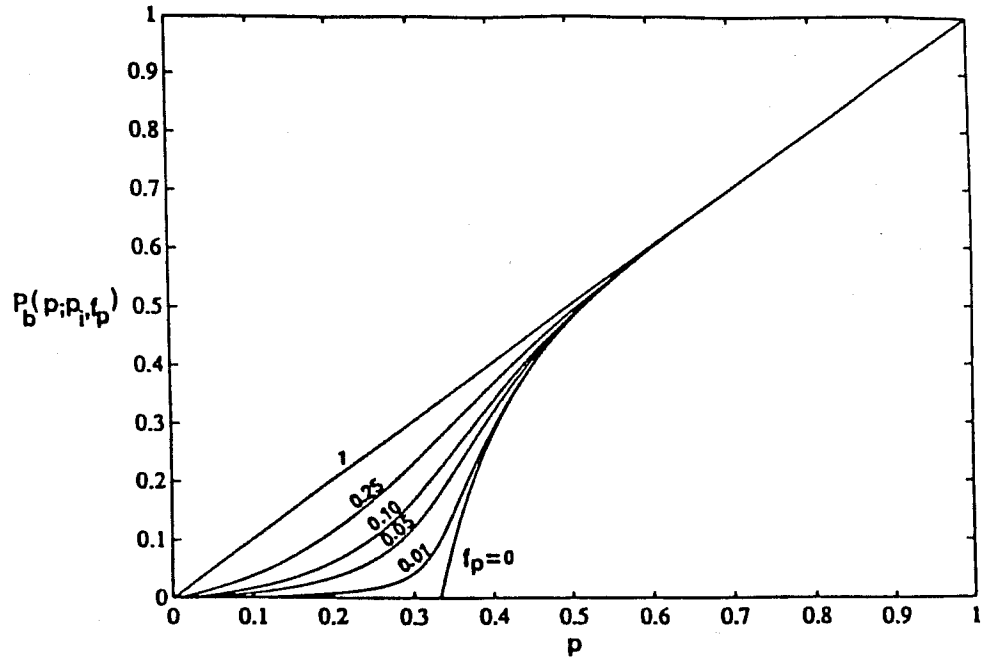

Figure 4: Accessible fraction of bonds as a function of allowed fraction p for various values of f_p: $Z = 4$, $p_i = 0$.

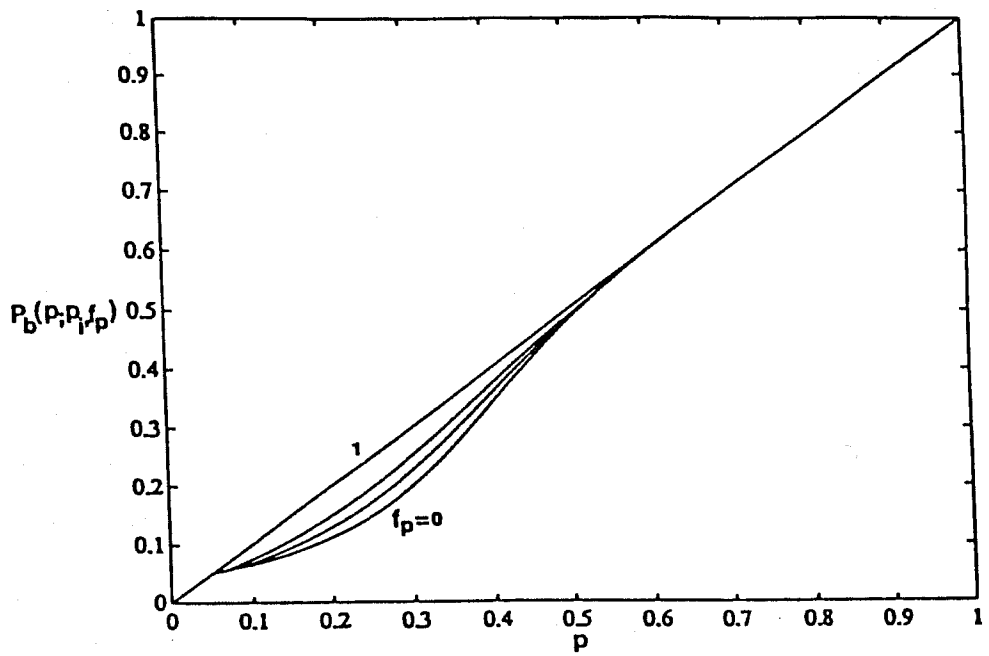

Figure 5: Accessible fraction of bonds as a function of allowed fraction p for various values of f_p: $Z = 4$, $p_i = 0$ (Intermediate curves for $f_p = 0.10$ and 0.25).

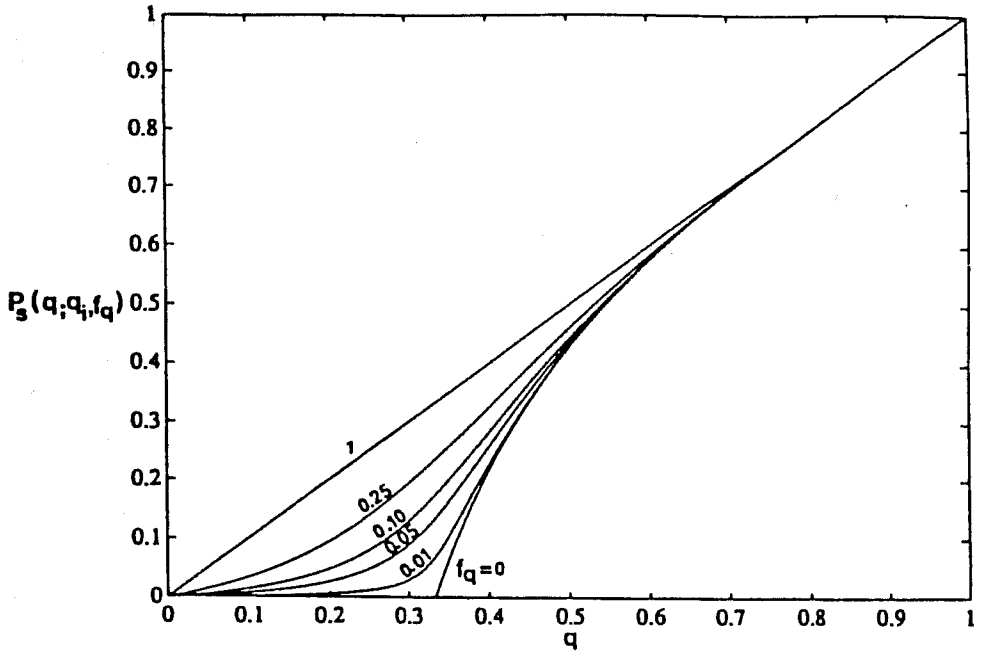

Figure 6: Accessible fraction of sites as a function of allowed fraction q for various values of f_q: $Z = 4$, $q_i = 0$.

Site Percolation

A similar approach is taken for site percolation. We shall omit the details and simply note that both the configuration coefficient and the perimeter are different than those in bond percolation [44, 80]. The final result is

$$P_s(q; q_i, f_q) = q - (1 - f_q)(q - q_i)[\frac{1-q}{1-q}]^Z, \tag{24}$$

where x solves 23 with q, q_i, f_q substituted in place of p, p_i, f_p, respectively. The accessibility functions are qualitatively similar to those in Fig. 4 as shown in Fig. 6.

Mixed Bond-Site Problem

We next examine the site accessibility in a bond-controlled process, which is most pertinent to capillary desorption, and to many other drainage processes as well. For simplicity, it is assumed that only sites are likely to generate sources (nucleation in pore bodies only), although the alternative is straightforward. The quantity of interest is the accessible fraction of sites, given an allowed fraction of bonds.

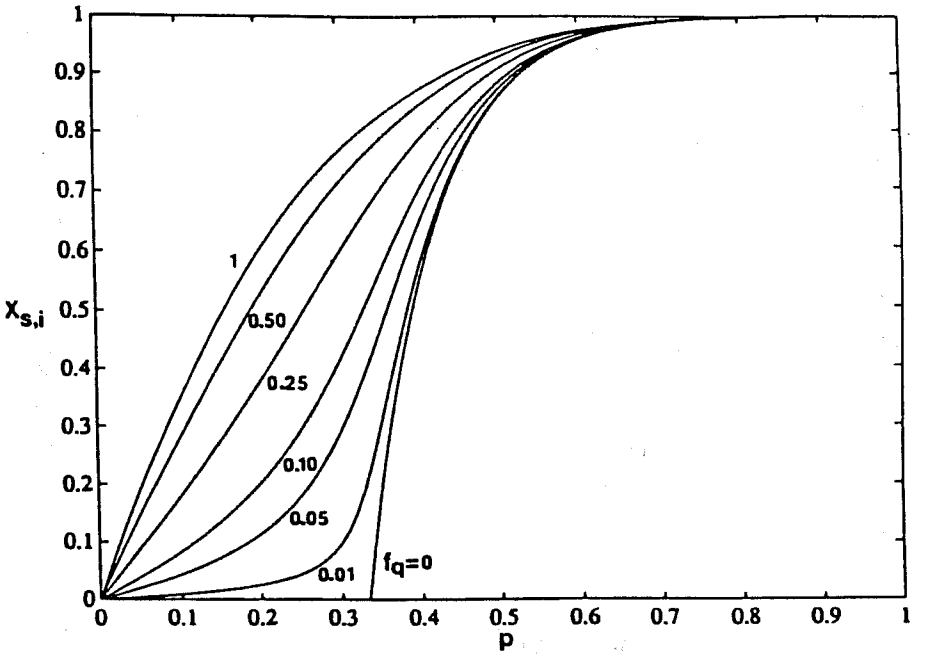

Figure 7: Accessible fraction of sites as a function of allowed fraction p for various values of f_q: $Z = 4$, $p_i = 0$.

Since the process is controlled by bonds, the fraction of isolated sites is determined by first evaluating the fraction of isolated bonds and subsequently calculating the number of associated sites. The accessible fraction $X_{s,i}$ will be

$$X_{s,i} = q - I_{s,b}(p; p_i, f_q). \tag{25}$$

As before, attention is paid to $I_{s,b}$. At any stage r_d, each bond of an isolated cluster has size in $[r_d, r_i]$ (probability $p - p_i$). The condition for the bond cluster to be isolated is that all perimeter sites have size in the interval $[0, r_d]$ (probability $1 - p$). Additionally, none of the sites contained in the isolated cluster may be a nucleation site. The probability of the latter event is $(1 - f_q)^{n+1}$. The density of isolated clusters of size n is thus

$$P_{b,n} = B_n(p - p_i)^n(1 - f_q)^{n+1}(1 - p)^{t_n}. \tag{26}$$

The number fraction of bond clusters of size n is simply $P_{b,n}/n$. The associated fraction of sites is obtained directly by noting that a bond cluster of size n defines a site cluster of size $n + 1$, that Z

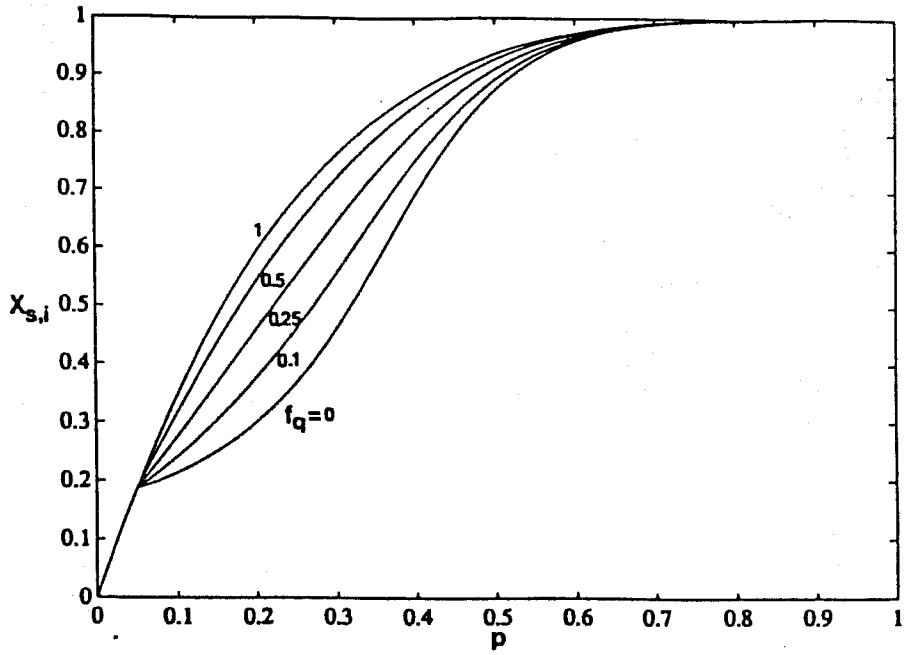

Figure 8: Accessible fraction of sites as a function of allowed fraction p for various values of f_q: $Z = 4$, $p_i = 0.05$.

bonds emanate from each site, and that each site is shared by two bonds. Then,

$$I_{s,b} = \frac{Z}{2}\sum_{n=1}^{\infty}\frac{n+1}{n}B_n(p-p_i)^n(1-f_q)^{n+1}(1-p)^{t_n}. \tag{27}$$

Evaluation of the series leads to the final result

$$X_{s,i} = [1-(1-p)^Z] - (1-f_q)[(\frac{1-p}{1-x})^Z - (1-p)^Z], \tag{28}$$

where x solves

$$x(1-x)^{Z-2} = (p-p_i)(1-f_q)(1-p)^{Z-2}. \tag{29}$$

In the limit $f_q = 0$, we obtain previously developed expressions for secondary desorption in the absence of nucleation ([80]). Figs. 7 and 8 show the results obtained for $Z = 4$, various values of f_q (taken constant), $p_i = 0$ and $p_i = 0.05$, respectively. As with Figs. 4, 5, a notable effect due to nucleation is observed.

2.3 ARBITRARY SIZE DISTRIBUTIONS

The previous expressions for the mixed problem were based on the assumption that site and bond distributions are related by (17). Fig. 9 shows a schematic of this constraint for a fixed bond size

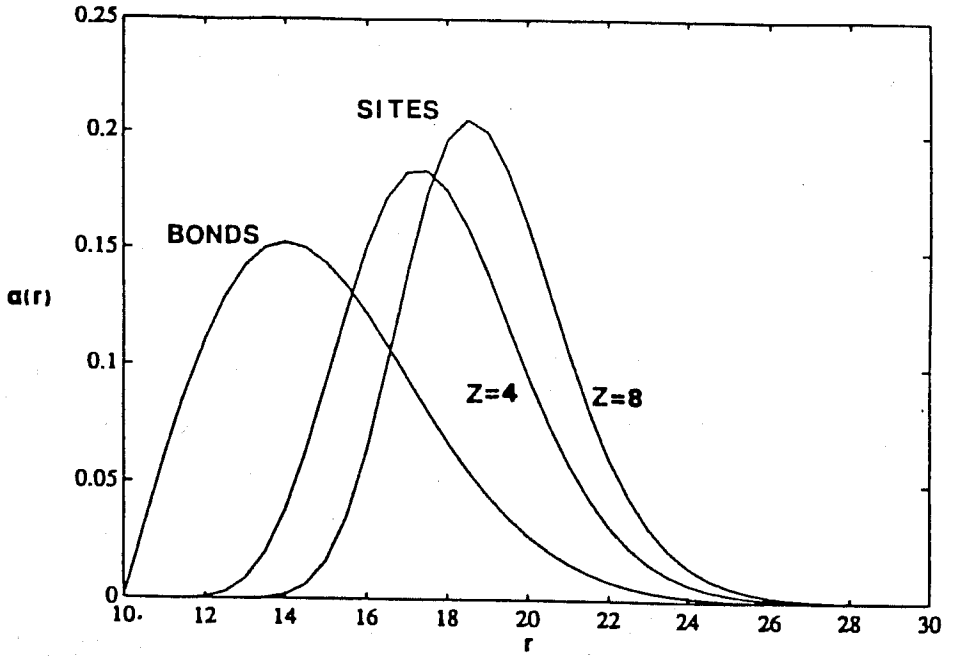

Figure 9: Effect of coordination number on limiting site size distribution.

distribution. An increase in Z leads to a corresponding shift of the site distribution toward larger sizes. This interesting effect is worth noting since it couples geometry and topology in the porous medium. The underlying principle is that no pore body has size smaller than its associated Z pore throats. However, as noted previously, expression (17) is only the marginal limit of the stronger statement [72]

$$q \geq 1 - (1-p)^Z, \tag{30}$$

for every q and p. In fact, it may be shown that the additional constraint

$$q \geq \sqrt{p}, \tag{31}$$

derived from the condition that a bond has size smaller than the adjacent two sites, must also be satisfied (see also [20]). Equivalently,

$$[\int_0^r \alpha_s(r')dr'] \leq \min[(\int_0^r \alpha_b(r')dr')^Z,\ \ 1 - (\int_r^\infty \alpha_b(r')dr')^{1/2}], \tag{32}$$

for every r. For any distributions, the equality sign must be obeyed at the limits $q = p = 0$ ($r = \infty$) and $q = p = 1$ ($r = 0$). Obviously, a large variety of such functions (e.g., overlapping, nonoverlapping) satisfy the above restrictions. Generalizing the previous results to arbitrary sizes

as dictated by (30,31) is not as trivial as it might appear. In fact, it is shown below that the limiting relationship (17) plays a rather special role in a network model and facilitates calculations considerably.

2.3.1 Associated Fraction q^*

To proceed, the associated fraction q^* will first be defined. Consider a fraction of bonds p and sites q, corresponding to the same radius, r,

$$\begin{aligned} p &= \int_r^\infty \alpha_b(r')dr', \\ q &= \int_r^\infty \alpha_s(r')dr', \end{aligned}$$

and assume that all such elements are actually allowed (they are occupied by vapor as in primary adsorption). By definition, all bonds are associated (terminate) with sites of size greater than r. The number fraction of these sites, q^*, will be termed the associated fraction. It will be shown that $q > q^*$, regardless of the particular size distributions,

$$q \geq q^* = 1 - (1-p)^Z. \tag{33}$$

The proof is straightforward: The probability that a randomly picked site is associated with at least one bond in $[r_d, \infty]$ (probability p) is equal to 1 minus the probability that all of the bonds emanating from it are in $[0, r_d]$ (each having probability $1-p$). The probability of the latter event is $(1-p)^Z$, and Eq. (33) follows immediately. The latter holds both below and above the percolation threshold, p_c, and yields the total fraction of sites associated with either finite or infinite bond clusters.

To obtain the fraction contained in finite clusters requires some analysis. Bond clusters of size n have the usual probability

$$P_n = B_n p^n (1-p)^{t_n}, \tag{34}$$

while their number is P_n/n. Applying the usual reasoning that Z bonds emanate from each site, each bond is shared by two sites, and $(n+1)$ sites associate with a bond cluster of size n, the total fraction of sites associated with finite bond clusters is

$$q_F^* = \frac{Z}{2}\sum_{n=1}^{\infty}(n+1)\frac{P_n}{n}$$

$$= \frac{Z}{2}\sum_{n=1}^{\infty}\frac{n+1}{n}B_n p^n(1-p)^{(Z-2)n+Z}. \tag{35}$$

The latter becomes

$$q_F^* = [\frac{1-p}{1-x}]^Z - (1-p)^Z, \tag{36}$$

where x is the solution of

$$x(1-x)^{Z-2} = p(1-p)^{Z-2}. \tag{37}$$

For $p < p_c = 1/(Z-1)$, the relevant root is $x = p$. Substitution in (36) yields (33) again. On the other hand, for $p > p_c$, (36) yields only the fraction associated with finite bond clusters. The fraction contained in the infinite bond cluster, q_∞^*, is obtained by deducting (36) from (33)

$$q_\infty^* = 1 - (\frac{x}{p})^{Z/(Z-2)}, \tag{38}$$

where x solves (37).

2.3.2 Absence of Nucleation

We are now in a position to proceed with the general problem. We shall first consider secondary desorption in the absence of nucleation, thereby extending the percolation problem in [80] to arbitrary size distributions. The mixed bond-site problem is examined.

At the conclusion of adsorption ($r = r_i$), a set of bonds and sites of fraction p_i and q_i, respectively, are vapor-occupied. Given p_i, the associated fraction of sites q_i^* is defined. The remainder set $(q_i - q_i^*)$ is occupied by vapor but it is associated (connected) with bonds that have size smaller than r_i. At any stage $r_d < r_i$ during secondary desorption, this fraction $(q_i - q_i^*)$ may further be viewed as connected to bonds in either $[r_d, r_i]$ (probability $p - p_i$) or in $[0, r_d]$ (probability $1 - p$).

Consider now an isolated bond cluster. It contains interior bonds in $[r_d, r_i]$ (probability $p - p_i$), perimeter bonds in $[0, r_d]$ (probability $1 - p$), and includes sites that may not be initial source sites. The probability for a site to satisfy the latter condition is $(1 - q_i)/(1 - q_i^*)$, if one notes that all sites in q_i^* are contained in clusters that have bonds in $[r_i, \infty]$ (probability p_i), thus, they cannot be associated with bonds of smaller size. The fraction of sites associated with such bond clusters is calculated as before. We obtain the isolated fraction

$$I_{s,b} = \frac{Z}{2}\sum_{n=1}^{\infty}\frac{n+1}{n}B_n(p-p_i)^n(1-p)^{t_n}[\frac{1-q_i}{1-q_i^*}]^{n+1}, \tag{39}$$

which, after evaluation of the series becomes

$$I_{s,b} = [(\frac{1-p}{1-x})^Z - (1-p)^Z]\frac{1-q_i}{1-q_i^*}, \tag{40}$$

where x is the solution of the equation

$$x(1-x)^{Z-2} = (p-p_i)(1-p)^{Z-2}\frac{1-q_i}{1-q_i^*}. \tag{41}$$

The accessible fraction of sites at any stage p can now be evaluated. It shall consist of three terms

$$X_{s,i} = q^* - I_{s,b} + S_i. \tag{42}$$

The presence of q^* instead of q on the first term reflects the fact that in this bond percolation process, only sites associated with allowed bonds (of fraction p) are eligible (contrast with (25). The second term is the usual isolated fraction. Finally, S_i denotes the fraction of initial vapor sites, which are surrounded by bonds of size in $[0, r_d]$ (probability $1-p$)

$$S_i = [\frac{q_i - q_i^*}{1-q_i^*}](1-p)^Z. \tag{43}$$

This latter set contains vapor-occupied sites not included in q^*, and must be accounted for. Upon substitution of (33), (40), and (43) in (42), the simple expression is obtained

$$X_{s,i} = 1 - [\frac{1-q_i}{1-q_i^*}][\frac{1-p}{1-x}]^Z, \tag{44}$$

where x solves (41). It is interesting to note that, in contrast to the nucleation case below, the accessibility functions are independent of the current value of the site fraction q, although they do depend on the initial value q_i. In the absence of nucleation, the only way a liquid-occupied site changes occupancy is by becoming connected to a source site via allowed bonds. This mechanism is independent of the site distribution function, $\alpha_s(r)$.

We test three limiting cases. First, $X_{s,i} = 1$ in the limit $q_i = 1$, as expected. Second, if $q_i = q_i^*$ (all source sites associated with source bonds), (44) and (41) reduce to the expressions derived previously ([80]). Finally, when $q_i = 0$, we obtain the ordinary percolation results in [71], since q_i^* and p_i are necessarily equal to zero. Figs. 10 and 11 show the resulting accessibility functions for the two values $p_i = 0$ and $p_i = 0.05$, for various values of q_i and for $Z = 4$. The notable departure from the previous cases ([80]) is stressed.

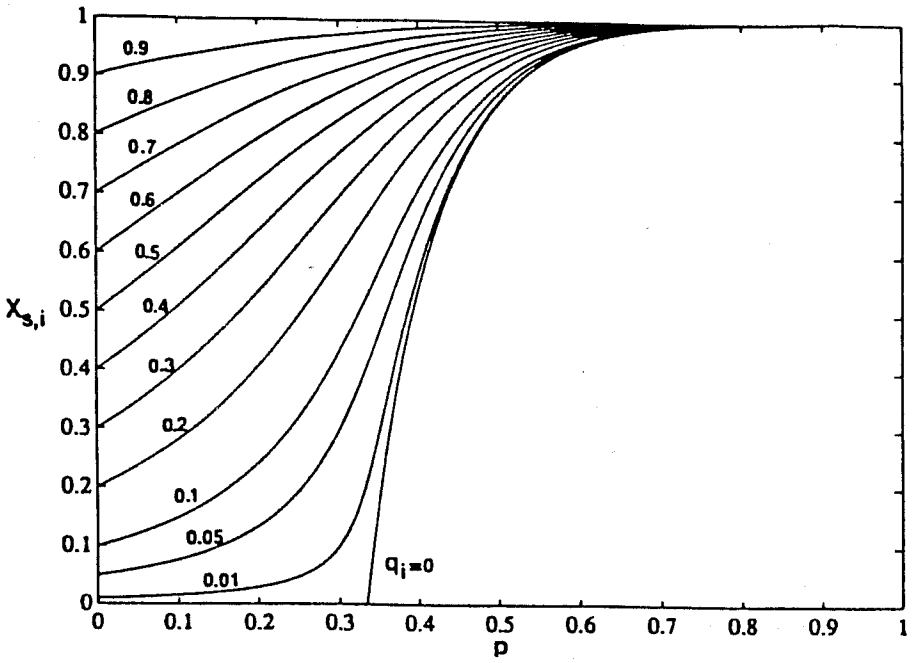

Figure 10: Accessible fraction of sites as a function of allowed fraction p for various values of q_i: Arbitrary size distributions, $Z = 4$, $f_q = 0$, $p_i = 0$.

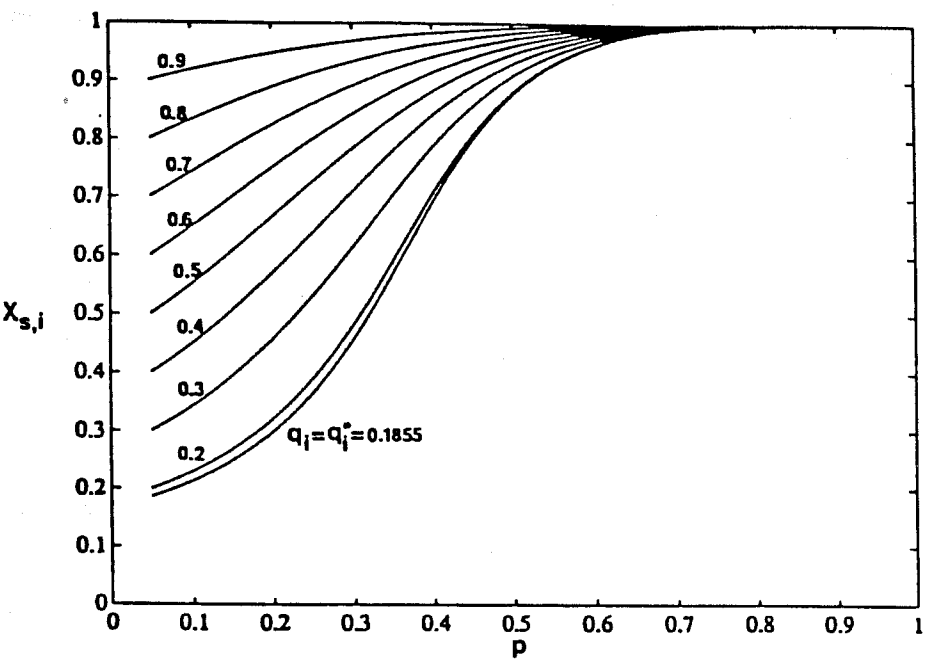

Figure 11: Accessible fraction of sites as a function of allowed fraction p for various values of q_i: Arbitrary size distributions, $Z = 4$, $f_q = 0$, $p_i = 0.05$.

2.3.3 Nucleation Effects

The above can be easily extended to include nucleation effects. For simplicity, only nucleation in sites (pore bodies) will be considered. At any stage r_d, a fraction (in general variable) f_q of the sites with radius $r > r_d$ can be activated to generate internal sources for vapor occupancy of adjacent sites and bonds. The method of evaluating accessibility is as follows.

We distinguish four sets of sites. One contains all sites associated with bonds in $[r_d, \infty]$, of fraction q^*. The second set is the usual isolated fraction, with the additional requirement that sites may neither be initial sources (probability per site $(1-q_i)/(1-q_i^*)$), nor nucleation sites (probability $1-f_q$). The isolated fraction becomes

$$I_{s,b} = \frac{Z}{2}\sum_{n=1}^{\infty}\frac{n+1}{n}B_n(p-p_i)^n(1-p)^{t_n}(1-f_q)^{n+1}[\frac{1-q_i}{1-q_i^*}]^{n+1}, \tag{45}$$

which is evaluated to yield

$$I_{s,b} = (1-f_q)[(\frac{1-p}{1-x})^Z - (1-p)^Z][\frac{1-q_i}{1-q_i^*}]. \tag{46}$$

The third set comprises sites that are initially occupied by vapor and completely surrounded by liquid-occupied bonds in $[0, r_d]$ (probability $1-p$), namely the set described by (46). The final set contains all sites that are in $[r_d, \infty]$, but not associated with bonds in $[r_d, \infty]$, they are initially not occupied by vapor (probability $(1-q_i)/(1-q_i^*)$), and they become nucleation sites (probability $(q-q^*)f_q$). The accessible fraction is, thus,

$$\begin{aligned} X_{s,i} &= [1-(1-p)^Z] - (1-f_q)(\frac{1-q_i}{1-q_i^*})[(\frac{1-p}{1-x})^Z - (1-p)^Z] \\ &+ (1-p)^Z(\frac{q_i-q_i^*}{1-q_i^*}) + (q-q^*)f_q(\frac{1-q_i}{1-q_i^*}), \end{aligned} \tag{47}$$

where x is the solution of

$$x(1-x)^{Z-2} = (p-p_i)(1-p)^{Z-2}(1-f_q)(\frac{1-q_i}{1-q_i^*}). \tag{48}$$

Note that, unlike the previous case, the site accessibility here also depends on the current value of q. One interesting limit is $p = 0$ in the case $q_i = p_i = 0$. Then, $X_{s,i} = qf_q$, as expected, since only the sites that can nucleate are occupied by vapor. Also in agreement, the percolation limit considered in Chapter [80] and [71] is obtained, when $q_i = p_i = 0$ and $f_q = 0$.

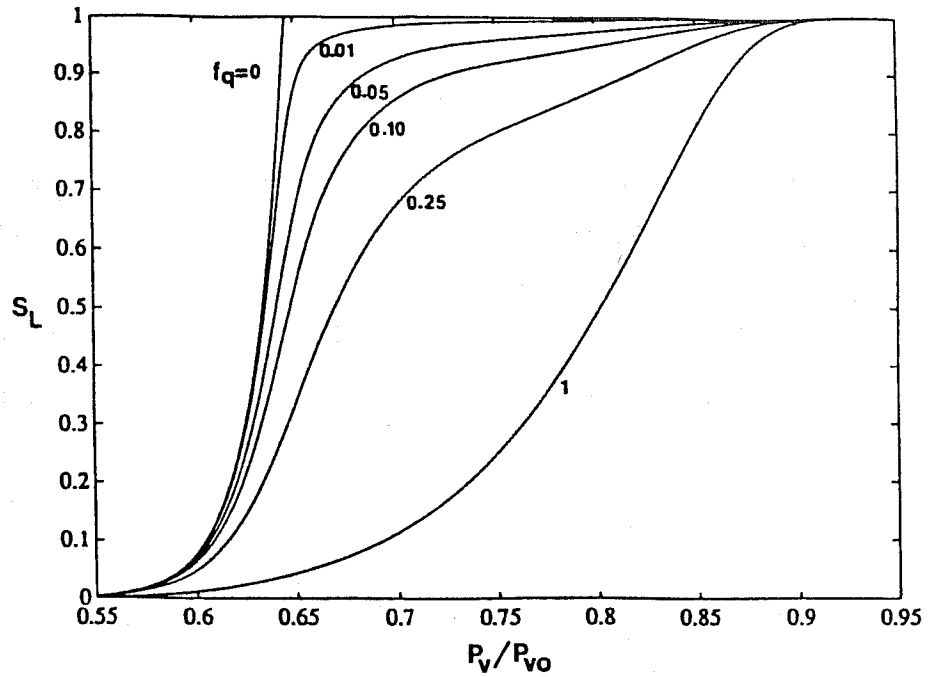

Figure 12: Model predictions of primary desorption curves for sorption of nitrogen for various values of f_q: $Z = 4$, f_q = constant.

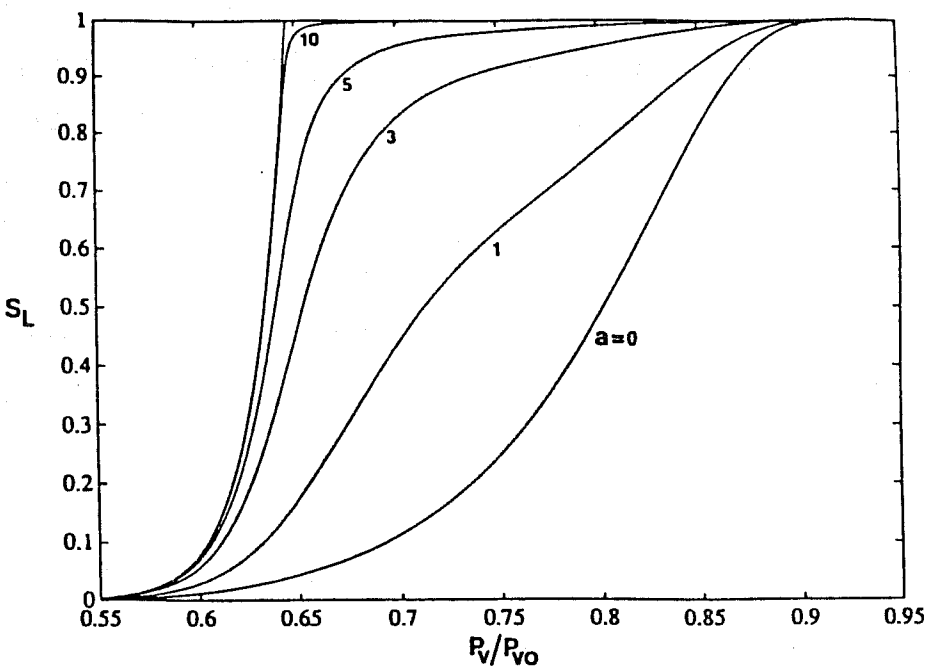

Figure 13: Model predictions of primary desorption curves for sorption of nitrogen for various values of f_q: $Z = 4$, $f_q = \exp(-aP_v/P_{vo})$.

2.4 DISCUSSION

An illustration of some of the above effects will be next presented. Figs. 12 and 13 depict calculated primary desorption curves for nitrogen at 78 ^oK. A Bethe lattice representation was used, with a coordination number $Z = 4$. Both bond and site sizes were assigned a Rayleigh distribution

$$\alpha_j(r) = \frac{\pi}{2}\frac{(r - r_{o,j})}{(r_{a,j} - r_{o,j})^2}\exp[-\frac{\pi}{4}\frac{(r - r_{o,j})^2}{(r_{a,j} - r_{o,j})^2}], \quad j = s, b, \tag{49}$$

with minimum and average values equal to $r_{o,b} = 10$ $\AA$ and $r_{a,b} = 20$ $\AA$ for bonds, and $r_{o,s} = 15$ and $r_{a,s} = 45$ for sites, respectively. Liquid saturations were evaluated using (47) along with the assumptions that only sites contribute to volume and the number fraction is also the volume fraction. The nucleation fraction f_q was held constant in one run (Fig. 12) and allowed to increase during the progress of desorption in the other (Fig. 13), according to the ad hoc expression, $f_q = \exp(-aP_v/P_{vo})$. To a different degree, both cases reflect the increasing likelihood of heterogeneous nucleation as the relative pressure decreases. We note no discernible differences in the results of these two different models. Both figures show that the desorption isotherm may rapidly lose its percolation character, provided that sufficient nucleation is allowed. The deviation resembles vapor compressibility [89] or finite size [109] effects. Similar effects exist in secondary desorption.

In the above, the nucleation fraction was left largely arbitrary. In reality, this is in general not the case, as pointed out by the simple model of Section 2.2.2. To illustrate the difference, nucleation effects corresponding to (16) are shown in Fig. 14, with all other parameters held constant. It is recalled that the parameter β is the ratio of pit size to pore size, in general a small number (e.g., 0.1-0.3). For the latter range, it is suggested from the results of Figure 14 that nucleation effects in capillary desorption may not be overemphasized. Equivalently, if either one of the previous ad hoc models were to be used, constant fraction f_q should be not greater than 0.05, while parameter a should be not smaller than 5. Of course, the self-similarity and uniformity assumed in (16) are not expected to hold in general, although the former is often a property of fractal structures. A more sophisticated model may perhaps be constructed with the parameter β being a distributed variable, to reflect wettability nonuniformity, and the additional increase in the fraction of activated nucleation sites upon a pressure decrease.

As stressed previously, homogeneous nucleation should be negligible in properly designed desorption experiments, while effects of heterogeneous nucleation may be present, since the latter is

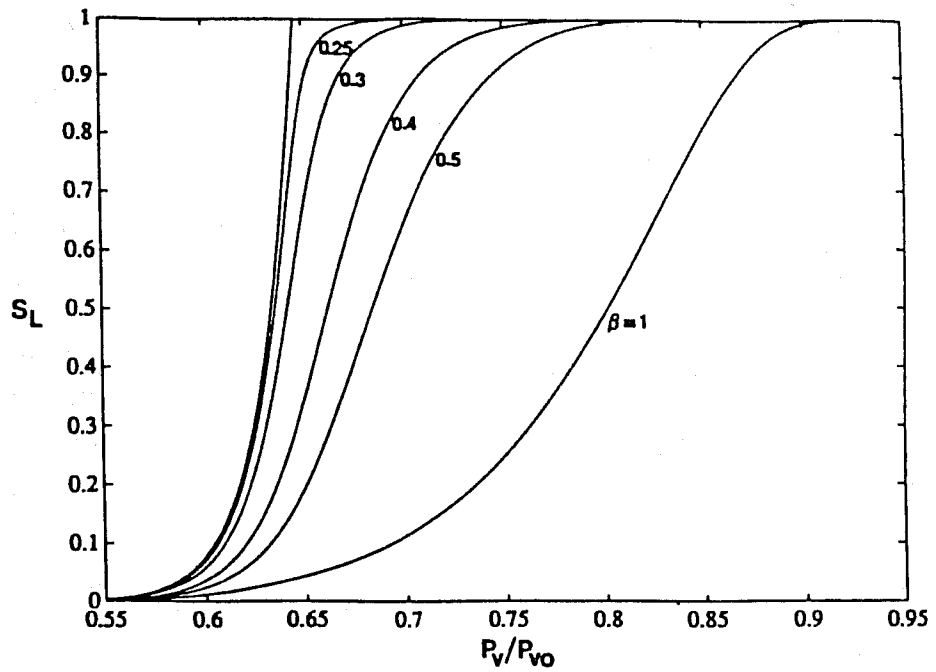

Figure 14: Model prediction of primary desorption curves for sorption of nitrogen for various values of β: $Z = 4$.

size-specific. As stressed above, and for typical cases, this likelihood (f_q) is expected to be small in the range of relative pressures near the onset of desorption. At the same time, it should be kept in mind that, in porous media with long tails in the size distributions and with sufficient heterogeneity in wettability properties, heterogeneous nucleation effects can become comparable to percolation. Such may be the case in phase change processes in natural porous rocks (e.g., geothermal reservoirs).

The effect of arbitrary size distributions on secondary desorption is shown in Fig. 15. To illustrate a notable feature, distributions with a maximum cut-off size in nucleation-free ($f_q = 0$) processes were considered. We take Rayleigh-type statistics with $r_o = 10$, $r_a = 15$, and $r_{b,max} = 25$ $\mathring{A}$ for bonds, and 15, 25, and 45 $\mathring{A}$ for sites, respectively. All other parameters take the same values as those in Figs. 12, 13. We note that some of the secondary isotherms are flat for a range of relative pressures after the initiation of desorption, since no phase change would occur until the pressure is reduced to that corresponding to the largest pore throat. This feature is inherently absent in media satisfying (17) and it could be used to identify the largest throat size, provided of course that other effects (resolution, nucleation, compressibility, etc.) would not obscure the

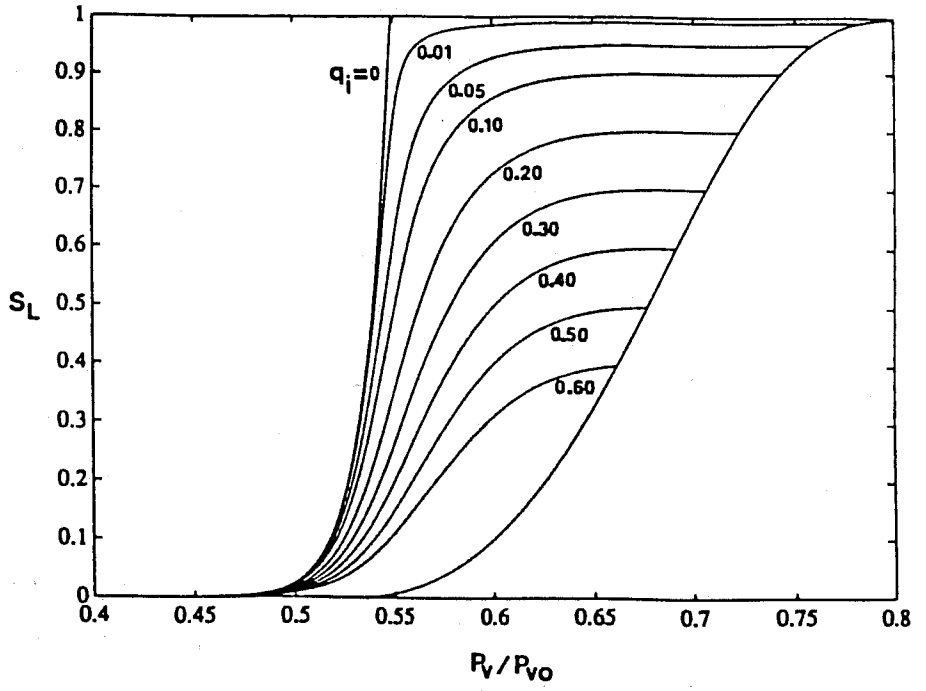

Figure 15: Model prediction of secondary desorption curves for sorption of nitrogen: $Z = 4$, $f_q = 0$.

interpretation of the data.

It should be emphasized that in a network model, bonds and sites can be assigned sizes at random provided that relation (32) is not violated. We recall that the first of the restrictions follows by noting that the fraction of sites in an interval (r_d, ∞) is, in general, greater than the fraction associated with bonds in the same size interval. Similarly, the second restriction expresses the fact that the fraction of bonds in the size interval $(0, r_d)$ is generally greater than the fraction associated with sites in the same size interval. When local hysteresis in bonds during the two processes (adsorption/desorption) is neglected, relationship (31) does not enter in any of the accessibility calculations although, of course, the distributions must still satisfy the restriction. Incorporating the local hysteresis into a network model does not appear to be as trivial as one might expect, even when the volumetric contribution of bonds is neglected. While primary processes and secondary adsorption remain unaffected by local hysteresis, secondary desorption would be altered. Additionally, if the bond volume is not ignored, all processes would be influenced. The significance of this effect should be investigated.

In reference [80], the relationship between the slopes of secondary desorption and primary

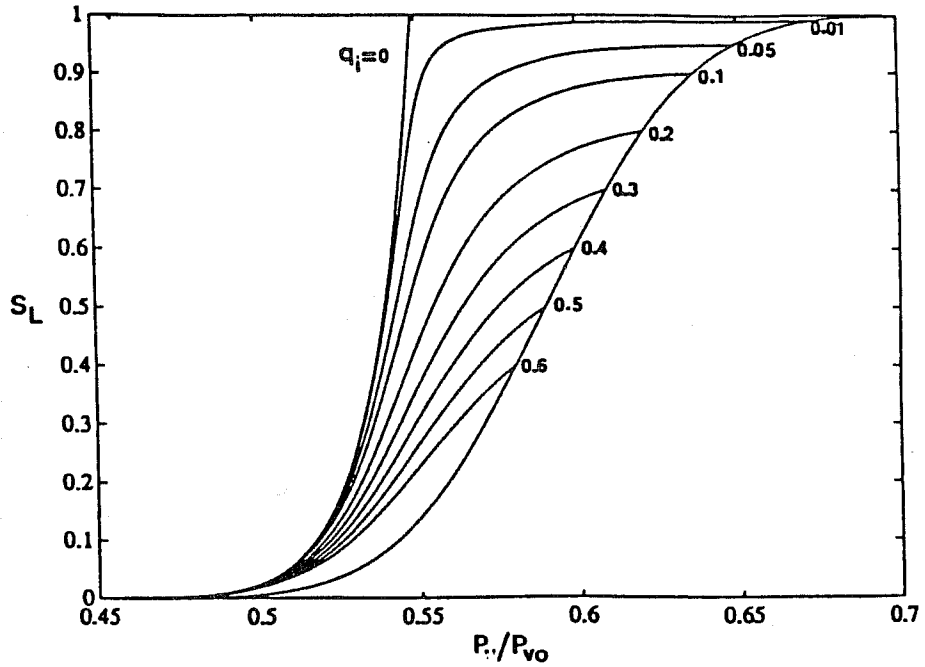

Figure 16: Model prediction of secondary desorption curves for sorption of nitrogen [$q = 1-(1-p)^5$]: $Z = 4$, $f_q = 0$.

adsorption at the onset of desorption,

$$\frac{dS_{L,SD}}{dS_{L,A}} = 1 - (1 - p_i)^{Z-1}, \tag{50}$$

was suggested as a means for the direct estimation of the throat density function $\alpha_b(r)$, subject to (17). The extension of (50) to the more realistic case (30) can be readily obtained:

$$\frac{dS_{L,SD}}{dS_{L,A}} = Z\frac{d(1-p_i)}{d(1-q_i)}\left[\frac{(1-q_i)}{(1-p_i)} - \frac{(1-q_i)^2}{(1-p_i)^2}\right]. \tag{51}$$

In contrast to (50), however, now it is a differential rather than an algebraic equation that relates data (LHS) to parameters (RHS). When (17) is assumed, (50) can be used to estimate p_i, and the adsorption data would yield the volume distribution $V_s(r)$. In the general case (33), on the other hand, an assumption about the volume distribution $V_s(r)$ is necessary, for further progress. The adsorption data may then yield q_i (hence, $\alpha_s(r)$), which is to be used for a (numerical) integration of (51). Fig. 16 portrays a typical schematic of secondary desorption isotherms for some model distribution satisfying (30). It can be reasonably argued that an assumption about the volume of a site is more justifiable than the postulate (17). For both cases, of course, the coordination number

Z must be properly chosen to match the percolation threshold. This may require a trial-and-error procedure. It also should be cautioned that relations (50), (51) have been derived based on a Bethe lattice representation and may not warrant application to other networks.

A limitation of the above analysis is the thermodynamic equilibrium assumed in the occupancy of pore elements, although one should also note the kinetic considerations in estimating nucleation effects. Equilibrium times associated with capillarity in porous media vary with the size distributions, among other variables, long times associated with systems with disparate scales [104]. Under this qualification, the above may be extended to other growth processes perhaps with some modifications. Nucleation in multicomponent systems in porous media (e.g., oil-gas mixtures) are interesting processes, where diffusion may introduce additional nonlocal effects. Application of the more general relationship (30, 31) to immiscible phase equilibria and flow (capillary pressure, phase permeabilities [56, 57]) would affect currently used models for quasistatic flow in porous media. Extensions to other related processes following the lines of [79] are obvious directions. Finally, the investigation of such processes in regular lattices may be worth considering.

2.5 SUMMARY AND CONCLUSIONS

The present study is an extension of previous work in capillary sorption processes in porous media. The issues of nucleation and pore size distributions were explored in more detail. It was concluded that nucleation may be negligible in typical vapor desorption experiments. Heterogeneous nucleation, being pore size-specific, has a higher likelihood to affect the desorption isotherms. Simple models were developed to account for the latter case in Bethe lattice pore networks. Deviations from a percolation behavior, previously attributed to compressibility [89] and finite size [109], can likewise be explained by nucleation.

Consideration of largely arbitrary pore size distributions leads to a nontrivial modification of the previous expressions. While primary desorption is unaffected, secondary processes are notably influenced, particularly in the presence of nucleation. It is suggested that such an effect is inherently present to any network model of porous media, and should be accounted for in the various capillary processes, where site occupancy and volumetric estimates are dictated from bond connectivity.

3 LIQUID-VAPOR PHASE CHANGE IN POROUS MEDIA

M. Parlar and Y.C. Yortsos

3.1 INTRODUCTION

Processes involving phase change in porous media are routinely encountered in numerous applications. The liquid-to-gas transition, in particular, is common to applications such as geothermal systems, thermal methods for oil recovery, solution gas-drive reservoirs and cavitation. With few exceptions, these phenomena have been treated on a phenomenological basis, where the important roles of the microstructure of the porous medium are largely ignored. And while there is wide recognition of the fundamental differences between internal and external drives, surprisingly little has been published to quantify such effects.

The change of phase in porous media is described by the two consecutive processes of nucleation and phase growth. For the porous media of interest to us, the nucleation mechanism is fundamentally identical to common nucleation, with due emphasis to heterogeneous nucleation (although see also Ref. [49] for phase transitions in tight porous media).

Bubble growth, on the other hand, is controlled by the pore wall curvature and geometry that may stabilize otherwise unstable gas bubbles. This is a basic difference to bubble growth in the bulk, a process studied in great detail since the pioneering works by Plesset and Zwick [85] and Scriven [93]. Additional parameters of importance in porous media involve the critical gas saturation, and the effect of imposed supersaturation (pressure decline or superheat in solution gas-drive or boiling) on the growth pattern of the gas phase. The geometry and topology of the porous medium constrains the growth of the new phase and poses novel problems.

In general, vapor-bubble dynamics are classified into two broad categories [84]: one involving vapor-bubble growth due to a reduction of the liquid pressure (sometimes to negative values, as in the case of homogeneous cavitation), and another involving vapor growth in a superheated liquid, corresponding to boiling. The two processes are physically similar in many respects: In addition to common inertia, viscous and surface forces, bubble growth is controlled by diffusion of the volatile species in the first case, and by diffusion (conduction) of heat in the latter. In this paper, however, our emphasis will be on the pressure reduction in a binary mixture consisting of a volatile (solution gas) and a non-volatile (oil) component, and we shall defer the analysis of boiling to a future study.

The body of literature on nucleation and bubble growth in bulk liquids is immense. A very selective and subjective review of relevant works will be briefly summarized here. The state of the art in homogeneous nucleation is reviewed by Binder [10] with emphasis on Monte-Carlo methods. From an engineering viewpoint, phase transitions are elucidated by Springer [98]. Heterogeneous nucleation is reviewed by Cole [22] who summarized the original ideas by Fisher [43], and Bankoff [5] in the context of boiling, and by Crum [26] in the context of cavitation. Additional contributions to heterogeneous nucleation were made by Ward and Forest [111], and by Forest [46] for a binary system, the homogeneous nucleation of which was first presented by Ward et al [110]. The reduction of the vapor pressure of the less volatile component (Kelvin equation) and the nuclei stability were thoroughly analysed. The homogeneous nucleation of multi-component mixtures was reviewed by Blander and Katz [13], and by Thome and Shock [103]. Effects of phase behavior in reducing the effective supersaturation were also highlighted.

Bubble growth in supersaturated systems has been treated in the seminal work by Scriven [93], where diffusive effects are considered in the absence of inertia, viscous and surface forces. Closed-form asymptotic solutions are obtained for the growth of bubbles in the bulk. The growth of an isolated spherical bubble by solute diffusion was numerically studied in the important papers by Szekely and Martins [101], and by Szekely and Fang [100]. These authors provide a comparative study of the significance of inertia, viscous, mass transfer, and non-equilibria effects in bubble growth.

A useful review of bubble dynamics in general, with emphasis on cavitation was presented by Plesset and Prosperetti [84]. These authors addressed in a subsequent publication [87] vapor growth in a superheated liquid. The various asymptotic, perturbation and approximate techniques in bubble growth and their domain of applicability were systematically appraised by Vrentas and Shin [107, 108]. Significantly fewer are studies in the growth of a population of bubbles, where various size bubbles compete for a fixed mass of solute through diffusion. We cite the work by Engelking [37] who applied coarsening ideas by Lifshitz and Slyozov [66] as also confirmed by Marqusee and Ross [68] to infer that initially broad population densities asymptotically peak to a single-(large) size distribution.

In sharp contrast, the literature on phase change and bubble growth in porous media is substantially leaner. Early experimental studies on nucleation focused, rather inconclusively, on the effect

of the rate of pressure decline [60, 63, 99, 115]. Similar experiments using glass micromodels were recently reported [28]. Theoretical issues of nucleation in the liquid-to-vapor transition in porous media were addressed in recent studies by Parlar and Yortsos [80], and by Hirasaki et al. [59], in the contexts of vapor desorption and cavitation in a capillary centrifuge. Both works emphasize the importance of heterogeneous nucleation in porous media. Parlar and Yortsos [80, 81] also proposed a quantitative nucleation model for estimating nucleation fractions.

Fundamental studies on the subsequent growth of the vapor phase are also sparse. The early literature reports on laboratory experiments that attempt to simulate a solution gas-drive process. The importance of diffusion was singled out by Handy [53]. Visualization experiments were reported by Chatenever et al. [19], and by Dumore [34], while an attempt to analyze the process was undertaken by Abgrall and Iffly [1]. The latter work, as well as that of Epstein [38] in the context of inertia-controlled bubble growth, essentially treat the porous medium as an equivalent "bulk" system, with limited regard due to the microgeometry. Bubble growth controlled by capillarity was considered in recent studies by Parlar and Yortsos [81, 80] on capillary desorption.

It must be apparent from the above brief review that the issues of phase change and vapor-bubble growth in a porous medium are far from being sufficiently explored. In view of the routine occurrence of such phenomena, an investigation of their basic features would be a worthwhile undertaking. This is the main objective of this section. As previously noted, we shall consider the phase change in the context of the solution gas-drive process, which for our purposes will be taken to consist of a liquid phase containing a volatile and a non-volatile species, and a gas phase containing the volatile component. The process is driven by a pressure decline below the "bubble point", P_b, of the mixture to the value P_∞. We shall examine the response of the system, namely nucleation and bubble growth, to the imposed supersaturation $\Delta P = P_b - P_\infty$.

By necessity, this section is presented in two parts, one on nucleation and the other on the subsequent gas-phase growth. The part on nucleation addresses issues of heterogeneous nucleation, the stability of nuclei in cavities along the pore walls, issues of nucleation rates and critical supersaturation. The part on phase growth is a study of the dominant processes summarized in terms of dimensionless parameters. Inertia, viscous, capillary and mass transfer effects are discussed in terms of the imposed supersaturation. Equilibrium states and their stability are investigated. We identify the pertinent regimes appropriate to specific cases and the associated growth patterns. In

the limit of quasi-static growth at low supersaturations, analytical expressions are proposed for critical gas saturation and gas relative permeabilities in terms of the structural characteristics of the porous medium.

3.2 NUCLEATION

The basic ideas underlying nucleation are common to any phase change. Here we shall briefly summarize essentials of nucleation theories in the context of liquid-to-vapor transition and, we will subsequently apply to the solution gas drive process in porous media.

Current homogeneous nucleation theories rely on the theory of fluctuations for the formation of critical size nuclei (embryos) [10]. This is a modern extension of the phenomenological approach [22, 98], which uses traditional thermodynamics and kinetics to determine equilibrium sizes, their stability, and rates of formation. As an example, we consider (metastable) equilibrium gas bubbles in the bulk of a liquid containing two species, only one of which (component 1) is volatile. Thermodynamic (mechanical and chemical) equilibrium defines the radius of curvature of the gas bubble.

$$P_V = P_L + \frac{2\gamma}{r}, \tag{52}$$

$$r = \frac{2\gamma}{KC - P_L}, \tag{53}$$

where P_V and P_L are the pressures in the gas and the liquid, respectively, and K is the solubility constant (see also below). For a fixed concentration C of the volatile species, (2) relates uniquely the equilibrium radius to the liquid pressure. The above is also valid for any equilibrium vapor-liquid interface including those in a cavity (typical of heterogeneous nucleation). When component 2 is slightly volatile, a similar expression can be also derived [110], that generalizes Kelvin's equation.

3.2.1 Gas Solubility

Implicit in the above derivation is the use of linear phase relations. Phase equilibria across a flat interface between a liquid and its vapor are in general quite complex. For simplicity, we shall postulate a linear relationship between the concentration of the volatile component (solution gas) at equilibrium, C_{sat}, and the liquid pressure, the latter being equal to the pressure of the vapor

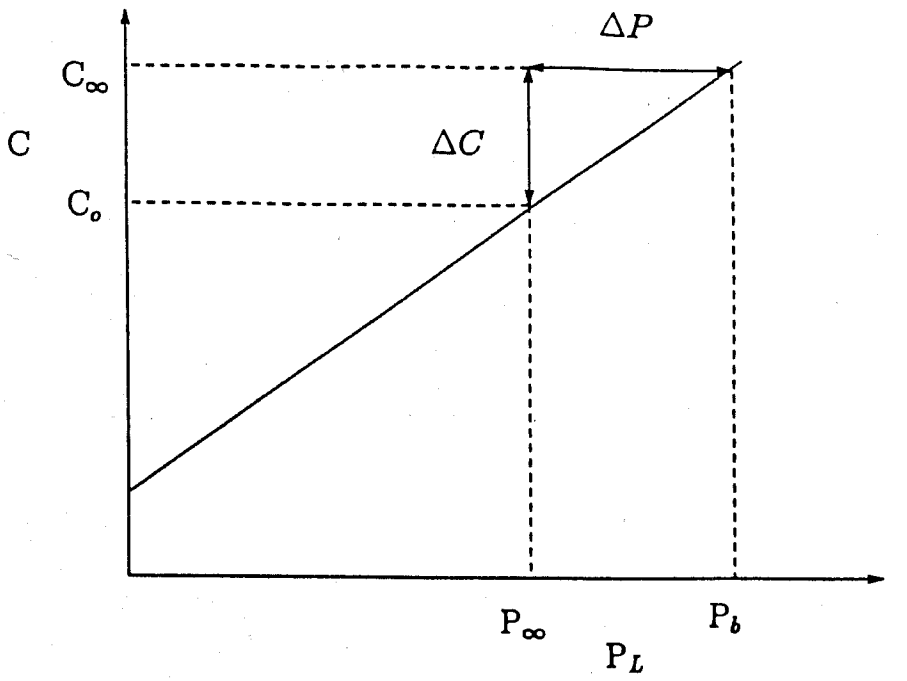

Figure 17: Gas solubility vs. pressure schematic.

when the interface is flat

$$P_L = KC_{sat}. \tag{54}$$

It follows that $P_b = KC_\infty$. A given pressure supersaturation ΔP may then be translated into an equivalent concentration supersaturation $\Delta C = C_\infty - C_o$ (Fig. 17). Although various laws based on an "ideal solution", such as Raoult's or Henry's laws, and typical gas-oil ratio curves (e.g., Fig. 3.1 in [25]) can be invoked to justify this approximation, we shall refrain from doing so, particularly since for small supersaturations, a linear relationship between pressure and concentration increments can always be assumed. Of course, the approximation can be severe for large supersaturations.

A more important issue in our context is the value of K, which for the system of Fig. 3.1 in [25], was estimated to be of the order of 3.75×10^4 psi/gr/cc. The latter value was obtained by using the arbitrary ratio of 6 between the molecular weights of solution and solute and taking the liquid density to be 0.8 gr/cc. Substantially more refined methods for phase equilibria can of course be used for an accurate estimate of the solubility constant K and its variation.

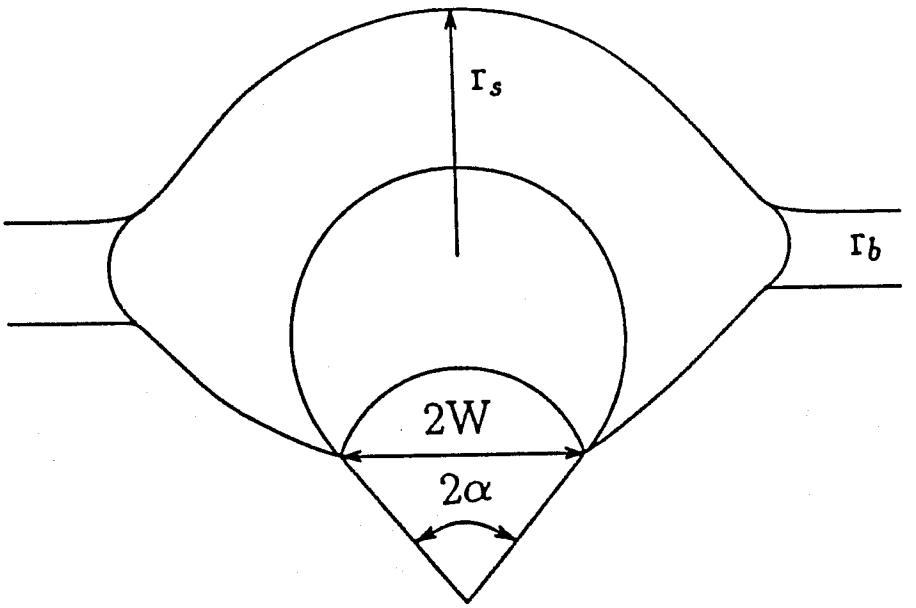

Figure 18: Schematic of a nucleation site in a host pore body.

3.2.2 Nucleation Rates

An important issue relevant to nucleation is the rate of generation of critical nuclei. In the case of homogeneous nucleation, classical kinetic theories can be used with relative success to predict the formation rate

$$J = \frac{dN}{dt} = \frac{N_o k_B T \rho_L \phi}{hM} \exp(-\frac{\Delta F}{k_B T}), \tag{55}$$

where $\Delta F = 4\pi\gamma r_c^2/3$ is the free energy to form the equilibrium nucleus, k_B and h the Boltzmann and Planck constants, respectively, and N_o is the Avogadro number. For heterogeneous nucleation, two approaches have been proposed, both of which rely on the existence of surface heterogeneities or nucleation sites (e.g., conical cavities) that are not liquid-wet. The most popular approach postulates that such sites contain pre-existing (or trapped) vapor, provided that certain requirements on the conical and contact angles are met [26]. In such a case, the issue of rate of nuclei formation is non-existent and the condition for nucleation is obtained by directly applying (2), with the radius of curvature evaluated as the conical pit mouth radius W (Figure 18)

$$KC - P_L = \frac{2\gamma}{W}. \tag{56}$$

The other approach parallels homogeneous nucleation in that pre-existing vapor is not required, although surface sites with the desired wettability and geometry must exist [22]. A nucleation rate expression similar to (55) is conjectured

$$J = \frac{dN}{dt} = K_{het} \exp(-\frac{\Delta F}{k_B T} f), \tag{57}$$

where K_{het} is a kinetic constant [43], and f is a function of site geometry and wettability, ranging between 1 and 0 in the limits of homogeneous and perfect heterogeneous nucleation, respectively. Equation (57) can then be used to calculate the nucleation pressure, or the critical supersaturation, usually defined by arbitrarily assuming $J = 1$ nucleus/sec-cc

$$r_N = (\frac{3k_B T \ln K_{het}}{4\pi\gamma f})^{1/2}. \tag{58}$$

The precise value assigned to J or K_{het} is immaterial [2]. For example, for the homogeneous nucleation of a liquid with molecular weight 100 and density 0.7 g/cc at 200 °F, the change of J from 1 to 10^8 reduces the nucleation radius from 21.7 to 19 $\mathring{A}$, clearly a negligible change.

3.2.3 Nucleation in Porous Media

During a liquid-to-gas transition in porous media, the occupancy of pores by the gas phase occurs either through access to bulk vapor (as in external gas/steam drive) or through a nucleation process inside the pores. The question arises, therefore, as to what nucleation mechanisms would be typically expected in a porous material.

Homogeneous nucleation can be discounted, since it requires the drastic conditions of absence of impurities, perfectly smooth and liquid wet solid surfaces, and no trapped gases. Moreover, as previously pointed out the nucleation radius for homogeneous nucleation is of the order of a few nm, with corresponding supersaturations of several thousand psi. Thus, unless the pore sizes are of the same order, homogeneous nucleation can be disregarded as a mechanism for bubble formation.

The selection of heterogeneous nucleation as the dominant mechanism drastically reduces the critical supersaturation, as interfaces of large radius of curvature can form in surface cavities, given the proper wettability conditions. Unfortunately, additional simplifications are necessary, if a quantitative model is to be further developed.

We proceed by representing the surface roughness by uniform wettability conical cavities, among which only the largest one needs to be considered. The contact angle in the cavity may take any

nonzero, but preferably high, value while complete wetting by liquid is assumed in the main pore body (Figure 18). Using elementary geometry, the volume of the bubble can be related to the radius of the gas-liquid interface. Figure 2 qualitatively portrays such a relationship for a hydrophilic cavity ($\theta - \alpha < \pi/2$), that satisfies the relation $W/r < \cos(\theta - \alpha)$. Hydrophobic cavities, first introduced by Harvey et al. [54], were considered by Hirasaki et al. [59]. To proceed further, we will assume that a self-similarity exists between the maximum size cavity and the size of the host pore body. Thus, the ratio $\beta = W/r$ will be taken constant. In the absence of additional information, this assumption is a reasonable one. Although the ensuing results are subject to this premise, however, most of the expressions obtained are also independently valid.

Consider now the nucleation process in a conical cavity, with curvature corresponding to the equilibrium value given by (56). The stability of mechanical equilibrium in gas-liquid interfaces in cavities was examined by various authors [46, 59, 111]. A quite general result is obtained: mechanically stable interfaces ($d^2\Delta F/dV_G^2 > 0$) require configurations such that $dr/dV < 0$, while mechanically unstable interfaces ($d^2\Delta F/dV_G^2 < 0$) correspond to $dr/dV > 0$. Thus, for the hydrophilic cavity shown in Figure 18 the gas-liquid interface is unstable within the cavity, but becomes stabilized at the pit mouth. Similar conclusions are drawn for the hydrophobic cavities with pre-existing vapor (where, now, the interface is stable inside the cavity as well). In both cases, the pit mouth radius W is the smallest possible radius for a stable equilibrium interface to exist in the cavity. Hence, W dictates the critical supersaturation (56), beyond which the pore body is substantially filled with vapor. It follows that the occupancy of a pore body via nucleation would occur at a specific supersaturation corresponding to (56) and, thus, be uniquely correlated to the pore body size, if the assumption on β is retained.

The fraction of pores that would nucleate (nucleation fraction) at a radius r_d corresponding to a given supersaturation (56) is thus

$$f_q = b\frac{\int_{r_d/\beta}^{\infty} \alpha_s(r)dr}{\int_{r_d}^{\infty} \alpha_s(r)dr}. \tag{59}$$

A constant b can also be introduced to allow favorable wettability conditions only for a fraction of such pits. This expression is needed for the evaluation of the accessibility functions [80, 81] that were derived independent of the distribution of cavity sizes. Figure 19 shows the relationship between β and f_q for b = 1 and for the pore size distributions shown in Figure 20. Relatively small

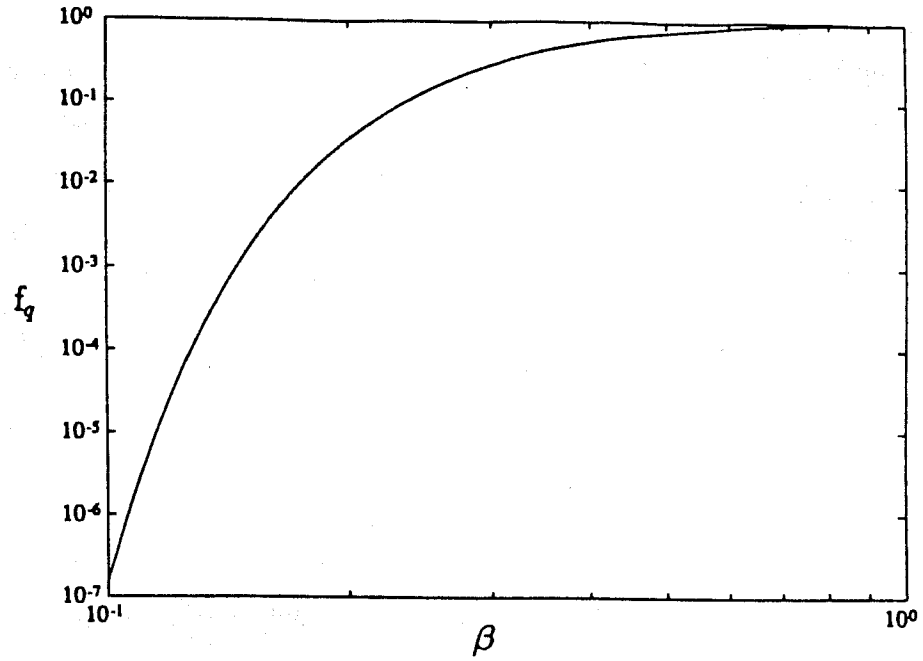

Figure 19: Nucleation fraction at threshold vs. β ($Z = 6$).

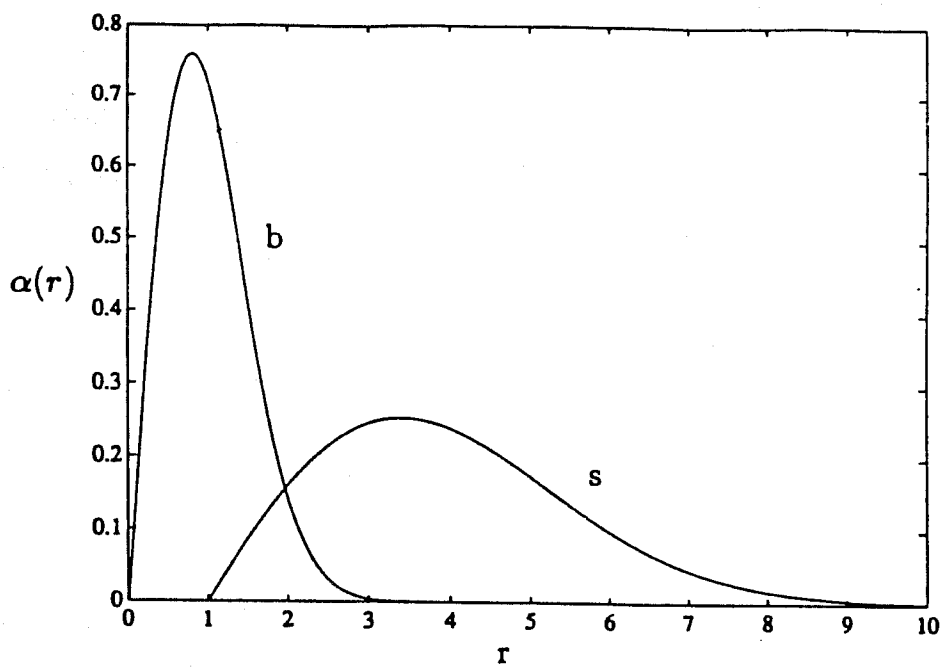

Figure 20: Pore body and pore throat size distributions.

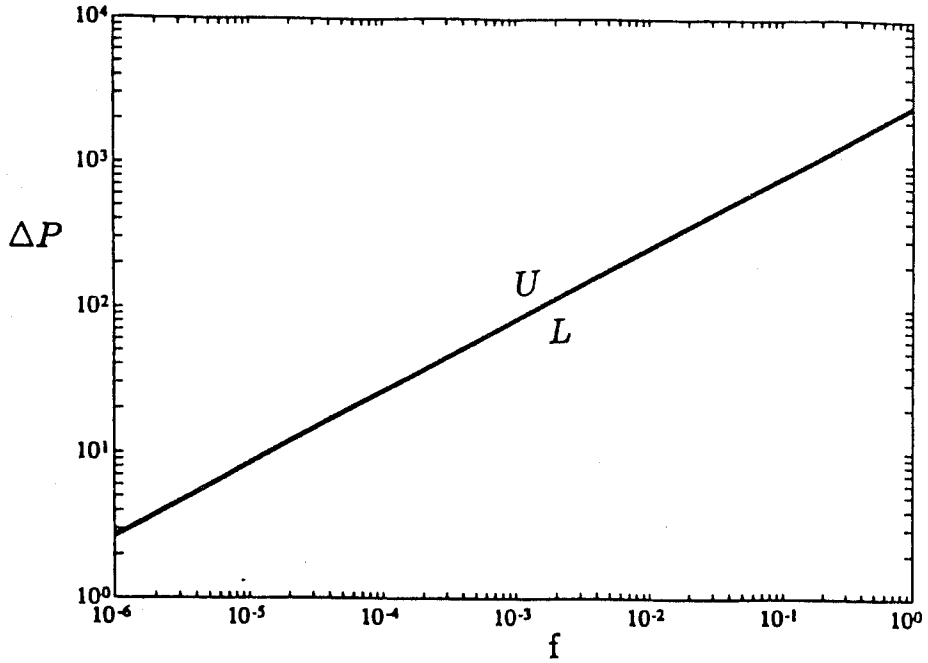

Figure 21: Critical supersaturation vs. f for various decline rates: $a = 1$ (U), $a = 10^{-4}$ psi/sec (L).

values of f_q are obtained for small β for the particular distributions taken. This model will later be used to calculate critical gas saturations and relative permeabilities.

3.2.4 Pressure Decline Rate

The effect of pressure decline rate on the critical supersaturation has been pursued by several investigators. In the absence of issues other than strict nucleation, an estimate of its effect can be directly obtained from the above analysis. For the present purposes, we shall define critical supersaturation as that necessary for the occupancy of a single (or a few) pore(s) with gas, although we are aware of other definitions that have also been used in the literature. If preexisting vapor exists in hydrophobic conical cavities, the activation of the latter is almost instantaneous as soon as the proper supersaturation is applied, thus no effect of pressure decline rate should be observed. The possibility of some effect may exist, in the case of hydrophilic cavities with no initially trapped vapor. A simple analysis, however, indicates that the effect is negligible.

Assuming that the nucleation rate expression (57) is applicable,

$$\frac{dN}{dt} = K_{het} \exp[-\frac{\lambda}{(\Delta P)^2}], \tag{60}$$

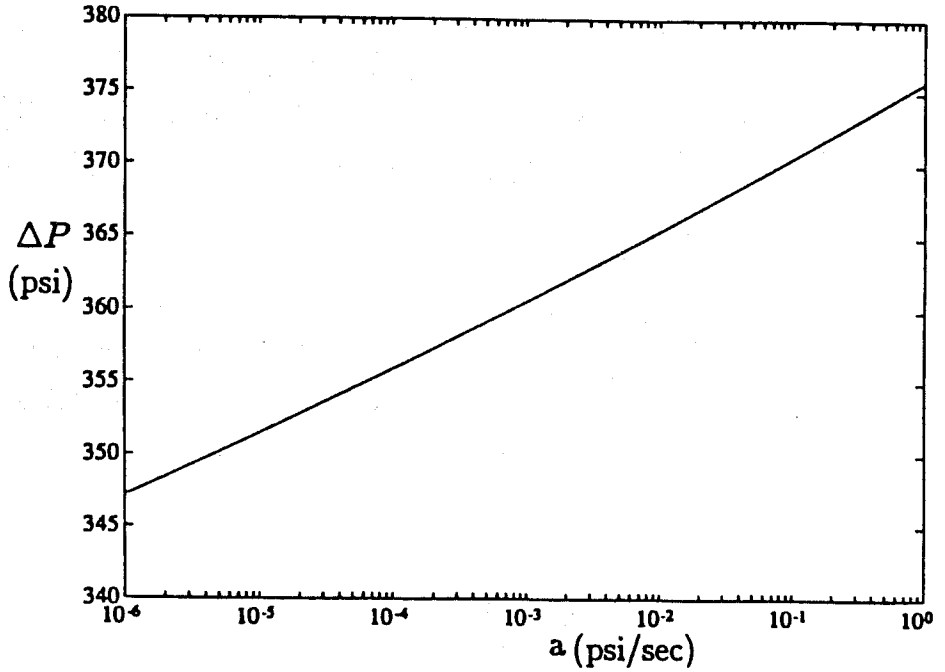

Figure 22: Critical supersaturation vs. pressure decline rate for $f = 0.1$

where $\lambda \doteq 16\pi\gamma^3 f/(3k_BT)$. For a pressure decline rate of the form $\Delta P = at$, an integration of (60) yields

$$\frac{aN}{K_{het}\sqrt{\lambda}} = \frac{1}{x}\exp(-x^2) - \sqrt{\pi}\,\mathrm{erfc}(x), \tag{61}$$

where $x = \sqrt{\lambda}/\Delta P$. The solution of (61) for $N = 1$ (arbitrarily selected but without loss in generality, as pointed out above) is shown in Figure 21 for various values of the wettability parameter f and the decline rate a. It is noted that, although the effect of f is very significant (Figure 21), as indeed expected, the pressure decline rate has a negligible influence on the supersaturation, even for variations spanning 5 orders of magnitude (Figure 22). One concludes that the critical supersaturation required for nucleation is a property of the liquid and the porous medium, and practically independent of external parameters.

3.2.5 Pore Body Occupancy

Upon establishment of the critical supersaturation, the bubble interface becomes mechanically unstable, thus growth occurs until the bubble radius reaches the pore body size (or detaches from the pit). Further growth results into a decreasing radius of curvature, due to the converging pore walls,

D	10^{-5} cm^2/sec
H_o^{-1}	50 μm
k	1 darcy
K	3.75×10^4 psi/gr/cm^3
M_1	20 gr/mol
P_b	2000 psi
T	30 °C
γ	30 dynes/cm
μ	10 cp
ρ	0.8 gr/cm^3

Table 1: Parameter values for bubble growth

and such configurations will be stable, if they would also happen to correspond to the equilibrium curvature as specified by the existing supersaturation. As shown in a later section, such interfaces are also stable to mass transfer. If the supersaturation is too large, invasion of surrounding pores by vapor will ensue, until an appropriate stabilizing pore geometry is encountered. It is worthwhile to stress this important characteristic of porous media, namely the stabilization of otherwise (in the bulk) unstable interfaces. As a closing note we demarkate the conditions necessary for the bubble not to detach from the cavity, before it grows to the pore body size. We shall balance surface and gravity forces to obtain

$$r < (\frac{3\beta c_t}{4}\frac{\gamma}{\rho_{LG}})^{1/2}, \tag{62}$$

where c_t is a cavity perimeter constant, equal to 2 for a flat surface. For the values of Table 1, a pore size r greater than about 400 μm is required in order for gravity-induced detachment to be of concern.

3.3 BUBBLE GROWTH

The preceding section described the conditions for the occupancy by the vapor phase of one (or a few connected) pore bodies. In the next part, the study of the growth of the vapor phase is undertaken.

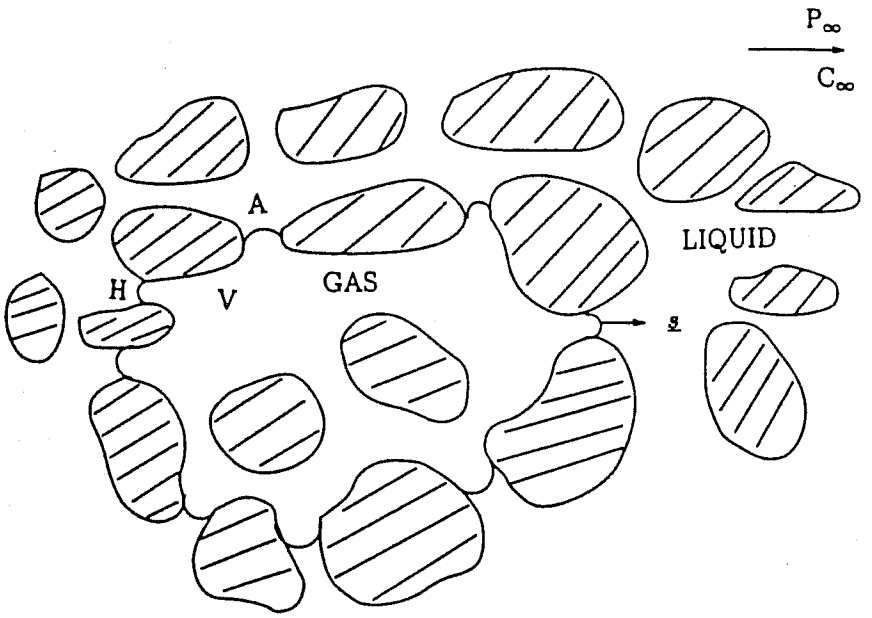

Figure 23: Schematic of a gas bubble in a porous medium.

For convenience, an isolated "bubble" is first, considered. An extension to a population of bubbles is discussed for a special case in a later section.

3.3.1 Single Bubble in Porous Medium

We shall consider the growth of a single vapor bubble occupying a small part of an infinitely large porous medium, the rest of which is filled with liquid (Figure 23). For the present purposes, other nucleation events are suppressed, and we need not specify in detail the conditions for the existence of the initial bubble. From its definition, the bubble is connected, although not necessarily spherical (although individual interface menisci are spherical). A supersaturation $\Delta P = P_b - P_\infty$, in general variable with time, but for the moment considered fixed, is assumed to apply far from the bubble. The system is taken "infinitely large" so that the solute concentration far from the bubble, C_∞, is constant and equal to the solubility at pressure P_b.

3.3.2 Equilibrium States

Preceding an analysis of growth, the study of possible equilibrium states is required. The question posed is whether a gas bubble can exist in a porous medium in stable equilibrium with a super-

saturated liquid. It is well known that a vapor bubble in an unbounded bulk liquid is in unstable mechanical equilibrium and will either grow indefinitely or collapse. Under the premise of chemical equilibrium, the stability of gas-liquid interfaces in the presence of constraining surfaces has been examined, as discussed in the nucleation part above. Those predictions imply that an equilibrium gas bubble located such that its mean curvature lies between the smallest pore body curvature (largest radius) and the smallest pore throat curvature (largest radius) associated with that pore body, is stable. Here, we shall also consider the stability of the interface to mass transfer.

We take a gas bubble in equilibrium, occupying volume V_o, at pressure P_{vo} and containing n_o moles. Concentration and pressure in the liquid are spatially uniform and equal to C_∞ and P_∞, respectively. Ideal gas conditions and linear phase equilibria dictate

$$KC_\infty V_o = n_o RT, \tag{63}$$

where R is the ideal gas constant, while mechanical equilibrium at the gas-liquid interface requires spherical-shape menisci of constant mean curvature H_o

$$KC_\infty - P_\infty = 2\gamma H_o. \tag{64}$$

Since the RHS in the above measures the capillary pressure of the porous medium, the present analysis is effectively meaningful only for low supersaturations. Equilibrium states at high supersaturations correspond to almost complete occupancy by the gas phase (with the possible exception of thin films). Although conditions of low supersaturation are certainly violated in typical laboratory experiments, they are more likely to be satisfied in a typical field case, where pressure decline rates on the order of psi/day or less may be common.

Consider small perturbations in the curvature of an equilibrium vapor-liquid meniscus located in a converging pore element (pore body to pore throat). Under the assumption of a constant liquid pressure and fast kinetics at the interface, an increase (decrease) in curvature implies a corresponding increase (decrease) in gas pressure, thus, an increase (decrease) in the concentration at the interface. A concentration gradient in the liquid phase develops that leads to a solute mass flux away from (towards) the interface, hence to a reduction (increase) in the gas phase volume. For a converging pore element, the latter implies a restoration of the initial curvature, thus stability. In the opposite case of a diverging pore, the mass transfer compounds the disturbance, and at least to first order, the equilibrium state is unstable.

Similar arguments also apply in the case where the gas phase surrounds a liquid "drop" and the liquid can escape through thin films. There, the liquid pressure may be taken constant and the previous approach is applicable. In the absence of thin films, however, the liquid compressibility becomes important. The decrease in liquid volume upon advancement of the interface results into a substantial increase in liquid pressure. When the curvature also increases (as is the case in converging pores) a concommitant increase in gas pressure and interface concentration follow, giving rise to the previous mass transfer argument. Again, such interfaces are stable to mass transfer. In the case of interfaces in diverging pores, there is a decrease in the interfacial curvature. The concommitant change in the gas phase pressure, however, is expected to be positive

$$\frac{dP_V}{dH} = (\gamma - \frac{dV_L/dH}{V_L c_p}) < 0, \tag{65}$$

due to the small liquid compressibility, c_p, which easily counterbalances capillary effects. A higher interface concentration follows, thus leading to a stabilizing effect. Therefore, in the absence of communication with the bulk, equilibrium gas-liquid interfaces surrounding liquid droplets are stable to mass transfer, regardless of the particular volume-curvature relationship.

3.3.3 Bubble Growth

The growth of a vapor bubble in a porous medium is controlled by forces similar to those in the bulk, namely inertia, viscous, surface and pressure. Supersaturation in the liquid drives the process, while the specific pore geometry of the porous medium constrains the growth pattern obtained. We shall, first, study growth due to a supersaturation ΔC, brought about by an imposed step change in the liquid pressure, ΔP. Following Szekely and Martins [101], we shall characterize the growth process in terms of suitable dimensionless groups. Typical parameter values used are listed in Table 1.

3.3.4 Dimensionless Groups

Denoting by H_o a reference mean curvature of the menisci of the initial bubble, we define the key dimensionless parameter

$$\Phi = \frac{2\gamma H_o}{\Delta P}. \tag{66}$$

Small supersaturations are comparable to surface forces and lead to O(1) or greater values in Φ, while large supersaturations correspond to $\Phi \ll 1$. In the present illustrations, the smallest value that Φ can attain is 10^{-5} (for $\Delta P \approx 2000$ psia). A dimensionless expression for the driving force for bubble growth is the Jacob number

$$\mathrm{Ja} = \frac{\Delta C}{\rho_G(P_\infty)}, \tag{67}$$

which can be also expresed in terms of Φ by use of (66) and the ideal gas law

$$\mathrm{Ja} = \frac{2\gamma RTH_o}{KM_1P_\infty}\frac{1}{\Phi}. \tag{68}$$

For relatively small supersaturations, $\Delta P \ll P_\infty$, we take $P_\infty \approx 2000$ psia, so that at these conditions the reference Jacob number is (Table 1)

$$\mathrm{Ja} = \frac{10^{-4}}{\Phi}. \tag{69}$$

Thus, for a small supersaturation, Ja is considerably less than O(1). On the other hand, for moderate and large supersaturations, P_∞ can be significantly small and Ja may reach values as high as 20000 (when P_∞ is O(1 psia)), or even higher at conditions of vacuum. Although Ja indicates the direction of growth, an additional useful indicator is the measure of diffusion vs. inertia effects expressed through the parameter

$$B = \frac{\mathrm{Ja}^2}{\sqrt{G}}, \tag{70}$$

where

$$G = \frac{R_o^2\Delta P}{\rho_L D^2}, \tag{71}$$

and R_o is the "bubble radius". According to Szekely and Martins [101], $B \ll 1$ signifies mass transfer (diffusion) control, while $B \gg 1$ denotes inertia-controlled process. In our case, a conservative estimate of B yields

$$B = 10^{-5}\mathrm{Ja}^2\Phi^{1/2}, \tag{72}$$

For small supersaturations, $B \ll 1$ and the process is clearly mass transfer controlled. Inertia control may set in the process only under severe conditions, most likely requiring application of vacuum. For example, even for a sharp reduction of P_∞ to 1 atm, the estimated value of B is only

O(1). Although atypical for a field case, processes with not small B may be used in laboratory experiments.

Significant other parameters are the Schmidt number of the liquid phase

$$\mathrm{Sc} = \frac{\mu}{\rho D} \approx 1.25 \times 10^4, \tag{73}$$

indicating fast momentum transfer compared to mass transfer, and a modified capillary number

$$N_{ca} = \frac{\mu D}{\gamma R_o} \approx 10^{-5}. \tag{74}$$

In the above, mass transfer control has been assumed in estimating liquid velocities and the "bubble radius" was conservatively approximated by 50 μm. We expect smaller values for N_{ca} when the bubble size is larger and when the supersaturation is smaller. In the latter case one may use a different time scale instead (see also below)

$$N_{ca} = \frac{\mu D}{\gamma R_o}\mathrm{Ja}^2, \tag{75}$$

which, for small Ja, unequivocally establishes capillary control in the momentum balance.

3.3.5 Bubble Growth Regimes

In discussing the growth of gas bubbles we shall proceed in order of increasing complexity from low to high supersaturations.

Low Supersaturations, $\Delta P \ll P_\infty$

We consider a small step reduction ΔP of the initial liquid pressure P_b to the value P_∞, which is still large for condition $\Delta P \ll P_\infty$ to be valid. This should be the case for field operations at low pressure decline rates (see also below). At these conditions, the growth process is mass transfer-controlled, inertia and viscous forces are negligible, and the solution density may be considered constant in the diffusion equation. The relevant equations in dimensional notation read as follows. In the pore space occupied by the liquid, one has

$$\frac{\partial C}{\partial t} + \underline{u} \cdot \nabla C = D\nabla^2 C, \tag{76}$$

$$\nabla \cdot \underline{u} = 0. \tag{77}$$

The gas phase is taken at spatially constant pressure P_V and has volume V_o. Denoting by A the gas-liquid interface (which excludes possible thin films), a mass balance at the interface gives

$$\rho_G \underline{u} \cdot \underline{s} = D \nabla C \cdot \underline{s}, \tag{78}$$

and in integrated form

$$\frac{d}{dt}[V \rho_G] = D \int_A \underline{s} \cdot \nabla C dA, \tag{79}$$

where $\underline{s}$ is the outwards pointing (from gas-to-liquid) normal. Ideal gas conditions, linear phase behavior and the Laplace equation complete the description

$$\rho_G = \frac{P_V M_1}{RT}, \tag{80}$$

$$P_V = KC\,|_A\,, \tag{81}$$

$$P_V = P_\infty + 2\gamma H, \tag{82}$$

where H is the mean curvature at the gas-liquid boundary, assumed prescribed by the pore geometry. The latter equation represents the momentum balance with negligible inertia and viscous effects. Boundary and initial conditions

$$\begin{aligned} C &\to C_\infty \quad \text{at} \quad \underline{r} \to \infty, \\ \underline{u} &\to 0 \quad \text{at} \quad \underline{r} \to \infty, \\ C &= C_\infty \quad \text{at} \quad t = 0, \end{aligned} \tag{83}$$

along with a specification of the initial "bubble" configuration are also needed.

The above system is, of course, too complex to be solved by simple methods. Fortunately, additional simplifications can be made with an appropriate dimensionless formulation. We scale spatial distance by an initial "bubble radius" R_o, time by $R_o^2/D\mathrm{Ja}$ and velocity by $D\mathrm{Ja}/R_o$, bubble volume by R_o^3 and interfacial area by R_o^2, and interfacial curvature by H_o (which is generally unrelated to R_o). We further define dimensionless concentration and gas pressure

$$\Sigma = \frac{C - C_o}{\Delta C}, \tag{84}$$

$$\Pi = \frac{P_V - P_\infty}{\Delta P}, \tag{85}$$

to obtain

$$\mathrm{Ja}\left(\frac{\partial \Sigma}{\partial \tau} + \underline{\nu} \cdot \nabla \Sigma\right) = \nabla^2 \Sigma, \tag{86}$$

$$\nabla \cdot \underline{\nu} = 0, \tag{87}$$

$$\Sigma = 1 \quad \text{at } \infty \text{ and at } \tau = 0, \tag{88}$$

where the nomenclature is self-evident, $\underline{\nu}$ being the dimensionless velocity, while at the gas-liquid interface we have

$$\nu_s = \frac{\partial \Sigma}{\partial s}, \tag{89}$$

$$\Pi = \Sigma, \tag{90}$$

$$\Pi = \Phi\eta, \tag{91}$$

where η is the dimensionless curvature. Finally, the growth of the dimensionless volume $\Upsilon = V/R_o^3$ satisfies the equation

$$\frac{d}{d\tau}[\Upsilon(1 + \Pi\frac{\Delta P}{P_\infty})] = \int_A \frac{\partial \Sigma}{\partial s} dA, \tag{92}$$

which, in our case of low supersaturation, becomes

$$\frac{d\Upsilon}{d\tau} = \int_A \frac{\partial \Sigma}{\partial s} dA. \tag{93}$$

It must be noted that the above dimensionless formulation was chosen so as to balance rates of growth with diffusion. It is then apparent that as long as $\Delta P/P_\infty$ is small, then $\mathrm{Ja} \ll 1$, and the mass transfer equation becomes

$$\nabla^2 \Sigma = 0, \tag{94}$$

implying that the concentration field is quasi-static. The quasi-static approximation is widely used in mass transfer involving growing phases at low supersaturations (e.g., Lifshitz and Slyozov [66]), it has been rigorously derived by Scriven [93] and confirmed numerically by Szekely and Martins [101], and other authors in various contexts.

The emergence of a quasi-static concentration field has a significant impact on the method of solution of the problem. Indeed, we shall show that our problem is mathematically equivalent to that of immiscible displacement, where a low viscosity gas injected at a source, immiscibly displaces an incompressible liquid of constant far-field pressure. A dimensionless formulation of the problem is presented in Appendix 8. Direct comparison of (259)–(263) with (88)–(94) shows that the two formulations are identical under the equivalence

$$\Sigma \leftrightarrow \Lambda \quad \text{and} \quad \Phi \leftrightarrow \Psi. \tag{95}$$

The immiscible displacement from a single source described in Appendix 8 results into various growth patterns depending on the relative importance of capillarity. When capillary forces predominate, the displacement is a percolation process, equilibrium states will be reached at the specified capillary pressure, and the associated patterns are well known (in either ordinary or invasion percolation). On the other hand, when viscous forces predominate, the displacement is of the DLA type, no equilibrium states are possible and the growth pattern is determined solely by the solution of the Laplace equation in the liquid.

Therefore, in view of the equivalence (95) we may then conjecture that at low supersaturations, the growth of the gas bubble is as follows:

(i) When $\Phi \sim O(1)$, i.e., $2\gamma H_o \sim \Delta P \ll P_\infty$, the process is (invasion) percolation, the properties of which have been extensively studied in recent years [116]. For a given ΔP satisfying the above, the bubble evolves towards an equilibrium percolation pattern, dictated by capillarity. It is apparent from (89–91), that the final pattern corresponds to $\eta = 1/\Phi$, ($\Sigma = 1$). In conjunction with the stability of equilibrium states discussed above, simple rules for the occupancy of the pore space by gas can be constructed: Pores with small and allowed curvature $\eta < 1/\Phi$, ($R > 2\gamma/\Delta P$) are occupied by gas, provided that they are accessible to the initial bubble. Predictions on critical gas saturation and relative permeabilities for this classical percolation problem are presented in a later section.

However, it should be cautioned that, although the final pattern is fixed, the rate of approach may be quite slow, as is also the case in similar capillary invasion processes [104], and may depend significantly on the size of the gas bubble before supersaturation was applied. An order of magnitude estimate for the dimensional time to equilibrium is

$$t_{eq} \sim \frac{k\xi^2}{\phi D \mathrm{Ja}^2}, \tag{96}$$

where k is the medium permeability (that scales pore length), ϕ is the porosity, and ξ is the dimensionless correlation length in the percolation process. The latter is generally O(1) away from the percolation threshold (i.e. at low and high gas saturation), but increases sharply near percolation (i.e. near the critical gas saturation). Although further research is certainly needed for definitive answers, the above can be used to provide plausible estimates on the range of pressure decline rates, where the above percolation regime is applicable. A practical approach is to approximate the continuous pressure decline as a sequence of quasi-static, small ΔP steps, and to ensure that

sufficient time has been allotted for equilibrium. For a pressure decline rate a, a characteristic time $t^* = \Delta P/a$ is defined. We shall demand $t^* \gg t_{eq}$, hence

$$a \ll \frac{\phi \Delta P D}{k\xi^2} \mathrm{Ja}^2. \tag{97}$$

Taking $\Phi \sim O(1)$, $\xi \sim O(1)$, and using (69), the above yields a typical estimate of $a \ll 10^{-4}$ psi/sec, far from percolation, which can be realistic in certain field cases. Of course, near the threshold, the diffusion process slows down considerably, and even lower decline rates are required for the percolation regime to be applicable.

(ii) <u>When $\Phi \ll 1$</u>, i.e., $2\gamma H_o \ll \Delta P \ll P_\infty$, the process is diffusion-limited, capillarity is unimportant, and the growth pattern should be of the DLA (Diffusion-Limited-Aggregation) type. Here, with the possible exception of trapped liquid, equilibrium states do not exist other than full occupancy of the medium by gas. Indeed, for $\Phi \ll 1$, equations (90), (91) give $\Sigma = 0$ at the gas-liquid interface, which in view of the far-field boundary condition $\Sigma = 1$ and (92) imply continuous growth. The growth pattern resembles that of viscous-controlled, immiscible displacement with unfavorable mobility ratio (Ca $\gg$ 1, $M \gg 1$), a process recently studied by a DLA approach [42]. The gas-occupied pore space is a fractal object of fixed fractal dimension. Evidently, in such cases the use of classical concepts such as relative permeabilities and critical gas saturation is inappropriate, although alternative methods have yet to be developed.

Processes with Φ values intermediate between the two extremes identified in (i) and (ii), are naturally more complex, and our understanding of the displacement properties is poor, at present. Likewise incomplete is our knowledge of processes with rapid enough pressure decline rate a, such that the above constraint (97) is violated. In conjunction with other topics outlined below, these issues call for further research.

Moderate Supersaturations, $\Delta P \sim P_\infty$

When the supersaturation step ΔP is comparable to the imposed liquid pressure P_∞ , surface forces are negligible in the momentum balance, ($\Phi \ll 1$), and inertia and viscous forces may still be neglected ($B \ll 1$). Thus, the process is, again, mass transfer-controlled, although now Ja $\sim O(1)$. Equations (76), (77) of the previous section still describe the growth, although a modification to account for liquid density changes must also be considered. Even in the absence of the latter,

however, the problem is quite complex, since the quasi-static approximation (94) is no longer valid when Ja is not small. Here the full diffusion-convection equation (76) must be considered, which is further coupled with the flow field in the liquid. The solution to this complex problem is beyond our scope.

Large Supersaturations, $\Delta P \gg P_\infty$

We conclude this part by noting that at large supersaturations, inertia and viscous effects previously ignored, acquire importance at the early stages of bubble growth, under conditions such that $B \gg 1$. Examination of (72) reveals that the latter condition demands high ΔP, low P_∞ (possibly vacuum) and low K (high gas solubility). In inertia-controlled growth the mass of gas in the bubble remains constant, and the bubble expands following a polytropic law [84]. A first attempt to the solution of this problem in porous media was undertaken by Epstein [38]. However, here too, the state of the art is quite unsatisfactory and in need of additional work.

3.3.6 Growth from Multiple Source Sites

A final remark is necessary concerning the growth of gas bubbles that originate from more than one nucleation sites. Our treatment of nucleation specifies that nucleation sites at various pore bodies are instantly activated when the local supersaturation reaches a threshold value characterizing the pore body. Thus, the possibility of growth from several sources is a real issue and must be addressed. In the next section, we present a solution to this problem for the case of low supersaturations or pressure decline rates, when capillarity predominates (case 3.3.5(i) above). A modification of percolation theory is implemented to account for growth from multiple sites. Unfortunately, the same cannot be done for any other case which are in need of further work. Finally, an application of the present study to finite systems which are closed to mass transfer should have an interest of its own. In such cases, growth, solute depletion, activation of nucleation sites and "bubble coalescence" occur simultaneously and the underlying competition should share features common to those studied by Lifshitz and Slyozov [66]. It must be remarked that several reported experiments operate under the constraints of finite solute mass.

3.4 PERCOLATION THEORY

It was pointed out above that at small supersaturations, induced by a low pressure decline rate, a quasi-static approximation applies. Gas phase occupancy is controlled by the capillary properties of the porous medium and can be simulated reasonably well with a percolation approach. Since nucleation must also be allowed, the usual percolation approach must be modified to account for generation at appropriate sites. Such a modification to ordinary percolation was recently presented for capillary desorption processes in Bethe lattices [80, 81]. Here, we shall follow an identical approach, although invasion percolation (that accounts for a finite compressibility of the trapped liquid) yields probably a better description. However, the ensuing errors are small, if the gas saturations are not too high, and negligible if the liquid can escape through thin films.

A network representation of the porous medium in terms of a Bethe lattice is taken. Although lacking the reconnection properties of regular networks (such as a cubic), Bethe lattices allow for closed-form solutions and yield reasonable approximations to real lattice properties, such as accessibility, provided that the percolation thresholds are matched. For reasons, previously outlined in detail, both site and bond (pore body and pore throat) distributions are considered. The rules for occupancy of the pore space by the gas phase were described in section 1 and can be briefly summarized as follows: Given a supersaturation $\Delta P = P_b - P_\infty$, pore bodies with size

$$r \geq r_d = \frac{2\gamma}{\Delta P}, \tag{98}$$

are allowed to be occupied. Those that are actually occupied, however, must be connected through occupied pore elements to source (nucleation) sites. Nucleation sites consist of all pore bodies with size

$$r \geq \frac{r_d}{\beta} = \frac{2\gamma}{\beta \Delta P}, \tag{99}$$

where β is a fraction, assumed small ($\beta < 1$). Along with appropriate probability densities and the accessibility expressions derived in section 1, the above rules are sufficient for a complete description of the process. We shall illustrate the determination of the critical gas saturation as a function of β, or equivalently the nucleation fraction f_q. Gas-phase relative permeability curves will also be derived.

3.4.1 Critical Gas Saturation

To determine the critical gas saturation, we consider the supersaturation ΔP_c corresponding to a value r_{dc} such that the allowed bond fraction is equal to the percolation threshold, p_c

$$\int_{r_{dc}}^{\infty} \alpha_b(r)dr = p_c = \frac{1}{Z-1}. \tag{100}$$

It must be noted that it is bond percolation that dictates connectivity, hence the bond distribution is used. Thus, the supersaturation ΔP_c at the onset of gas flow

$$\Delta P_c = \frac{2\gamma}{r_{dc}}, \tag{101}$$

where r_{dc} solves (100), is fixed for fixed Z and $\alpha_b(r)$. Higher values in the coordination number and larger throat sizes (permeability) yield correspondingly lower critical supersaturation. The critical gas saturation S_{gc}, is obtained by adding the volumetric contributions of the pore elements associated with the infinitely-connected bonds (those on the percolation cluster) to those connected to nucleation sites that happen not to belong on the percolation cluster. For example, the number fraction of such sites (termed *accessible*) is given by

$$X_{s,o} = q^* - (1-f_q)[(\frac{1-p}{1-x})^Z - (1-p)^Z] + (q-q^*)f_q, \tag{102}$$

where

$$q = \int_{r_d}^{\infty} \alpha_s(r)dr \quad \text{and} \quad q^* = 1-(1-p)^Z, \tag{103}$$

and x solves

$$x(1-x)^{Z-2} = (1-f_q)p(1-p)^{Z-2}. \tag{104}$$

The corresponding saturation can then be directly obtained. Results are shown in Figure 24. We note that S_{gc} crucially depends on the nucleation fraction (equivalently on β), ranging from zero, in the absence of nucleation, to values as large as

$$S_{gc} = 1-(1-p_c)^Z. \tag{105}$$

A precise determination, of course, requires among other input the accurate allotment of volume to occupied sites and bonds, as well as their respective distributions. These parameters should vary among the various porous media. For instance, some interesting results arise when a finite maximum

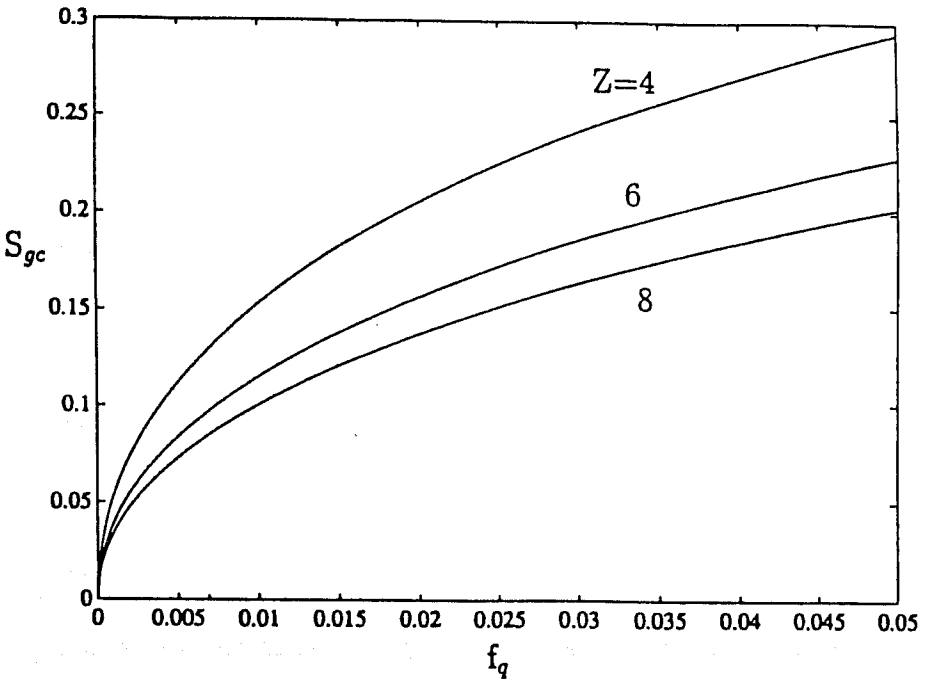

Figure 24: Critical gas saturation for various nucleation fractions.

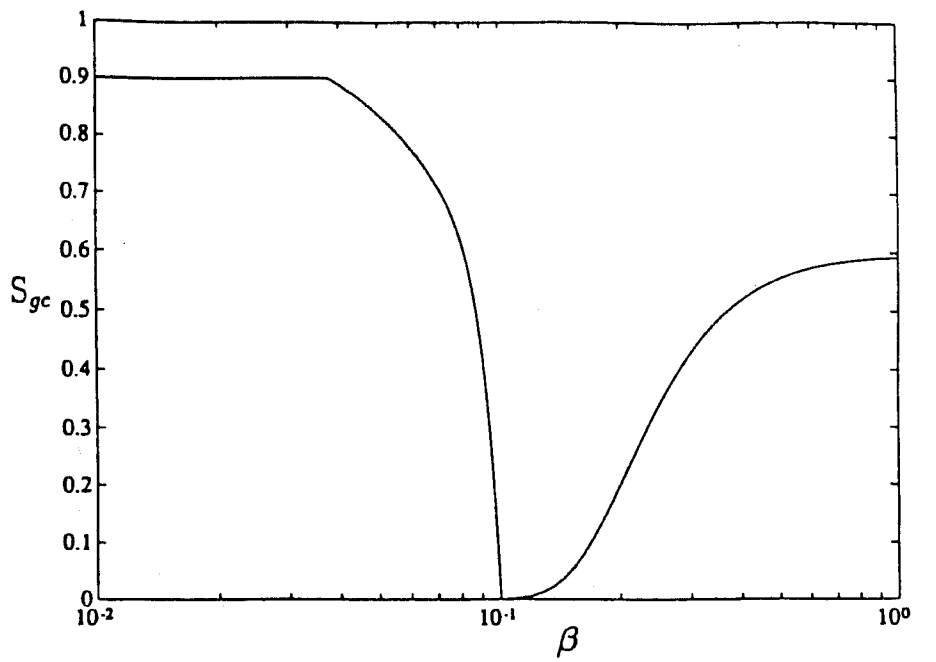

Figure 25: Critical gas saturation as a function of β ($\kappa = 0.1$)

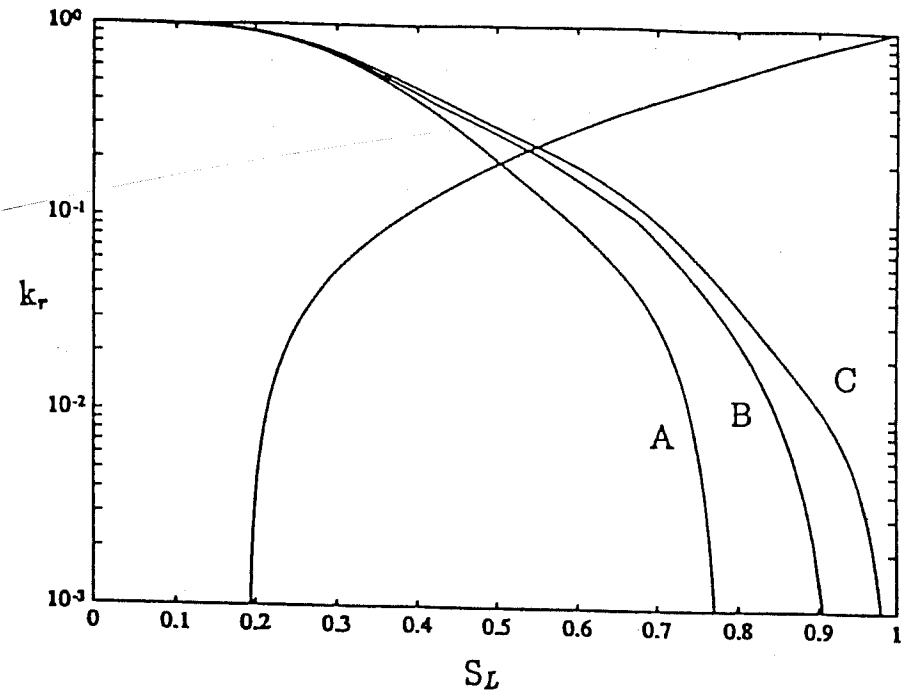

Figure 26: Internal (A,B) and external (C) gas drive relative permeabilities, β = 0.20, 0.16, 0, respectively (Z=6).

cutoff in the body size distribution is taken, such that the ratio $\kappa = r_{dc}/r_{s,max}$ is not identically zero. Depending on the position of β relative to this ratio, S_{gc} displays different sensitivity (Figure 25). Values of β to the left of κ correspond to cases such that although conditions for bond percolation exist, gas phase occupancy has not occurred because of lack of nucleation sites. When the first (or first few) such site(s) is (are) created (at $r_d = \beta r_{s,max}$) the infinite cluster corresponding to that value would eventually become occupied and takes on a relatively large value.

3.4.2 Relative Permeabilities

Given pore element occupancies the associated relative permeability curves can also be constructed. The approach was pioneered by Heiba et al.[57, 56] and applied to a single component steam-water system by Parlar and Yortsos [79] where a detailed account of the technical issues is given. Drainage relative permeability pairs corresponding to internal gas drive are shown in Figure 26 for different values of β. It is evident that the difference in the curves between internal and external drive is reflected by a difference in β, thus nucleation. For $S_{gc} \approx 0$, the difference between the two processes is negligible. As nucleation events increase (and $\beta > \kappa$), S_{gc} increases, and the curve shifts to the

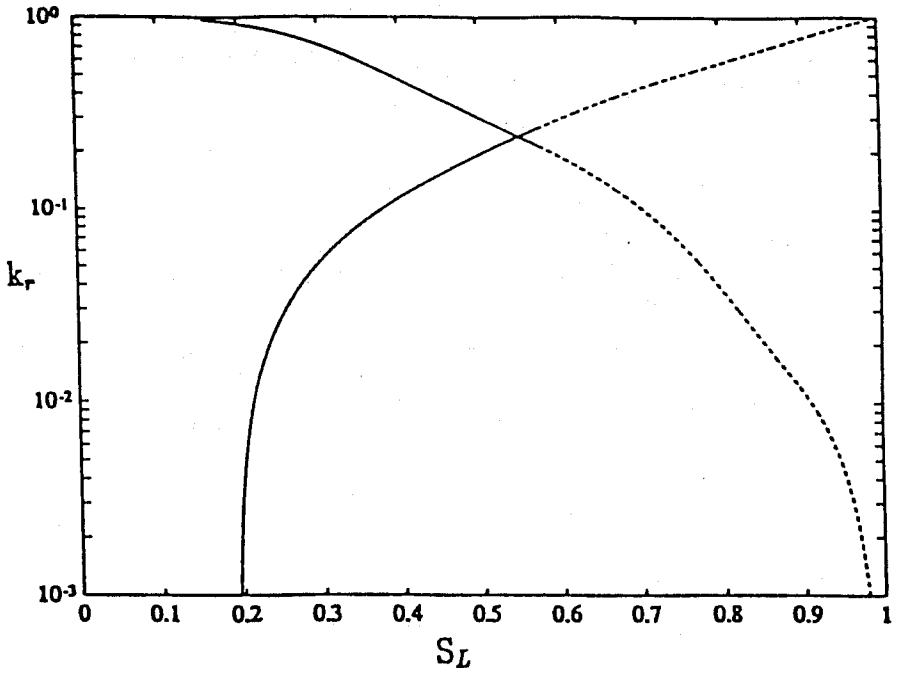

Figure 27: Internal gas drive relative permeabilities ($Z = 6$, $\beta = 0.09$, $\kappa = 0.10$).

left. The effect can become as pronounced as allowed by the magnitude of S_{gc}. Note that in these cases, $k_{rg}(S_{gc}) = 0$, while for $S_g < S_{gc}$, $k_{rg} = 0$ and $k_{rL} < 1$.

On the other hand, when nucleation effects are suppressed ($\beta < \kappa$), there is a sudden appearance of a flowing gas phase saturation, and the relative permeability curve k_{rg} practically coincides with that of an external drive, with the exception of course that it commences at S_{gc} (Fig. 27). Besides the obvious exceptions, the relative permeability to liquid is not significantly affected and remains approximately the same in either internal or external drive.

3.5 SUMMARY AND CONCLUSIONS

In this section, a study of the basic mechanisms involved in solution-gas drive and other related liquid-to-vapor transitions in porous media was initiated. The principal issues of nucleation, supersaturation and gas-phase growth were examined. A simple geometric model was presented for heterogeneous nucleation on the pore walls which was shown to be the dominant nucleation mechanism. It was, thereby, concluded that, for otherwise identical conditions, nucleation events are likely to occur in the larger pore bodies first, and that the supersaturation needed for the appearance of the first bubble should be largely independent of features unrelated to the porous media

nature (such as, for example, the rate of pressure decline).

A detailed study of the phenomena involved in the growth of a single gas bubble in an unbounded porous medium was next considered. The effects of capillarity, mass transfer, inertia and viscous stresses were discussed. It was shown that at small supersaturations, stable equilibrium gas bubbles in converging pore elements are possible. Complementing the stability to mechanical equilibrium, stability to mass transfer was demonstrated. This is an essential requirement for the validity of the quasi-static, percolation approach at low supersaturations.

The gas-phase growth was parametrized by various dimensionless groups and the $\Delta P/P_\infty$ ratio. For small values of the latter, it was shown that the process is mass transfer-controlled, and the concentration field is quasi-static. When capillary effects dominate, ($\Phi >> 1$) the process was mapped to (invasion) percolation, while in the opposite case ($\Phi << 1$) the identification with a DLA-like process was suggested. For larger values of the ratio, the process is still mass transfer-controlled, although the diffusion is not quasi-static any longer. Inertia, viscous and density effects at large supersaturations were discussed but not explored. Issues of activation of additional nucleation sites, competition in growth and a finite supply were identified as important, but likewise were not explored.

Limiting constraints on the pressure decline rate for the quasi-static percolation approach to be valid were derived. Based on the latter, a mechanistic model was developed that accounted for growth from multiple source sites. The critical gas saturation, S_{gc}, was obtained and shown to depend crucially on the nucleation characteristics (taken here as a geometrical input) of the porous medium. Relative permeability curves pertaining to internal gas drive were also developed. Related issues for higher supersaturations were not, however, discussed. The investigation highlighted the challenging issues associated with phase transition and growth in porous media and identified areas for future research. Processes, such as solution-gas drive, cavitation and boiling in porous media would be the beneficiaries of such future advances.

4 A STUDY OF STEADY-STATE STEAM-WATER COUNTERFLOW IN POROUS MEDIA

C. Satik, M. Parlar and Y.C. Yortsos

4.1 INTRODUCTION

The steady-state counterflow of a liquid and its vapor in porous media arises in many processes driven by temperature gradients. Large scale applications involve geothermal systems [113, 95, 91, 12], thermal oil recovery [86], and nuclear waste disposal [32, 16], among others. Investigations on the laboratory scale have emphasized porous heat pipes [50, 78] and boiling processes [31, 35, 24]. All these studies share common aspects, principally the phase change and its interplay with fluid flow, heat transfer and capillarity.

Although change of fluid phase in porous media is fundamental to such routine applications as drying [94], a precise description of the process is not presently available. Issues of nucleation, stability of equilibrium states, supersaturation and heat and mass transfer are yet to be fully explored. Instead, the traditional approach is taken that vapor and liquid phases individually obey Darcy's law with saturation-dependent permeabilities.

Steady-state vapor-liquid flows in porous media have been modeled with such methodology for several decades [74]. Notable recent applications to steam-water counterflow include the works by Martin et al. [69], Schubert and Straus [92], Bau and Torrance [7], and Udell [105, 106]. The first two studies analyze the problem in the geothermal context, by neglecting capillarity, but including heat conduction. Udell [105, 106] considers the heat pipe version, in which capillarity predominates, but conduction is neglected. Finally, Bau and Torrance [7] present a simplified analysis where both conduction and capillarity are assumed negligible.

While previous studies have been instrumental in enhancing our understanding of the counterflow process, several areas are still obscure and in need of further investigation. In the context of a heat pipe, unresolved is the role of heat conduction, particularly as it regards the critical heat flux in bottom heating [7, 105, 106]. The characterization of the flow regime for heat fluxes lower than the critical is also incomplete. The tacit, and unrealistic, assumption of an infinite, two-phase zone of constant saturation has not been questionned. Finally, unclear is the role and the importance of Kelvin effects in the process description. In the context of geothermal systems, the possible

existence of two systems (vapor- and liquid-dominated) has long been proposed [69]. However, the question of selection of the particular regime also remains open.

The difficulty in obtaining answers to these questions is due to the approximations inherent to the various models, and the fact that they become singular in the region of interest. To alleviate this problem, a more detailed study is necessary. In recognition of the fact that all the above applications represent essentially the same problem (although temperature gradients, thus flow directions, may be of opposite sign), a common formalism should be possible. Specific cases should then arise in the appropriate limits. This forms the main objective of this work. We shall consider a complete formulation that includes capillarity, heat conduction, phase change and vapor pressure lowering.

The flow model follows an extension of Darcy's law using relative permeabilities, and allows for vapor pressure lowering due to Kelvin effects. Both representations are based on the premise of capillary control at the pore level, usually enforced for low values of capillary and Bond numbers, and when temperature gradients are relatively low. Implicit is also the assumption that pore wall curvature stabilizes vapor-liquid interfaces. Such conditions are necessary for a process description in terms of saturation-dependent relative permeabilties and capillary pressure functions. Precise criteria for their validity are currently under development, paralleling recent advances in the related problem of bubble growth in porous media by diffusion [118], where such and other issues have been addressed.

We proceed by deriving a dimensionless representation applicable to a general steady-state, vapor-liquid counterflow. The heat pipe and geothermal problems are subsequently analysed separately. We investigate boundary layers due to vapor pressure lowering and heat conduction in the first case, and due to capillarity in the latter. The nature of the critical heat flux for bottom heating in a heat pipe problem, and its dependence on process parameters are examined in detail. Finally, for both heat pipe and geothermal problems we identify regimes, where steady-state counterflow may not exist.

4.2 FORMULATION

We consider the steady state, countercurrent flow of a single component, two-phase, liquid-vapor (e.g. steam-water) system. As a result of an externally imposed heat flux q_h, three regions develop

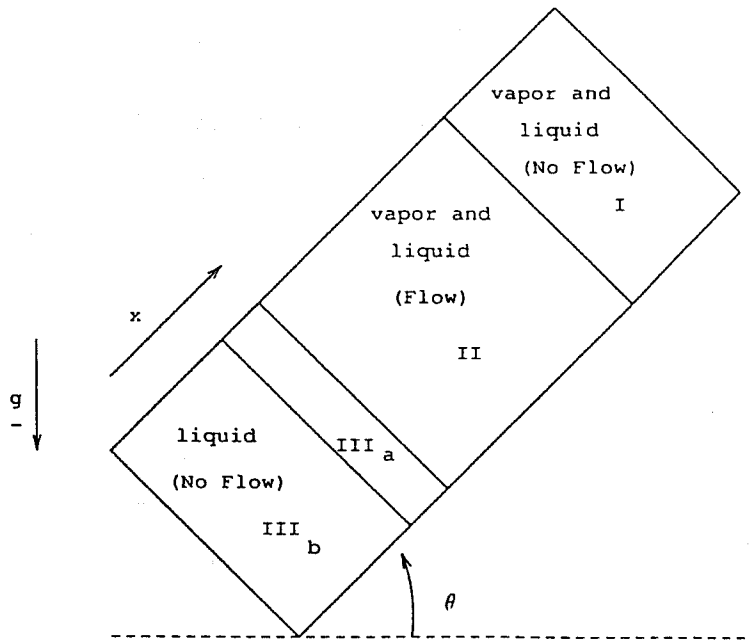

Figure 28: Countercurrent flow schematic.

[105]: Two no-flow regions (I or III in Fig. 28) containing mostly vapor or liquid, respectively, and an intermediate two- phase region (II), where counterflow occurs. In our notation, the space coordinate x increases in the direction from the liquid to the vapor. The system is inclined at an angle θ with respect to the horizontal, such that when $0 < \theta < \pi$ vapor is at the top, while the vapor zone is at the bottom in the other case ($\pi < \theta < 2\pi$) .

Application of a momentum balance to the fluid phases gives

$$V_{Lx} = -\frac{k}{\mu_L} k_{rL} \left(\frac{\partial P_L}{\partial x} + \rho_L g \sin\theta \right) \tag{106}$$

$$V_{Vx} = -\frac{k}{\mu_V} k_{rV} \left(\frac{\partial P_V}{\partial x} + \rho_V g \sin\theta \right) \tag{107}$$

where the relative permeabilities k_{rL} and k_{rV} depend on the liquid saturation, S. This formulation ignores viscous coupling between the two phases [62]. The two pressures are related via the capillary pressure function

$$P_V - P_L = P_c(S) = \frac{\sigma}{\sqrt{k}} J(S) \tag{108}$$

where the typical representation in terms of a Leverett J function was introduced.

Permeability and capillary pressure functions are controlled by pore space geometry and topology. Typical schematics are shown in Figure 29. The residual saturation values (S_{Lr}, S_{Vr}), below

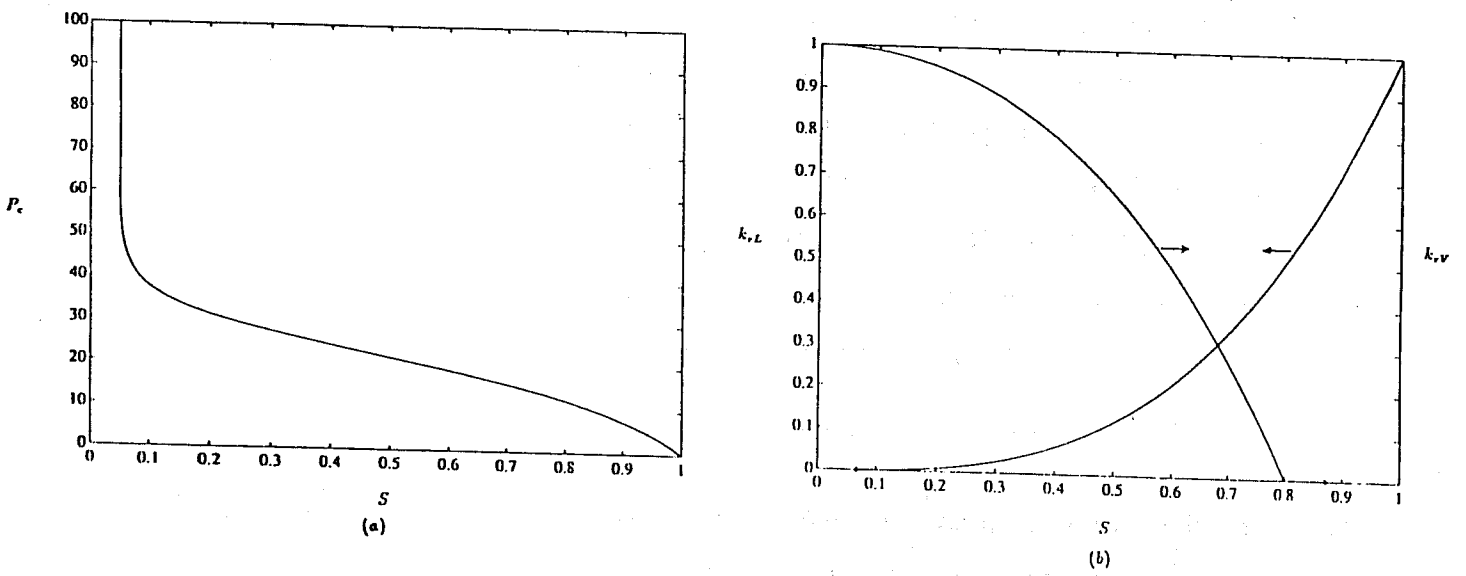

Figure 29: Schematics of capillary Pressure (a) and relative permability Curves (b).

which flow of the respective phases ceases, should be noted. Significantly, and contrary to non-condensing phases, however, the capillary pressure is not singular at the residual values. Salient features of such properties for vapor-liquid systems are discussed elsewhere, following a percolation approach [118], [79]. In the ensuing use will be made of simple, although ad hoc, numerical expressions.

For the vapor pressure we take

$$P_V = P_{Vo}(T) exp\left(-\frac{v_L}{RT} P_c(S)\right) \tag{109}$$

to describe pressure lowering, and use the Clausius-Clapeyron formula

$$P_{Vo}(T) = P_{Vo}(T_o) exp\left(\frac{L_v M}{R}\left(\frac{1}{T_o} - \frac{1}{T}\right)\right) \tag{110}$$

for phase equilibria. Mass and thermal energy balances complete the formulation

$$\rho_L V_{Lx} + \rho_V V_{Vx} = 0 \tag{111}$$

$$\rho_V L_V V_{Vx} + q_h = \lambda \frac{\partial T}{\partial x} \tag{112}$$

To avoid unnecessary complications, all fluid properties are taken independent of P and T. Due to different flow behavior the various regimes are examined separately.

(i) No-Flow Regions

Region I is a no-flow, mostly vapor-occupied zone, where

$$0 \leq S \leq S_{Lr} \tag{113}$$

thus $k_{rL}(S) = 0$, $V_{Lx} = 0$ and, from (6), $V_{Vx} = 0$. At the residual value S_{Lr}, bulk liquid in the pore space becomes disconnected, and bulk flow ceases. The liquid being strongly wetting keeps hydraulic continuity in the form of thin film flow, even for $S < S_{Lr}$. These rates are quite low, however, and will not be considered here. Thus, the pressure of the vapor phase is hydrostatic and the temperature distribution linear

$$P_V = P_I - \rho_V g x \sin\theta \tag{114}$$

$$T = T_I + \lambda_I q_h x \tag{115}$$

where P_I, T_I are constants. A saturation profile results

$$J(S) = \frac{1}{b} ln\left(\frac{P_{Vo}(T_I + \lambda_I q_h x)}{P_I - \rho_V g x \sin\theta}\right) \tag{116}$$

where the dimensionless group $b = \sigma v_L / RT\sqrt{k}$ parametrizes Kelvin effects. For media of practical interest ($b \ll 1$) , the liquid is at low saturation ($J(S) \gg 1$) in most of region I, and exists in a pendular state. Recent works [73] have thoroughly elucidated the capillary pressure- saturation relationship in this regime. The extent (x_1) of the vapor zone I is demarkated by setting $S = S_{Lr}$ in (11). For $b \ll 1$, one may approximate

$$P_{Vo}(T_I + \lambda_I q_h x_1) \simeq P_I - \rho_V g x_1 \sin\theta \tag{117}$$

which is the condition for vapor saturation, and determines the boundary of the two regions I, II. The sharp saturation rise to the residual value S_{Lr} near the boundary (where the logarithm in (116) becomes of order b) should be noted.

Likewise, region III is a no-flow, mostly liquid-occupied zone, where

$$1 - S_{Vr} \leq S \leq 1 \tag{118}$$

thus, $k_{rV}(S) = 0$, $V_{Vx} = 0$, and, from (7) , $V_{Lx} = 0$. Pressure and temperature profiles are linear

$$P_L = P_{III} - \rho_L g x \sin\theta \tag{119}$$

$$T = T_{III} + \lambda_{III} q_h x \tag{120}$$

with P_{III}, T_{III} appropriate constants. In contrast to region I, where a saturation profile exists due to wettability, the bulk of region III (IIIb in Figure 28) is at S = 1. Saturation changes are confined within a narrow sub-domain (IIIa), the boundary of which (x_3) is the solution of $P_c = 0$

$$P_{Vo}(T_{III} + \lambda_{III} q_h x_3) = P_{III} - \rho_L g x_3 \sin\theta \tag{121}$$

To the left lies boundary x_2 , obtained by taking $S = 1 - S_{V_r}$, and by neglecting the Kelvin effect

$$P_{Vo}(T_{III} + \lambda_{III} q_h x_2) = P_{III} - \rho_L g x_2 \sin\theta + \frac{\sigma}{\sqrt{k}} J(1 - S_{V_r}) \tag{122}$$

(ii) Flow Region

The region of two-phase, countercurrent flow is the most interesting. It is here, where condensation and evaporation occur, and where the interplay between phase change, heat transfer and capillarity is most pronounced. Saturation and temperature profiles are described by two coupled equations obtained by combining (106)-(112). After considerable algebra the following system is obtained

$$\frac{d\tau}{d\xi} = \frac{H(\tau, S)}{F(\tau, S)} \tag{123}$$

$$\frac{dS}{d\xi} = \frac{G(\tau, S)}{F(\tau, S)\frac{dJ}{dS}} \tag{124}$$

where

$$H = k_{rL}[(1 + bR_pA)R_h + \sin\theta k_{rV}(bR_mA - R_vR_c)] + bk_{rV}\beta R_pR_hA \tag{125}$$

$$F = k_{rL}[1 + bR_pA + k_{rV}KR_m\frac{A}{\tau^2}] + bk_{rV}\beta R_pA \tag{126}$$

$$G = k_{rL}[\sin\theta R_l + KR_pR_h\frac{A}{\tau^2} + \sin\theta k_{rV}KR_m\frac{A}{\tau^2}] + \beta k_{rV}[\sin\theta R_v + KR_pR_h\frac{A}{\tau^2}] \tag{127}$$

Dimensionless notation has been used, with ξ denoting distance normalized by $\sigma/\sqrt{k}g\Delta\rho$, to reflect competition between gravity and capillarity, and τ denoting temperature normalized by a suitably chosen temperature T_o. Variable A is a vapor pressure normalized by the saturation pressure at T_o and includes Kelvin effects

$$A = exp\left(K(1 - \frac{1}{\tau}) - bJ(S)\right) \tag{128}$$

The various dimensionless groups are defined in the Nomenclature and they are functions of the fluid and rock properties, with the exception of R_h

$$R_h = \frac{q_h \sigma}{\lambda_{II} T_o \sqrt{k} g \Delta\rho} \tag{129}$$

which is a measure of the imposed heat flux, and is simply related to the parameters ω or Γ [105], [92]

$$\omega = \frac{R_p R_h}{R_m} = \frac{\lambda_{II} \Gamma \mu_V}{k L_V g \Delta\rho \rho_V} \tag{130}$$

The above constitute an initial value problem to be solved subject to appropriate initial conditions. For the heat pipe problem [105] we shall take

$$\tau = \frac{T_1}{T_o} \quad ; \quad S = S_{Lr} \quad at \ \xi = \xi_1 \tag{131}$$

where $T_1 = T_o + \lambda_I q_h x_1$, the reference temperature T_o corresponds to the (dry) end of the vapor zone, and the integration is in the direction of decreasing ξ. For the geothermal problem [92] we shall consider

$$\tau = 1 \quad ; \quad S = 1 \quad at \quad \xi = 0 \tag{132}$$

where T_o corresponds to the boundary of regions IIIa-IIIb, and the integration is in the direction of increasing ξ. Forward integration of (123) and (124) subject to (131) and (132) uniquely determines saturation and temperature profiles.

For future reference the dimensionless vapor flow velocity V_{Vx}, normalized by $k\Delta\rho g/\mu_V$, is also derived

$$V_{Vx} = -\frac{k_{rV} k_{rL} [\sin\theta R_v - b R_p A + K R_p R_h \frac{A}{\tau^2}]}{F(\tau, S)} \tag{133}$$

It must be remarked that, for all practical purposes ($b \ll 1$), the magnitude, but not the sign, of the angle θ can be scaled out in (123), (124), and(133), by rescaling the space variable ξ by $|\sin\theta|$ and the heat flux term R_h (or ω) by $1/|\sin\theta|$. Thus, it only suffices to study the generic cases $\theta = \pi/2, \ 3\pi/2$.

Contrasted to the above, and excluding field-scale numerical simulators, present models are quite simpler. The most advanced belongs to Udell [105, 106], for the heat pipe and to Schubert and Straus [92], for the geothermal problem. These models arise as limiting cases of the above formulation as will be shown below. To facilitate the presentation, however, the two cases are examined separately.

4.3 HEAT PIPE PROBLEM

In the context of the heat pipe problem we shall investigate Kelvin and heat conduction effects, and will explore the critical heat flux curve. For this purpose, we will frequently refer to the model in [105, 106], the corresponding temperature, saturation and vapor flux of which will be denoted by Θ, Σ, and Ψ, respectively. In our notation, the analysis in [105, 106] is tantamount to taking $b \ll 1$, and $KR_m \gg 1$ with R_h/R_m fixed, the latter condition corresponding to negligible heat conduction. Indeed, at these limits, the vapor flow rate (133) reduces to

$$V_{Vx} \longrightarrow \Psi = \omega \tag{134}$$

and the saturation eqn (124) becomes uncoupled from temperature

$$J' \frac{d\Sigma}{d\xi} = \sin\theta + \omega \left(\frac{1}{k_{rV}} + \frac{\beta}{k_{rL}} \right) \tag{135}$$

The above two limits delineate the validity of the previous results. The condition for negligible Kelvin effects, $b \ll 1$, is generally well satisfied for most porous media of practical interest (e.g. permeabilities exceeding O(md)). Neglecting heat conduction, on the other hand, requires $KR_m \gg 1$ at fixed R_h/R_m, a significantly tighter restriction (e.g. $k \gg O(100$ md) for the experiment in [105]. Substantial changes may result when this condition is not satisfied, as shown in the next section.

4.4 BOUNDARY LAYER ANALYSIS

As a consequence of the conditions $b \ll 1$, $1/KR_m \ll 1$ two boundary layers arise at the ends of region II. This is evident from (134) which requires a step change in the vapor flux, thus infinitely large evaporation-condensation rates at the boundaries. In actuality, however, the vapor flux vanishes smoothly at the two boundaries (where the two relative permeabilities also vanish), as can be seen from an expansion of the full expression (133)

$$V_{Vx} \sim \begin{cases} -\dfrac{k_{rL} KR_h}{b\beta\tau^2} & ; \quad S \to S_{Lr} \\ \\ -\dfrac{k_{rV} KR_p R_h A}{\tau^2} & ; \quad S \to 1 - S_{vr} \end{cases} \tag{136}$$

We analyse the solution in the two regions by considering the more general case $b \ll 1$, finite KR_m, which is widely applicable to a large class of porous media.

(i) Case $b \ll 1$, Finite KR_m

Here, the outer solution outside the boundary layer (superscript (o)) is obtained by neglecting Kelvin effects in (123), (124) and (133)

$$\frac{d\tau^{(o)}}{d\xi} = \frac{R_h - k_{rV} R_v R_c}{1 + k_{rV} \dfrac{KR_m A}{(\tau^{(o)})^2}} \tag{137}$$

$$\frac{dS^{(o)}}{d\xi} = \frac{G(\tau^{(o)}, S^{(o)})}{k_{rL}(1 + k_{rV} \dfrac{KR_m A}{(\tau^{(o)})^2}) J'(S^{(o)})} \tag{138}$$

$$V_{Vx}^{(o)} = -\frac{\sin\theta \, k_{rV}[R_v + KR_p R_h \dfrac{A}{(\tau^{(o)})^2}]}{1 + k_{rV} \dfrac{KR_m A}{(\tau^{(o)})^2}} \tag{139}$$

Near S_{Lr} the saturation (although not the temperature) gradient diverges, thus a saturation rescaling is needed. We take the typical expansion, $k_{rL} \sim L(S - S_{Lr})^n$, where $L > 0$ is constant and $n > 1$, and rescale

$$S = S_{Lr} + b^{\alpha}\sigma(z) \tag{140}$$

$$\xi = \xi_1 - b^{\kappa} z \tag{141}$$

with $\alpha, \kappa > 0$ to be determined. Substitution into the full equations (123) and (124), subsequent expansion and use of dominant balance [9], results into

$$\alpha = \frac{1}{n} \tag{142}$$

$$\kappa = 1 + \frac{1}{n} \tag{143}$$

One immediately concludes that the (evaporation) boundary layer is of the order $b^{1 + \frac{1}{n}}$. The corresponding vapor flux in the boundary layer is obtained from (133)

$$V_{Vx} = \frac{V_{Vx}^{(o)}(S_{Lr})}{1 + c\,\sigma^{-n}} \tag{144}$$

It correctly predicts the vanishing of V_{Vx} at the one end ($\sigma = 0$) and the asymptotic approach to the outer value, $V_{Vx}^{(o)}(S_{Lr})$, at the other ($\sigma \to \infty$) (Figure 30a). In turn, the saturation profile can be also constructed

$$\sigma + \frac{\sigma^{n+1}}{(n+1)c} = -ez \tag{145}$$

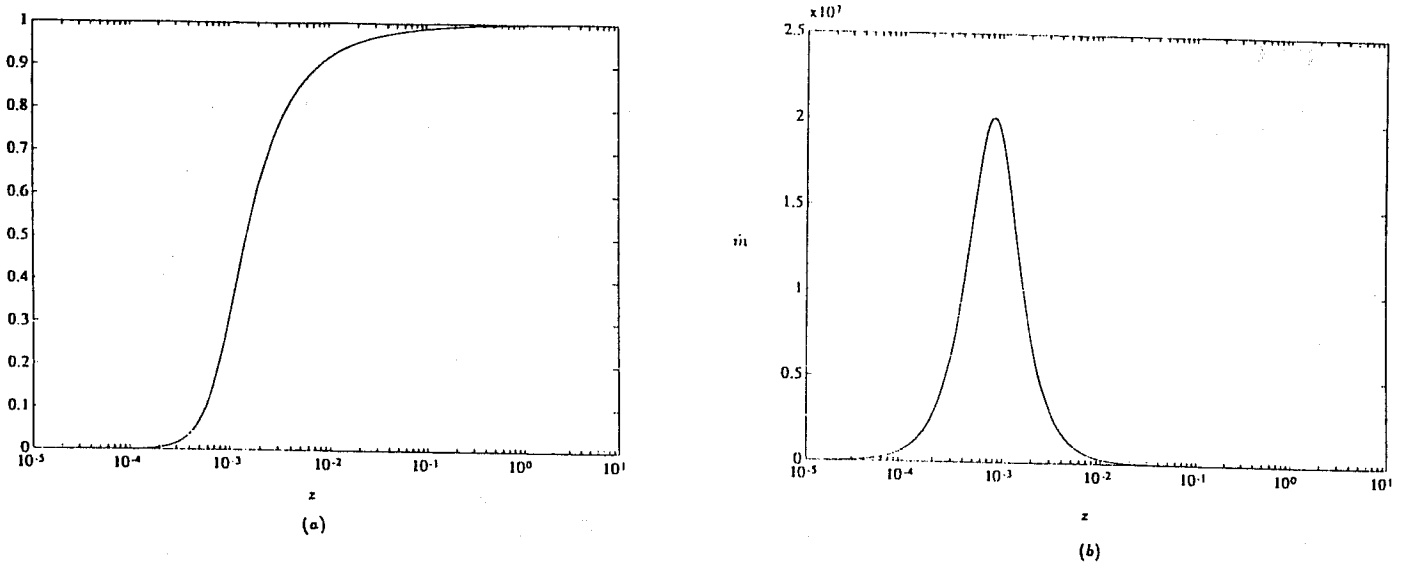

Figure 30: Boundary layer profiles: normalized vapor flux (a) and evaporation rate (b).

thus, the dimensionless evaporation rate $\dot{m} = \dfrac{dV_{Vx}}{d\xi}$ can be evaluated

$$\dot{m} = \frac{f\,\sigma^{n-1}}{b^{1+\frac{1}{n}}[1+\dfrac{\sigma^n}{c}]^3} \tag{146}$$

where c, e and f are process constants (Appendix B). A normalized plot is shown in Figure 30b. It is noted that all evaporation takes place within the boundary layer, $\dot{m}$ increasing from zero to a maximum value, before rapidly decaying to zero at the end of the boundary layer ($z \to +\infty$) . The local rates intensify for smaller values of b, for example when the permeability increases, such that the total evaporation rate over the layer remains finite

$$I = \int_0^{+\infty} b^{1+\frac{1}{n}}\,\dot{m}\,dz = -\frac{fc}{en} \tag{147}$$

Of course, the latter equals the jump in the outer value $V_{Vx}^{(o)}(S_{Lr})$, which is discontinuous at S_{Vr}.

The above analysis shows that the evaporation region is a thin layer of order $b^{1+\frac{1}{n}}$ at the interface between dry and two-phase zones, and is principally controlled by vapor pressure lowering. Outside this layer in region II, Kelvin effects are insignificant, regardless of the value of KR_m, and

the process is well described by the outer solutions (123), (137) and (139). In particular, the latter shows that the vapor flux magnitude $\mid V_{Vx} \mid$ continuously decreases, as S increases, suggesting that condensation occurs over the entire two-phase zone, and not strictly at the end as normally assumed. On the other hand, local condensation rates depend on the value of KR_m. For large values of the latter, as implicitly taken in [105, 106], condensation is restricted on a boundary layer at the interface between liquid and two-phase zones. This boundary layer is due to heat conduction alone.

(ii) Case $b \ll 1$, $KR_m \gg 1$, R_h/R_m Finite

In this limit, the outer solutions (Θ, Σ and Ψ) are given by expressions (134) and (135) and

$$R_p \frac{d\Theta}{d\xi} = \frac{\omega - k_{rV} R_v}{\frac{KA}{\Theta^2} k_{rV}} \tag{148}$$

Under the tacit, and sufficient, assumption $b \ll \delta \equiv 1/KR_m$, the previous analysis is valid, and only the boundary layer near $1 - S_{Vr}$ needs be considered. Now, however, the temperature gradient also diverges. To proceed, we first note that to first-order the boundary temperature at ξ_2 is given by the outer solution by combining (138) and (148) and integrating across the two-phase zone

$$R_p(A_2 - A_1) = \omega \int_{S_{Lr}}^{1-S_{Vr}} \frac{J'(S)dS}{k_{rV}[\sin\theta + \omega(\frac{1}{k_{rV}} + \frac{\beta}{k_{rL}})]} \tag{149}$$

Here $A = \exp[K(1 - \frac{1}{\Theta})]$ and it was implied that the denominator does not vanish (see also below). Next, we rescale saturation, spatial distance and temperature as before

$$S = 1 - S_{Vr} - \delta^{\alpha}\sigma(z) \tag{150}$$

$$\xi - \xi_2 = \delta^{\kappa} z \tag{151}$$

$$\Theta = \Theta_2 + \delta^{\gamma}\eta(z) \tag{152}$$

to obtain with the use of dominant balance

$$\alpha = \gamma = \frac{1}{m} \tag{153}$$

$$\kappa = 1 + \frac{1}{m} \tag{154}$$

where m is the exponent in the permeability expansion $k_{rV} \sim M(1 - S - S_{Vr})^m$. The rescaled saturation satisfies the equation

$$\frac{d\sigma}{dz} = -\frac{\omega G}{J'(1 - S_{Vr})[1 + MG\sigma^m]} \tag{155}$$

where $G = A_2/\Theta_2^2$. An analysis similar to the previous applies, and identical results can be reached regarding condensation rates. For example, the vapor flux inside the boundary layer has the form

$$V_{Vx}^{(o)} = -\frac{\omega}{1 + \frac{\sigma^{-m}}{LG}} \tag{156}$$

which correctly predicts that V_{Vx} vanishes at $1 - S_{Vr}$ ($\sigma = 0$) and approaches the asymptotic value $-\omega$ in the outer limit ($\sigma \to \infty$). We omit further details and only mention that both the boundary location and the boundary temperature are accurately approximated at large KR_m from the outer solutions. At such conditions, vapor condensation is restricted in a boundary layer of width $\delta^{1+\frac{1}{m}}$ at the end of the two-phase zone, and the temperature drop across the two-phase region is given by (149), which reflects solely the interaction between capillarity and phase change.

We conclude that in the general case of practical interest, evaporation occurs only within a boundary layer in the vicinity of the vapor zone, outside of which vapor pressure lowering due to Kelvin effects can be safely neglected. By contrast, condensation is driven by heat conduction and, unless $\delta = 1/KR_m \ll 1$, it may not be neglected in the bulk of the two-phase zone. It is expected that in several practical applications KR_m is not necessarily large, thus previous results [7, 105, 106] may be inapplicable. The effect is most significant in the estimation of the critical heat flux.

Critical Heat Flux

To proceed, a numerical scheme based on stiff ODE solvers was used, the integration starting from region I and consecutively marching through regions II and III. Standard runs were carried out at the conditions of Table 2. An illustration of the applicability of the scheme is shown in Figure 31, where temperature and saturation profiles corresponding to the experiment in [105] ($\theta = \pi/2$, $b = 0.0001346, KR_m = 5184.033$) are plotted.

An excellent match is obtained between experimental and theoretical predictions for the temperature profile. Lack of data for saturation does not permit an assesment of the functional forms

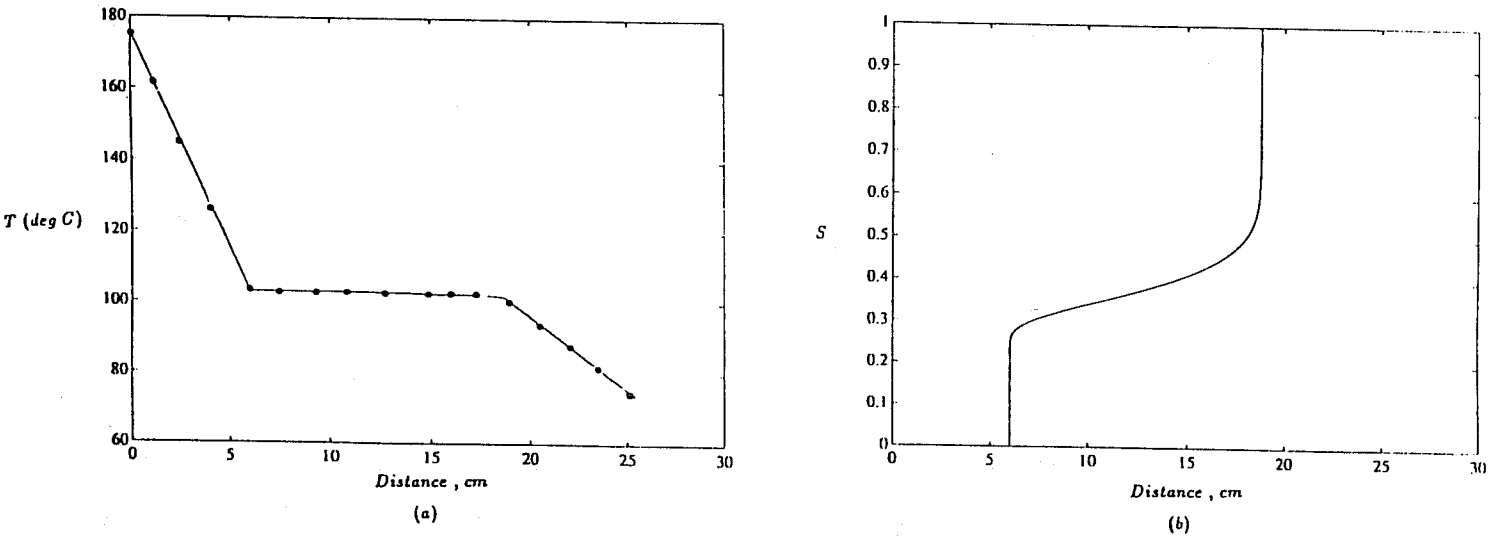

Figure 31: Profiles corresponding to ref.[105]: temperature (a) and liquid saturation (b). dots in (a) correspond to experimental points [105]

$S_{Lr} = 0.20$
$S_{Vr} = 0.05$
$T_o = 171.1$ C
$P_o = 15$ psi
$\sigma = 58.91$ dynes/cm
$v_L = 18.76$ cc/mole
$\rho_L = 0.9606$ g/cm^3
$\rho_V = 0.0006$ g/cm^3
$\mu_L = 2.824\ 10^{-3}$ g/cm-sec
$\mu_V = 1.260\ 10^{-4}$ g/cm-sec
$\lambda_I = 3.0$ W/m-K
$\lambda_{III} = 1.2$ W/m-K

$$\lambda_{II} = \frac{\lambda_I - \lambda_{III}}{2}(1. - S_{Vr} - S_{Lr}) + \lambda_{III}$$

$$k_{rL} = (\frac{S - S_{Lr}}{1 - S_{Lr}})^3$$

$$k_{rV} = (\frac{1 - S_{Vr} - S}{1 - S_{Vr}})^3$$

$$P_c = 2.24 - 2.75S + 1.3S^2$$

Table 2: Parameter values for steam-water counterflow

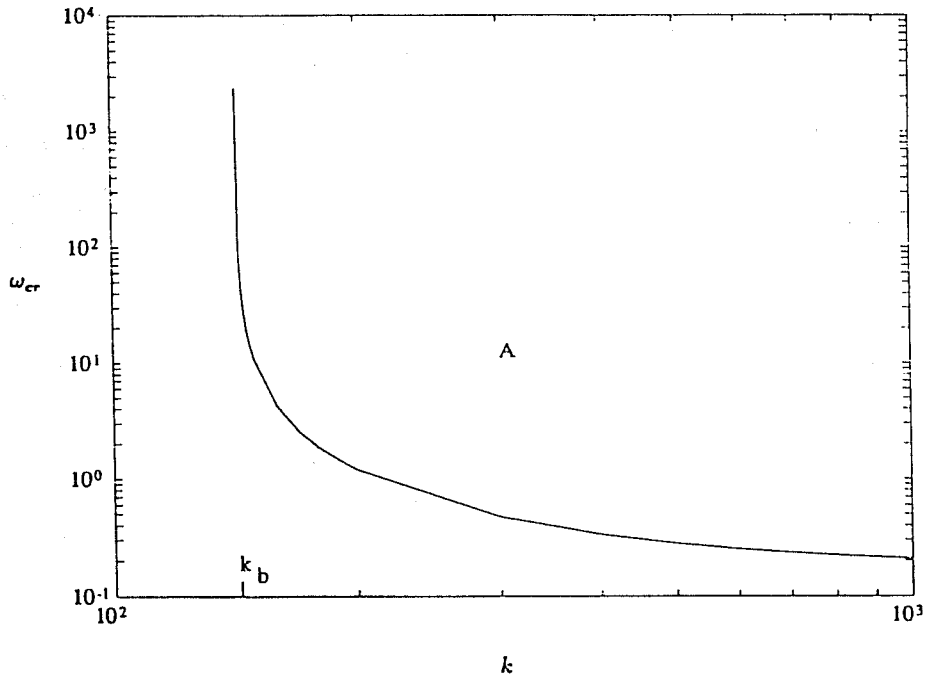

Figure 32: Critical heat flux as a function of permeability for bottom heating.

used for relative permeabilities and capillary pressure. However, the plot exhibits the expected salient boundary layer features (it must be noted that $P_c(0)$ is finite in the present model).

Subsequently, a systematic numerical study was undertaken. In general, results consistent with [105, 106] were obtained in the limit of large KR_m. For example, in the more interesting case of bottom heating [106], critical heat flux values ω_{cr} were found, such that for $\omega/(-\sin\theta) > \omega_{cr}$ a two-phase zone exists of a length that decreases as ω increases. This behavior was thoroughly analysed previously [106]. Unexplored in past investigations, however, were the effects of KR_m and the nature of the solution for $\omega < \omega_{cr}$.

While at large KR_m (or k) the critical flux was indeed found to approach the asymptote [106]

$$\omega_{cr} = (-\sin\theta)\ \max_S \left\{ \frac{k_{rL} k_{rV}}{(k_{rL} + \beta k_{rV})} \right\} \tag{157}$$

which is largely independent of process parameters, it was also found that ω_{cr} slowly increases with decreasing KR_m (or k), and rapidly diverges when a critical permeability value k_b is approached (Figure 32). This singular behavior was verified for a host of parameter values, the standard case yielding the estimate $k_b = 144$ md, well within the range of natural reservoir rocks.

This interesting feature has not been noted before and may lead to significant implications.

Given a process, a critical value k_b can be demarkated such that steady-state solutions are possible for $k > k_b$, in which case a minimum heat flux is required (region A in Fig. 32). The magnitude of the latter is not constant, although it approaches at large k the no-conduction asymptote (157). In the opposite case, $\omega < \omega_{cr}$ or $k < k_b$, saturation and temperature profiles are ill-behaved, in a manner to be precisely specified below, and the existence of steady-state solutions must be seriously questionned.

The sensitivity of k_b was subsequently investigated. Thermal conductivity was found to have no effect on k_b, although it significantly influences the shape and magnitude of the critical curve. A sensitivity, generally weak, was observed upon an increase in the residual saturations (which lead to a decrease of the overall permeabilities in the model of Table 1), the trend being a somewhat higher threshold k_b at lower residual saturations.

Most significant were the effects of capillarity and the imposed pressure P_o (Fig. 33). In both cases, the threshold value varied significantly, roughly in proportion to the square of σ/P_o . While substantial changes in σ mainly require changes in the fluid chemistry, large variations in P_o can be accomplished with relative ease. Therefore, a wide variation in k_b is possible. For the typical conditions of previous laboratory experiments, relatively high thresholds should be expected. By contrast, k_b values of O(μd) would be obtained in typical geothermal systems involving large pressures.

An interpretation of the critical permeability value is offered in the following. Prior to this, numerical results for top heating are also presented. As expected, no constraint in the process parameters exists at large KR_m. At smaller permeability values, however, a sensitivity similar to the previous was detected and a similar (although not as sharp) threshold k_t was identified. Now, steady-states are possible for any heat flux value, if $k > k_t$, and for sufficiently low heat flux values, $\omega < \omega_{cr}$ if $k < k_t$ (region A in Fig. 34). In the opposite case (B in Fig. 34), a steady-state counterflow may not be sustained. Sensitivity studies revealed features similar to the case of bottom heating. Capillarity and imposed pressure P_o were found to be the most important variables. In fact, the two thresholds k_t and k_b were found to practically coincide.

A pictorial schematic of the above is shown in Fig. 35, where the composite of the critical heat flux ω_{cr} near the critical region was constructed. For the case of top heating ($0 < \theta < \pi$), steady-state solutions are possible within the "tunnel" at the front-left, the cross section of which expands

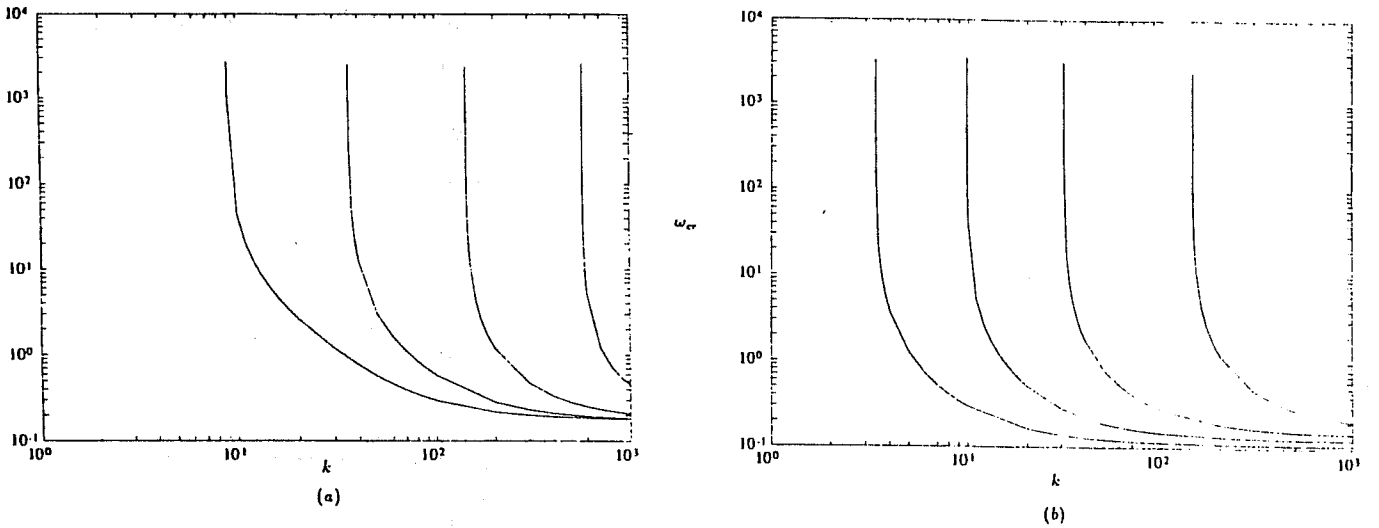

Figure 33: Effect of surface tension (a: $\sigma = 14.7275, 29.455, 58.91, 117.82$, from left to right) and imposed pressure (b: $P_o = 80$, 50, 30, 15, from left to right) on the critical heat flux curve.

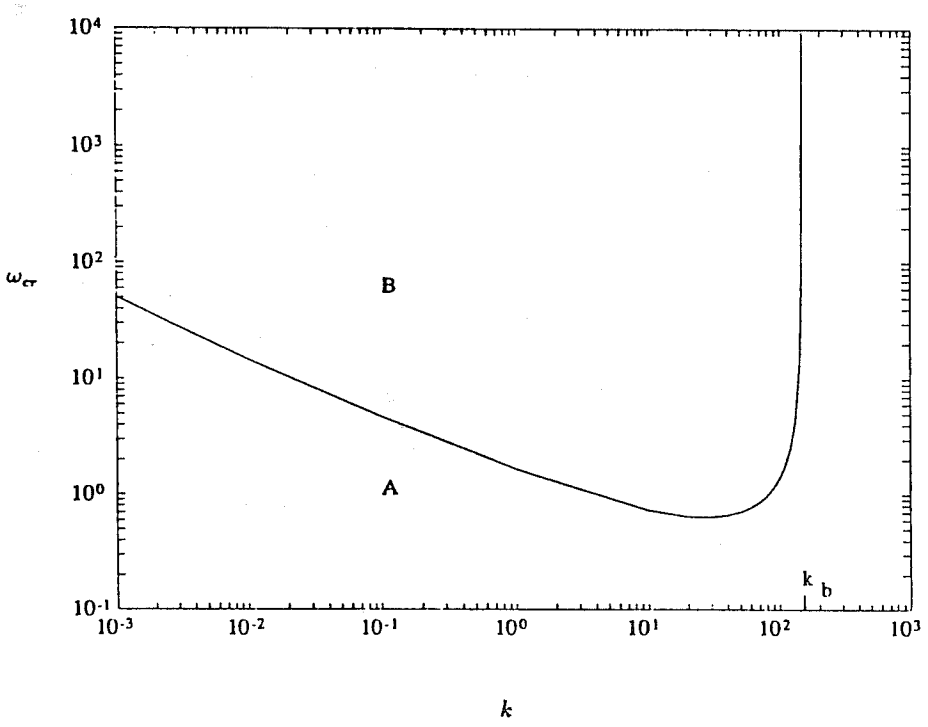

Figure 34: Critical heat flux as a function of permeability for both top and bottom heating.

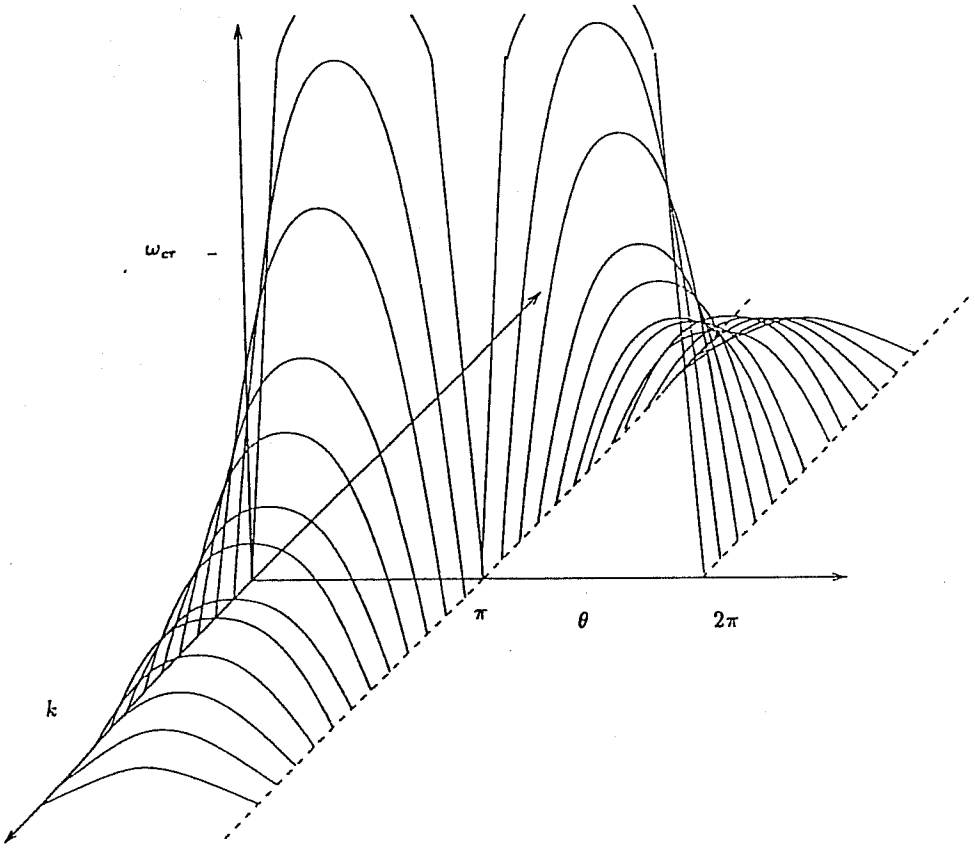

Figure 35: Composite schematic of critical heat flux curve for both top and bottom heating.

to an infinitely large value when $k > k_b$. Conversely, in the case of bottom heating ($\pi < \theta < 2\pi$), steady-states can be sustained only outside the "tunnel" at the back-right, the cross-section of which also diverges when $k < k_b$.

To analyze the critical heat flux curve, the nature of the solution for $\omega < \omega_{cr}$ must be examined. We consider a representative example of bottom heating, with k=1d and parameter values $S_{Lr} = S_{Vr} = 0$. Here the critical heat flux is $\omega_{cr} = 0.45$, a significantly larger value than 0.306348 obtained from the estimate (157). A sequence of (τ, S) and (ξ, S) trajectories are shown in Figures 36-38 for the values $\omega = 0.1, 0.4$, and 0.5, respectively. Plotted also are the level curves when the numerator in (124) vanishes, $G(\tau, S) = 0$, a condition necessary for the change of slope in the (τ, S) trajectory.

The first case (Figure 36) is characteristic of one kind of ill-condition, namely the domain $G > 0$ is disconnected and does not extend over the entire saturation interval. As a result, the solution trajectory changes slope at some point (A in Fig. 36), and further penetration into the two-phase region leads to progressively higher steam saturation and unphysically low temperatures. Previous investigators [7], [106] have speculated that a two-phase zone of "infinite" length would develop under such conditions. While it is true that penetration depth for a given saturation is significantly higher (Figure 36), and in fact it should increase even more as KR_m increases (both the trajectory

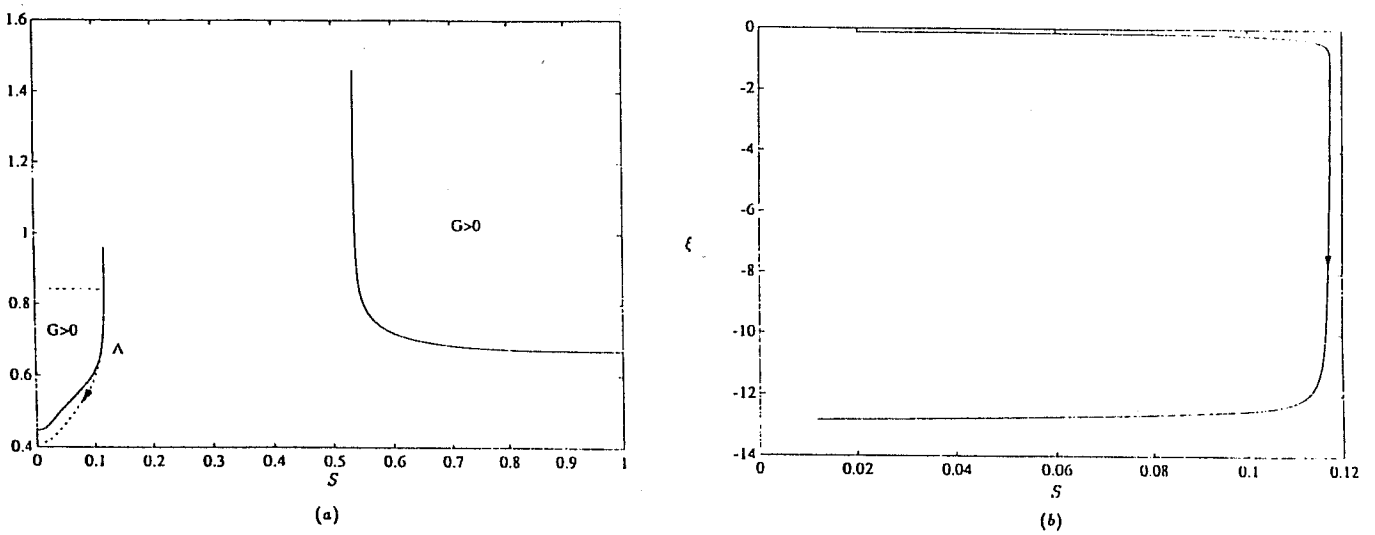

Figure 36: Solution trajectories for bottom heating and $\omega = 0.1$: temperature vs. saturation (a) and saturation vs. distance (b). the solid curves in (a) correspond to $G = 0$.

and the $G = 0$ level curve becoming steeper in the latter case), our results show that unrealistically low temperatures and vapor pressures are eventually reached and the two-phase zone terminates at non-physical values. We argue against the existence of a steady-state under such conditions.

The second case (Figure 37) is characteristic of a different kind of ill-condition. Although the domain $G > 0$ spans the entire saturation interval (0, 1), the value of ω is not high enough, thus the (τ, S) trajectory intersects the $G = 0$ curve before it reaches the end of the two-phase zone. This condition is entirely due to the finite value in KR_m, the no-conduction model predicting no pathological behavior for $\omega > 0.306348$, as pointed out above. By contrast, at the point of intersection A, the saturation profile exhibits a turning point and the ill-condition of the previous case is encountered. For sufficiently large values of ω, however, the two curves are at large enough distance, such that the solution trajectory terminates at the end of the two-phase zone before intersection, and a true heat pipe is established (Fig. 38). Smaller values in k lead to increasingly larger critical heat flux values and, at least within a certain range of k away from k_b, the above interpetation of the ω_{cr} vs k curve applies.

While the departure of ω_{cr} from the asymptote (157) was attributed primarily to conduction,

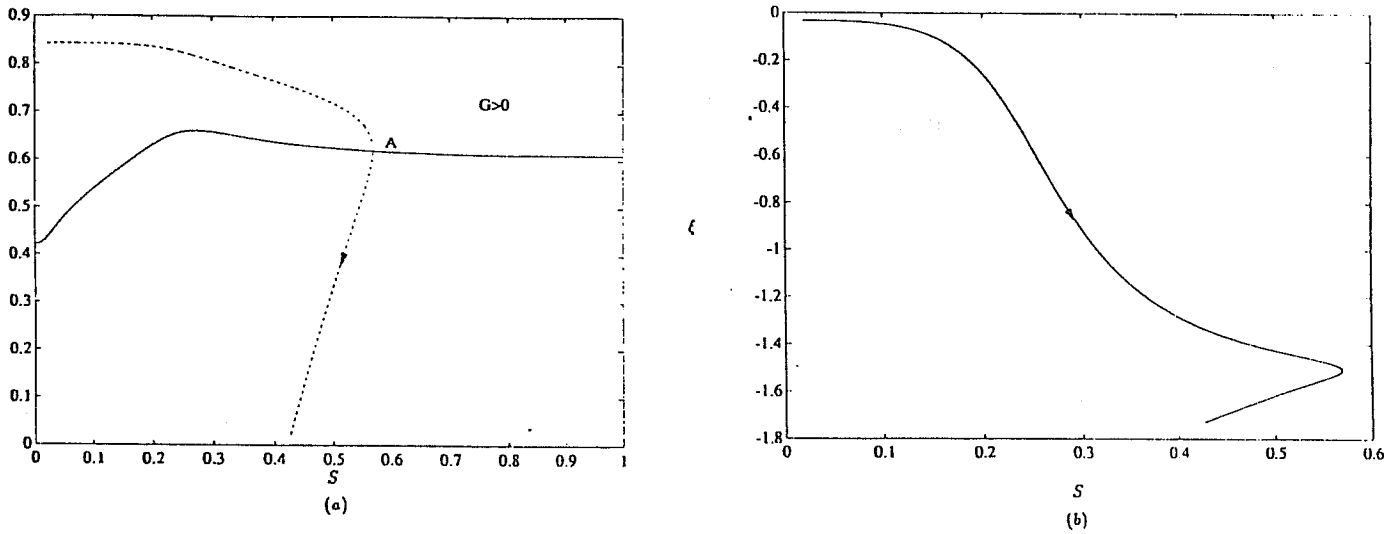

Figure 37: Solution trajectories for bottom heating and $\omega = 0.4$: temperature vs. saturation (a) and saturation vs. distance (b). the solid curves in (a) correspond to $G = 0$.

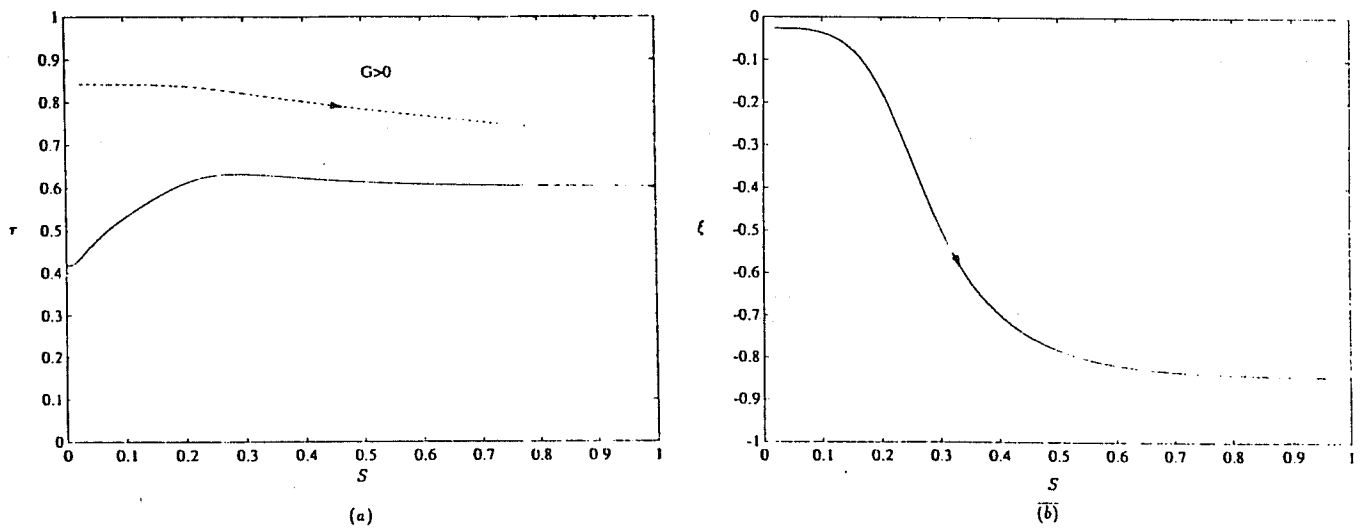

Figure 38: Solution trajectories for bottom heating and $\omega = 0.5$: temperature vs. saturation (a) and saturation vs. distance (b). the solid curves in (a) correspond to $G = 0$.

near the critical region ($k \sim k_b$) capillarity becomes predominant. The condition determining ω_{cr} still remains the same, namely that a turning point in the saturation profile develops. It was numerically observed that here, the latter occurs at the end of the two-phase zone, where $S \to 1 - S_{Vr}$ and $k_{rV} \to 0$. Substitution in $G = 0$, then yields

$$\frac{\omega_{cr}}{-\sin\theta} \simeq \frac{1}{KR_m}\left(\frac{\tau^2}{A}\right)_2 \gg 1 \tag{158}$$

The novel feature, however, is that now ω_{cr} becomes infinitely large as k approaches k_b, which in view of the finite value of KR_m must be attributed to the vanishing of the vapor pressure A_2. An estimate of the latter can be obtained from (123) and (124) by taking the large ω limit

$$R_p \frac{KA}{\tau^2}\frac{d\tau}{dS} = \frac{dJ}{dS}\frac{k_{rL}}{(k_{rL} + \beta k_{rV})} \tag{159}$$

which is further integrated to

$$R_p(A_2 - A_1) \simeq \int_{S_{Lr}}^{1-S_{vr}} \frac{k_{rL}J'(S)dS}{(k_{rL} + \beta k_{rV})} \tag{160}$$

Expectedly, this is also the limit of (149) for the case of horizontal heating. Thus, the critical threshold k_b can be determined in the limit $A_2 \ll 1$

$$k_b \simeq \left(\frac{\sigma}{P_o}\right)^2 \left[\int_{S_{Lr}}^{1-S_{vr}} (-\frac{dJ}{dS})\frac{k_{rL}dS}{(k_{rL} + \beta k_{rV})}\right]^2 \tag{161}$$

The above contains all essential features of the threshold value numerically observed, notably the square dependence on the ratio σ/P_o and the weaker effect of relative permeabilities. The agreement between numerical and analytical results is excellent, as illustrated in Figure 39. After additional algebra, an estimate of the critical curve near k_b may be also derived

$$\frac{\omega_{cr}}{-\sin\theta} \sim \frac{(\text{const})}{KR_m(k - k_b)(\ln \mid k - k_b \mid)^2} \tag{162}$$

The latter contains through R_m the numerically observed effect of λ. As noted, conductivity does not affect the threshold value, although it influences the shape of the critical curve.

Identical considerations apply for the case of top heating. The onset of critical behavior was numerically found to coincide with unphysically low temperatures, first encountered at the end of the two-phase region. In the limit $1 \ll \omega < \omega_{cr}$ it is easily shown that the previous analysis holds identically.

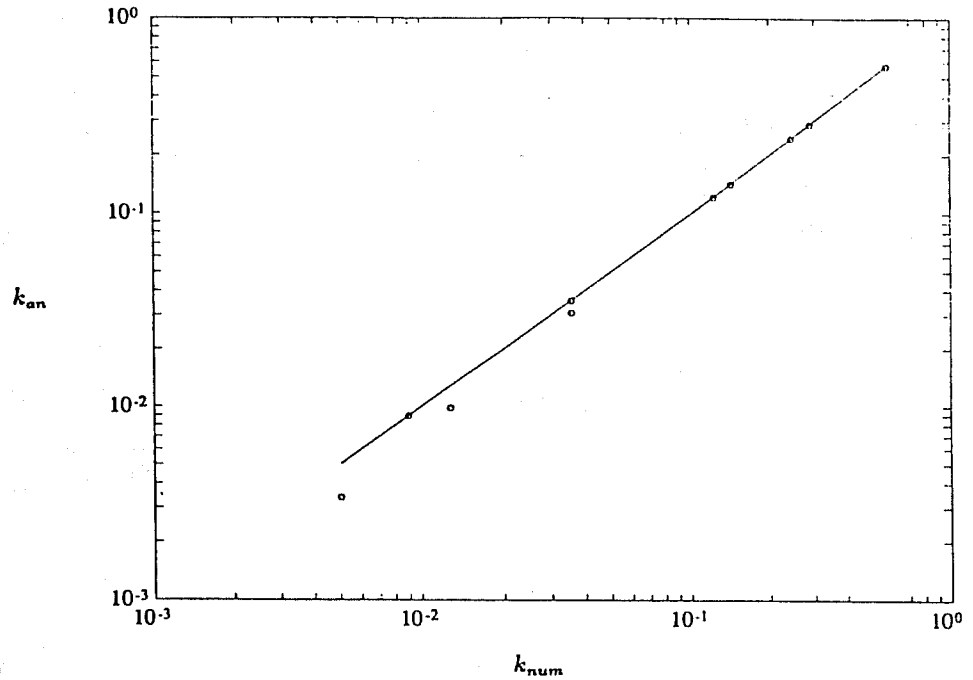

Figure 39: Numerical (dots) and analytical (line) predictions of threshold permeabilities for variable pressure, interfacial tension, residual saturations and thermal conductivities.

To provide a more physical understanding, we first consider the horizontal case, $\theta = 0$. For negligible Kelvin and other secondary effects, the two-phase flow region starts when the vapor becomes saturated, $P_V = P_o$. Counterflow in this region is possible only because of capillarity. In fact, the changes in vapor pressure and capillary pressure are interrelated

$$dP_V = \frac{k_{rL}}{k_{rL} + \beta k_{rV}} dP_c \tag{163}$$

As long as capillarity is not strong, the vapor pressure drop across the region is not large

$$P_V = P_o - \int_0^{P_c(S_{Lr})} \frac{k_{rL}}{k_{rL} + \beta k_{rV}} dP_c \tag{164}$$

and $P_V > 0$. Problems arise when the permeability is low, such that capillarity is large enough for the RHS to become negative. It is straightforward to show that the onset of this condition occurs at the above threshold, k_b. Below this value, capillarity imposes large pressure drops, thus negative values for P_V result with catastrophic consequences on the temperature profile. Clearly, k_b (or k_t) also denotes the lowest permeability value below which steady-state, horizontal counterflow cannot be sustained.

When the medium is inclined, gravity opposes or supplements capillary action, depending on whether the vapor overlies or underlies the liquid. For instance, the expression equivalent to (164) is

$$P_V = P_o - \int_0^{P_c(S_{Lr})} \frac{k_{rL}}{k_{rL} + \beta k_{rV}} dP_c + \rho_L g \sin\theta \int_{x_2}^{x_1} I dx \tag{165}$$

where

$$I = \frac{k_{rL} + \beta R_v k_{rV}}{k_{rL} + \beta k_{rV}} \tag{166}$$

When heating is from the top, capillary pressure is counterbalanced by adverse gravity effects, and a two-phase region may exist even for $k < k_t$, provided that the heat flux is small enough. For this, it is recalled that the extent of the two-phase zone increases as the heat flux decreases. Certainly, heat transfer is of importance here. Opposite considerations apply for the case of bottom heating. At least near k_b, gravity would supplement capillarity in increasing pressure drops, with a contribution roughly proportional to the extent of the two-phase zone. At low $\omega < \omega_{cr}$, the latter is large enough and a steady-state cannot be sustained.

One concludes that consideration of conduction and lower permeability values in the heat pipe problem leads to unexpected, non-trivial corrections, particularly for the case of bottom heating. The relevance of the threshold k_b to heat pipe problems cannot be discounted. A possible distinction from the geothermal problem to be discussed in the following, is the emphasis on capillarity, a measure of which is the parameter R_p. For values of the latter of O(1) or less, the corresponding k_b value would be of the same order with the medium permeability (compare eq.(161)), and the regimes analysed above are likely to be encountered in a heat pipe problem.

4.5 GEOTHERMAL PROBLEM

The next part of this paper addresses the geothermal version of the steady-state, vapor-liquid counterflow, specifically the problem considered by Martin et al. [69] and Schubert and Straus [92] among others. Here $0 < \theta < \pi$, but the heating is from the bottom, namely the imposed temperature gradient and heat flux are negative (in the direction from the liquid to the vapor). As noted before, we shall take reference values corresponding to the liquid- two-phase zone interface, where for simplicity the value $S_{Vr} = 0$ will be assumed. Integration proceeds in the positive ξ direction, from the liquid towards the vapor. The condition derived in [92] is also recalled that the underlying liquid is subcooled, hence the temperature gradient or the heat flux may not exceed an

upper limit. In our notation one obtains

$$-\omega < \frac{R_l}{KR_m} \sim \frac{1}{KR_m} \tag{167}$$

To obtain the geothermal problem from the original formulation (123)-(127), the following limit is considered in the absence of Kelvin effects

$$KR_p \gg 1 \tag{168}$$

With reference conditions corresponding to the top of the liquid zone the above reads in dimensional notation

$$\frac{L_v P_o M_w}{RT_o} \gg \frac{\sigma}{\sqrt{k}} \tag{169}$$

Consistent with [69, 92] conditions (168) or (169) imply that capillarity is of secondary importance and sharply differentiate geothermal and heat pipe problems. To proceed we utilize (168) in (123)-(127) and obtain

$$\frac{d\tau}{dS} = -\epsilon \frac{k_{rL}[KR_m(-\omega) + KR_m R_v k_{rV}]\frac{dJ}{dS}}{G(\tau, S)} \tag{170}$$

$$\frac{dS}{d\xi} = \frac{G(\tau, S)}{k_{rL}[1 + KR_m \frac{A}{\tau^2} k_{rV}]\frac{dJ}{dS}} \tag{171}$$

where we denoted $\epsilon = 1/KR_p$ and

$$G(\tau, S) = k_{rL}[R_l + KR_m \omega \frac{A}{\tau^2} + KR_m \frac{A}{\tau^2} k_{rV}] + \beta k_{rV}[R_v + KR_m \omega \frac{A}{\tau^2}] \tag{172}$$

In general, G and $KR_m\omega$ are of O(1) or less (compare with (167)). Thus, in the geothermal limit $\epsilon \ll 1$, solution trajectories (τ, S) have constant temperature, in regions where G is not small, and closely follow the $G = 0$ curve, otherwise (Figure 40a). In the region of constant temperature, the saturation changes rapidly over an interval of O(1) in length (which, as recalled, expresses a balance between gravity and capillarity in the present notation). It is in this region, where capillarity influences the saturation profile, and which was considered a sharp interface in the previous works [69, 92].

Significant temperature changes start occuring when the solution trajectory approaches the curve $G(\tau, S) = 0$. For the conditions of Figure 40, the latter is precisely the vapor-dominated limit analysed by Schubert and Straus [92] for a simpler model with straight-line relative permeabilities. As is apparent from (171), the saturation gradient is very small ($G \ll 1$) in this domain, thus,

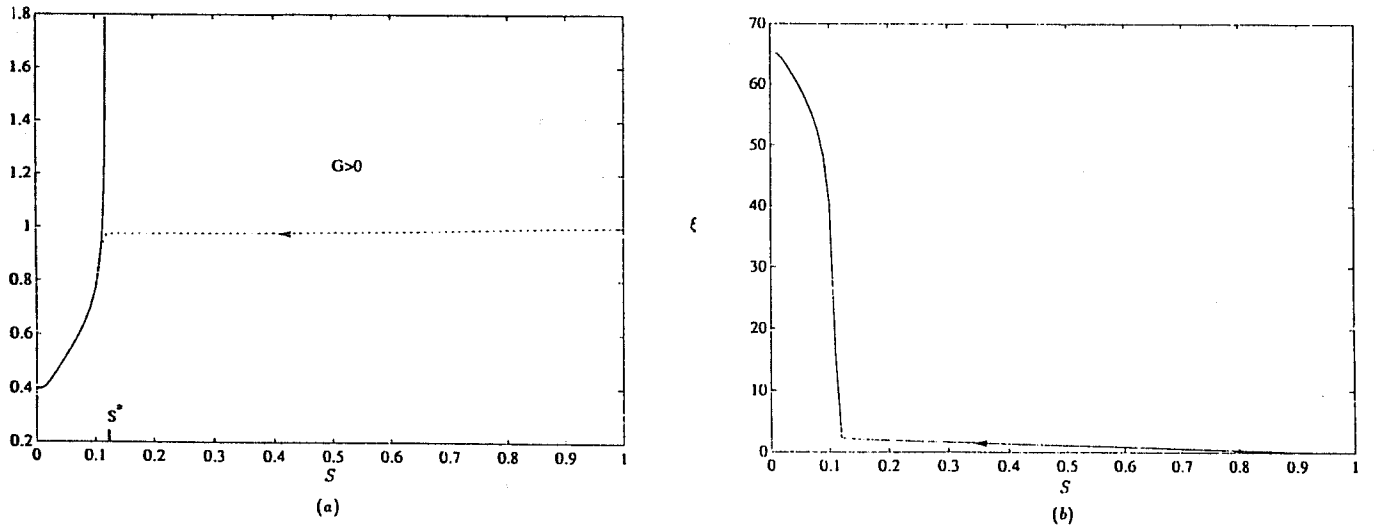

Figure 40: Solution trajectories for the geothermal problem and $\epsilon = 0.0265275$: temperature vs. saturation (a) and saturation vs. distance (b). the solid curves in (a) correspond to $G = 0$.

the extent of the region is quite large (Fig. 40b). In the limit $\epsilon \ll 1$, the region commences at saturation S^* satisfying $G(1, S^*) = 0$, a condition previously derived in different notation [92]. At larger values of ϵ, capillarity can become important and must be also considered (Fig. 41). Here, although ultimately attracted to the curve $G(\tau, S) = 0$, the solution trajectory shows substantial temperature variation before the vapor-dominated region is entered.

With an approximation that rapidly improves as ϵ diminishes, the previous analysis [92] describes the behavior of steam-water counterflow in the geothermal context with excellent accuracy. Considerations similar to [92] were also advanced by Martin et al. in an earlier publication [69]. While identifying the vapor-dominated regime, Martin et al. additionally proposed the existence of liquid-dominated regions. The present formulation readily yields such solutions as well. For this, it is required that the equation $G(1, S^*) = 0$ admits two solutions, a condition demanding higher values in ω.

At such conditions, the (τ, S) diagram is divided into three regions (two far regions with $G < 0$ and a middle one with $G > 0$) by the two branches of the curve $G = 0$ (Figure 42). In the present context, the proposed theory [69] can then be interpreted as follows: Vapor- or liquid- dominated

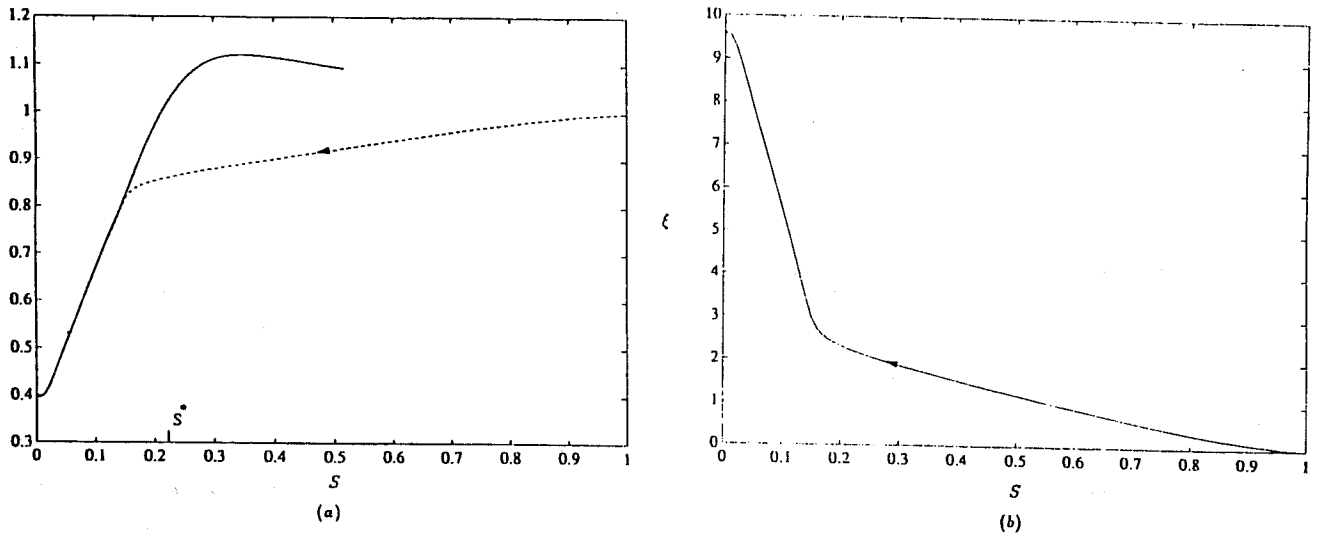

Figure 41: Solution trajectories for the geothermal problem and $\epsilon = 0.0838876$: temperature vs. saturation (a) and saturation vs. distance (b). the solid curves in (a) correspond to $G = 0$.

regimes commence at points A or B, respectively, where $G(1, S^*) = 0$, and they subsequently follow the respective branches of $G(\tau, S) = 0$ (paths AV, BL, respectively). Such behavior appears consistent with (170) and (171) in the limit $\epsilon \ll 1$, but it is doubtful that it actually materializes.

By definition, a solution trajectory must originate form the top of the liquid zone (point C, where $G < 0$), other starting conditions being impossible in a steady-state counterflow system. This trajectory has a negative slope and rapidly approaches the $G = 0$ branch to which it becomes parallel (dashed line pathd CD in Figure 42). Somewhat similar to the heat pipe problem (Figure 36), the solution trajectory crosses over to the middle region ($G > 0$), thus acquires positive slope and parallels the branch $G = 0$ from the other side (note that the two curves practically coincide in Figure 42).

While being different than that previously proposed (path BL), this solution is not acceptable either. An inspection of (171) reveals that ξ must decrease along the path CD, contradicting the requirement that, by convention, ξ increases in the direction from the "liquid" to the "vapor". The other alternative, namely the trajectory extending from point C in the direction opposite to D, is also rejected as it leads to saturation values larger than one. It becomes evident that under such

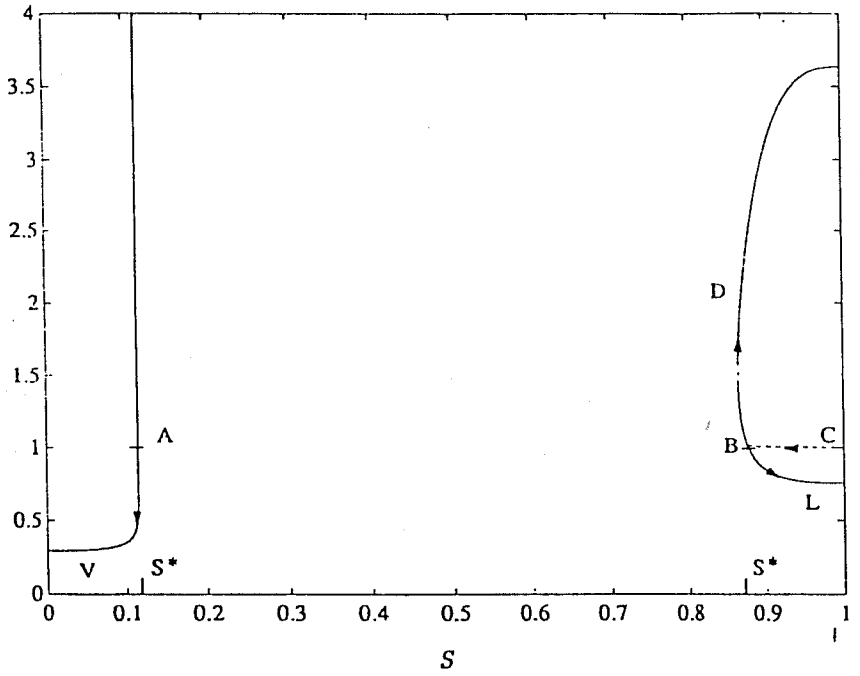

Figure 42: Solution Trajectories for the geothermal problem, with heat flux exceeding the critical limit. The solid curves correspond to $G = 0$.

heat flux conditions a liquid-dominated regime is not realistic, while the vapor-dominated regime is never reached, certainly not when the starting point is the top of the liquid zone, as assumed throughout. One is led to conjecture that steady-state solutions are not possible for such cases, which require that the heat flux exceeds a certain value. The latter is easily determined to be the upper bound (167). The implied contradiction serves to reinforce the above conclusion.

A final remark is also appropriate regarding the analysis presented by Bau and Torrance [7]. These authors examine a configuration with $\theta = 3\pi/2$ and bottom heating (steam at the bottom, temperature gradient in the direction from the vapor to the liquid zone), a problem analyzed in the heat pipe section. In addition to conduction, however, they also neglect capillarity. Because of the latter, some similarities with the geothermal problem may exist. In our formulation, their analysis corresponds to the conditions $KR_p \gg 1, KR_m \gg 1$. By simple rearrangement, equations (123)-(127) read for this problem

$$\frac{d\tau}{dS} = \epsilon \frac{k_{rL}(\omega + k_{rV}R_v)\frac{dJ}{dS}}{G(\tau, S)\frac{A}{\tau^2}} \tag{173}$$

$$\frac{dS}{d\xi} = \frac{G(\tau, S)}{k_{rL} k_{rV}} \frac{dS}{dJ} \tag{174}$$

where $\epsilon = 1/KR_p$ and

$$G(\tau, S) = (k_{rL} + \beta k_{rV})\omega - k_{rL} k_{rV} \tag{175}$$

It readily follows that despite the small capillary effects, the problem is of the same nature as that of the heat pipe thoroughly analysed before. Thus, identical conclusions must be reached regarding solution trajectories and the critical heat flux value, ω_{cr}, which is the necessary lower limit for the existence of a steady-state, steam-water counterflow. Under the implied assumption of negligible conduction, $KR_m \gg 1$, this critical value coincides with the asymptote (157).

4.6 CONCLUSIONS

In this section we have attempted to unify the description of a diverse set of problems arising in heat pipe and geothermal contexts that contain the common mechanism of steady-state, vapor-liquid counterflow. The formalism introduced encompasses several previous studies, which arise as special cases at various limits. In particular, a quantitative assesment of the importance of gravity, capillarity, phase equilibria, heat conduction and Kelvin effects becomes possible.

In the context of the heat pipe problem, it was shown that Kelvin effects are of significance only over a narrow boundary layer at the vapor-two phase boundary, and are otherwise negligible in the counterflow region. Heat conduction was found to influence saturation and temperature profiles near the other end of the two-phase region. It was conjectured that for the case of bottom heating, steady-state counterflow is not possible when the heat flux is below a critical value. Contrary to previous results, the latter is constant only in the limit of large permeability. A permeability threshold value k_b was identified, such that no steady-state counterflow can exist for media of lower permeability. The treshold reflects capillary effects and is mainly a function of the imposed pressure.

The geothermal problem was similarly analysed. The results of Schubert and Straus [92], where capillarity is neglected, were recovered as a limiting case of the present formulation. The same limit is also applicable for the cases discussed by Martin et al. [69]. However, the liquid-dominated regime suggested in the latter was found to lead to non-physical predictions, and it was suggested that such a steady-state may not be reached. It is hoped that the present analysis clarifies several

of the issues involved in steady-state, vapor-liquid counterflow, and that it may be useful as a backbone for further studies in this area.

5 FLOW OF FOAMING SOLUTIONS IN POROUS MEDIA

S. Baghdikian and L.L. Handy

5.1 INTERFACIAL TENSION MEASUREMENTS

In order to reduce residual oil saturations using foaming solutions, the capillary number may be increased by both decreasing the mobility of the gas phase and by reducing the interfacial tension between the aqueous phase and the oil phase. Interfacial tensions were measured for several surfactants which are known to be good foaming agents. Of these, the best in this respect was Shell Enordet LTS18. However, LTS18 is not completely in solution nor is it a good foamer at room temperature. At higher temperatures, its solubility and foamability increase but the interfacial tension also increases. What oil recovery results we have to date indicate that, if any additional oil is recovered with foaming solutions, it is recovered at high gas-and water-to oil ratios. For the time being we have discontinued our efforts on this particular research objective, but it appears we would have to use two surfactants to increase the capillary number enough to affect residual oil saturations–one for a foamer and another to reduce the interfacial tension.

The interfacial tension between oil and surfactant solution was measured using a spinning drop apparatus. Low values of IFT were not obtained with the Chevron Chaser SD1000. Figure 43 shows the IFT between dodecane and SD1000 as a function of temperature. The IFT is reduced by a factor of about 10 as compared to oil-brine IFT. In oil displacement experiments with foam the pressure drop was increased by a factor of 10. This translates to an increase of the capillary number by a factor of 100. However, the residual oil saturation was not reduced any further than in the case of simultaneous gas and brine injection.

The effect of temperature on IFT with LTS18 is shown in Figure 44. This surfactant reduces the IFT by a factor of 10 as compared to SD1000. However, this surfactant is not a good foaming agent at room temperature.

5.2 FOAM INCUBATION PERIOD

The study of foam flow mechanisms, with special emphasis on the conditions under which foam formation is initiated in a porous medium, was done using Chevron SD1000. Some runs were initi-

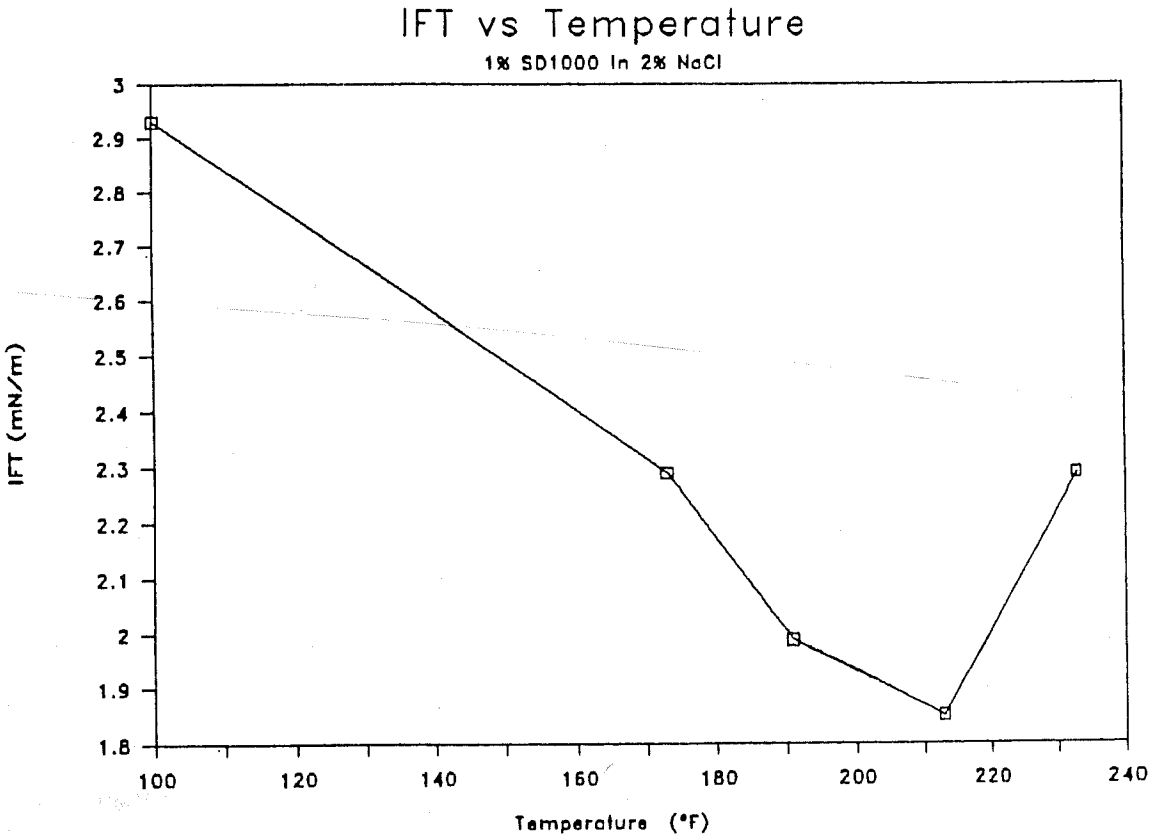

Figure 43: Interfacial tension of 1% SD1000 in 2% NaCl with dodecane vs. temperature.

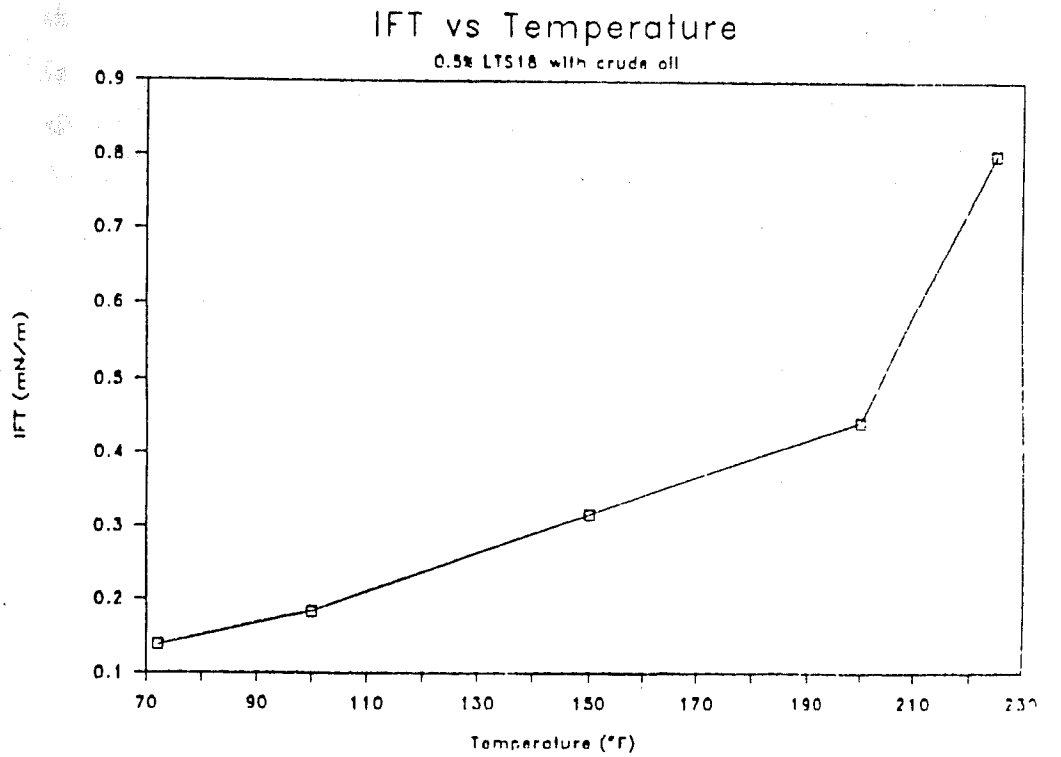

Figure 44: Interfacial tension of 0.5% LTS18 with Huntington Beach crude oil vs. temperature.

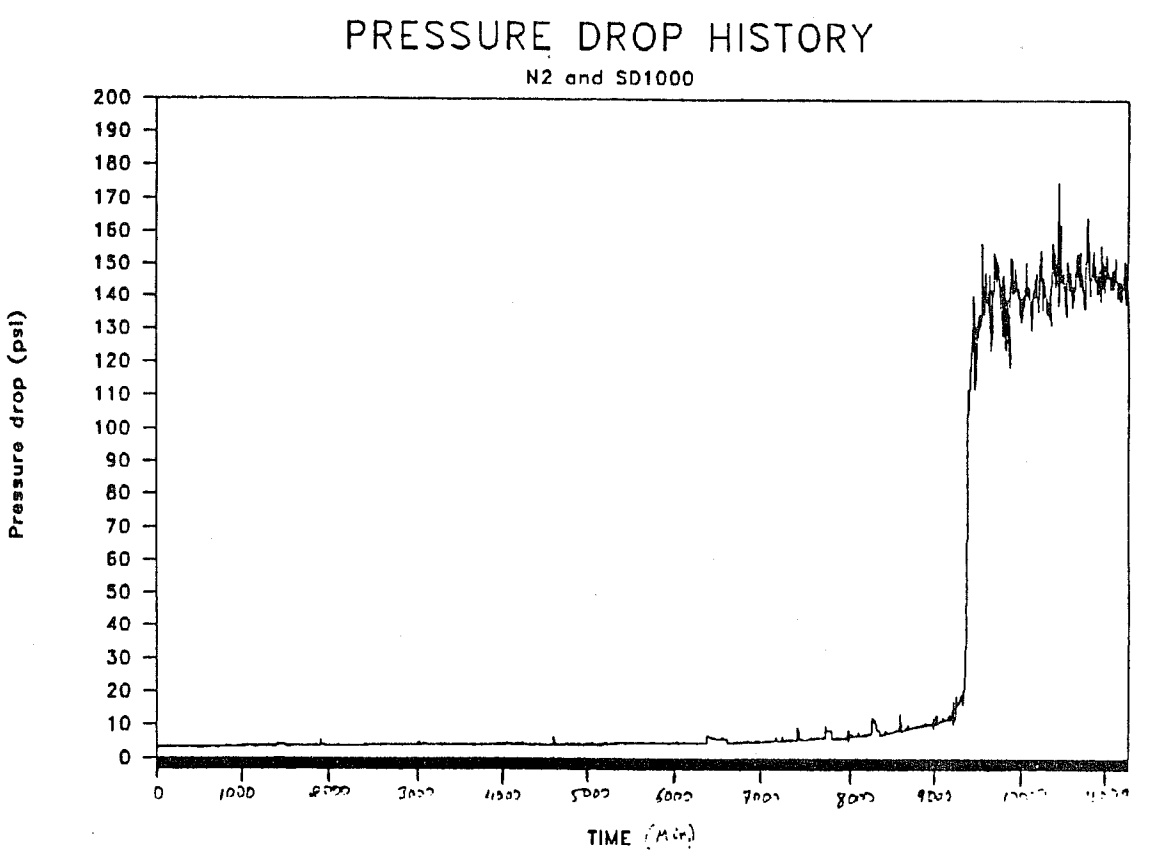

Figure 45: Pressure drop history with simultaneous flow of gas and surfactant solution.

ated in 4 inch long cores (1 inch in diameter). After surfactant adsorption was satisfied by injecting SD1000, gas injection was started. Soon after foam formed, the pressure increased so rapidly that the experiment had to be stopped. The same experiment was performed with lower injection rates. It took a while before the pressure upstream of the core increased. A third experiment was started with even lower rates. It took about six days of injection before the pressure kicked off (see Fig. 45). It is worth noting that in all cases, the pressure surge occurred when the pressure drop reached about the 10 psi range.

The conditions for this last experiment were as follows:

- Absolute permeability: $k_a = 700$ md
- Surfactant flowrate: $q_w = 0.175$ mL/min
- Gas flowrate: $q_g = 1.40$ mL/min
- Liquid Volume Fraction: LVF = 0.11
- Gas Frontal Advance Rate: v = 14 m/Day

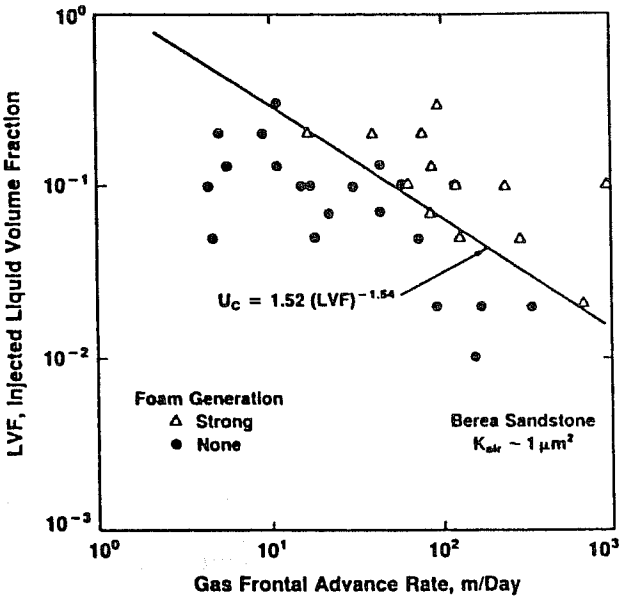

Figure 46: Critical velocity for foam generation in Berea sandstone cores during co-injection of nitrogen and surfactant solution (from Friedman et al. [47]).

Recently, Friedmann et al.[47] reported that there exist a critical velocity for foam to form (see Fig. 46). Based on that equation ($v_c = 1.52(LVF)^{-1.54}$), the minimum velocity in our experiment should be about 40 m/day for foam to form. The actual flow velocity being much lower than the critical one should inhibit the formation of foam. However, foam formation did take place as observed in the pressure history in Figure 45. It would be interesting to investigate the effect of flow rate on foam formation in the presence of oil.

Further experiments were performed to better define the conditions under which foam formation is initiated. We observed that experiments run under different conditions of flowrate and back pressure behave quite differently.

Figure 47 shows the pressure drop history of several corefloods performed under different back pressures and flowrates. Experiments run without back pressure indicate a higher initial pressure drop due to a higher gas expansion ratio as the gas is flowing. One can also deduce that the higher the liquid rate, the higher the ultimate pressure drop will be and the quicker it will get there.

Other corefloods were performed using a prefoamer (see section 5.3). The pressure drop history is shown in Figure 48. One can see that the effect of higher gas injection rate simply shortens the

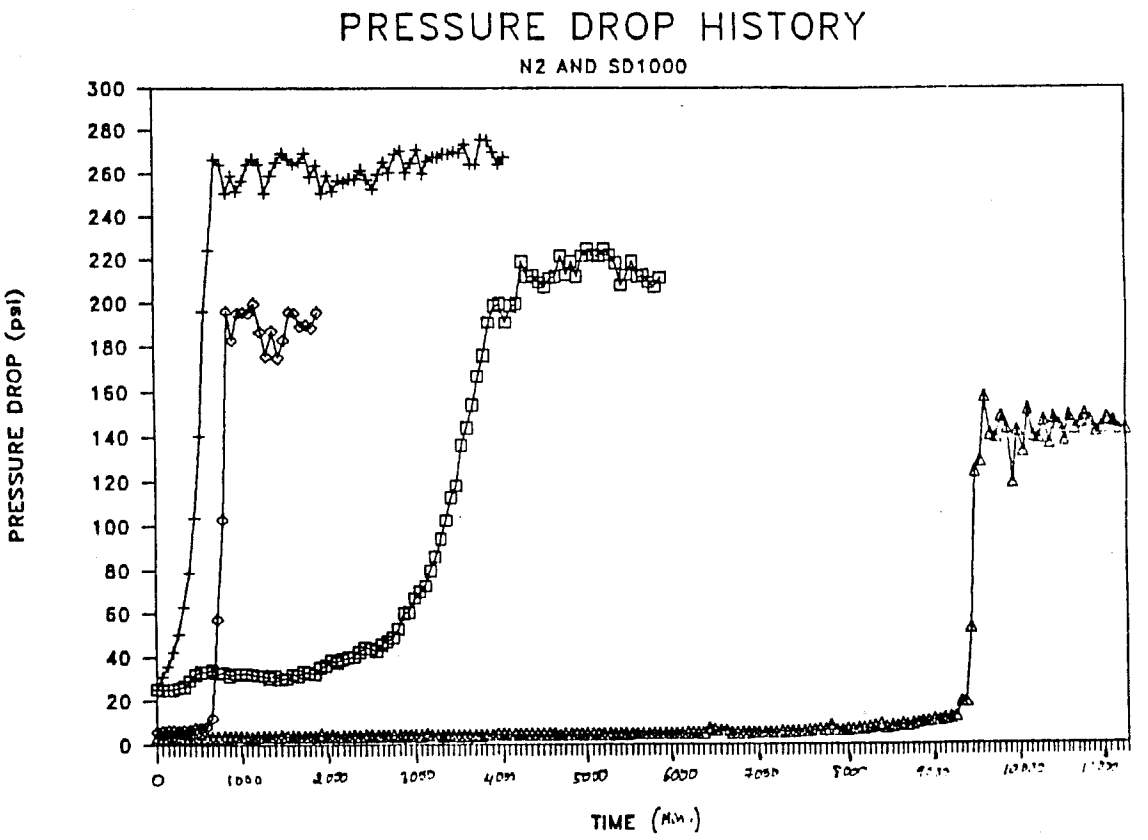

Figure 47: Pressure drop history during simultaneous injection of nitrogen and SD1000 in Berea sandstone.

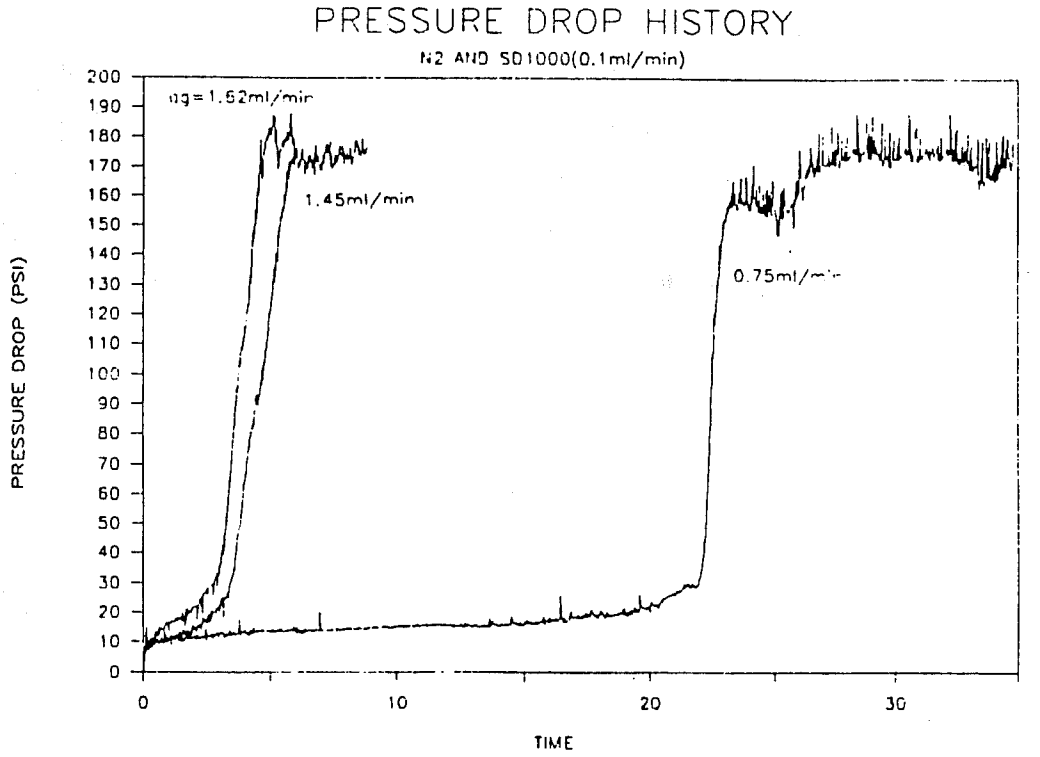

Figure 48: Pressure drop history during simultaneous injection of nitrogen and SD1000 in Berea sandstone at various gas flowrates.

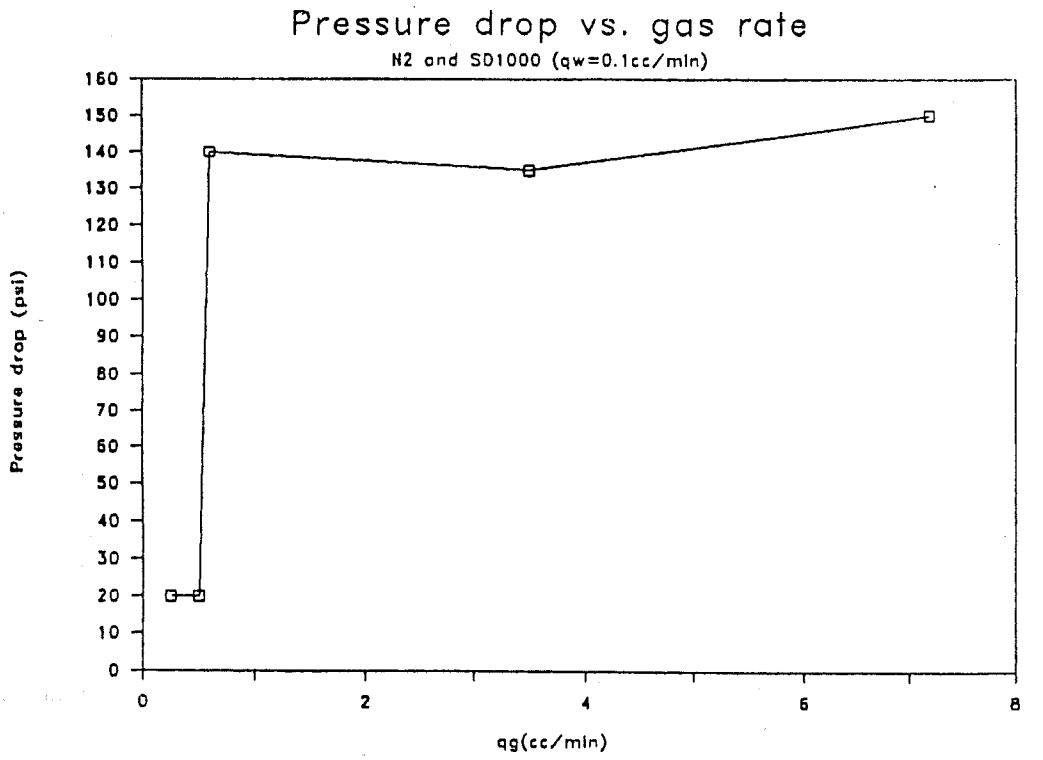

Figure 49: Relationship between pressure drop and gas injection rate at constant surfactant injection rate.

incubation period for the system to reach the steady state pressure drop of about 180 psi.

The effect of gas injection rate as a function of pressure drop is shown in Figure 49. There seems to be a critical gas rate to cause foaming and a significant pressure gradient. These experiments were performed with a back pressure of 110 psi.

With no back pressure present, the effect of surfactant injection rate as a function of pressure drop is shown in Figure 50. The surfactant rate was changed and the ultimate pressure drop was recorded. Changing the rate from 0.2cc/min down to 0.1cc/min and then back up to 0.2cc/min caused the pressure drop to decrease and then attain the initial value.

An experiment was performed where the rates of gas and surfactant flow were varied at different steps and the pressure drop monitored. However, often it is not possible to duplicate results. Within the accuracy that was possible to achieve, a discontinuity was observed in the increase of pressure drop with an increase in flowrate. No significant pressure drop hysteresis was noticed during the imbibition or the drainage cycle with changing flowrates. Persoff et al.[82] had noticed that changing the liquid flowrate does not change the saturations significantly, although foam flow resistance increases.

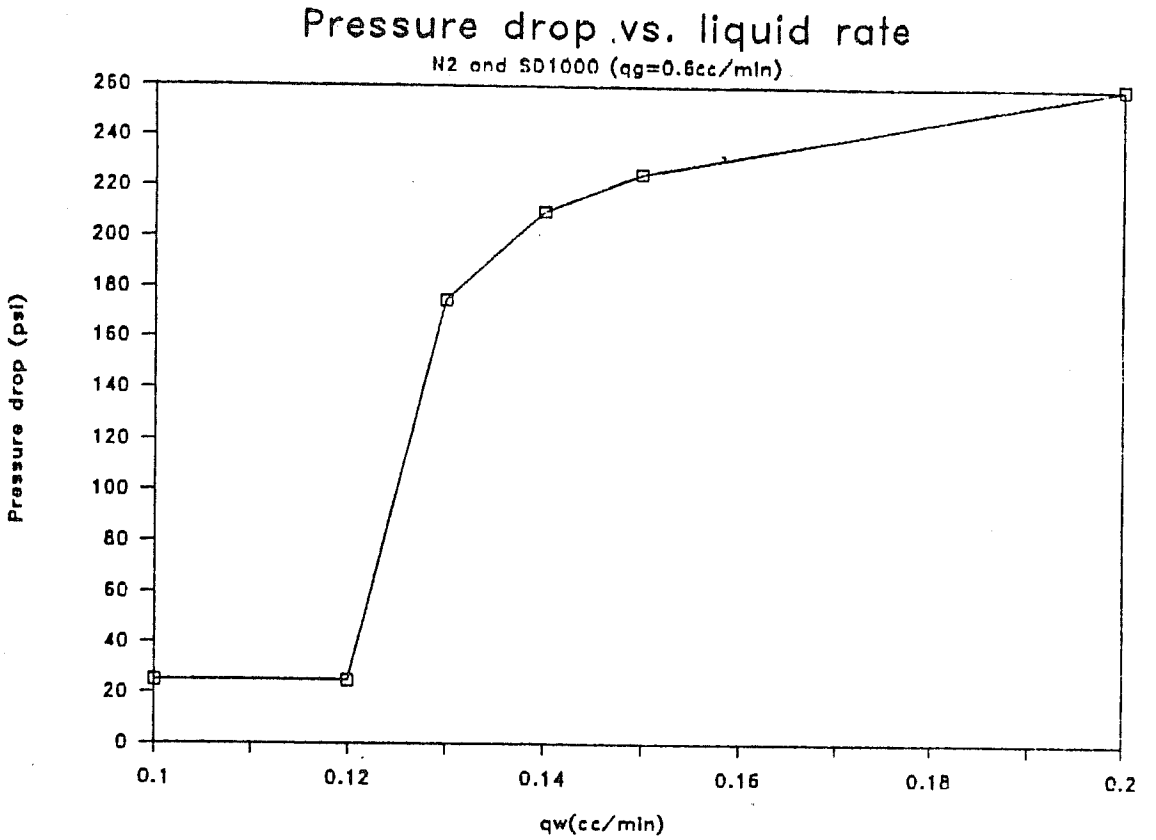

Figure 50: Relationship between pressure drop and surfactant injection rate at constant gas injection rate.

The conditions that trigger a high pressure drop across the core are still not well understood. In order to study the conditions that promote a fine textured foam formation, the pressure history of different flow experiments were monitored. Upon comparison of the pressure response with the flow conditions, it became apparent that the results are in agreement with what Persoff et al.[82] recently reported.

The liquid saturation in the core has an average value of about 35%. Injecting 24PV's of surfactant solution at 0.57m/D after reaching steady-state foam flow conditions, increased the liquid saturation to about 45%. Injecting 11PV's of gas at 2.2m/D reduced the liquid saturation to about 17%. The presence of the surfactant in the liquid phase prevents a wide range of saturation to occur.

Persoff et al.'s[82] observation of a constant pressure gradient with a constant liquid velocity, while varying the gas velocity, is in agreement with our results. The pressure drop obtained in the core increases with increasing liquid velocity and is independent of gas velocity.

5.3 EFFECT OF FOAM GENERATOR

The effects of using a foam generator in simultaneous injection of gas and surfactant solution was evaluated. The use of a foam generator increased the steady-state pressure drop attained in the experiment. Under all flow conditions, the use of a foam generator enhances the texture of the foam. This in turn contributes to a higher pressure gradient. When injecting foaming solutions, the use of a foam generator mixes the fluids before entering the porous medium whereas the lack of a foam generator causes the fluids to enter the core in slugs. It is apparent that a minimum pressure gradient is needed in order to form a fine textured foam.

De Vries et al.[30] did not notice any influence on their results upon varying the injected foam texture by varying the properties of the foam generator. In their experiments, the pressure drop was measured in a very short section in the middle of the core. Therefore, the foam texture is changed by the porous medium by the time it reaches the middle section of the core.

6 MODIFICATION OF BUCKLEY-LEVERETT AND JBN METHODS FOR POWER-LAW FLUIDS

M. Salman, S. Baghdikian, L.L. Handy and Y.C. Yortsos

6.1 INTRODUCTION

The use of non-Newtonian fluids for purposes of mobility control is a routine operation in EOR processes. A variety of rheologically complex fluids ranging from polymer solutions to gels, foams and other additives are injected to improve sweep efficiencies, divert displacing fluids and preferentially block swept zones [117]. In contrast to Newtonian fluids, however, the state of the art in the modeling of flow of non-Newtonian fluids, either single- or multiphase, in porous media is far from complete. As a rule, the interplay of the nonlinear fluid rheology with the porespace geometry and flow paths results in complicated problems, that prohibit the direct passage from the micro-(pore) to the macroscale [96]. Thus, with few exceptions, laws analogous to Darcy's for flow of non-Newtonian fluids in porous media have not been developed.

Although frequently used in practice, the direct application of single capillary flow expressions to porous media is in principle erroneous. The pore level relationship $\Delta p/l = f(q)$ must in general be replaced at the macroscopic level by a different relation $\Delta p/L = F(Q, ...)$, where F is a function different than f. The important exception involves power-law fluids [65]. For such cases, the power-law relationship between pressure drop and flow rate in a single capillary survives the averaging over the multitude of interconnected pores. As a result, the local expressions for the well-studied single capillary problem [21, 102], can be extrapolated to a porous medium, subject to appropriate rescaling and modification.

Although this was apparently accepted without questioning, to the knowledge of these authors, the first rigorous argument for its support was provided by Larson [65]. It was shown that the power-law and its exponent remain the same for both the single capillary and the porous media, which represents a significant advance for process modeling. The problem becomes then the determination of the appropriate prefactor in the macroscopic expression, in principle a mere computational task. Expressions currently used rely on the inaccurate model of a bundle of parallel capillaries [21, 102], although more rigorous results [97, 17, 119] are rapidly emerging.

Similar issues arise in the simultaneous flow of a pair of immiscible fluids in porous media.

However, when one or both of the two fluids are of the power-law type and the displacement at the porescale is controlled by capillarity, the partition of the fluids in the pore network is rate-independent. The concept of saturation-dependent relative permeability is then applicable, perhaps in a modified form, to account for possible effects on the power-law exponent [119]. Under this premise of capillary control ($N_{ca} \ll 1$), the macroscopic displacement can then be simulated in a straightforward fashion.

Despite the considerable extent of applications involving non-Newtonian fluids in porous media, it is surprising to note that the counterparts of familiar notions such as the fractional flow function, the Buckley-Leverett displacement and the JBN method, have not appeared in the literature. The need is particularly felt in the interpretation of transient displacements in flow experiments, where a non-Newtonian (perhaps power-law) fluid is involved [90, 121, 88]. Under such conditions, it is not at all clear that the traditional JBN method [61] holds, or that the relative permeabilities so obtained are meaningful. The development of alternatives must then be sought, starting with the solution of the underlying displacement process.

In this section we present such an approach. We consider the modification of the JBN method when power-law fluids are involved in either drainage or imbibition, and examine the sensitivity of the results to the rheological aspects of the fluid. In the process, we also need to solve the associated Buckley-Leverett displacement equations. Generalizations to fluids of a more general rheology are then suggested. The section is organized as follows: The basic aspects of the model that lead to rate-dependent fractional flow are first reviewed. Buckley-Leverett solutions and frontal displacement features are next derived. The proper modification to the JBN method is subsequently presented. Sensitivity studies and generalizations complete the study.

6.2 BUCKLEY-LEVERETT ANALYSIS

6.2.1 Fractional Flow

We consider the simultaneous flow of two immiscible phases in a horizontal porous medium, under local capillary control. Although straightforward, effects of gravity are not considered. For simplicity, we take the "oleic" phase (subscript o) to be Newtonian and non-wetting, and the "polymer solution" phase (subscript p) to be a power-law, wetting fluid. The bulk rheology of the latter is described by a power-law, which for one-dimensional shear flow reads [11]

$$\tau_{yx} = K\gamma^n \tag{176}$$

Here τ_{yx} is the shear stress, $\gamma = |du_x/dy|$ is the rate of shear, n is the power-law exponent and K is the consistency index, the latter two being functions of the fluid composition.

The extension of Darcy's law to describe single-phase flow of a power-law fluid in porous media is formally taken

$$u^n = -(\frac{k}{m})(\frac{\partial p}{\partial x}) \tag{177}$$

where k is the permeability to a Newtonian fluid. Parameter m has the dimensions *viscosity* / *velocity*$^{n-1}$ and the dependence

$$m = AKk^{(1-n)/2} \tag{178}$$

The dimensionless prefactor A is a function of the geometry and topology of the medium, in general unknown, although various simplifying estimates have appeared based on parallel capillary models [21, 102]

$$A = \frac{1}{12}\left(\frac{9n+3}{n}\right)^n (150\phi)^{(1-n)/2} \tag{179}$$

$$A = 2\left(\frac{n\phi}{3n+1}\right)^{-n}\left(\frac{8}{\phi}\right)^{-(n+1)/2} \tag{180}$$

It was previously noted that the above expressions are in principle not accurate and should be replaced by their analogues, e.g. those obtained from network studies [97, 17, 119]. A note must also be made regarding the permeability value above. In the absence of adsorption and inaccessible pore volume effects, the single-phase (e.g. brine) permeability value applies. In the more likely opposite case, however, a different value is assumed: that corresponding to a different porespace, where pores have effective sizes reduced by the adsorbed layer, a fraction of smaller pores have become plugged and are inaccessible, and a slip condition at the pore walls may be applicable [96, 121]. With the assumption of irreversible adsorption, this permeability value is obtained upon exhaustively displacing (steady-state conditions) the polymer solution by brine. For the case of transient displacement, however, significant complications may arise depending on the particular displacement history [88]. Such issues are not considered in the present study, which focuses primarily on rate effects on the displacement.

Consider, now, the extension to two-phase flow and formally take

$$u_o = -\left(\frac{kk_{ro}}{\mu_o}\right)\left(\frac{\partial p_o}{\partial x}\right) \tag{181}$$

$$(u_p)^n = -\left(\frac{kk_{rp}}{m}\right)\left(\frac{\partial p_p}{\partial x}\right) \tag{182}$$

The relative permeabilities, k_{ro} and k_{rp}, thus introduced are independent of flow rate, as long as capillarity controls at the porescale and adsorption/inaccessibility effects are rate-independent. However, k_{rp} (and to a lesser extent, k_{ro}) may be functions of n [119], and are not necessarily identical to those for an "oil-water" pair. It is also noted that the parameters k_{rp} and m appear in the relative conductance combination k_{rp}/m. Thus a determination of both values simultaneously is unlikely. For this reason, we elect to assign all saturation dependence into k_{rp} and simply take m to be the single-phase constant given in (177)-(178).

Before proceeding further, it is useful to define the parameter ($n \neq 1$)

$$H = \left(\frac{\mu_o}{m}\right)^{1/(n-1)} \tag{183}$$

with dimensions of velocity. This parameter is the ratio of a characteristic pore size (e.g. square root of permeability) to a characteristic time

$$H \sim k^{1/2}\left(\frac{\mu_o}{K}\right)^{1/(n-1)} \tag{184}$$

and depends on both the porous medium and the fluid compositions. Thus, flow rate effects enter via the dimensionless ratio

$$\alpha = \frac{u_t}{H} \tag{185}$$

where u_t is the total flow velocity.

We proceed by neglecting capillarity at the macroscale to obtain

$$(u_p)^n = (u_o)(H)^{n-1}\Lambda(S_p) \tag{186}$$

where

$$\Lambda(S_p) = \frac{k_{rp}(S_p)}{k_{ro}(S_p)} \tag{187}$$

and substitute in the fractional flow $f_p = u_p/u_t$ to get the relation

$$\frac{1-f_p}{(f_p)^n} = (\alpha)^{n-1}\frac{1}{\Lambda} \tag{188}$$

Contrary to the Newtonian case, the fractional flow f_p is not explicit. It is obtained instead as the (only acceptable) root of the algebraic equation (188). Significantly, f_p now depends on the total rate as well, in addition to the exponent n and the saturation S_p.

To illustrate various effects, fractional flow curves were constructed based on the following relative permeability functions

$$k_{rp} = S^3, \qquad k_{ro} = (1-S)^2 \tag{189}$$

where S is the normalized saturation $S = (S_p - S_{pr})/(1 - S_{pr} - S_{or})$. For convenience, the relative permeabilities are taken independent of n, although this may not be appropriate near the residual saturation of the power-law fluid. We restate, however, our intention to study effects of flow rate, and we defer the reader to a more complete analysis of saturation and exponent effects in a related study [119].

The effect of flow rate is shown in Figures 51a and 51b, for shear thinning and shear thickening fluids, respectively. As anticipated, for the case of shear thinning (Fig. 51a), the fractional flow curves shift to the right (become more favorable in terms of displacement efficiency) when α decreases (lower flow rate or higher permeability media). While for shear thickening fluids (Fig. 51b), the fractional flow is lowered at larger values of α (higher flow rate or low permeability media). A simple asymptotic expression for the fractional flow f_p near the residual value

$$f_p \sim \frac{(S_p - S_{pr})^{\tau/n}}{\alpha^{(1-1/n)}} \tag{190}$$

verifies the above. τ is the power-law exponent in the relative permeability.

The effect of n for otherwise constant values of α is less apparent. A simple analysis in this case shows that f_p is an increasing function of n, if the condition $\alpha f_p < 1$ is satisfied (Figure 52a), and a decreasing function of n, otherwise. For large enough flow rates (or values of α), therefore, the f_p curve rotates towards the vertical as the fluid becomes more shear thickening (Figures 52b, 52c).

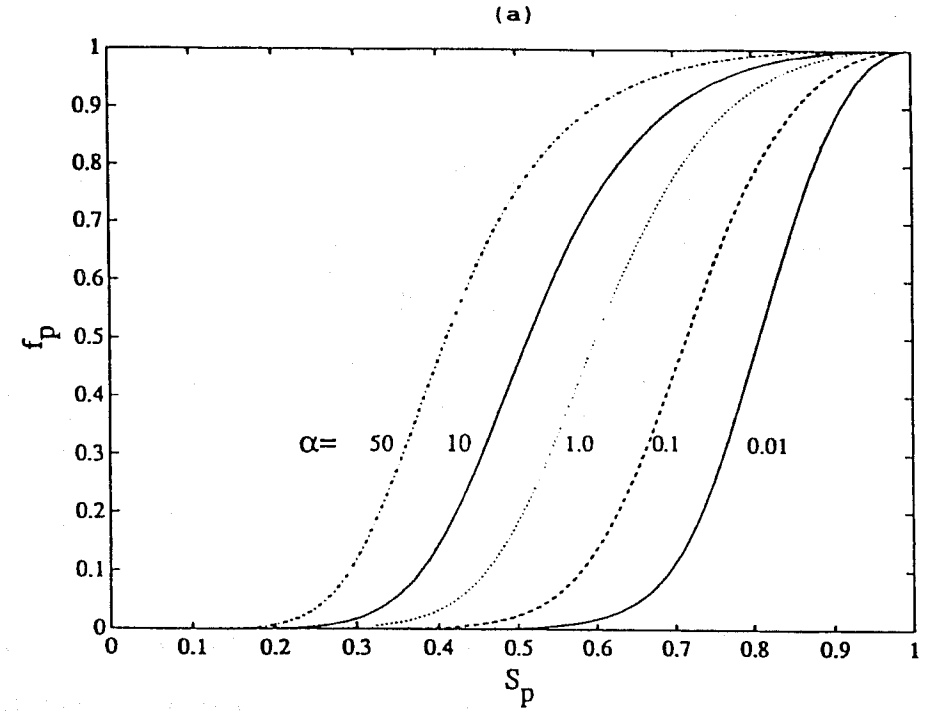

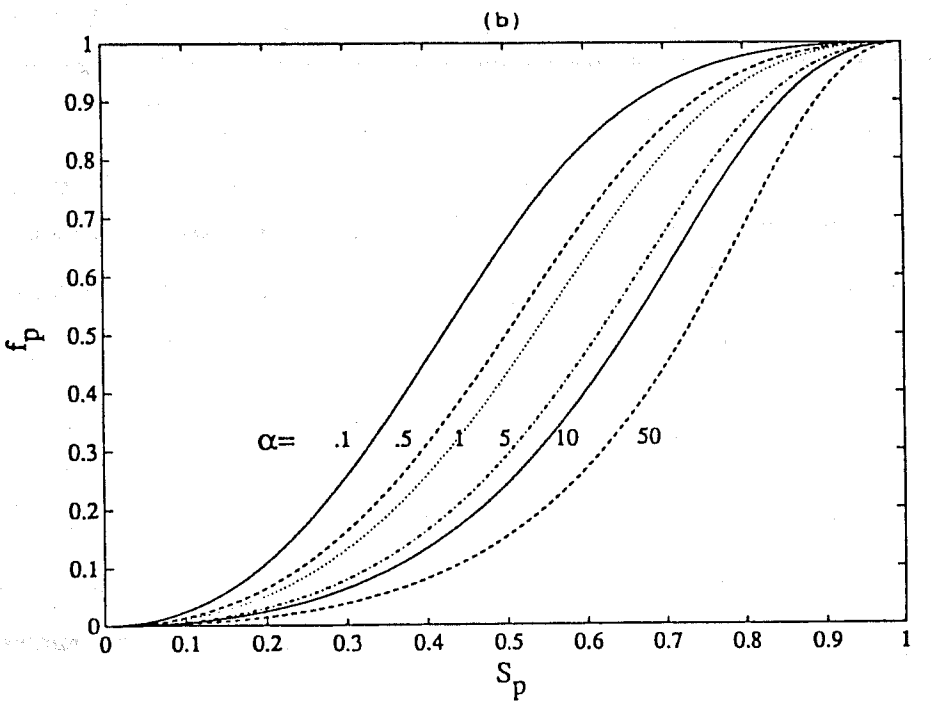

Figure 51: Effect of flow rate on fractional flow f_p: (a) shear thinning (n=0.5), (b) shear thickening (n=1.5).

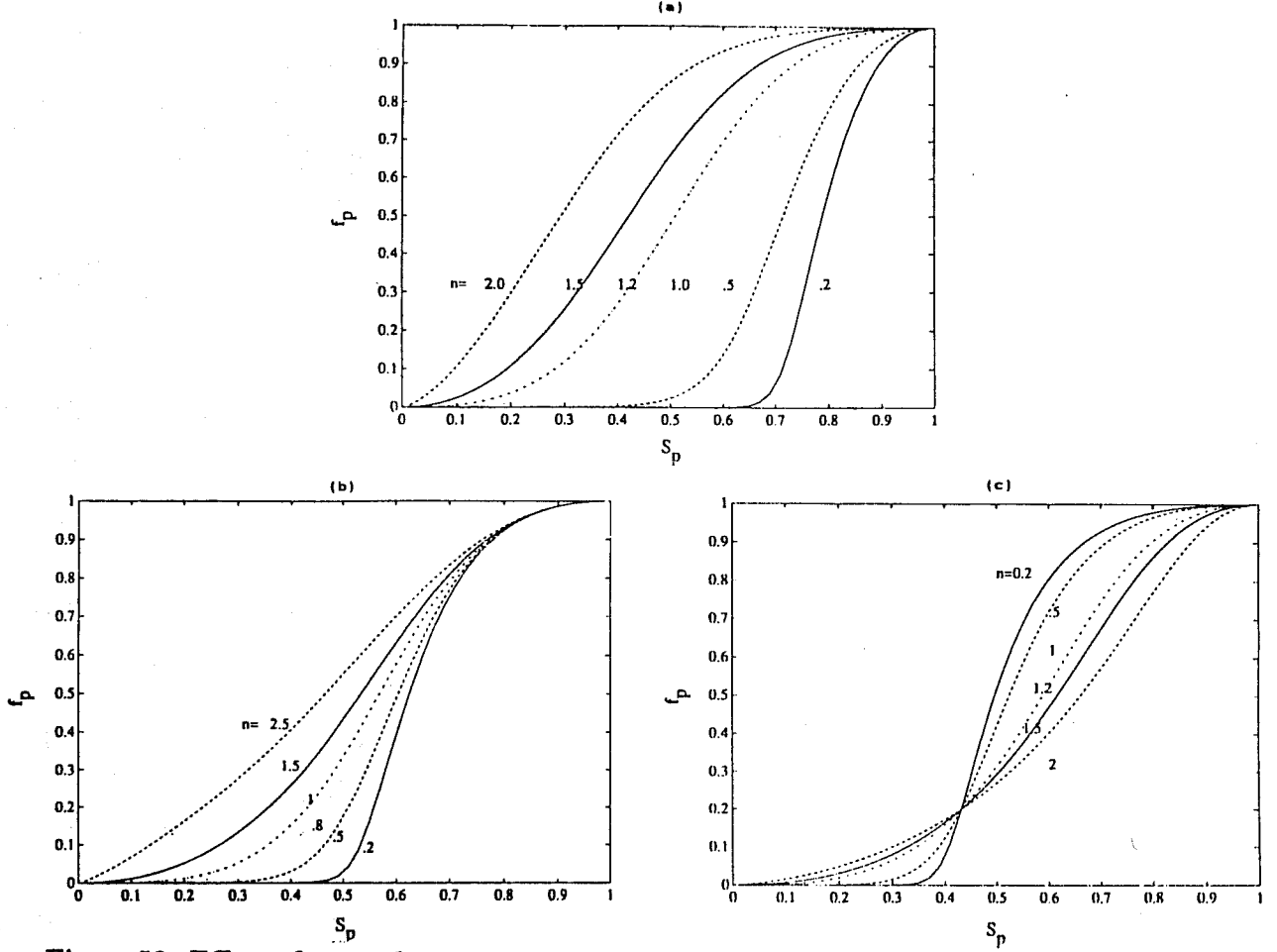

Figure 52: Effect of power-law exponent on fractional flow f_p: (a) low rates (α=0.1), (b) moderate rates (α=1), (c) high rates (α=5).

6.2.2 Frontal Displacement

We consider next the simultaneous flow of the two fluids at constant injection rate u_t. The displacement is described by the same equations as in the case of Newtonian fluids

$$\frac{\partial S_p}{\partial t} + \frac{\partial f_p}{\partial x} = 0 \tag{191}$$

where, now, f_p solves (188). This is the prototypical first order, hyperbolic equation, solvable by characteristics [114] and typically involves a shock front and the associated tangent construction. We shall focus on the case of imbibition (power-law fluid displacing a Newtonian fluid). The front saturation, S_{pF}, is obtained from the shock condition

$$\frac{f_{pF}}{S_{pF} - S_{pr}} = \frac{df_p}{dS_p} \tag{192}$$

along with (188). Further manipulation leads to an equivalent expression

$$\left(\frac{S_{pF} - S_{pr}}{\Lambda}\right) \frac{d\Lambda}{dS_p} = \frac{f_p + n(1 - f_p)}{1 - f_p} \tag{193}$$

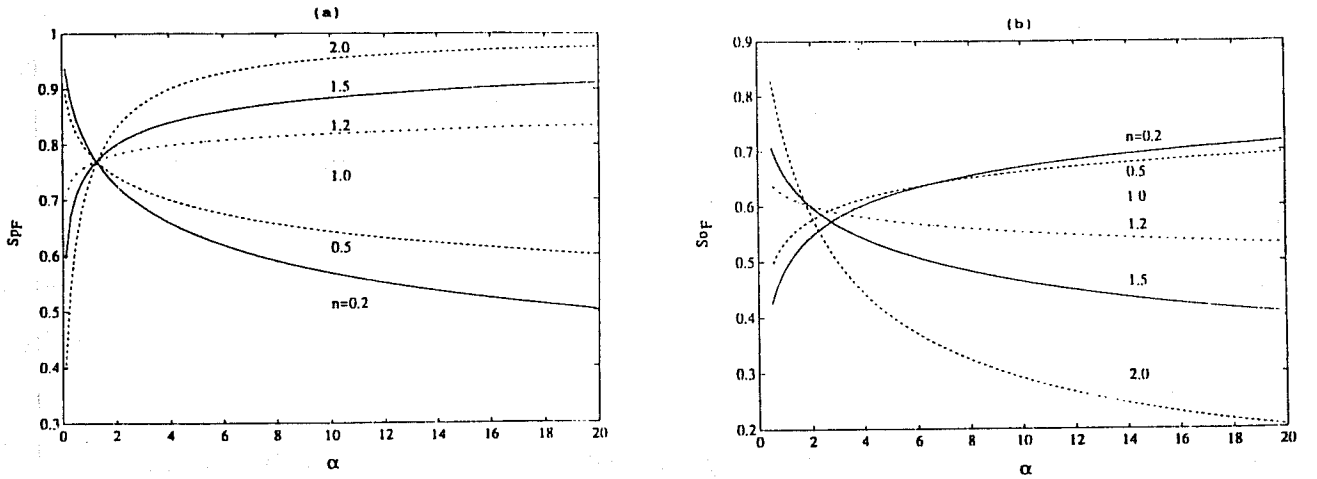

Figure 53: Front saturation as a function of rate and power-law exponent: (a) imbibition, (b) drainage.

Similar results are obtained for the drainage case, where now

$$\left(\frac{S_{pi} - S_{pF}}{\Lambda}\right)\frac{d\Lambda}{dS_p} = 1 + \frac{n(1-f_p)}{f_p} \tag{194}$$

The front saturation is plotted as a function of rate and exponent in Figures 53a and 53b, for the cases of imbibition and drainage, respectively. The results for imbibition are quite instructive and elucidate the importance of rate (Figure 53a). Front saturations and displacement efficiencies increase with rate for shear thickening fluids. Opposite behavior is exhibited in the shear thinning case. However, shear thickening yields results of higher efficiency only when the rate is large enough. For values of α less than approximately one (Figure 53a), a shear thinning fluid would lead to better recoveries. The latter case is of course favored at lower rates, higher permeabilities and more viscous oils. Similar results are obtained for a drainage process (Figure 53b).

Upon construction of the front saturation, other displacement features (average saturation, breakthrough times, etc.) are obtained as in a standard Buckley-Leverett process. The exception is the Johnson-Bossler-Neuman method, which requires additional modification.

6.3 MODIFICATION OF THE JBN METHOD

6.3.1 Power-Law Fluids

We first consider a drainage process where a non-wetting, Newtonian fluid displaces a wetting, power-law fluid. This rather unconventional process is experimentally desirable so that a wider range of saturations becomes available for relative permeability determination [88]. The pressure drop across the core in the period following breakthrough is

$$\Delta p = \int_0^L \frac{(u_p)^n m}{k k_{rp}} dx \tag{195}$$

where capillary effects have been neglected. For convenience, we further define dimensionless distance $x_D = x/L$, time $t_D = \int_0^t u_t dt/\phi L$ and pressure drop $\Delta p_D = \Delta p k/[L(u_t)^n m]$, to obtain

$$\Delta p_D = \int_0^1 \frac{(f_p)^n}{k_{rp}} dx_D \tag{196}$$

From the Buckley-Leverett solution, x_D and f_p' are interchangeable

$$x_D = t_D f_p' \tag{197}$$

so that (196) becomes

$$\Delta p_D = t_D \int_0^{f_{pL}'} \frac{(f_p)^n}{k_{rp}} df_p' \tag{198}$$

where subscript L refers to the producing side. Following the JBN approach, we next take $z = 1/t_D = f_{pL}'$ and rewrite (198) as

$$z\Delta p_D = \int_0^z \frac{(f_p)^n}{k_{rp}} df_p' \tag{199}$$

Differentiating and making use of (188) finally leads to

$$\left[\frac{d(z\Delta p_D)}{dz}\right]\left[\frac{d(\Delta p_D/t_D)}{d(1/t_D)}\right] = \frac{(f_p)^n}{k_{rp}} \tag{200}$$

which in dimensional notation reads

$$\frac{k}{mL(u_t)^n}\frac{d(\Delta p/Q_t)}{d(1/Q_t)} = \left(\frac{1}{k_{rp}}\right)_L (f_p)^n \tag{201}$$

With the exception of $k_{rp}(S_{pL})$, all other quantities in (201) are measurable. It should be noted that were m allowed to vary with S_p, the ratio of k_{rp}/m would appear instead of k_{rp} above. Of course, other JBN expressions, such as end saturation S_{pL} and producing fraction remain unchanged as given by

$$Q_p = S_{pi} - S_{pL} + Q_t f_{pL} \tag{202}$$

It is apparent from (201) that for the case of a power-law fluid, the traditional method must be slightly modified. The correction applies after the determination of f_{pL} from the slope m_1 of the $\log Q_t$ vs. Q_p plot (or the Q_t vs. Q_p plot), and the measurement of the end saturation S_{pL} (eq. (202)). To find the relative permeability k_{rp}, the slope m_2 of the $\Delta p/(Q_t/\phi AL)$ vs. $\phi AL/Q_t$ plot is taken and eq. (201) is used

$$k_{rp} = \frac{Lm(u_t f_{pL})^n}{k m_2} \tag{203}$$

The exponent n on the RHS above should be noted. On the other hand, no modification is needed for k_{ro}, which can be found with the standard approach

$$k_{ro} = \left(\frac{Lu_t}{k}\right) \mu_o \frac{(1 - f_{pL})}{m_2} \tag{204}$$

Identical expressions apply for the imbibition process. The above show that no interpretation error is incurred if the standard JBN method is used for the relative permeability of the Newtonian fluid. By contrast, errors are anticipated for the relative permeability of the power-law fluid, as demonstrated below.

6.3.2 Application

To illustrate the need for a JBN modification, numerical data generated from the Buckley-Leverett solution were interpreted by using both unmodified and modified JBN expressions. The data were obtained by calculating the producing-end saturation from the solution of (188) and

$$\left(\frac{1}{\Lambda}\right) \frac{d\Lambda}{dS_p}(t_D) = \frac{f_p + n(1 - f_p)}{f_p(1 - f_p)} \tag{205}$$

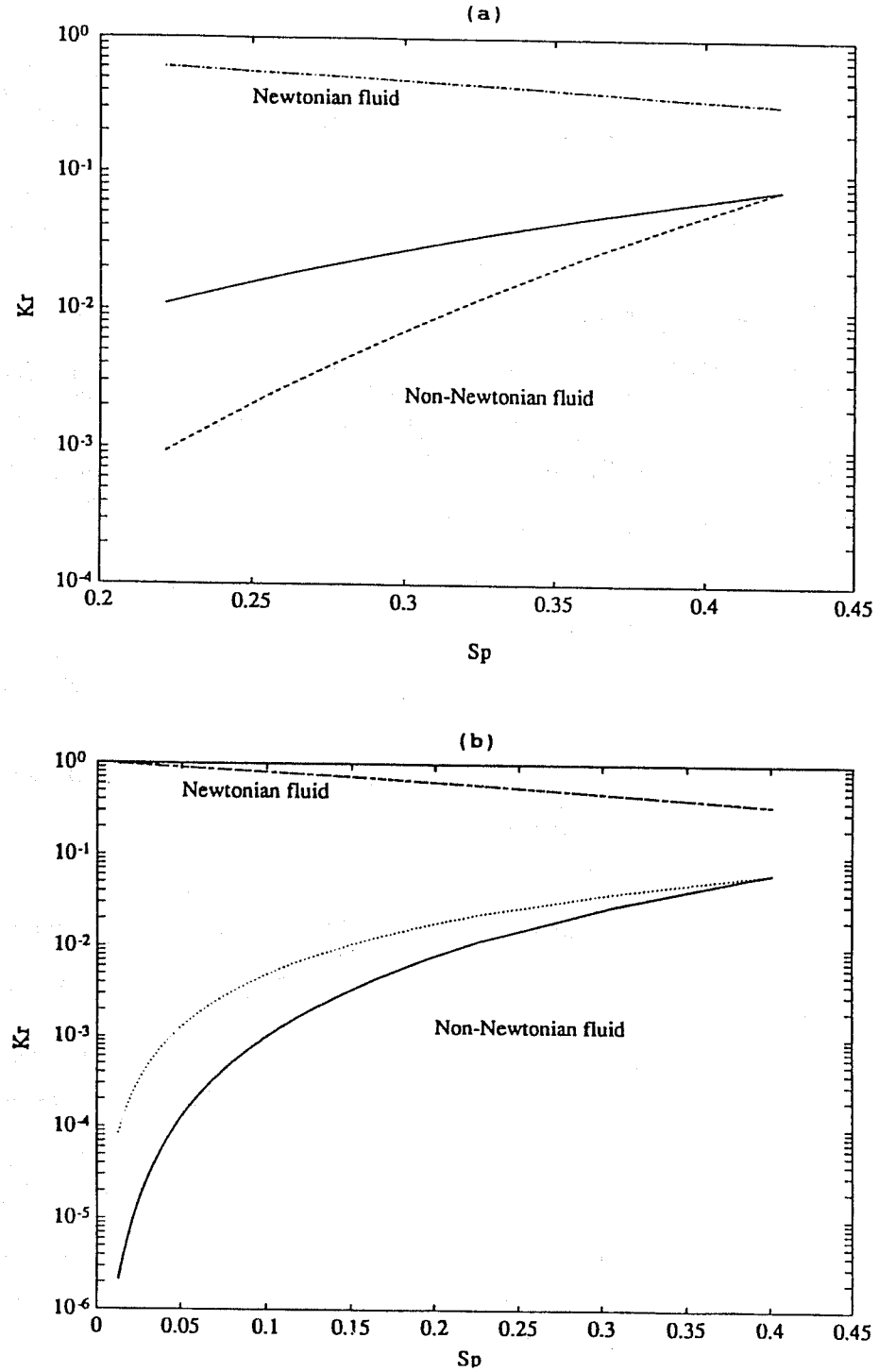

Figure 54: Relative permeabilities calculated by unmodified and modified (solid curve) JBN methods for drainage and α=2: (a) shear thinning (n=0.5), (b) shear thickening (n=1.5).

The latter is obtained by evaluating df_p/dS_p and setting $df_p/dS_p = 1/t_D$ at $x = L$. Pressure data for the drainage case were in turn simulated using the formula

$$\Delta p_D = t_D \int_0^{1/t_D} \frac{(f_p)^n}{k_{rp}} df_p' \tag{206}$$

where the integrand is an implicit function of f_p'. Similar equations apply for the imbibition case. Analysis of the numerically generated data was based on interpolation using cubic splines. Typical results are shown in Figure 54 for a drainage process. In both shear thinning (Figure 54a) and shear thickening (Figure 54b) cases, the relative permeability to the Newtonian fluid (here taken from (189)) is reproduced accurately with the unmodified JBN method. In fact, the two curves coincide to the plotter accuracy.

By contrast, significant errors are predicted for the relative permeability of the power-law fluid. While the modified version (solid curve) reproduces reliably the input relative permeability, the unmodified original version (broken line) shows substantial error, even for the rather mild parameter values used in the illustrations. In general, the unmodified version shows an erroneously higher (lower) sensitivity to saturation for the shear thinning (thickening) case. Otherwise stated, the drainage data under- (over) estimates the relative permeability to the shear thinning (thickening) phase if evaluated with the original JBN method. Similar differences exist for imbibition, although the error involved is not detectable in the narrow saturation range usually involved with such process (Fig. 55).

6.3.3 Generalization

A simple physical interpretation of the proposed JBN modification is possible, if (201) is expressed in the form

$$m_2 \frac{k}{L u_t \mu_{app,L}} = \left(\frac{f_p}{k_{rp}}\right)_L \tag{207}$$

where

$$\mu_{app,L} = m(u_t f_{pL})^{n-1} \tag{208}$$

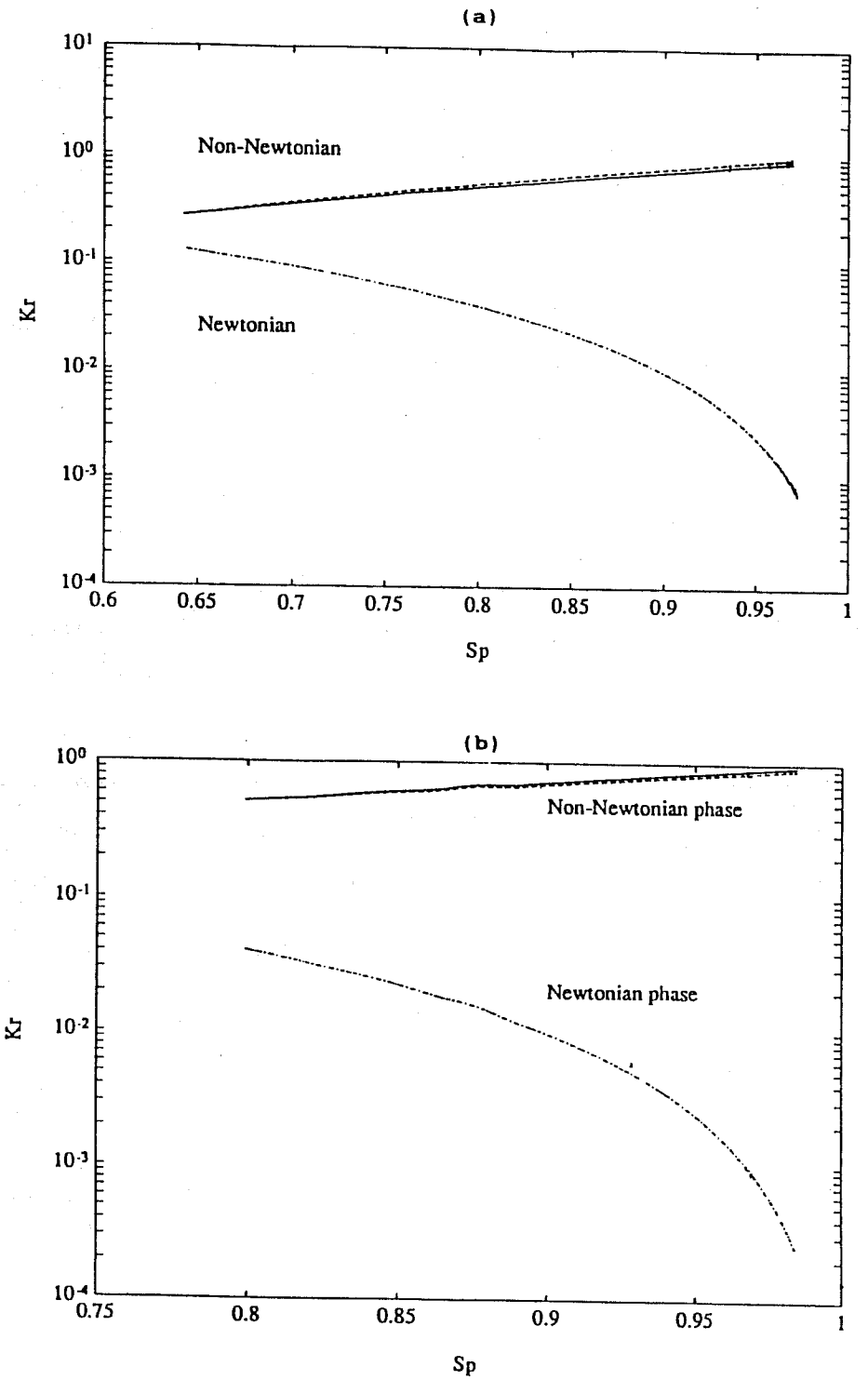

Figure 55: Relative permeabilities calculated by unmodified and modified (solid curve) JBN methods for imbibition: (a) shear thinning (n=0.5 and α=10), (b) shear thickening (n=1.5 and α=0.2).

is the apparent viscosity of the power-law fluid evaluated at the conditions of the outlet end. The implication is that the original JBN method can be applicable, provided that the apparent fluid viscosity at the production end is used. The latter of course is variable with the wetting fluid velocity, thus it changes as f_{pL} changes. In the JBN method terminology, the "reference Δp" does not remain constant, but varies during the course of the process. It is, therefore, conjectured that a similar correction may apply for any other fluid rheology. This is indeed true as can be readily shown. For example, if the generalized counterpart of (192) is postulated to be

$$u_p = -\left[\frac{k k_{rp}(S_p; u_p)}{\mu(u_p)}\right] \frac{\partial P_p}{\partial x} \tag{209}$$

where k_{rp} may depend on rate, we shall have the implicit relations

$$u_p = f_p u_t \tag{210}$$

$$f_p = \frac{1}{1 + \mu_p(u_p)/\mu_o \Lambda(S_p; u_p)} \tag{211}$$

The saturation profile is then implicitly given by (191) as before. Rearrangement of the integrals following the previous approach leads after considerable calculations to an expression identical to (207) where the apparent viscosity is evaluated at the conditions of the producing end, $\mu_{app,L} = \mu(f_p u_t)$. Independent knowledge of the apparent viscosity in the porous medium as a function of rate allows the evaluation of the relative permeability. Equivalently, this implies that all saturation effects are assigned to the relative permeability and that the fluid viscosity is only affected by the flow rate. Unfortunately, this is only possible for power-law fluids where saturation and rate effects can be decoupled. For fluids other than power-law, the relative permeability would depend, in general, on the flow rate of the fluid as well, the latter being itself a function of the relative permeabilities of the two fluids. Considerable care must then be exercised in order to extract the correct flow rate dependence and to decouple it from the saturation dependence.

6.4 CONCLUDING REMARKS

In this section salient features of immiscible displacement in porous media when one of the two fluids is of the power-law type were examined. It was shown that the Buckley-Leverett theory for 1-D displacement is applicable, provided that the fractional flow is appropriately evaluated. Effects of

rate and power-law exponent were studied and found to affect significantly the displacement profiles. In addition, a modification of the JBN method was proposed for the interpretation of unsteady-state experiments to measure relative permeabilities. It was found that direct application of the original method leads to substantial errors and under- (over) estimates the saturation sensitivity of the relative permeability of the power-law fluid in the shear thinning (thickening) case. A generalization to fluids of other rheology was also proposed.

7 CAUSTIC FLOODING AT ELEVATED TEMPERATURES

R. Aflaki and L. L. Handy

7.1 INTRODUCTION

The objective of this work is to establish pH and chemical composition profiles as a function of length in caustic flooding at flow conditions. This would enable us to evaluate the state of final equilibrium and to better forecast the performance of caustic flooding at reservoir conditions. It has been recently shown that clays cause mineral transformation during caustic flooding. However, such reactions and their effects have been studied only in batch experiments. In this work,we extend the study of this clay-caustic interaction to dynamic systems. The nature of the reaction is also examined. Finally, in previous flow experiments only the effluent has been monitored for variables such as pH, Si, Al and Na. This work presents an improved experimental technique that allows for chemical composition profiles to be obtained at several points in the core.

7.2 EXPERIMENTAL

The porous medium is made up of four Berea sandstone cores (1" diameter and 8" long) arranged in series and placed in a constant temperature oven. Sampling is possible through by-pass lines, while effluent pH is measured by an in-line probe.

Experiments were done in three series. In each experiment we started with the highest flow rate. When no change was observed in the effluent pH, a steady state was assumed. The flow was subsequently diverted for sampling to the end of 3rd, 2nd and 1st cores consecutively. The samples were analyzed for Si and Al concentrations using atomic adsorption. After sampling, either the temperature was raised or the flow rate was reduced, depending on the particular experiment, and the same procedure was repeated.

Three sets of experiments were done corresponding to the following:

1st Set: $T = 180°C$; injected solution pH = 12.87, no NaCl; initial rate = 0.9 ft/day varied down to 0.4 ft/day.

2nd Set: $T = 180°C$; injected pH solution = 12.87 with 2% NaCl; initial rate = 4.8 ft/day varied down to 0.2 ft/day.

3rd Set: initial T = 70°C varied up to 180°C; injected pH solution = 12.87 with 2% NaCl; initial rate = 4.8 ft/day varied down to 0.4 ft/day.

All cores were saturated with 2% NaCl and flooded with 2% brine prior to caustic injection.

7.3 RESULTS AND DISCUSSION

The following results were obtained for the first set:

Fig. 56 shows a plot of pH vs. pore volume injected. Surprisingly, the caustic breakthrough was delayed much longer than anticipated. However, after 16 PV the effluent pH increased to 12.1. Sampling was done after 14 PV had been injected corresponding to conditions before steady- state was achieved. Samples were also taken after steady-state was established. Fig. 57 shows effluent Si concentration vs. PV injected; Si eluted at about the same time that caustic broke through. Fig. 58 shows pH vs. dimensionless length. Comparing the unsteady and steady-states the advance of the the high pH front can be visualized. This front moved slowly and it broke through after injection of 16 PV. At 0.4 ft/day the residence time was increased. Thereafter, lower pH or higher consumption was noticed. Fig. 59 shows Si concentration as a function of dimensionless length. There are no data between the injection point and the end of the first core; however, it is evident that the concentration in solution of Si increased to values at least as high as the concentration at the end of the first core. After the increase in Si concentration, a steady decline down to the effluent end was observed. This decline coincides with the change of slope in Fig. 58. Also as the high pH front advanced, the high Si concentration advanced accordingly.

The duration of this experiment was 30 days, and a total of 25 PV was injected.

The second set of experiments was next performed:

In this set of experiments the procedure is slightly different from the previous. A more extensive pre-flush was done to ensure complete divalent cation exchange. During pre-flush, the effluent end pH was monitored and when the effluent end pH stabilized around neutral pH it was assumed that the divalent ion-exchange was completed. The caustic solution contained 2% NaCl and the experiment started at a higher rate. It is believed that ion exchange is a fast reversible reaction that causes a delay in caustic breakthrough. This delay is usually within a maximum of 2 PV. If the residence time is high enough (such as in a batch experiment), there is a competition between dissolution and ion exchange reaction. In order to minimize the effect of dissolution, the starting

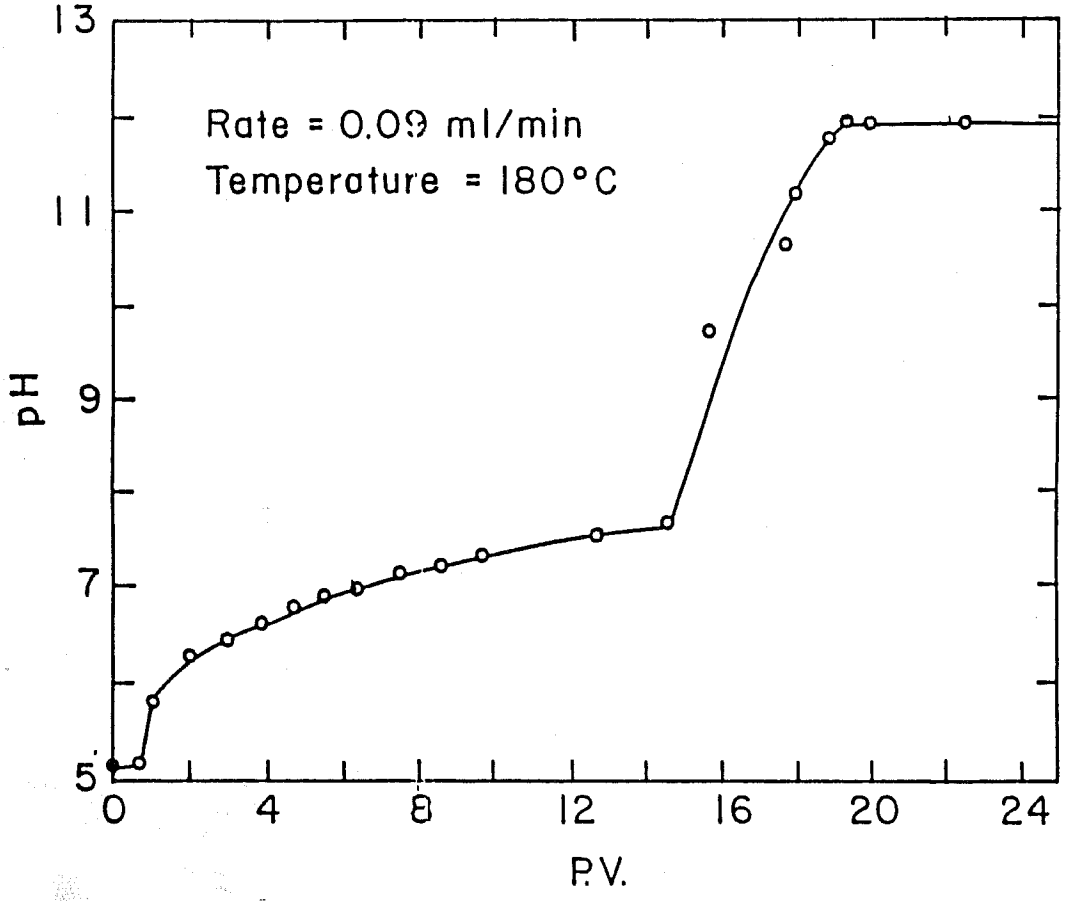

Figure 56: Effluent pH vs. PV injected for set 1.

rate was increased to 4.8 ft/day in this set. Adding NaCl to the caustic solution increases the amount of ion exchange. Therefore more sites will be satisfied and once again a complete ion exchange is ensured.

Fig. 60 shows the effluent end pH vs. pore volume injected at the starting rate of 4.8 ft/day. The pH broke through after 1.5 PV which was considerably faster than the previous experiment (Fig. 56). The pH was stabilized at 11.7, the difference between the stabilized pH and the injected pH being attributed to the dissolution reaction. Once the pH stabilized, samples were taken between cores. Following this, the rate was reduced to 0.9 ft/day. The rate was further reduced to 0.4 and 0.2 ft/day successively in the above manner. Fig. 61 shows a plot of pH vs. dimensionless length. As the rate was reduced, lower pH and higher hydroxyl ion consumption was noticed, indicating that final equilibrium had not been achieved. Also a change in the slope is noticed similar to the results of the previous experiment (Fig. 58). After the rate was reduced to 0.9 ft/day, the high pH front lagged behind. This lower rate provided a higher residence time for the deposition reaction to take place. This is evident from Fig. 62 which shows silica vs dimensionless length. A change of slope is noticed, coinciding with the change of slope in Fig. 61. High pH was observed at the place of high silica concentration. These fronts move slowly due to the slow reaction. In

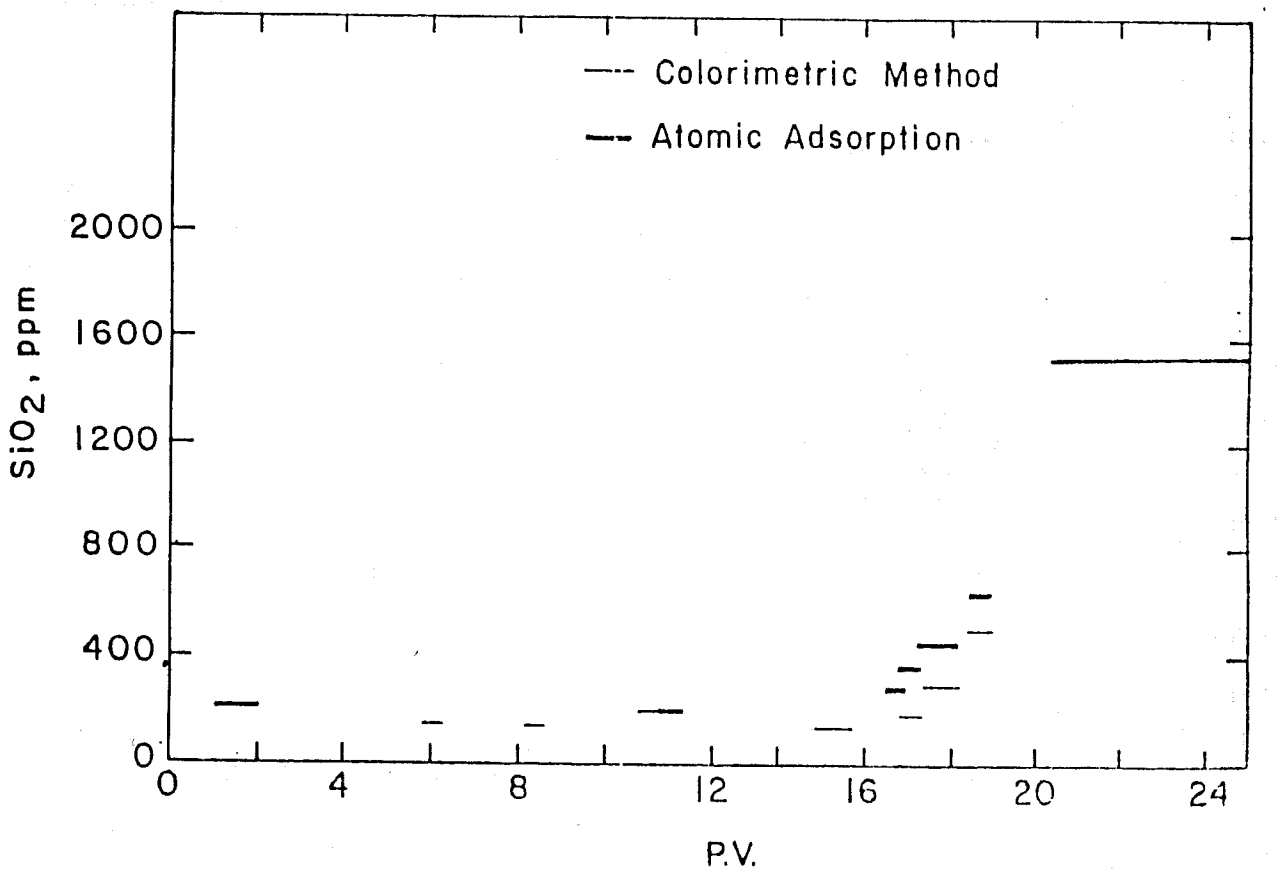

Figure 57: Effluent Si concentration vs. PV injected for set 1.

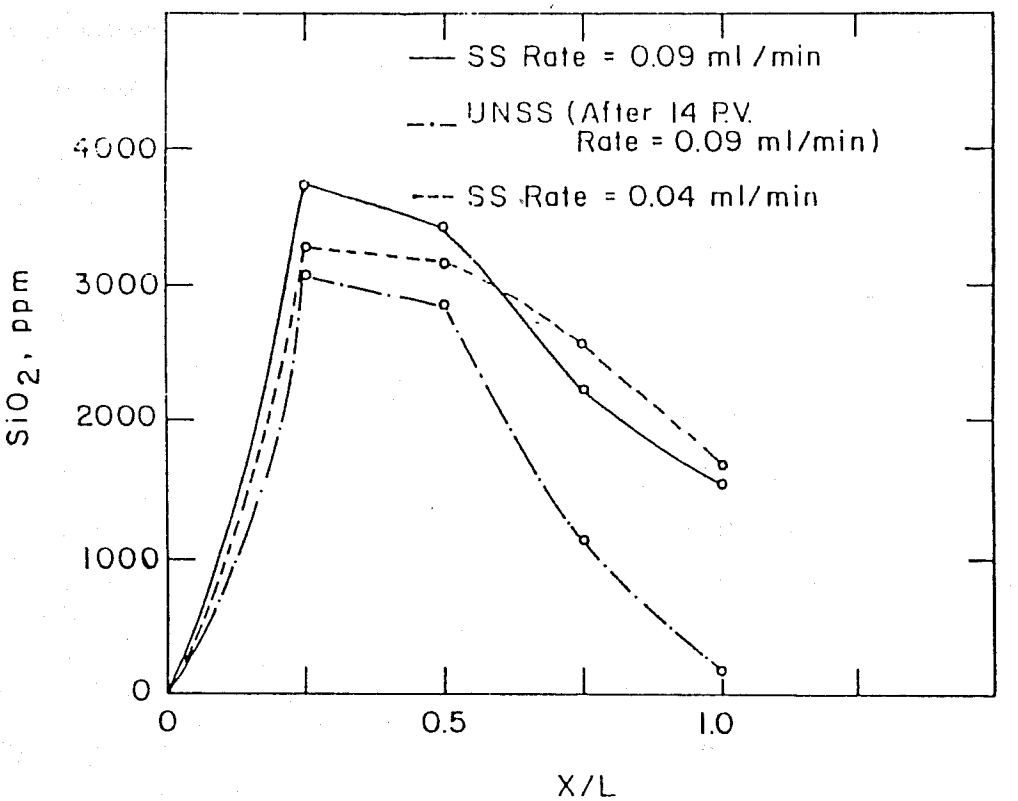

Figure 58: Profile of pH vs. length for set 1.

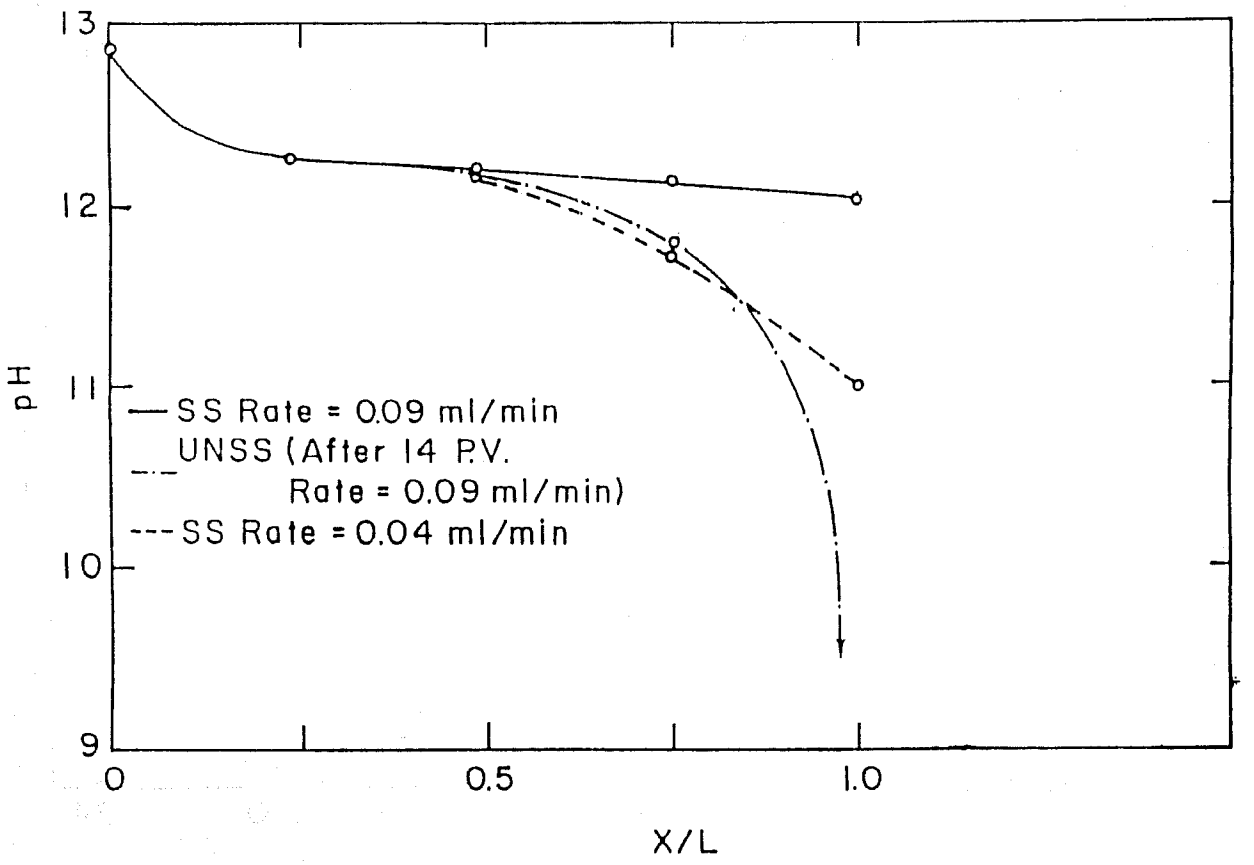

Figure 59: Profile of Si concentration vs. length for set 1.

this set of experiments sufficient time was not allowed for these fronts to breakthrough, therefore a steady-state was not achieved. The effluent end and in-between core samples were analyzed for aluminum using atomic-adsorption. Fig. 63 shows Al_2O_3 concentration vs. dimensionless length. The samples at the end of the first, second and fourth cores did not show any detectable aluminum. However, at the end of the third core, some aluminum was measured.

The duration of this experiment was 30 days and a total of 22 PV was injected.

The final set of experiments involved a study of the effect of temperature. This experiment started at an initial rate of 4.8 ft/day and temperature of 70°C. After steady-state was achieved, the rate was reduced to 0.9 ft/day. Following steady-states at lower rates, the temperature was increased, and the same procedure was repeated for higher temperatures. The temperature was increased up to 180°C in this manner.

At lower temperatures(up to 120°C), no significant pH drop was observed. At this point, it should be mentioned that since the effluent pH is measured at room temperature it is possible that the silicate ionization reactions are reversed upon cooling, to release OH ion. The measured effluent pH is used only as a guideline rather than a variable for exact consumption calculations. At low temparatures, due to the insignificant consumption, and also most of it being in the form of

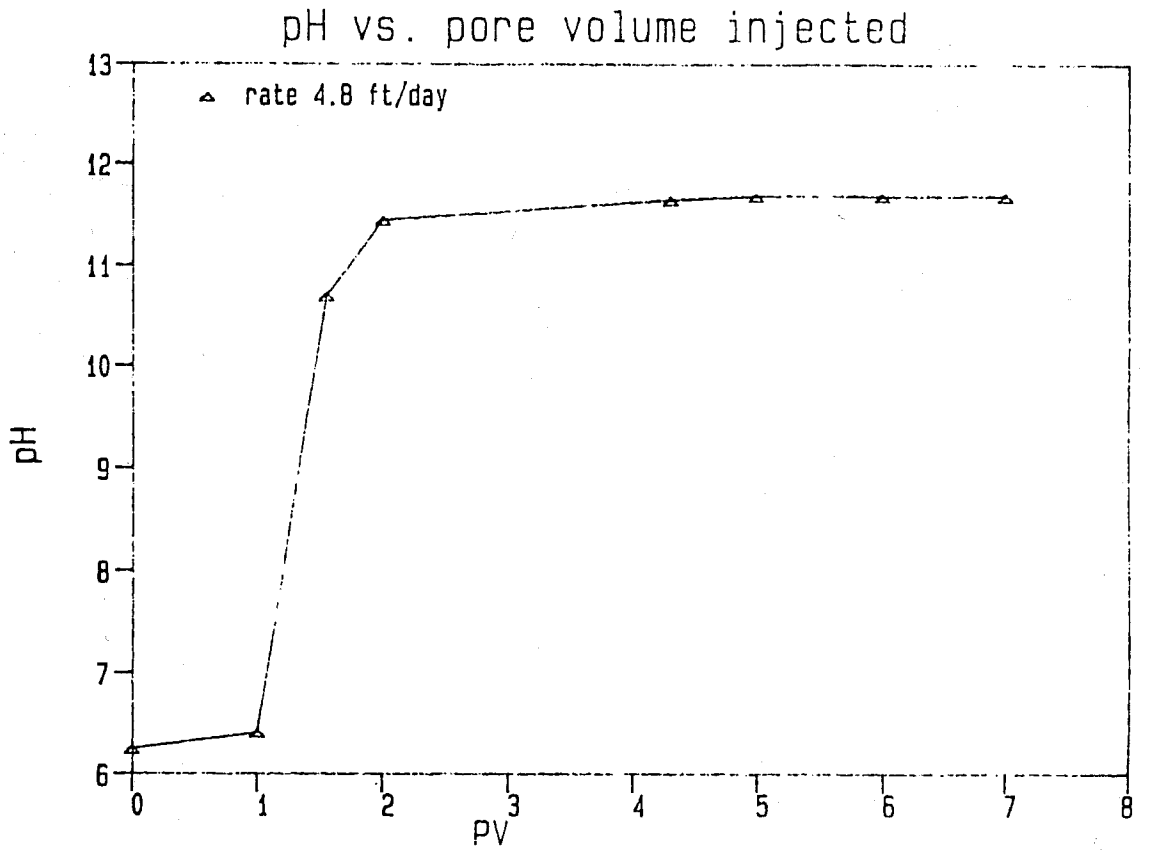

Figure 60: Effluent pH vs. PV injected for set 2.

reversible reactions, it is possible that the effluent pH is over-estimated. The silica concentration is significantly lower than that observed at higher temperatures. As the rate was lowered to 0.9 ft/day, higher silica concentration was observed at the effluent, although no change in pH was observed. This indicates that consumption was taking place but it could not be detected by the measurements of the pH probe.

At 100°C slightly higher levels of silica concentration compared to 70°C were observed. However, final equilibrium at this temperature was not achieved either. This can be concluded from the observed higher silica concentration upon the reduction of the rate from 1 ft/day to 0.9 ft/day. At lower temperatures, the reaction is slow and the state of final equilibrium is reached at much higher residence times which could not be provided in this setup.

At 120°C a reduction in pH was observed. Fig. 64 shows pH vs. dimensionless length at different temperatures. Fig. 65 shows silica concentration vs. dimensionless length at 150°C. Compared to 100°C the silica concentration at the effluent is more than double and even higher concentrations were observed at the end of second and third cores. Also, there is an indication of silica deposition somewhere after the end of the third core.

Once the temperature was increased to 150°C a significant reduction in pH was observed, the

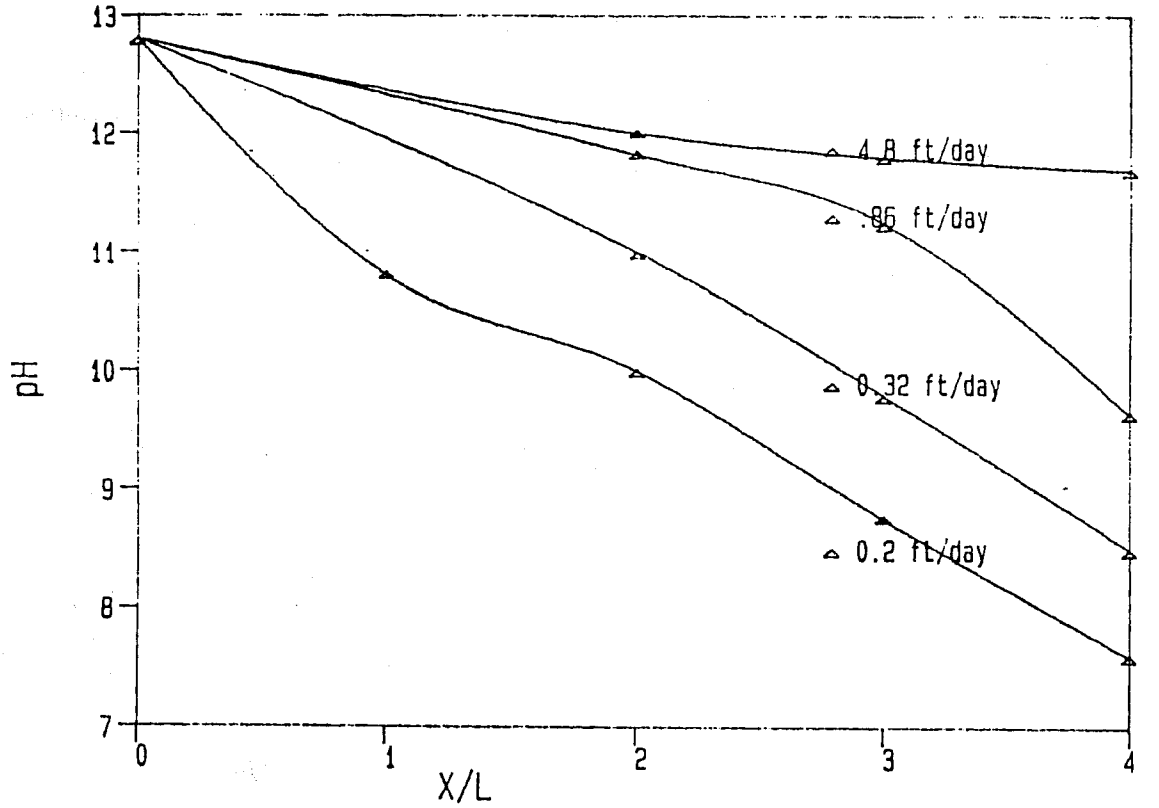

Figure 61: Profile of pH vs. length for set 2.

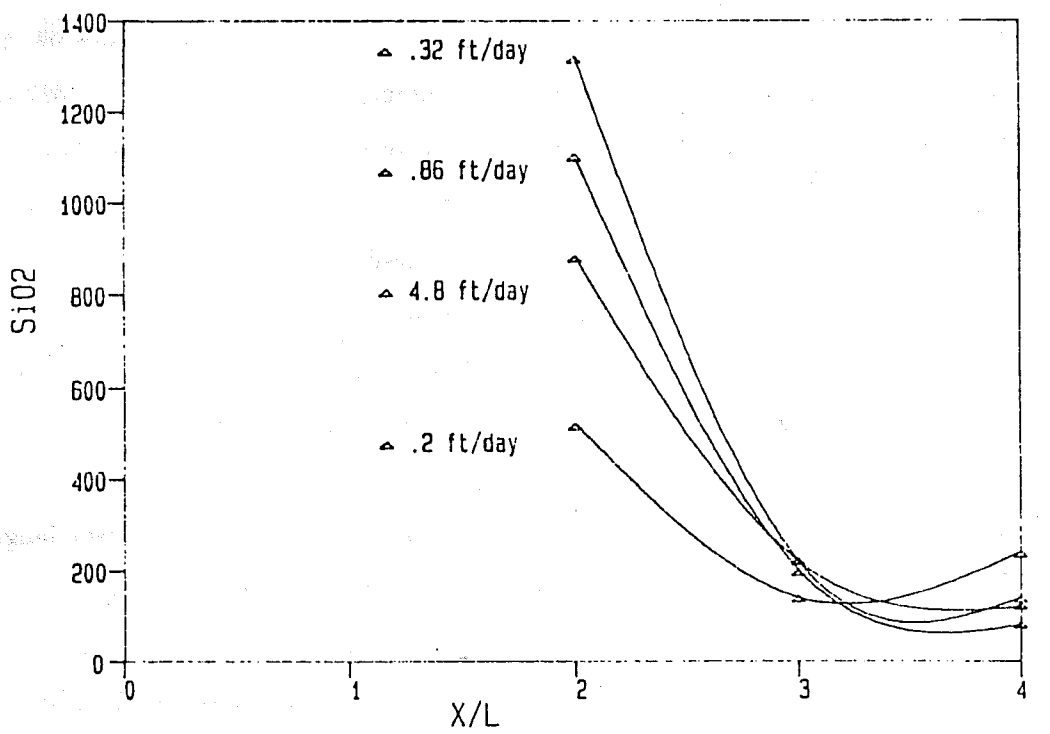

Figure 62: Profile of Si concentration vs. length for set 2.

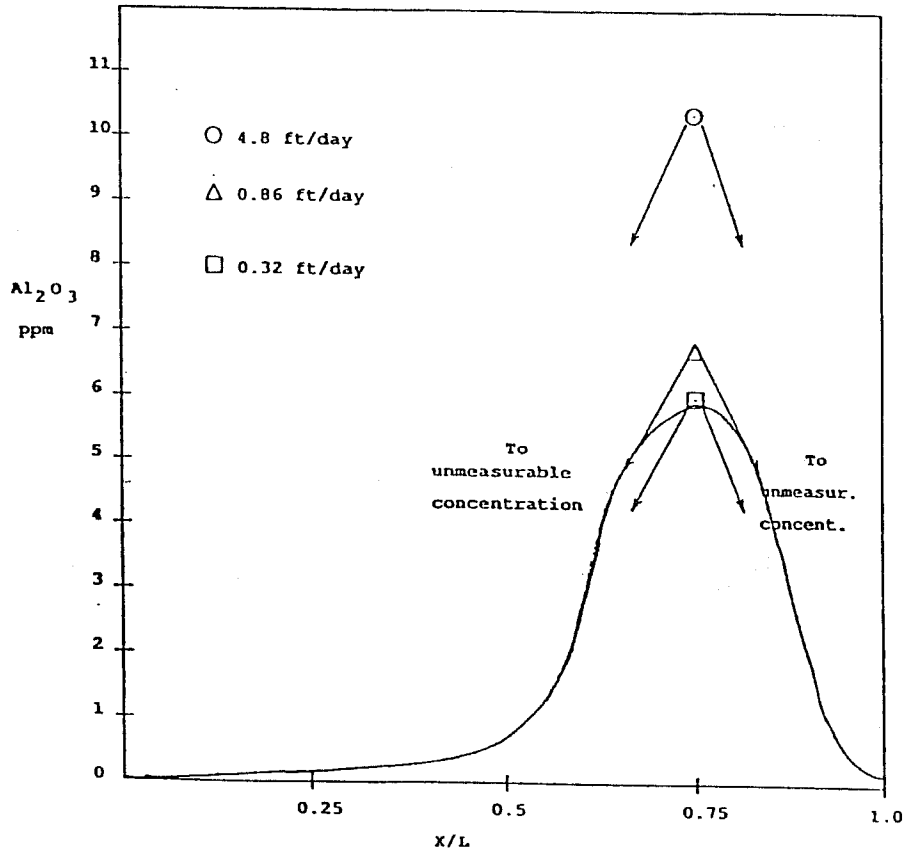

Figure 63: Profile of Al concentration vs. length for set 2.

pH decreasing to 7.42. However, subsequently it slowly rose to 12.1. Fig. 64 shows the pH vs. dimensionless length for 150°C. The samples were taken at different pore volume injected. Curve 1 is at 3.6 PV, curve 2 is at 7.4 PV, and curve 3 is after total of 11 PV injected, at which time steady-state was established. This delayed high pH front breakthrough is similar to set 1 and set 2. In set 1, the high pH front breakthrough occurred after 16 PV, and in set 2 after a total injection of 22 PV the high pH breakthrough was never detected. Fig. 65 shows silica vs. dimensionless length at 150°C and the rate of .9 ft/day. The advance of high pH front coincides with the advance of high silica concentration not only at the effluent, but also throughout the system at any time. Once the steady-state at .9 ft/day was established the rate was reduced to .4 ft/day. Upon rate reduction, no further change in effluent pH was noticed. However, the samples taken in-between the cores show slightly higher pH at the end of the third core. Fig. 65 also shows silica vs. dimensionless length at 150°C at the rate of .4 ft/day. There is no apparent change in the effluent pH and silica concentration, compared to .9 ft/day. However, slightly higher silica concentrations at the end of the third core were noticed. This coincides with the slightly higher pH at the end of the third core. These slight changes show that further increase in pH or silica concentration might be noticeable, were enough residence time allowed.

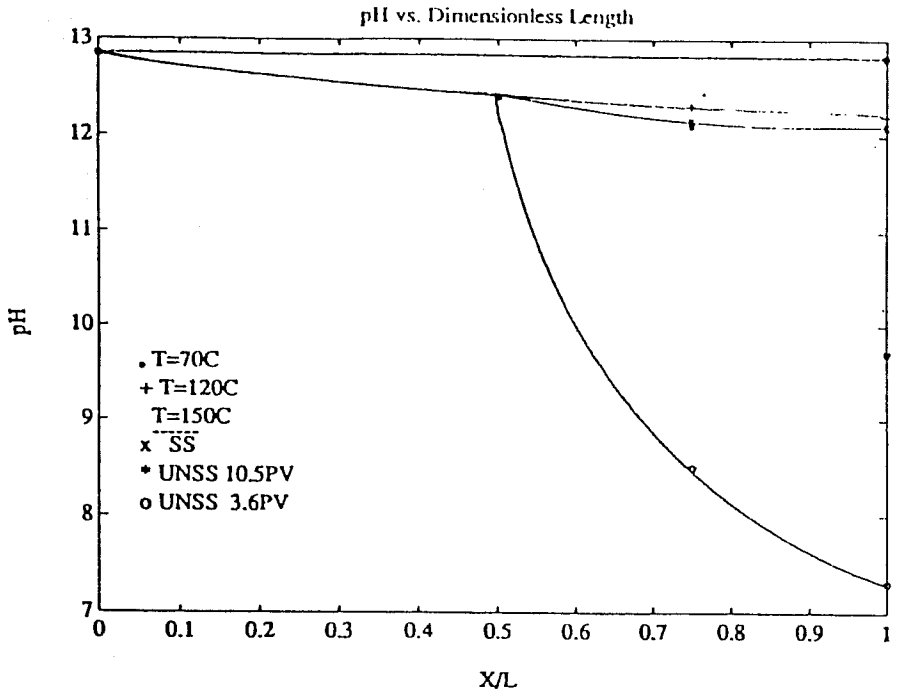

Figure 64: Profile of pH vs. length for set 3 at various temperatures.

Keeping the rate constant at .4 ft/day the temperature was finally increased to 180°C. The pH dropped to 11, and stayed practically constant. Assuming that steady-state was achieved, samples in between cores were taken. pH profile and silica concentration profile are similar to those of Set 1 at the same rate.

Fig. 66 shows the effluent pH, silica and alumina concentration vs. pore volume injected throughout the experiment. Up to 120°C, silica concentration increases as the rate is decreased or the temperature is increased as predicted by the dissolution reaction and its constant. At 150°C upon the increase of temperature the pH dropped following drop in silica concentration, which suggests a different kind of reaction, one in which both silica and hydroxyl ion are consumed. Once the pH increased to higher values, the silica concentration also increased. However, the silica concentration leveled off at lower concentration than 120°C, indicating lower solubility at 150°C. Also in Fig. 66 Al concentration vs. pore volume injected is shown. At the beginning, alumina, pH and silica eluted at the same time. At 70°C and after alumina concentration reached the maximum, it dropped continuously until it leveled off at a constant value. The same trend in alumina concentration was previously reported and attributed to the formation of new alumina silicates. Also at 70°C the pH dropped for a short period of time, but subsequently increased again.

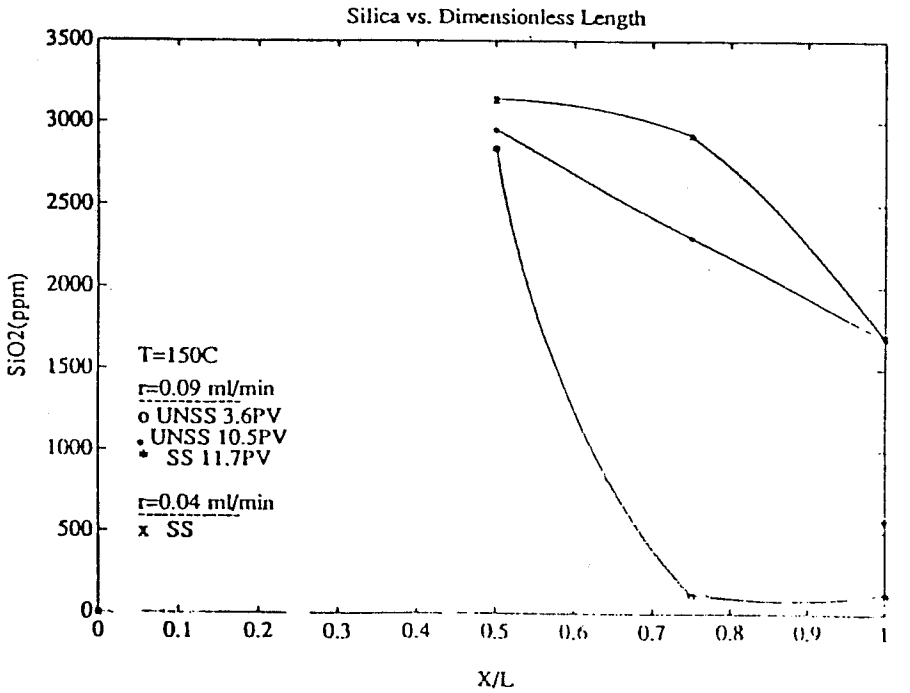

Figure 65: Profile of Si concentration vs. length for set 3 at 150°C and various rates.

A simultaneous reduction in alumina concentration followed. At 150°C the trend is different than that observed at 70°C. Significantly at 150°C no alumina was present in solution to react with the soluble silica and to form alumino-silicates. Alumina disappeared from the solution completely, sometime after the temperature was increased to 120°C.

From the results of the above experiments it can be concluded that a reaction other than dissolution reaction is responsible for the uptake of hydroxyl ion. This reaction causes a delay in caustic breakthrough, and consumes hydroxyl ion as well as silica, since the sharp decline in hydroxyl ion coincides with a sharp decline in silica concentration. Interaction of caustic with alumina oxide, clays and other oxide surfaces are suggested as being responsible for the uptake of the silica and hydroxyl ion. The effect of kaolinite on silica dissolution was studied recently by some researchers and silica deposition has been noticed. They have described the silica deposition as a mineral transformation reaction in which silica reacts with alumina along with hydroxyl ion to form alumino-silicates of the zeolite family. Different reactions have been proposed to describe the above reaction.

Our results can be explained based on a chemisorption reaction. In this reaction the silicic acid is adsorbed onto the surface which is negatively charged. In this step, hydrogen ion is released

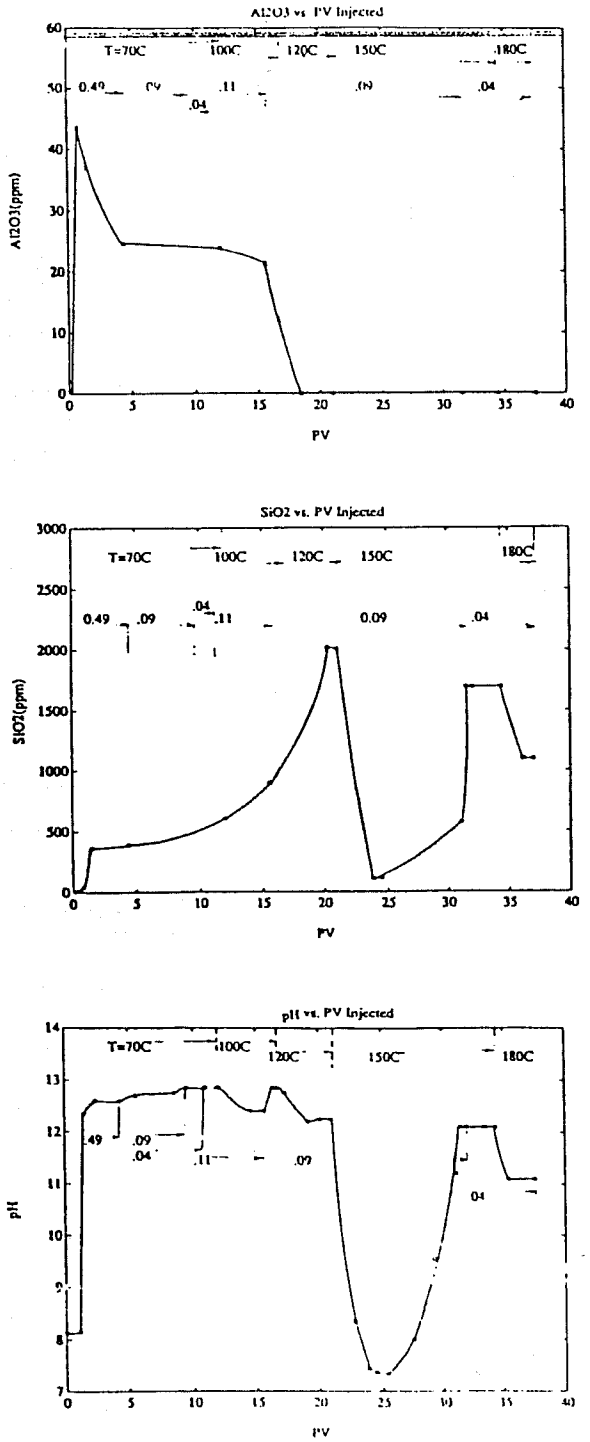

Figure 66: Composite effluent concentrations for set 3.

from the surface. In the next step the sodium/hydrogen ion exchange takes place causing further hydroxyl ion consumption. In this scheme, no alumina solution is required.

The chemisorption reaction is temperature-dependent, at lower temperatures no significant drop in either pH or silica being observed. This reaction is also rate- dependent. This can be concluded from the results of the second experiments and from the comparison of the results of the first and the second experiment. At lower rates the drop in silica concentration was more significant and the caustic breakthrough occured faster at the higher rate.

7.4 CONCLUSIONS

The following conclusions have been reached in this work:

1. Effluent silica concentration can not be reliably used as a sole measure of the amount of consumption.

2. Clays contribute to consumption significantly through chemisorption reactions.

3. Chemisorption manifests itself in a manner similar to ion exchange reaction causing a delay in caustic breakthrough.

4. Chemisorption reaction is temperature-dependent. At low temperatures, the amount of consumption is negligible and breakthrough is not delayed.

5. Upon completion of chemisorption, new equilibrium will be established. These results show that the amount of consumption after reaching equlibrium is due to dissolution and is not very significant.

8 CAPILLARY EFFECTS IN STEADY-STATE FLOW IN HETEROGENEOUS CORES

J. Chang and Y.C. Yortsos

8.1 INTRODUCTION

Effects of heterogeneity in immiscible flow in porous media are usually associated with mobility contrast and viscous fingering (for example, see recent discussions by Giordano [48] and Araktingi and Orr[3]). This is typically the case in predominantly parallel flows, occurring in stratified layered media, and for large enough flow rates and spatial scales so that capillary effects are negligible. Such nominally miscible displacements are presently simulated in considerable detail (e.g. Crump [27]).

At the same time, permeability variations affect capillary pressure characteristics (e.g. through the Leverett J-function, Bear [8]). Contrary to the miscible case, capillary heterogeneity is most pronounced when the flow is in series, and the flow rates low enough for the displacement to be practically one-dimensional. Typical examples in opposite ends of this occurrence are the familiar end-effects in immiscible flow (corresponding to an infinitely large permeability contrast), and the no-flow, static saturation distribution in a layered system (Collins [23], Marle [67]).

For a number of laboratory studies, the condition of one-dimensional, macroscopic flows is essential. Steady- and unsteady-state methods for measuring relative permeabilities are notable, routine examples. For most fluid pairs, enforcement of this condition dictates flow rates low enough for capillarity to suppress viscous fingering in the transverse direction (Peters and Flock [83] Yortsos and Hickernell [120]). Capillarity is then comparable to viscous forces over length scales of the order of core width or higher. At such conditions, any capillary heterogeneity in the direction of the displacement will be manifested over macroscopic (core) scales. Indicative of this is the reported relevance of end effects in relative permeability measurements (Odeh and Dotson [77]).

The increasing awareness of the heterogeneous nature of geological porous media (e.g. Lake and Carroll [64]), has led to renewed efforts towards a better understanding of the associated transport processes. This paper addresses one such issue, namely the effect of capillary heterogeneity in immiscible displacement. A limiting case of such effect involves equilibrium saturation profiles in a heterogeneous core at static conditions, thoroughly studied before on the basis of capillary

continuity (Bear [8] , Collins [23] , Marle [67]). An increase (decrease) in wetting phase saturation accompanies a decrease (increase) in permeability, with the saturation roughly displaying a mirror image of the permeability. With the exception of outflow end-effects, however, little is known about corresponding profiles for the general case of flow systems.

In a recent study (Chang and Yortsos [18], hereafter denoted as Part I), we presented a numerical investigation of the effects of capillary heterogeneity, induced by permeability variations, in the case of transient, immiscible displacement. The saturation response varied considerably as a function of the flowing fraction, the mobility ratio, the wettability and the spatial correlation of the heterogeneity. Furthermore, the simple argument of capillary continuity was found insufficient in interpreting the trends observed.

As a companion to Part I, this section presents a study of the steady-state displacement in a heterogeneous core with emphasis on capillary effects. To illustrate qualitative trends we first examine two model cases that allow for exact solutions, a linear (ramp) and a piecewise linear, periodic (sawtooth) variation in the capillary variable $\tau(\sim \sqrt{k})$. General qualitative results are subsequently obtained for arbitrary distributions. The study is completed with numerical solutions that illustrate effects of randomness and spatial correlation. The results provide a simple explanation of several of the effects observed in Part I, and elucidate the role of the various parameters, such as fractional flow, mobility ratio, spatial correlation and permeability contrast. Fractional flow and capillary pressure "composition paths" are also supplied. The analysis contains as special cases the opposite limits of static (no flow) distribution and outlet end-effects.

8.2 FORMULATION

We consider the steady, one-dimensional flow, at total rate q, of two immiscible phases (subscripts w and o to denote "water" and "oil", respectively). A heterogeneous medium is assumed, such that the capillary pressure varies spatially, e.g. according to the Leverett relationship

$$p_c = \frac{\gamma\sqrt{\phi}}{\sqrt{k}} J(S_w) \tag{212}$$

Although distribution in other parameters, such as wettability ($\gamma \cos\theta$) can be readily considered, the analysis is restricted to variable permeability only. Letting k^* denote a characteristic value for

the latter, the dimensionless parameter

$$\tau = \sqrt{k/k^*} \tag{213}$$

measures, in the present context, the heterogeneity of the medium. As in Part I, the ensuing formulation assumes that dimensionless quantities (relative permeabilities and the capillary J-function) are only functions of the saturation. This approximation is not strictly accurate and is discussed later in some detail.

Using standard terminology and notation, the steady-state profile is described by the following

$$\frac{k k_{ro}(S_w) f_w(S_w)}{\mu_o q} \frac{dp_c}{dx} = F_i - f_w(S_w) \tag{214}$$

where F_i is the flow fraction of phase w at injection. We normalize further by denoting

$$\zeta = x/L \tag{215}$$

$$u = \frac{S_w - S_{wc}}{1 - S_{wc} - S_{or}} \tag{216}$$

$$\varepsilon = \frac{\gamma\sqrt{k^*\phi}}{L\mu_o q} \tag{217}$$

$$F(u) = f_w(S_w) \tag{218}$$

$$G(u) = k_{ro} J(S_w) f_w(S_w) \tag{219}$$

$$H(u) = -k_{ro} f_w(S_w) J'(u) \tag{220}$$

$$\tau'(\zeta) = d\tau(\zeta)/d\zeta \tag{221}$$

to obtain

$$F(u) - \varepsilon G(u)\tau'(\zeta) - F_i = \varepsilon\tau(\zeta) H(u) \frac{du}{d\zeta} \tag{222}$$

In the above, L is a macroscopic length scaling heterogeneity. As in Part I, the following functional forms are used for calculation convenience

$$k_{rw} = u^3 \tag{223}$$

$$k_{ro} = (1-u)^2 \tag{224}$$

$$J(u) = (1-u)(2u^2 - 2u + 1) \tag{225}$$

where u denotes the saturation of the wetting phase. Typical schematics of the functions $F(u)$, $J(u)$, $G(u)$ and $H(u)$ for water-wet systems are shown in Figure 67, where the solution u_i of $F(u) = F_i$ is

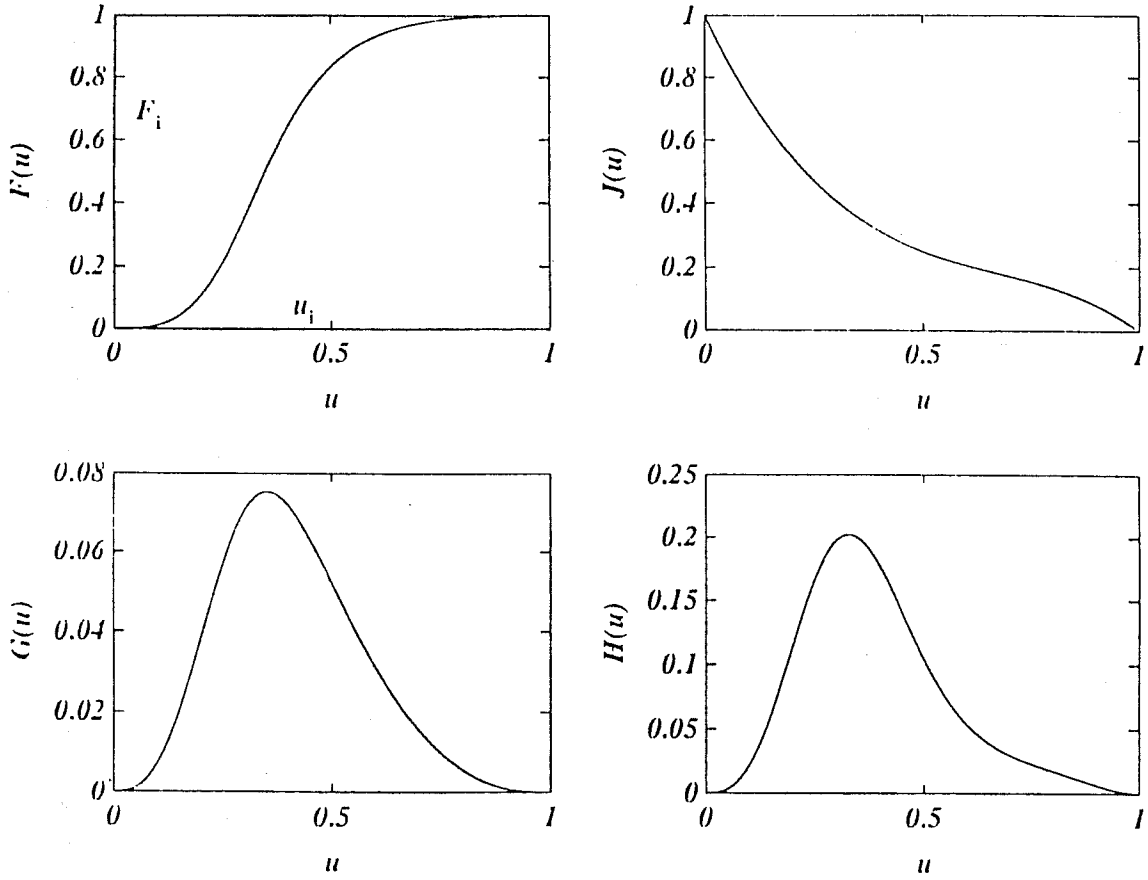

Figure 67: Schematic of functions F, J, G, and H for $M = 10$.

also identified. Particular functions for the heterogeneity variable τ will be assigned below. In all cases, the core length is assumed large enough, compared to the heterogeneity scale, so that injection/production end-effects are not relevant. In the analytical model we consider a linear change in the form of a ramp and a periodic profile in the form of a sawtooth, while variously correlated variations are taken for the numerical investigation.

8.3 ANALYTICAL RESULTS

(i) Step-like change

We consider the saturation response to the step-like change (Figure 68 a)

$$\tau = \begin{cases} \tau_- & \zeta < -1 \\ a\zeta + b & -1 < \zeta < 1 \\ \tau_+ & \zeta > 1 \end{cases} \tag{226}$$

where a is the slope $(\tau_+ - \tau_-)/2$ and b the average $(\tau_+ + \tau_-)/2$. It must be noted that for convenience in graphics, permeability and saturation profiles in all figures were plotted vs. an appropriately

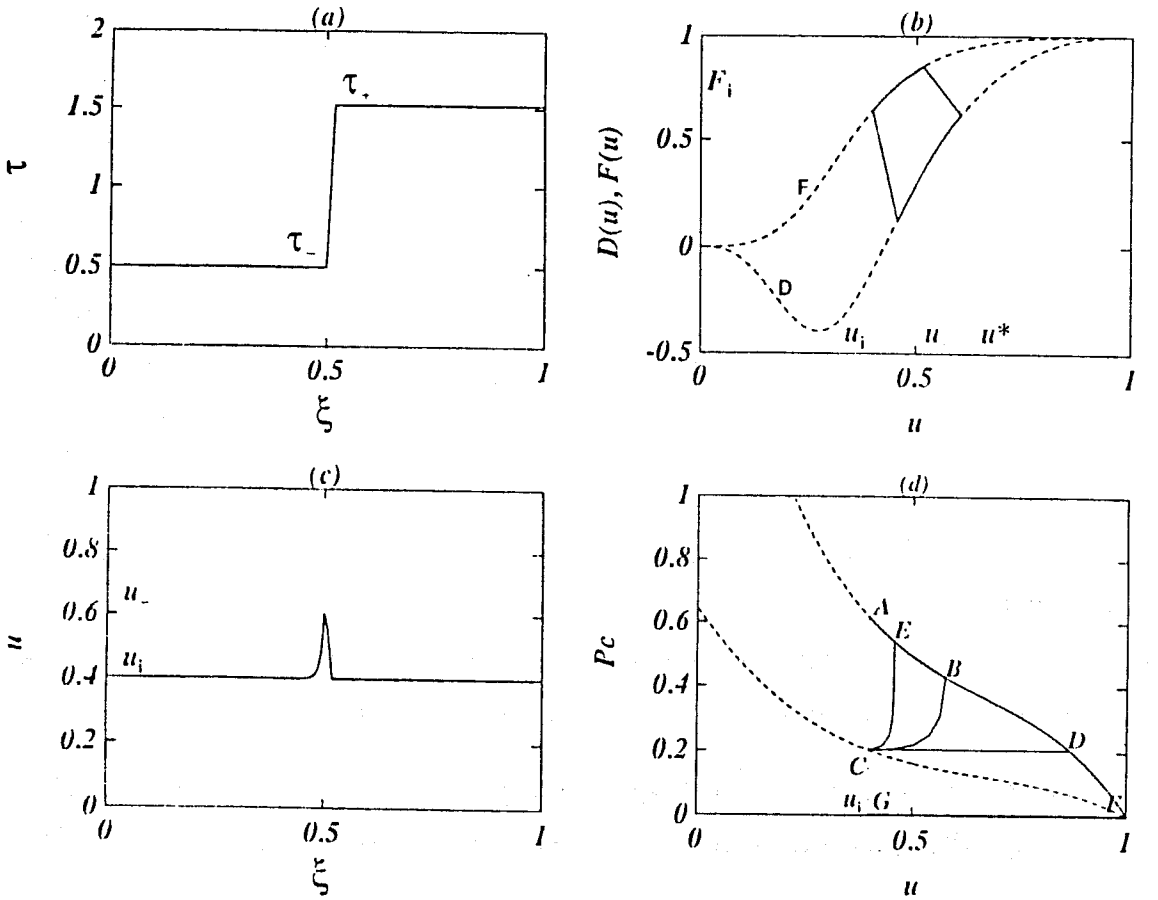

Figure 68: Step-like(ramp) model with increasing pemeability ($\lambda = 8$). (a) τ profile, (b) D and F functions and compositions paths, (c) u profile, (d) composition paths in p_c vs. u diagram.

rescaled space variable ξ always varying in (0,1). The steady-state equation (222) takes the form

$$F(u) - F_i = \varepsilon \tau_- H(u) \frac{du}{d\zeta} \qquad \zeta < -1 \tag{227}$$

$$F(u) - a\varepsilon G(u) - F_i = \varepsilon (a\zeta + b) H(u) \frac{du}{d\zeta} \qquad -1 < \zeta < 1 \tag{228}$$

$$F(u) - F_i = \varepsilon \tau_+ H(u) \frac{du}{d\zeta} \qquad 1 < \zeta \tag{229}$$

For the linear variation (226), equations (227–229) can be integrated by quadratures

$$\varepsilon \int_{u_-}^{u} \frac{H(u)du}{F(u) - F_i} = \frac{\zeta + 1}{\tau_-} \qquad \zeta < -1 \tag{230}$$

$$\varepsilon a \int_{u_+}^{u} \frac{H(u)du}{F(u) - a\varepsilon G(u) - F_i} = \ln \frac{\tau_-}{\tau_+} \qquad -1 < \zeta < 1 \tag{231}$$

$$\varepsilon \int_{u_+}^{u} \frac{H(u)du}{F(u) - F_i} = \frac{\zeta - 1}{\tau_+} \qquad 1 < \zeta \tag{232}$$

In the above, we defined the constants of integration $u_- = u(-1)$, $u_+ = u(1)$, while continuity in saturation was assumed at $\zeta = 1$. Far from the heterogeneity, the saturation takes the constant value u_i dictated from the injected fraction. Note that $u \equiv u_i$ is also a solution of (227, 229). This

value is the same in both outer regions, in view of the assumption on the relative permeabilities. (In the opposite case, the values may slightly differ from each other, with no qualitative effect, as discussed below).

To proceed, we first show that in the interval $\zeta > 1$, $u \equiv u_i$. Indeed, if $u_+ > u_-$, equation (232) requires either $u > u_+$ or $u < u_i$, for $\zeta - 1$ to be positive. The first condition yields an ever increasing u, while the second an ever decreasing u, both of which are inadmissible. Likewise, if $u_+ < u_i$, equation (232) requires either $u > u_i$ or $u < u_+$, also unacceptable for the same reason. The only possibility left is $u_+ = u_i$, which in turn requires $u \equiv u_i$ for $\zeta > 1$.

It remains to evaluate u_-. Use of the above in (231) yields by continuity at $\zeta = -1$

$$\int_{u_i}^{u_-} \frac{H(u)du}{F(u) - \lambda G(u) - F_i} = \frac{1}{\lambda} \ln \frac{\tau_-}{\tau_+} \tag{233}$$

where the relevant parameter $\lambda = a\varepsilon$ was also defined. Thus, the complete solution is described by (230) and

$$\lambda \int_{u_i}^{u} \frac{H(u)du}{F(u) - \lambda G(u) - F_i} = \ln \frac{\tau}{\tau_+} \qquad -1 < \zeta < 1 \tag{234}$$

$$u = u_i \qquad 1 < \zeta \tag{235}$$

where u_- solves (233). To locate u_- with respect to u_i, we consider the two cases:

(a) Increasing permeability, $a > 0$

Here, the RHS of (234) is negative, implying two possibilities: $u_- > u_i$ and $D(u) \equiv F(u) - aG(u) < F_i$ in (u_i, u_-), or $u_- < u_i$ and $D(u) > F_i$ in (u_-, u_+). For increasing permeability, $aG(u) > 0$, thus, $D(u_i) < F_i$, which promptly disqualifies the second option. It follows that $u_* > u_- > u_i$, where u_* is the solution of $D(u) = F_i$ (Figure 68 b).

A schematic of $D(u)$ in the fractional flow diagram (dashed lines in Figure 68 b) resembles a fractional flow function in the presence of gravity in an "updip" displacement. The associated saturation profile is shown in Figure 68 c. The saturation builds up in the low permeability region, $\zeta < -1$, to the maximum value u_- determined from (233), before it declines continuously inside the region of permeability variation $-1 < \zeta < 1$ to the final value u_i.

A physical interpretation to the above can be readily provided. For the wetting fluid to flow at steady conditions in a progressively higher permeability medium, its saturation must decrease, in accordance with capillary continuity. Since, however, both asymptotic saturation values are equal,

this can only be accomplished if the wetting fluid builds up a high enough saturation in the low permeability part. We portray the corresponding "composition path" in the fractional flow diagram (solid lines in Figure 68 b) and in a (dimensional) capillary pressure vs. saturation diagram (Figure 68 d. line ABC). Note the difference with the path dictated from capillary continuity alone (solid line DC, Figure 68 d). The essence of the above argument remains the same when the relative permeabilities, thus the saturations, are different in the two outer regions.

It is worthwhile to examine the sensitivity of u_- to λ, also expressed in terms of dimensional variables as

$$\lambda = \frac{\gamma\sqrt{\phi}}{\mu_o q}\frac{(\sqrt{k_+} - \sqrt{k_-})}{L} \tag{236}$$

An increase in λ is obtained by an increase in the permeability difference and/or by a decrease in the flow rate, or the heterogeneity length. For simplicity, we shall take a constant, and finite, permeability contrast. By differentiating (233) with respect to λ

$$\frac{du_-}{d\lambda} = \int_{u_i}^{u_-} \frac{H(u)[F(u) - F_i]du}{[F(u) - \lambda G(u) - F_i]^2} > 0 \tag{237}$$

i. e., it is straightforward to show that u_- is an increasing function of λ. A "composition path" corresponding to a lower value of λ is portrayed in Figure 68 d (line AEC).

The behavior at large λ is interesting. By rearrangement, we obtain

$$\int_{u_i}^{u_-} \frac{H(u)du}{\frac{F(u) - F_i}{\lambda} - G(u)} = \ln\frac{\tau_-}{\tau_+} \tag{238}$$

which for large enough λ yields

$$\int_{u_i}^{u_-} \frac{H(u)du}{G(u)} = \ln\frac{\tau_+}{\tau_-} \tag{239}$$

In view of (215–221), the above can be reformulated to

$$\frac{J(u_-)}{\tau_-} = \frac{J(u_+)}{\tau_+} \tag{240}$$

which is the condition for continuity in capillary pressure

$$p_c(u_-) = p_c(u_+) \tag{241}$$

Therefore, in this limit, the saturation u_- takes its highest value (path ADC), as dictated from standard end-effect arguments at static conditions. The limit can be independently reached by

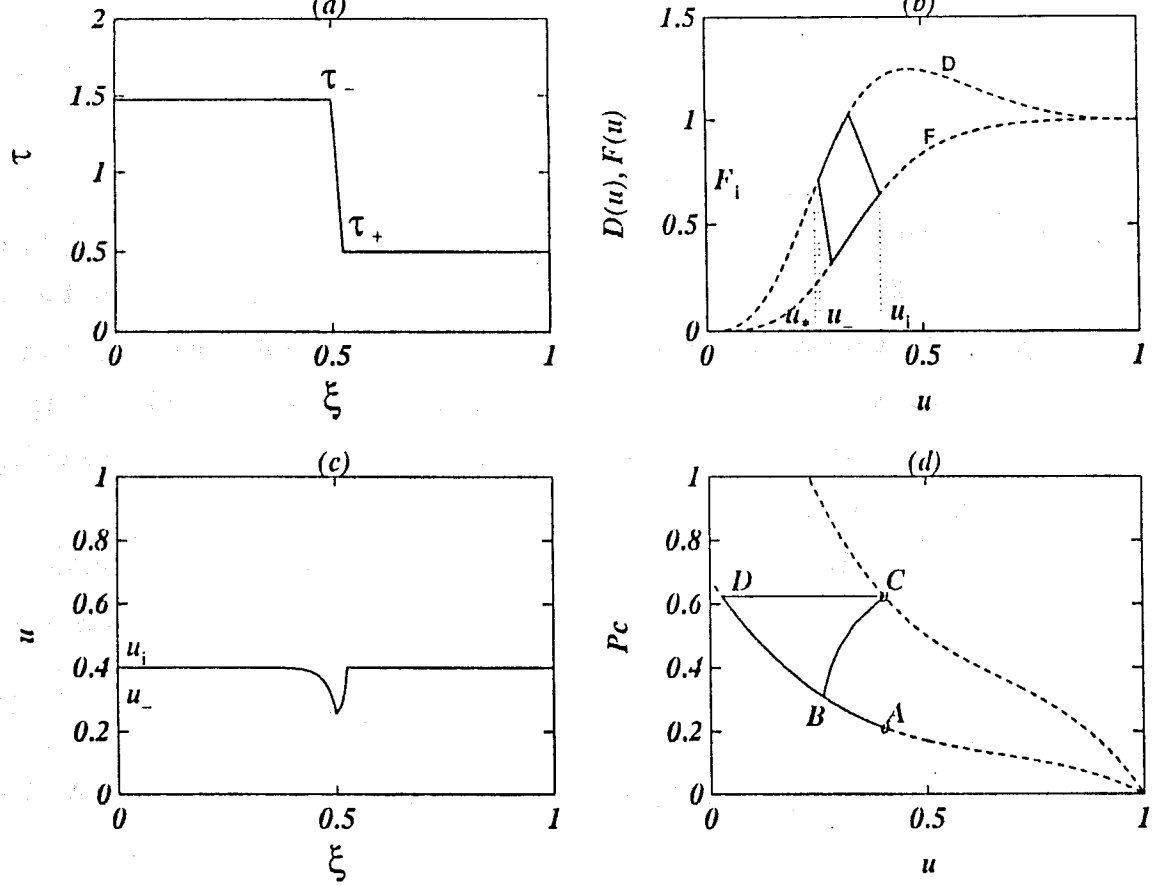

Figure 69: Step-like(ramp) model with decreasing pemeability ($\lambda = -8$). (a) τ profile, (b) D and F functions and compositions paths, (c) u profile, (d) composition paths in p_c vs. u diagram.

either a sharp discontinuity (rapid variation) or by a vanishing flow rate (static conditions). In the former case, the saturation profile contains a kink (in the shape of $\wedge$), that coincides with the gradient in τ (also a $\wedge$-like kink). This behavior was frequently exhibited in the unsteady-state profiles of Part I, which can now be properly interpreted (see also below). It is also remarked that the analysis above holds equally well for infinitely large permeability contrast ($\tau_+ \gg \tau_-$, the latter value held constant). Since λ is large under this condition as well, the previous result (240) is valid, with $u_- \rightarrow 1$ (path AFG in Figure 68 d). The condition of maximum wetting phase saturation build-up for simultaneous flow is, of course, the well known end-effect in the producing side of a core.

(b) Decreasing permeability, $a < 0$

For the case of decreasing permeability (Figure 69 a), an analysis similar to the previous holds. Salient features are the following: a and λ being negative, the function $D(u)$ lies to the left of $F(u)$, thus resembling flow in the presence of gravity in a "downdip" displacement (dashed lines in Figure 69). The solution u_- in equation (233) now satisfies $u_* < u_- < u_i$, thus the saturation profile is a "mirror image" of the previous (Figure 69 c). The physical interpretation is also straightforward.

Capillary continuity requires an increase in wetting saturation as the permeability decreases, and this can only be accomplished by a fall-off of the wetting saturation near the end of the high permeability region. "Composition paths" are shown in Figures 69 b, d (solid lines, and line ABC, respectively). The difference with the path dictated from capillary continuity alone (line DC) should be noted. As before, u_- is monotonically varying with λ, with u_- approaching the static value $u_- = 0$ in the limit $\lambda \to -\infty$ (steep gradient or static conditions).

We shall complete the analysis by considering the other limit, $\lambda \to 0$, obtained at high enough rates (or at weak heterogeneity). Then, $u_- \sim u_i$ and the integral in (233) is reformulated as follows

$$H(u_i) \int_{u_i}^{u_-} \frac{du}{\lambda G(u_i) - F'(u)(u - u_i)} \approx \frac{1}{\lambda} \ln \frac{\tau_+}{\tau_-} \tag{242}$$

where $F(u)$, $G(u)$ and $H(u)$ were expanded and only leading order terms were retained. Upon integration and rearrangement, the final result is obtained

$$u_- = u_i + \frac{\lambda G(u_i)}{F'(u_i)} \left[1 - \left(\frac{\tau_+}{\tau_-} \right)^{-\frac{F'(u_i)}{\lambda H(u_i)}} \right] \tag{243}$$

where certain regularity conditions on $F(u)$, $F'(u)$ and $H(u)$ have been assumed.

With the aid of the fractional flow diagrams, the above analysis can be used to illustrate effects of other parameters. We shall consider injection fraction and mobility ratio.

For $a > 0$, an increase in the fraction F_i results into higher values for u_-. However, the amplitude of the response, $u_- - u_i$ diminishes at large enough fractions and vanishes when only wetting fluid is injected (F_i, u_i, u_-, all approach 1). At this condition, capillary heterogeneity is of no relevance. By contrast, when F_i approaches zero (or when mostly non-wetting fluid is injected), a saturation response exists given by (233) with $F_i = 0$. Opposite effects are obtained when $a < 0$. Here the response vanishes when mostly non-wetting fluid is injected, while it remains significant in the other limit ($F_i = 1$). The above trends were detected in the transient displacement studies of Part I.

The effect of the mobility ratio M cannot be identified as readily. However, some conclusions may be drawn in limiting cases. Thus for $a > 0$, the response is highly pronounced when the mobility ratio is large ($M \gg 1$), and, barely noticeable in the opposite case ($M \ll 1$). Opposite trends are expected when $a < 0$. A note should finally be made regarding wettability. If u is taken

as the saturation of the non-wetting phase, results follow in a straightforward manner, and they are qualitatively the same to the above, subject to the transformation $\tau' \to -\tau'$.

(ii) Periodic variation

To simulate a periodic variation we consider a model with τ piecewise linear in the form of a sawtooth (Figure 70 a). With appropriate rescaling we may take for a periodic cell

$$\tau = \begin{cases} a_-\zeta + \tau_+; & -1 < \zeta < 0 \\ a_+\zeta + \tau_+; & 0 < \zeta < \ell \end{cases} \tag{244}$$

where a_-, a_+ and ℓ are arbitrary. Defining parameters as before, we shall obtain the solutions

$$\lambda_- \int_{u_-}^{u} \frac{H(u)du}{F(u) - \lambda_- G(u) - F_i} = \ln \frac{\tau}{\tau_-} \qquad -1 < \zeta < 0 \tag{245}$$

and

$$\lambda_+ \int_{u_+}^{u} \frac{H(u)du}{F(u) - \lambda_+ G(u) - F_i} = \ln \frac{\tau}{\tau_+} \qquad 0 < \zeta < \ell \tag{246}$$

The two unknowns, u_- and u_+ are determined from continuity at $\zeta = 0$ and periodicity at $\zeta = \ell$

$$\lambda_+ \int_{u_+}^{u} \frac{H(u)du}{F(u) - \lambda_+ G(u) - F_i} = \lambda_- \int_{u_-}^{u} \frac{H(u)du}{F(u) - \lambda_- G(u) - F_i} = \ln \frac{\tau_-}{\tau_+} \tag{247}$$

Note also the simpler form obtained by rearrangement

$$\int_{u_+}^{u_-} \frac{H(u)[F(u) - F_i]du}{[F(u) - \lambda_+ G(u) - F_i][F(u) - \lambda_- G(u) - F_i]} = 0 \tag{248}$$

Without loss in generality, we take $\lambda_+ < 0$, $\lambda_- > 0$ (Figure 4*a*). As above, we also define functions $D_-(u)$ and $D_+(u)$ to construct the fractional flow schematic (dashed line in Figure 70 b).

Consider, now, the saturations u_-^*, u_+^* where $D_-(u) = F_i$, $D_+(u) = F_i$, respectively. The fractional flow diagram is divided into four regions, within each of which the sign of the integrand in (248) is constant. From the latter, u_- and u_+ may not fall into the same region. Furthermore, neither saturation may lie in regions I or IV (otherwise, the saturation will assume somewhere the values u_-^* or u_+^*, where one of the integrals in (247) is singular). It follows that the two saturations must lie in II and III. Using one of (247), we then have

$$\int_{u_+}^{u_-} \frac{H(u)du}{F(u) - \lambda_- G(u) - F_i} = \frac{1}{\lambda_-} \ln \frac{\tau_-}{\tau_+} < 0 \tag{249}$$

which can be satisfied by either one of the following: $u_- > u_+$ and $D_-(u) < F_i$, or $u_- < u_+$ and $D_-(u) > F_i$. For the latter to be valid, u_- (therefore, u_+) must lie in region IV, a case already excluded. It follows that $u_+ < u_i < u_-$. It is then easily shown that u decreases monotonically in (-1, 0), acquires its lowest value, u_+, at $\zeta = 0$, and it increases monotonically in (0, ℓ) to its highest value, u_- at $\zeta = \ell$. A schematic ($\ell = 1$) is shown in Figure 70 c. Thus, the wetting phase saturation follows a pattern which is "anti-symmetric" to that of the permeability. The saturation falls-off as the permeability rises, and builds-up in regions of permeability decrease. Corresponding paths in the fractional flow and the capillary pressure diagrams (line ABA) are shown in Figures 70 b, d. The path rotates towards the horizontal (CDC) in the limit of sharper heterogeneity (or at static conditions), and towards the vertical (EFE) in the limit of weaker heterogeneity (or higher flow rates) as shown in Figure 70 e. It can be easily shown that the corresponding limits in the two cases are $u_+ = u_+^*$, $u_- = u_-^*$, and $u_+ = u_- = u_i$, respectively.

8.4 GENERALIZATIONS AND NUMERICAL RESULTS

(i) Some General Results

Although the above analytical models provide considerable insight, they are restrictive in certain respects. For example, the sawtooth model predicts that saturation maxima and minima coincide with changes in τ', a feature not noted in numerical simulations with smoother profiles. Figure 71 shows the response to a sinusoidal variation. Close inspection reveals that there is no correspondence between the location of maxima and minima of τ and u . A similar discrepancy arises between the ramp model studied above, and one where the step change is simulated by a smoother, hyperbolic tangent profile.

To understand the qualitative response to more general profiles, we consider an arbitrary interval, e.g. interval KL in Figure 72 a, where τ' varies monotonically between two extreme values (negative and positive, respectively). We shall define as in the previous cases the function D, here a function of ζ as well (since λ is now ζ-dependent)

$$\lambda(\zeta) = \varepsilon\tau'(\zeta) \tag{250}$$

$$D(u;\zeta) = F(u) - \lambda(\zeta)G(u) \tag{251}$$

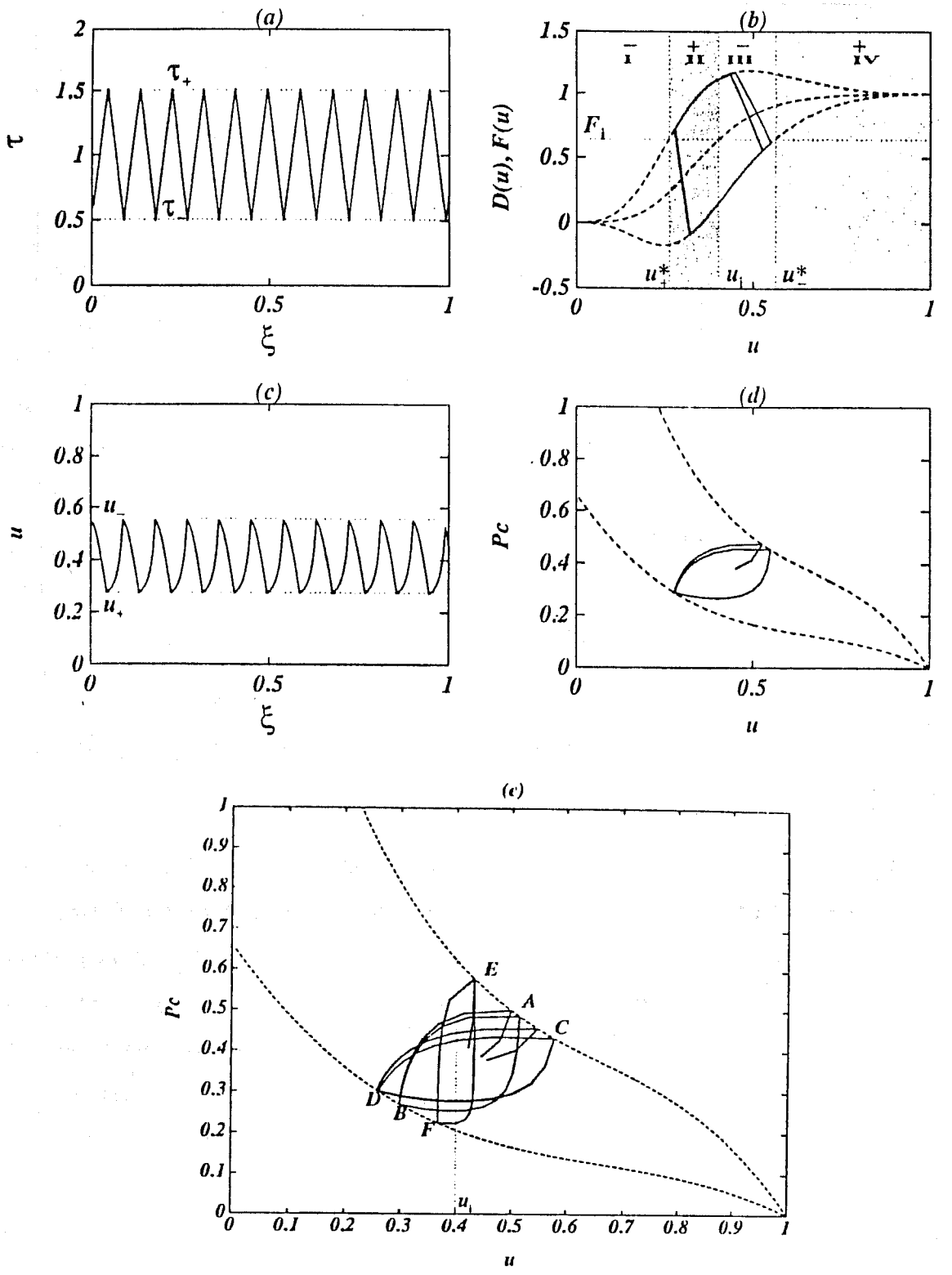

Figure 70: Periodic (Sawtooth) model ($\lambda_- = 2.7\lambda_+ = -2.7$). ($a$) τ profile, (b) D and F functions and compositions paths, (c) u profile, (d) composition paths in p_c vs. u diagram (e) effect of ε on composition paths ($\varepsilon = 0.05,\ 0.20,\ 0.40$, for EFE, ABA, CDC).

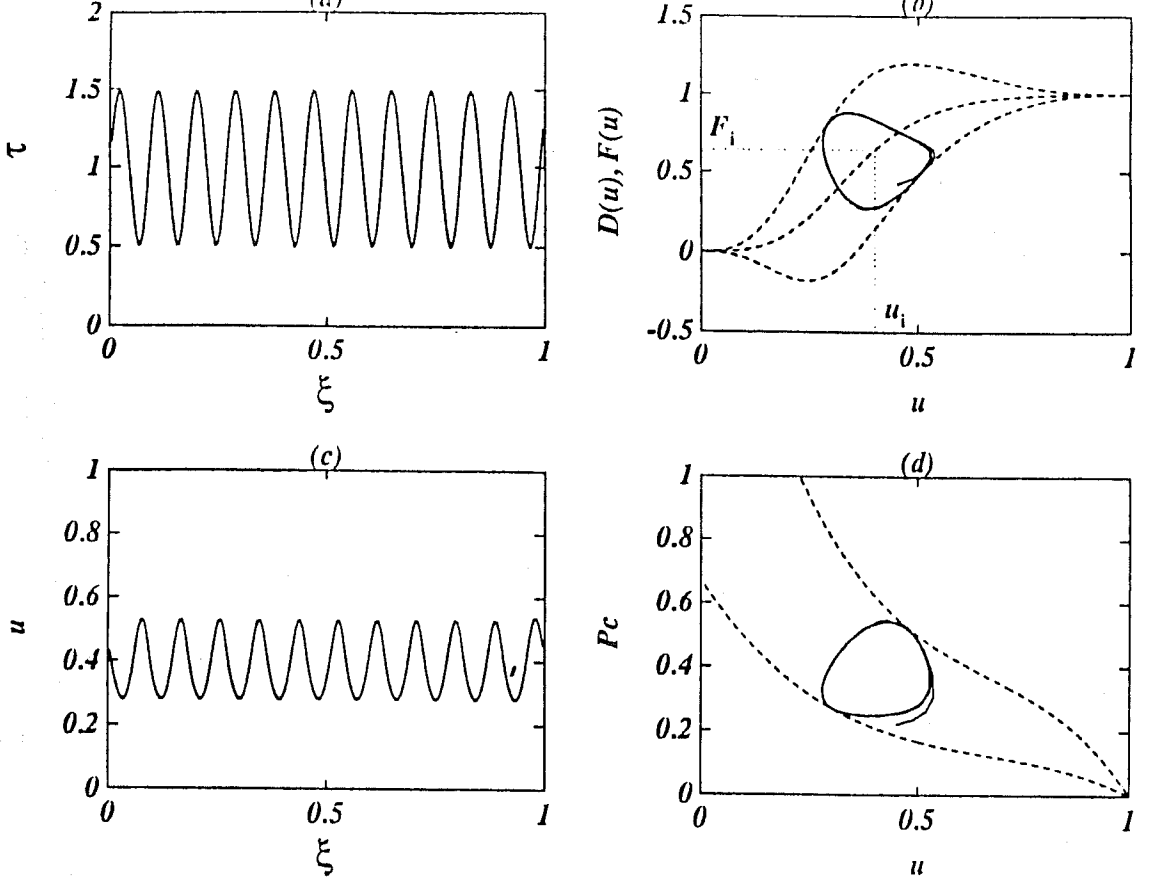

Figure 71: Sinusoidal model ($\varepsilon = 0.2$). (a) τ profile, (b) D and F functions and compositions paths, (c) u profile, (d) composition paths in p_c vs. u diagram.

The limiting curves, D_- and D_+, corresponding to $\lambda_{min} = \varepsilon\tau'_{min} < 0$ and $\lambda_{max} = \varepsilon\tau'_{max} > 0$, are shown in Figure 72 b (dashed lines). Consider also the curve $F(u)$ (which is a D function with $\lambda = \varepsilon\tau' = 0$) and the constant F_i. Note that D_-, D_+ correspond to inflection points, while F is associated with maxima and minima of the τ profile. The four curves D_-, D_+, F, and F_i divide the diagram into four regions I, II, III, IV, which join at point O, and which have the following properties in view of (222)

Region I: $d\tau/d\zeta < 0,\ du/d\zeta > 0$

Region II: $d\tau/d\zeta > 0,\ du/d\zeta > 0$

Region III: $d\tau/d\zeta > 0,\ du/d\zeta < 0$

Region IV: $d\tau/d\zeta < 0,\ du/d\zeta < 0$

It is then straightforward to show the following (Figure 72 a):

i. On composition paths in this diagram, the direction of increasing ζ is clockwise.

ii. Composition paths encircle point O, by intersecting $F(u)$ twice (above and below O, points

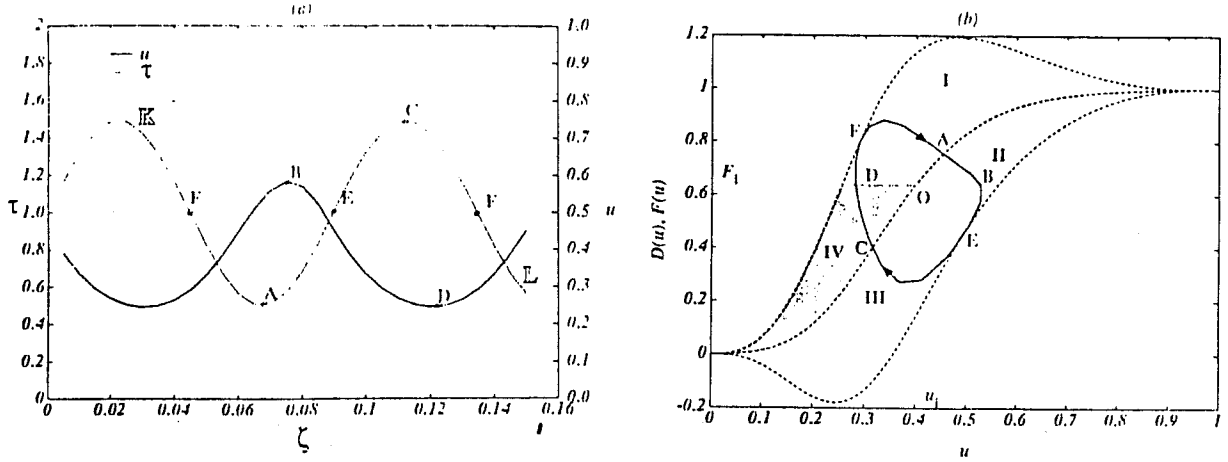

Figure 72: General model. (a) τ and u profiles, (b) D and F functions and compositions paths.

A and C respectively) and by intersecting F_i twice (to the right and left of O, points B and D respectively).

iii. Composition paths are tangent to D_- and D_+ curves in the upper left (I) and the lower right (III) regions, (points E and F), respectively.

It follows that u attains its maximum at B, and its minimum at D. Therefore, the location of the various features in the direction of increasing ζ, is as follows, starting from an inflection point (minimum of τ', point (F)):

Increase in u $\Rightarrow$ τ reaches a minimum (A) $\Rightarrow$ u reaches a maximum (B) $\Rightarrow$ decrease in u $\Rightarrow$ τ reaches an inflection point (E) $\Rightarrow$ decrease in u $\Rightarrow$ τ reaches a maximum (C) $\Rightarrow$ u reaches a minimum (D) $\Rightarrow$ τ reaches an inflection point (F).

Therefore, local maxima (minima) of u are sandwiched between local minima (maxima) and local inflection points of τ. A richer illustration of this is shown in Figure 73 for a profile with modulated waveform. The previous analytical results are also consistent with the above rules, since in a sawtooth profile, inflection points coincide with maxima (or minima) of τ, thus with minima (or maxima) of u , as indeed portrayed in Figure 71. Likewise, as ε increases, the maxima (minima)

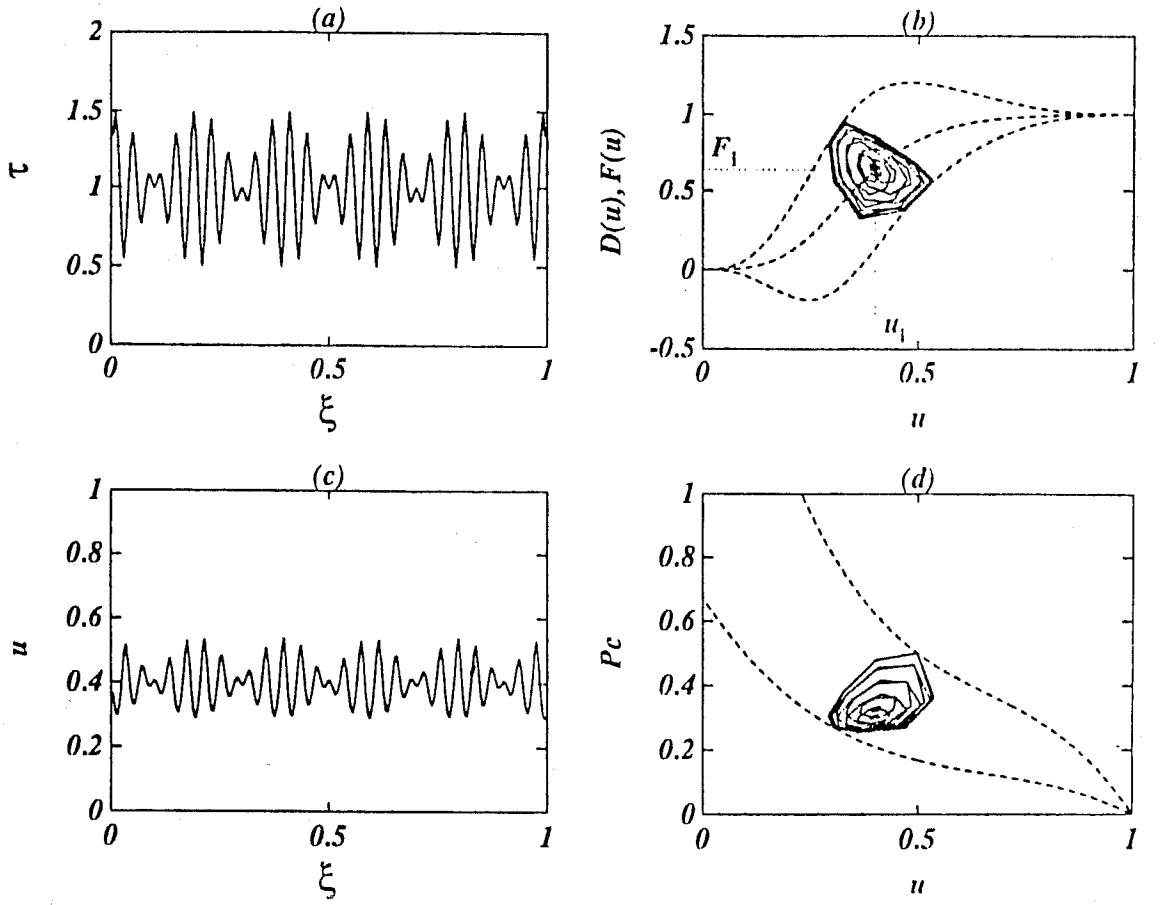

Figure 73: Modulated waveform model ($\varepsilon = 0.1$). (a) τ profile, (b) D and F functions and compositions paths, (c) u profile, (d) composition paths in p_c vs. u diagram.

of τ approach the minima (maxima) of u, so that in the static, no-flow limit, u and τ are exactly antisymmetric. The same correspondence should be expected when τ has sharp variations (see below).

(ii) Numerical Results

We complete the presentation with numerical simulation results for some model cases. All simulations were performed backwards in ζ, starting with the condition $u(1) = u_i$. A standard Newton-Raphson method was used. Shown in Figure 74 are the results corresponding to a set of equal length intervals with a random distribution of τ. In general, the predictions of the ramp problem are well followed here, as expected. The next set corresponds to profiles constructed from the trace of fBm (fractional Brownian motion), recently conjectured to represent natural porous media (Hewett [58], 1986). Shown are the simulations corresponding to uncorrelated white noise (Figure 75) and correlated statistics with fractal dimension $D = 1.2, 1.8$ (Figure 76, 77). The intensity of the response is shown to decrease as the correlation becomes stronger (and as ε decreases). This is consistent with the analysis above, where lower values of λ here induced by large L (strong spatial

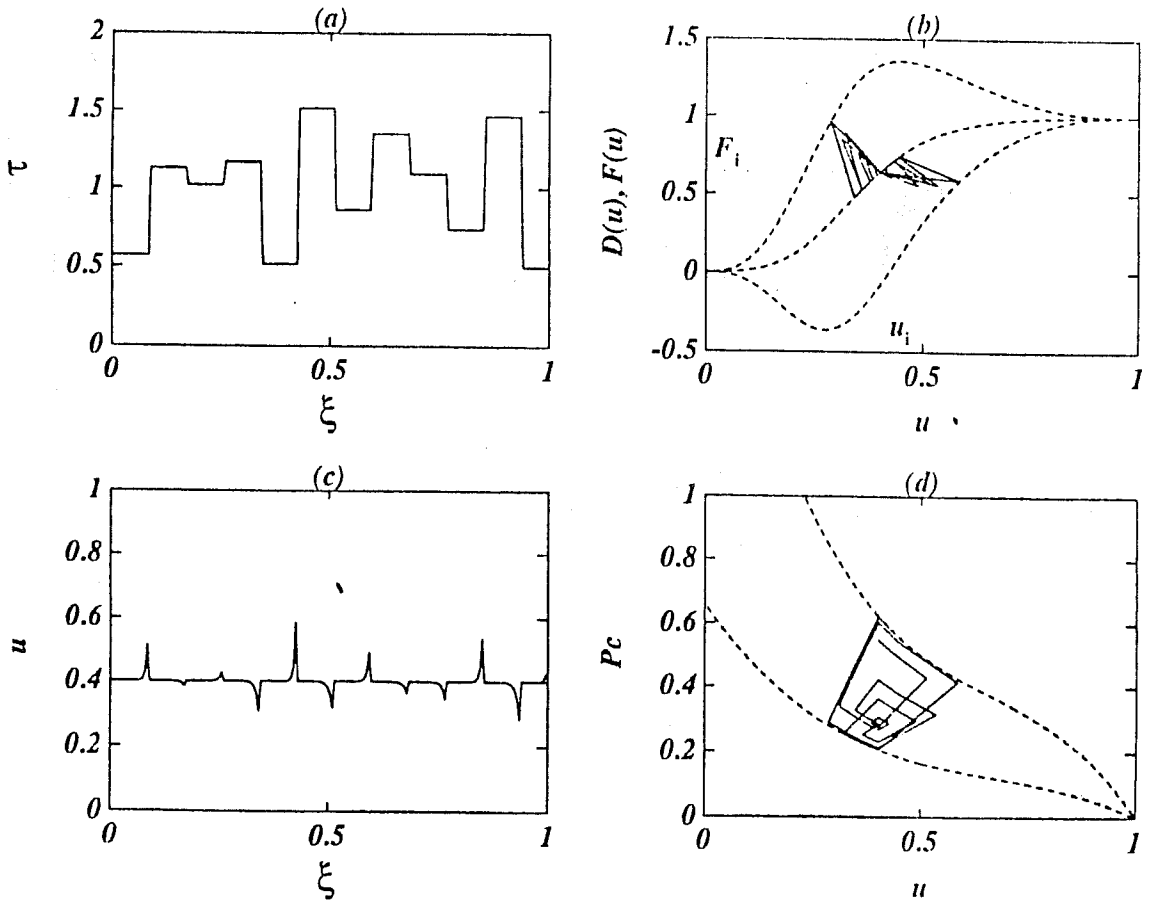

Figure 74: Random series model ($\varepsilon = 0.05$, $a_{max} = 40$). (a) τ profile, (b) D and F functions and compositions paths, (c) u profile, (d) composition paths in p_c vs. u diagram.

correlation), lead to a weaker response. The behavior should be contrasted to the apposite trend of higher sensitivity with increased spatial correlation, for the case of viscosity dominated displacement. Careful examination shows that the general predictions of the preceding section are also satisfied in the numerical simulations. The composition paths in the fractional flow and capillary pressure diagrams are noteworthy in their complexity, which is, of course, only a reflection of the imposed heterogeneity. The clockwise rotation of the paths with an increase in ε discussed above was also verified.

The effects of other process parameters, such as mobility ratio, injection fraction and wettability follow in a straightforward manner from the analysis of the step-profile.

8.5 DISCUSSION

The preceding analysis examined in detail the steady-state saturation response to heterogeneity in capillarity (akin to macroscopic pining). Although it was implied that the latter is due primarily to permeability changes, the analysis applies equally well to wettability variations, under the postulated assumption that relative permeabilities are unaffected. This assumption needs to be

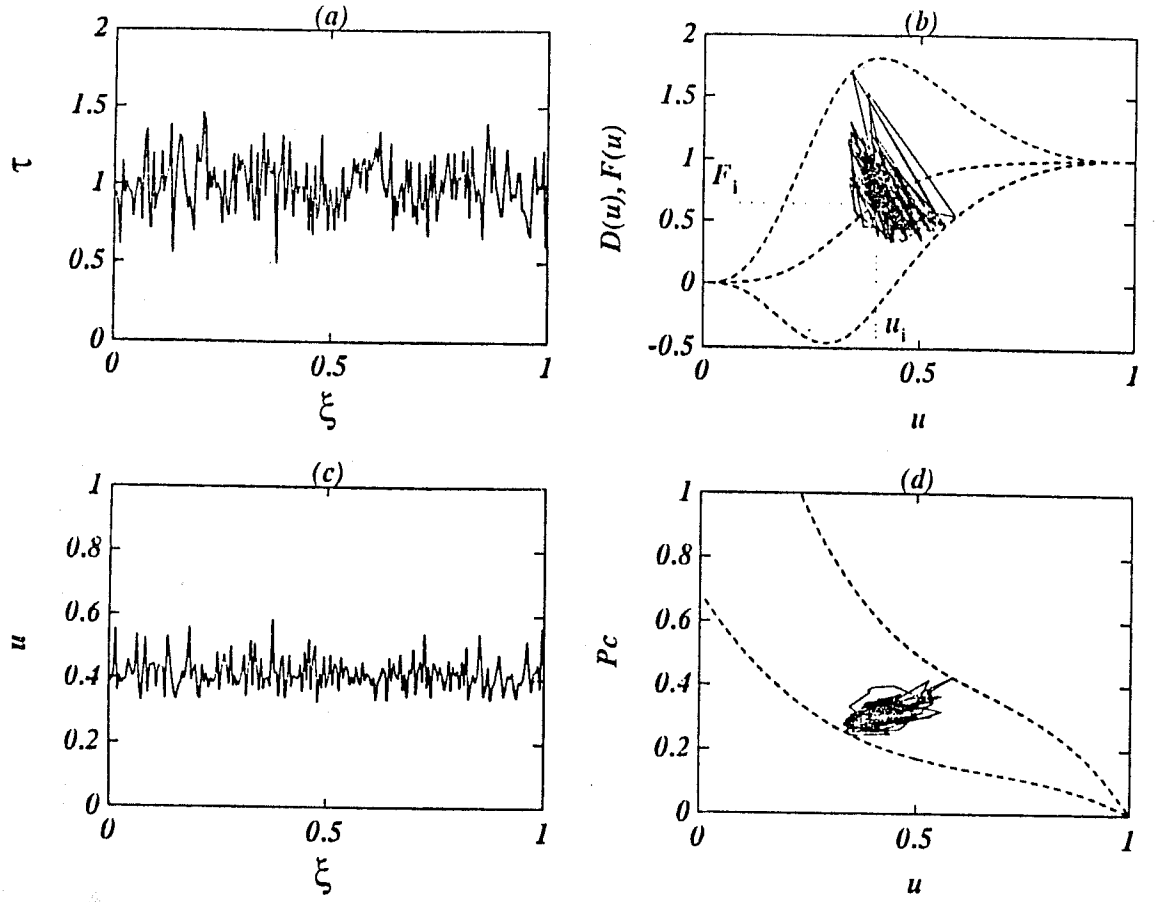

Figure 75: White noise ($\varepsilon = 0.1$). (a) τ profile, (b) D and F functions and compositions paths, (c) u profile, (d) composition paths in p_c vs. u diagram.

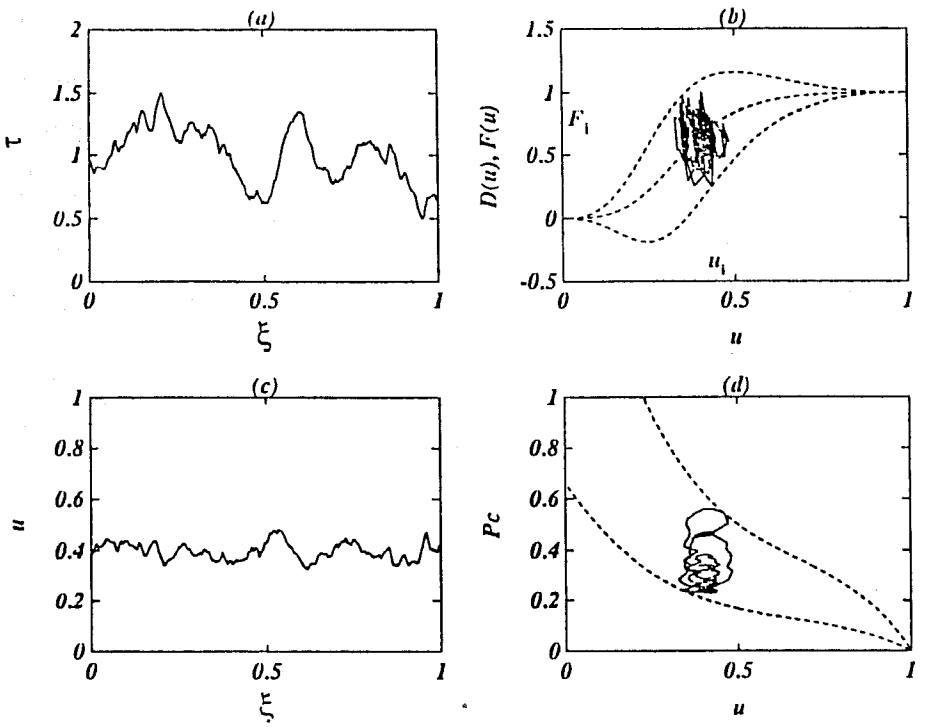

Figure 76: Fractal statistics ($D = 1.2$, $\varepsilon = 0.30$). (a) τ profile, (b) D and F functions and compositions paths, (c) u profile, (d) composition paths in p_c vs. u diagram.

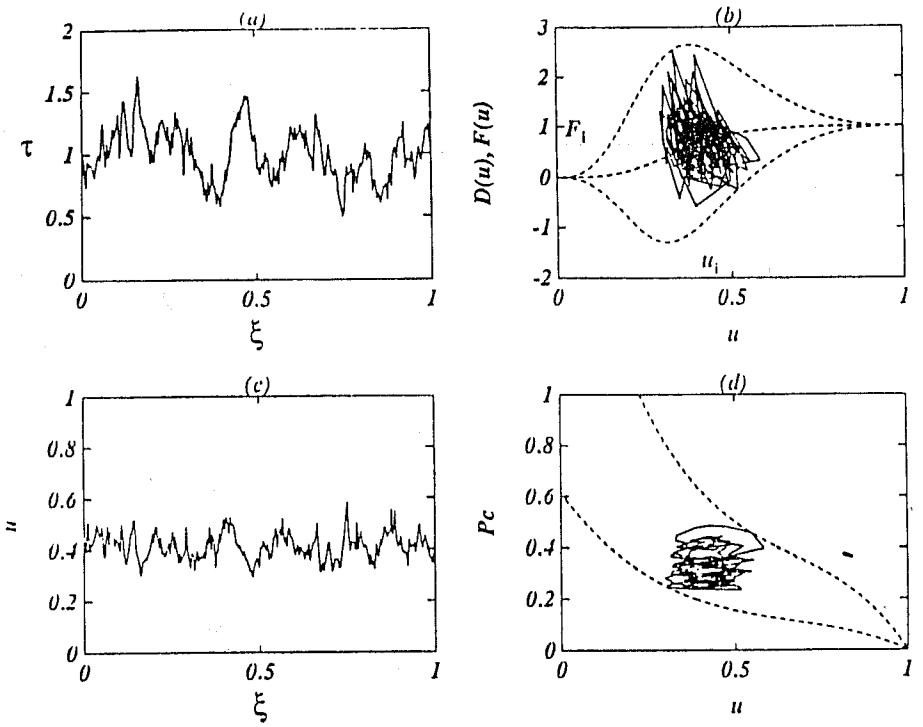

Figure 77: Fractal statistics ($D = 1.7$, $\varepsilon = 0.30$). (a) τ profile, (b) D and F functions and compositions paths, (c) u profile, (d) composition paths in p_c vs. u diagram.

discussed in some detail.

Changes in permeability reflect the combined variation of pore size, geometry or topology (see for instance Thompson[104] and ought to affect relative permeabilities, at least to some extent. The precise effect depends significantly on the cause of the variation. For an exact treatment, one must characterize the macroscopic (core) heterogeneity in terms of spatial variation in the pore size distribution and topology, extract the corresponding permeability variation from an appropriate model and evaluate relative permeabilities and the Leverett function. The approach of Heiba [56] for expressing the latter in terms of the pore microstructure offers an attractive option. Of course, this method would require a precise description, involving to a great extent the geologic and diagenetic history, a process specific to the porous medium.

On the other hand, if the permeability heterogeneity arises from a certain variation in the pore size, it is likely that changes in the (dimensionless) relative permeabilities and Leverett function (that affect functions F, G and H) would be small. This is certainly the case for pore-size distributions that vary in a self-similar manner, as can be readily shown by applying a network model. Keeping in mind the possible limitations, and, mostly, for simplicity, we have taken this latter ap-

proach to use permeability as a descriptor of heterogeneity, and keeping unchanged dimensionless functions such as relative permeabilities. Nevertheless it should be pointed out that the errors involved with such approximations do not alter the qualitative features of the response, in particular the composition paths.

The analysis presented above generalizes to flow conditions, previous results on capillary heterogeneity in static systems, and complements our numerical investigation of transient displacement (Part I). Saturation profiles of the latter exhibited several of the features shown here, as the transient states rapidly settle into a quasi-steady state with locally constant flowing fraction. It was shown that the saturation response faithfully reproduces permeability changes (namely local maxima and minima), under any conditions. On the other hand, the magnitude and phase lag of the response (roughly equal to $5\pi/4$ for the sinusoidal case) depend significantly on the parameter λ, and indirectly on the displacement properties (mobility ratio, etc.), with stronger responses obtained at larger values of λ.

A practical question that may arise in this context is the use of saturation profiles at steady-state to uncover capillary (and possibly, permeability) heterogeneity. Expectedly, the answer is not unequivocal. Determination of absolute values is quite difficult, since it would require knowledge of additional unknown variables, such as the J function, etc., as can be seen in the simplest of cases (ramp model). Somewhat promising appears to be the estimation of the power spectrum. For the case of the sinusoidal variation, this is self-evident. More complex variations need additional study, specifically as it pertains to the effect of the macroscopic capillary number, ε.

Shown in Figure 78 are the power spectra for τ and u corresponding to the static case (ε formally infinite, u obtained from eqn (240)) with τ satisfying fBm with $D = 1.2$. The two spectra are sufficiently close and the fractal dimension can be estimated from the slope in the plot to a satisfactory precision (1.25 vs. the actual value 1.20). Necessary condition for this is a rather mild variation in τ so that the response in u is almost linear (otherwise some nonlinear estimation methods must be used). The agreement gradually deteriorates at smaller values of ε (Figure 79 a), with quite large deviations at lower values (Figure 79 b). One concludes that a large enough ε is required for good estimates. For systems with a fixed scale of heterogeneity, an increase in ε necessitates the decrease of the overall flow rate, possibly a matter of experimental inconvenience regarding equilibrium times. On the other hand, for the fractal statistics of the type above, this

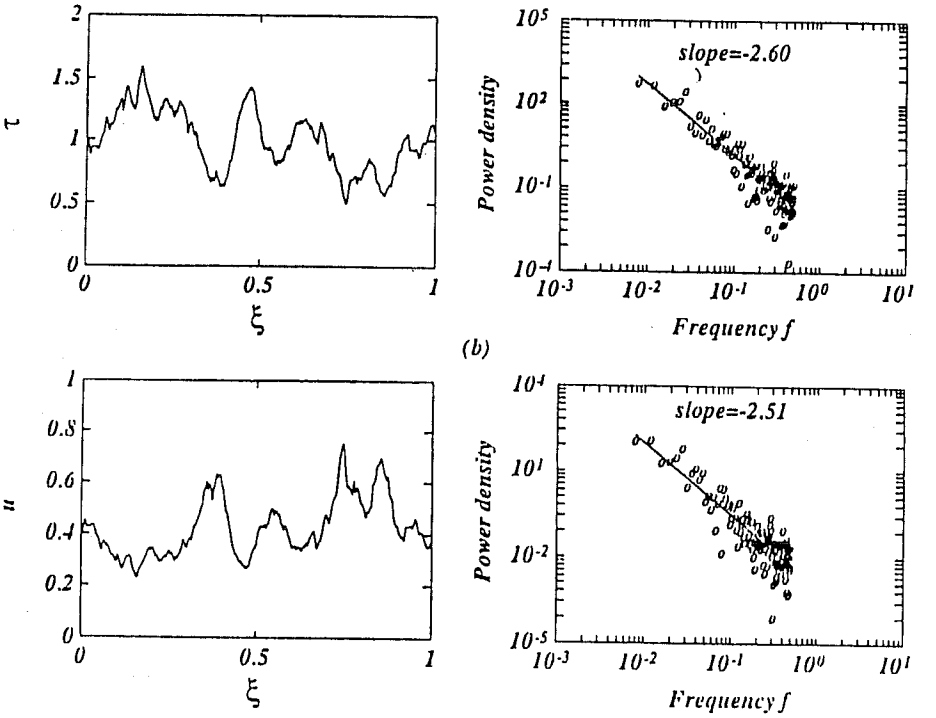

Figure 78: Power spectra, fractal statistics ($D = 1.2, \varepsilon = \infty$). ($a$) τ profile, (b) u profile.

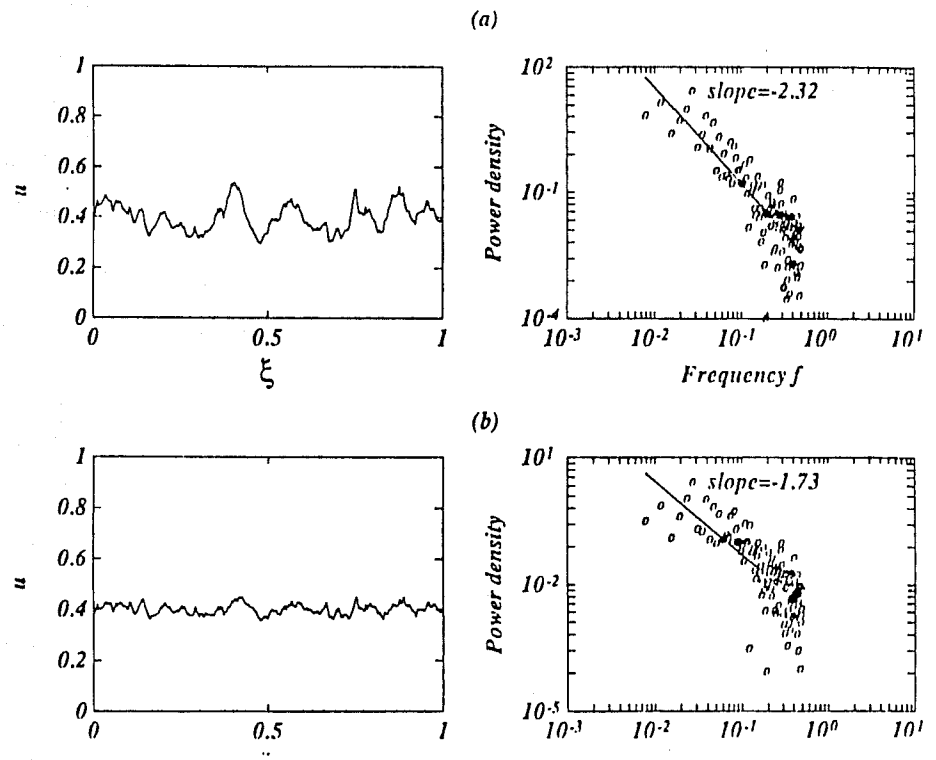

Figure 79: Power spectra, fractal statistics ($D = 1.2$). (a) $\varepsilon = 0.50$, (b) $\varepsilon = 0.10$.

may be also accomplished with an increase in the resolution of the saturation probe (effectively decreasing L), provided of course that the latter exceeds lower cutoffs of the fractal statistics and upper cutoffs for a continuum description. These simple observations provide only a cursory overview of the practical issue. Further study of this problem and development of some practical approaches would be desirable undertakings. It is hoped that the present analysis would be helpful for such investigations.

SUMMARY AND FUTURE WORK

Substantial progress has been made in our understanding of the mechanisms involved in vapor-liquid flow in porous media:

The onset of phase change (nucleation) has been analysed in detail. It is found that the critical supersaturation is independent of the rate of pressure (temperature) decline, although a significant dependence exists on the ensuing phase growth. The nucleation model proposed shows that as a rule, nucleation effects are of a secondary quantitative importance. Critical gas saturations were predicted in the range 0.01-0.1. Effects of general pore size distributions were also examined. Our work also finds application to the related processes of cavitation and capillary desorption.

The phase growth following nucleation was classified according to the magnitude of the externally imposed supersaturation. This is a significant accomplishment that allows for the first time a systematic approach to the problem of vapor (bubble) growth in porous media. It was established that the practice usually taken in the simulation of field processes is valid, as long as the supersaturation decline rates are low enough (substantially lower than 1 psi/day for the case of solution gas-drive). Appropriate criteria were developed and relative permeability curves were predicted. The need for further work when the above criteria are not satisfied was emphasized.

Appropriate macroscopic models for the steady, countercurrent flow of steam and water that include heat conduction, capillary and Kelvin effects were formulated and solved. Such processes found applications in steam injection and geothermal systems among others. It was established that Kelvin effects are of importance in the boundary between dry and two-phase regions, and are negligible otherwise. Careful study of the critical heat flux for the case of bottom heating showed that a threshold permeability value exists, below which steady states may not exist. In addition, we have accomplished a unified description of both heat pipe and geothermal problems and showed how the various problems emerge as limiting cases. In this context, a previously proposed conjecture on the existence of liquid-dominated steam- water systems, was found to be invalid.

Steady-state experiments with foaming solutions verified the existence of a critical flow rate, above which the pressure drop increased severalfold. The latter was found to be independent of the flow direction (drainage or imbibition) or the gas velocity. Emphasis has also been placed on the end effects associated with laboratory core floods. Foam incubation phenomena have been observed and are currently under investigation. Expectedly, the use of a prefoamer at the inlet led

to enhanced foam texture and a higher pressure drop within the core.

In parallel, we were able to extend the traditional Buckley- Leverett and JBN methods for non-Newtonian fluids of the power- law type. This has important implications in the prediction of displacement efficiencies with the use of power-law additives. Shear-thickening fluids show improved performance at higher flow rates, and lower permeability media, the opposite being true for shear-thinning fluids. The JBN modification quantifies the error incurred if the original method is used to interpret unsteady- state relative permeability experiments, and should be of direct use to laboratory experiments involving foams.

Our work on the use of caustic additives at elevated temperatures was completed by examining caustic consumption and silica dissolution in long cores. Our experimental evidence strongly indicates that caustic consumption and the associated pH decline are significant in the presence of clay at elevated (higher than 120°C) temperatures. We have attributed this to a reaction between silica and alumina in solution to form alumino-silicates. We are led to the conclusion that caustic solutions are not expected to be effective as steam additives in reservoirs containing clays. In view of this result, further work in the area is not planned.

Considerable advances have been made in understanding effects of capillary heterogeneity under non-static (flow) conditions. We have shown how the saturation profiles are affected in a region of permeability variation due to capillarity, and we examined the effects of flow rate, fractional flow, mobility ratio, wettability, and permeability contrast. These results are useful in processes in heterogeneous media, e.g. in steam injection in fractured systems, and in foam flow.

This work contributes to the DOE EOR research in several ways: The complete development of a chemical-steam simulator would allow field-scale sensitivity studies, particularly the investigation of heterogeneity effects, at a considerably low cost. Many other users are expected to benefit from such publicly available software. The fundamental understanding of vapor-liquid flow is paramount to further improvements in steamfloods, to solution gas-drive, to gas condensate reservoirs and to several other processes. The correct representation of the phenomena at the pore level is necessary for the accurate description at the larger, macroscopic scale and the subsequent assessment of process performance in more complex systems, including naturally fractured reservoirs, heterogeneous and fractal media.

Our work in the use of steam additives has obvious implications to oil recovery. The dual role

of mobility reduction and residual saturation decrease played by foaming solutions, is still to be fully explored. The effect of permeability heterogeneity on the formation and propagation of foams is a real issue, and may alleviate the requirement of large pressure drops. The potential to EOR processes can hardly be overstated. On the other hand, the detrimental caustic consumption at higher temperatures, effectively rules out the suitability of caustic as a viable steam additive.

Future research plans include the following:

1. We plan to continue work on the development of the chemical- steam simulator. We anticipate accelerated progress in the near future.

2. We shall continue our work on vapor-liquid flow. On the theoretical side, we shall address issues of heat transfer, heat flux and rate of supersaturation increase on the vapor phase growth. Concurrent and countercurrent flows at the pore level will be studied. Effects of thin films and gravity, and the presence of a third liquid phase will be considered, in an effort to quantify residual oil saturations. On the experimental side, work on vapor-liquid flow involving micromodels and Hele-Shaw cells is planned. The latter is prerequisite to steam injection in fractured systems. On the macroscopic side, we shall investigate vapor-liquid phenomena in regions of large permeability heterogeneity, e.g. naturally fractured systems and fractal media.

3. Further work in the area of foams and other steam additives for mobility control is planned. The role of permeability heterogeneity on the foam properties will be investigated. The properties of steam foams and their effectiveness in the presence of oil will be also examined. In parallel, modeling efforts for the flow of non-Newtonian fluids in porous media will continue with emphasis on the importance of spatial correlations in the properties of the porous medium.

PUBLICATIONS

The following publications have resulted from this research during the period reported:

1. Parlar, M., and Yortsos, Y.C., "Percolation Theory of Vapor Adsorption-Desorption Processes in Porous Media", J. Colloid Interface Sci., **124**, 162-176 (1988).

2. Parlar, M., and Yortsos, Y.C., "Nucleation and Pore Geometry Effects in Capillary Desorption Processes in Porous Media", J. Colloid Interface Sci., **132**, 425-443 (1989).

3. Yortsos, Y.C., and Parlar, M., "Phase Change in Binary Mixtures in Porous Media: Application to Solution Gas-Drive", paper SPE 19697 presented at the 64th SPE Annual Fall Meeting, San Antonio, TX (October 8-11, 1989).

4. Parlar, M., Ph. D. Thesis, Department of Petroleum Engineering, University of Southern California (September 1989).

5. Satik, C., Parlar, M., and Yortsos, Y.C., "A Study of Steady- State Steam-Water Counterflow in Porous Media", Int. J. Heat Mass Transfer, submitted (1989).

6. Salman, M., Baghdikian, S.Y., Handy, L.L., and Yortsos, Y.C., "Modification of Buckley-Leverett and JBN Methods for Power-Law Fluids", SPERE, submitted (1989).

7. Saneie, S., and Yortsos, Y.C., "Kinetics of Silica Dissolution and Hydroxyl Ion Consumption in Alkaline Flloding", paper SPE 17410 presented at the 1989 California Regional Meeting, Long Beach CA (March 23-25, 1988).

8. Aflaki, R., Ph. D. Thesis, Department of Petroleum Engineering, University of Southern California (December 1989, expected).

9. Chang, J., and Yortsos, Y.C., "Capillary Effects in Steady- State Flow in Heterogeneous Cores", Trans. Porous Media, accepted (1989).

10. Huh, D.G., and Handy, L.L., "Comparison of Steady- and Unsteady-State Flow of Gas and Foaming Solutions in Porous Media", SPERE, **4**, 77-85 (1989).

References

[1] E. Abgrall and R. Iffly. Physical study of flows by expansion of dissolved gas. *Rev. IFP* (Sept.-Oct. 1973) 667-692 (in French).

[2] A.W. Adamson. *Physical Chemistry of Surfaces.* Wiley, New York, 1982.

[3] U.G. Araktingi and F.M Orr. Viscous fingering in heterogeneous porous media. *Paper SPE 18095 presented at the 63rd Annual SPE Fall Meeting, Houston, TX.*, 1988.

[4] D. Avnir, D. Farin, and P. Pfeifer. Surface geometric irregularity of particulate materials: The fractal approach. *J. Coll. Intf. Sci.*, 103:112–123, 1985.

[5] S.G. Bankoff. Ebullition from solid surfaces in the absence of a pre-existing gaseous phase. *Trans. ASME* (May 1957) 735-740.

[6] E.P. Barrett, L.G. Joyner, and P.P. Halenda. The determination of pore volume and area distributions in porous substances. *J. Amer. Chem. Soc.*, 73:373–380, 1951.

[7] H. H. Bau and K.E. Torrance. Boiling in low-permeability porous materials. *Int. J. Heat Mass Transfer*, 25:45–54, 1982.

[8] J. Bear. *Dynamics of Fluids in Porous Media.* American Elsevier, 1972.

[9] C. M. Bender and S. A. Orszag. *Advanced Mathematical Methods for Scientists and Engineers.* McGraw Hill, New York (1978).

[10] K. Binder. Theory of first-order phase transitions. *Rep. Prog. Phys.*, 50:783–859, 1987.

[11] R.B. Bird, W.E. Stewart, and E.N. Lightfoot. *Transport Phenomena.* J. Wiley, N.Y., 1960.

[12] N. E. Bixler and C. R. Carrigan. Enhanced heat transfer in partially-saturated hydrothermal systems. *Geophysical Res. Letters*, 13:42–45, 1986.

[13] M. Blander and J.L. Katz. Bubble nucleation in liquids. *AIChE J.*, 21:833–848, 1975.

[14] A.J. Brown. PhD thesis, University of Bristol, 1963.

[15] S. Brunauer, P.H. Emmett, and E. Teller. Adsorption of gases in multimolecular layers. *J. Amer. Chem. Soc.*, 60:309–319, 1938.

[16] J. M. Buchlin. Transport processes associated with nuclear reactor safety. *Proceedings NATO/ASI on Transport in Porous Media (Y. Corapcioglu and J. Bear, eds.) Pullman, Wa.*, July 9-18 1989.

[17] W.J. Cannella, C. Huh, and R.S. Seright. Prediction of xanthan rheology in porous media. *Paper SPE 18089*, 1988.

[18] J. Chang and Y.C. Yortsos. Effect of heterogeneity on Buckley-Leverett displacement. *Paper SPE 18798 presented at the SPE California Regional Meeting, Bakersfield, CA.*, 1989.

[19] A. Chatenever, M.K. Indra, and J.R. Kyte. Microscopic observations of solution gas drive behavior. *J.Pet.Tech.* (June 1959) 13-15.

[20] I. Chatzis and F.A.L. Dullien. The modeling of mercury porosimetry and the relative permeability of mercury in sandstones using percolation theory. *Int. Chem. Eng.*, 25:47–66, 1985.

[21] R.H. Christopher and S. Middleman. Power-law flow through a packed tube. *Ind. Eng. Chem. Fund.*, 4:422–426, 1965.

[22] R. Cole. Boiling nucleation. *Adv. Heat Trans.*, 10:85–166, 1974.

[23] R. E. Collins. *Flow of Fluids Through Porous Materials.* Petroleum Publishing Co., Tulsa, OK, 1976.

[24] K. Cornwell, B. G. Nair, and T. D. Patten. Observation of boiling in porous media. *Int. J. Heat Mass Transfer*, 19:236–238, 1976.

[25] B.C. Craft and M.F. Hawkins. *Applied Petroleum Reservoir Engineering.* Prentice-Hall, Englewood Cliffs, 1959.

[26] L.A. Crum. Nucleation and stabilization of microbubbles in liquids. *Appl. Sci. Res.*, 38:101–115, 1982.

[27] J. G. Crump. Detailed simulation of the effects of process parameters on adverse mobility ratio displacement. *Paper SPE 17337 presented at the 6th SPE/DOE Symposium on Enhanced Oil Recovery, Tulsa, OK*, 1988.

[28] A. Danesh, J.M. Peden, D. Krinis, and G.D. Henderson. Pore level visual investigation of oil recovery by solution gas drive and gas injection. *Paper SPE 16956 presented at the 1987 SPE Annual Meeting, Dallas, TX, Sept. 27-30.*, 1987.

[29] J.H. de Boer, B.C. Lippens, B.G. Linsen, J.C.P. Broekhoff, A. van den Heuvel, and Th.J. Osinga. The t-curve of multimolecular N_2-adsorption. *J. Coll. Intf. Sci.*, 21:405–414, 1966.

[30] A.S. de Vries and K. Wit. Rheology of gas/water foam in the quality range relevant to steam foam. *Paper SPE 18075*, 1988.

[31] V. Dhir and I. Catton. Dryout heat fluxes for inductively heated particulate beds. *J. Heat Transfer*, 99:250–256, 1977.

[32] C. Doughty and K. Pruess. A semianalytical solution for heat-pipe effects near high-level nuclear waste packages burried in partially saturated geological media. *Int. J. Heat Mass Transfer*, 31:79–90, 1988.

[33] M.M. Dubinin. Capillary evaporation and information on structure of adsorbent pores. *J. Coll. Intf. Sci.*, 77:84–90, 1980.

[34] J.M. Dumore. Development of gas saturation during solution gas drive in an oil layer below a gas cap. *SPEJ* (Sept. 1970) 211-218.

[35] E. R. G. Eckert, R. J. Goldstein, A. I. Behbahani, and R. Hain. Boiling in an unconstricted granular medium. *Int. J. Heat Mass Trans.*, 28:1187–1196, 1985.

[36] P.H. Emmett and M. Cines. Adsorption of argon, nitrogen, and butane on porous glass. *J. Phys. Chem.*, 51:1248–1262, 1947.

[37] P.C. Engelking. Lifetimes of metastable microbubbles. *J. Phys. Chem.*, 89:1520–1523, 1985.

[38] D. Epstein. Expansion of a high-pressure gas sphere in a highly porous medium. *J. Geophys. Res.*, 72:3701–3710, 1967.

[39] D.H. Everett. *The Solid-Gas Interface.* Dekker, New York, 1967. (E.A. Flood, editor).

[40] D.H. Everett. Thermodynamics of multiphase fluids in porous media. *J. Coll. Intf. Sci.*, 52:189–198, 1975.

[41] D.H. Everett and J.M. Haynes. Model studies of capillary condensation. *J. Coll. Intf. Sci.*, 38:125–137, 1972.

[42] J. Feder. *Fractals.* Plenum, New York, 1988.

[43] J.C. Fisher. The fracture of liquids. *J. Appl. Phys.*, 19:1062–1067, 1948.

[44] M.E. Fisher and J.W. Essam. Some cluster size and percolation problems. *J. Math. Phys.*, 2:609–619, 1961.

[45] P.J. Flory. *Principles of Polymer Chemistry.* Cornell Univ. Press, New York, 1953.

[46] T.W. Forest. The stability of gaseous nuclei at liquid-solid interfaces. *J. Appl. Phys.*, 53:6191–6201, 1982.

[47] F. Friedmann, W.H. Chen, and P.A. Gauglitz. Experimental and simulation study of high-temperature foam displacement in porous media. *Paper SPE 17357*, 1988.

[48] R.M. Giordano, S.J. Salter, and K.K. Mohanty. The effects of permeability variations on flow in porous media. *Paper SPE 14365 presented at the 60th Annual SPE Fall Meeting, Las Vegas, NV*, 1985.

[49] M.C. Goh, W.I. Goldburg, and C.M. Knobler. Phase separation of a binary liquid mixture in a porous medium. *Phys. Rev. Lett.*, 58:1008–1011, 1987.

[50] E. E. Gomma and W. H. Somerton. The behavior of multifluid-saturated formations, part ii: Effect of vapor saturation-heat pipe concept and apparent, thermal conductivity. *Paper SPE 4896-B, Proc. Soc. Petroleum Engineers, California Regional Meeting, San Francisco*, April (1974).

[51] S.J. Gregg. Sixty years in the physical adsorption of gases. *Coll. Surf.*, 21:109–124, 1986.

[52] S.J. Gregg and K.S.W. Sing. *Adsorption, Surface Area and Porosity.* Academic Press, New York, 1982.

[53] L.L. Handy. A laboratory study of oil recovery by solution gas drive. *Trans. AIME*, 213:310–315, 1958.

[54] E.N. Harvey, D.K. Barnes, W.D. McElroy, A.H. Whiteley, D.C. Pease, and K.W. Cooper. Bubble formation in animals. *J. Cell. Comp. Physiol.*, 24:1–34, 1944.

[55] J.M. Haynes and F.G. McCaffery. Light scattering and capillary condensation in porous media. *J. Coll. Intf. Sci.*, 59:24–30, 1977.

[56] A.A. Heiba, H.T. Davis, and L.E. Scriven. Effect of wettability on two-phase relative permeabilities and capillary pressures. *Paper SPE 12172 presented at the 1983 SPE Annual Meeting, San Francisco, CA, Oct. 5-8*, 1983.

[57] A.A. Heiba, M. Sahimi, L.E. Scriven, and H.T. Davis. Percolation theory of two-phase relative permeability. *Paper SPE 11015 presented at the 1982 SPE Annual Meeting, New Orleans, LA, Sept. 26-29*, 1982.

[58] T.A Hewett. Fractal distribution of reservoir heterogeneity and their influence on fluid transport. *Paper SPE 15386 presented at the 61st Annual SPE Fall Meeting, New Orleans, LA*, 1986.

[59] G.J. Hirasaki, D.J. O'Meara Jr., and J.A. Rohan. Centrifuge measurements of capillary pressure: Part 2 - cavitation. *Paper SPE 18592 presented at the 1988 SPE Annual Meeting, Houston, TX, Oct. 2-5.*, 1988.

[60] E.B. Hunt Jr. and V.J. Berry Jr. Evolution of gas from liquids flowing through porous media. *AIChE J*, 2:560–567, 1956.

[61] E.F. Johnson, D.P. Bossler, and V.O. Newmann. Calculation of relative permeability from displacement experiments. *Trans. AIME*, 216:370–372, 1959.

[62] F. Kalaydjian. A macroscopic description of multi phase flow in porous media involving spacetime evolution of fluid/fluid interface. *Transport In Porous Media*, 2:537–552, 1987.

[63] H.T. Kennedy and C.R. Olson. Bubble formation in supersaturated hydrocarbon mixtures. *Trans. AIME*, 195:271–278, 1952.

[64] L.W. Lake and H.B. (eds.) Carroll. *Reservoir Characterization.* Academic Press, 1986.

[65] R.G. Larson. Derivation of generalized Darcy equations for creeping flow in porous media. *Ind. Eng. Chem. Fund.*, 20:132–137, 1981.

[66] I.M. Lifshitz and V.V. Slyozov. The kinetics of precipitation from supersaturated solid solutions. *J. Phys. Chem. Solids*, 19:35–50, 1961.

[67] C.M. Marle. *Multiphase Flow in Porous Media.* Gulf Publishing, Editions Techinip, Paris, 1981.

[68] J.A. Marqusee and J. Ross. Kinetics of phase transitions: Theory of Ostwald ripening. *J. Chem. Phys.*, 79:373–378, 1983.

[69] J. C. Martin, R. E. Wegner, and F. J. Kelsey. One-dimensional convective and conductive heat flow. *Preceedings Second Workshop Geothermal Reservoir Engineering*, Dec. 1-3, 1976.

[70] G. Mason. The effect of pore lattice structure on the pore size distributions calculated from sorption isotherms using percolation theory. *J. Coll. Intf. Sci.*, 95:277–278, 1983.

[71] G. Mason. A model of adsorption-desorption hysteresis in which hysteresis is primarily developed by the interconnections in a network of pores. *Proc. R. Soc. Lond.*, A390:47–72, 1983.

[72] G. Mason. Determination of the pore-size distributions and pore-space interconnectivity of vycor porous glass from adsorption-desorption hysteresis capillary condensation isotherms. *Proc. R. Soc. Lond.*, A415:453–486, 1988.

[73] J. C. Melrose. Use of water vapor desorption data in the determination of capillary pressures. *Paper SPE 16286*, 1988.

[74] F. G. Miller. Steady flow of two-phase single-component fluids through porous media. *Petroleum Trans., AIME*, 192:205, 1951.

[75] N.R. Morrow. Physics and thermodynamics of capillary action in porous media. *Ind. Eng. Chem. Fund.*, 62:32–56, 1970.

[76] A.V. Neimark. Analysis of capillary condensation and desorption processes by means of percolation theory methods. *Coll. J.*, 46:813–819, 1984.

[77] A.S. Odeh and B.J. Dotson. A method for reducing the rate effect on oil and water relative permeabilities calculated from dynamic displacement data. *Paper SPE 14417 presented at the 60th Annual SPE Fall Meeting, Las Vegas, NV*, 1985.

[78] Y. Ogniewicz and C. L. Tien. Porous heat pipe, in heat transfer, thermal control and heat pipes (edited by W. B. Olstad). *Progress in Astronautics (Series Editor M. Summerfield) 329-345, AIAA, New York. Presented as paper 79-1093, AIAA 14th Thermophysics Conf., Orlando, Florida*, June (1979).

[79] M. Parlar and Y.C. Yortsos. Percolation theory of steam-water relative permeability. *Paper SPE 16969 presented at the 1987 Annual Meeting, Dallas, TX, Sept. 27-30.*, 1987.

[80] M. Parlar and Y.C. Yortsos. Percolation theory of adsorption-desorption processes in porous materials. *J. Coll. Intf. Sci.*, 124:162–176, 1988.

[81] M. Parlar and Y.C. Yortsos. Nucleation and pore geometry effects on capillary desorption processes in porous media. *J. Coll. Intf. Sci.*, 132:425–443, 1989.

[82] P. Persoff, C.J. Radke, K. Pruess, S.M. Benson, and P.A. Witherspoon. A laboratory investigation of foam flow in sandstone at elevated pressure. *Paper SPE 18781*, 1989.

[83] E.J. Peters and D.L. Flock. The onset of instability during two-phase immiscible displacement in porous media. *Soc. Pet. Eng. J.*, 4:133, 1981.

[84] M.S. Plesset and A. Prosperetti. Bubble dynamics and cavitation. *Ann. Rev. Fluid Mech.*, 9:145–185, 1977.

[85] M.S. Plesset and S.A. Zwick. The growth of vapor bubbles in superheated liquids. *J. Appl. Phys.*, 25:493–500, 1954.

[86] M. Prats. *Thermal Recovery.* SPE Monograph, Vol. 7, Dallas,Texas (1982).

[87] A. Prosperetti and M.S. Plesset. Vapour bubble growth in a superheated liquid. *J. Fluid Mech.*, 85:349–368, 1978.

[88] M.J. Salman. *Factors Affecting Relative Permeabilities During Simultaneous Flow of Oil and Polymer Solution Through Porous Media.* PhD thesis, University of Southern California, Los Angeles, 1989.

[89] R.S. Schechter, W.H. Wade, and J.A. Wingrave. Sorption isotherm hysteresis turbidity phenomena in mesoporous media. *J. Coll. Intf. Sci.*, 59:7–23, 1977.

[90] F.N. Schneider and W.W. Owens. Steady-state measurements of relative permeability for polymer-oil systems. *Paper SPE 9408*, 1980.

[91] G. Schubert and J. M. Straus. Two-phase convection in a porous medium. *J. Geophys. Res.*, 82:3411–3421, 1977.

[92] G. Schubert and J. M. Straus. Steam-water counterflow in porous media. *J. Geophysical Res.*, 84:1621, 1979.

[93] L.E. Scriven. On the dynamics of phase growth. *Chem. Eng. Sci.*, 10:1–13, 1959.

[94] T. M. Shaw. Drying as an immiscible displacement process with fluid counterflow. *Physical Review Letters*, 59:1671, 1987.

[95] C. H. Sondergeld and L. Turcotte. An experimental study of two phase convection in a porous medium with applications to geological problems. *J. Geophys. Res.*, 82:2045–2053, 1977.

[96] K.S. Sorbie. Network modeling of xanthan rheology in porous media in the presence of depleted layer effects. *Paper SPE 19651*, 1989.

[97] K.S. Sorbie, P.J. Clifford, and E.R.W. Jones. The rheology of pseudoplastic fluids in porous media using network modeling. *J. Coll. Intf. Sci.*, 130:508–534, 1989.

[98] G.S. Springer. Homogeneous nucleation. *Adv. Heat Trans.*, 14:281–346, 1978.

[99] C.R. Stewart, E.B. Hunt Jr., F.N. Schneider, T.M. Geffen, and V.J. Berry Jr. The role of bubble formation in oil recovery by solution gas drives in limestones. *Trans. AIME*, 201:294–301, 1954.

[100] J. Szekely and S.D. Fang. Non-equilibrium effects in the growth of spherical gas bubbles due to solute diffusion-II: The combined effects of viscosity, liquid inertia, surface tension, and surface kinetics. *Chem. Eng. Sci.*, 28:2127–2140, 1973.

[101] J. Szekely and G.P. Martins. Non-equilibrium effects in the growth of spherical gas bubbles due to solute diffusion. *Chem. Eng. Sci.*, 26:147–159, 1971.

[102] D. Teeuw and F. Hesselink. Power-law flow and hydrodynamic behavior of biopolymer solutions in porous media. *Paper SPE 8962*, 1980.

[103] J.R. Thome and R.A.W. Shock. Boiling of multicomponent liquid mixtures. *Adv. Heat Trans.*, 16:60–153, 1980.

[104] A.H. Thompson, A.J. Katz, and C.E. Krohn. The microgeometry and transport properties of sedimentary rock. *Adv. Phys.*, 36:625–694, 1987.

[105] K. S. Udell. Heat transfer in porous media heated from above with evaporation, condensation, and capillary effects. *J. Heat Trans.*, 105:485–492, 1983.

[106] K. S. Udell. Heat transfer in porous media considering phase change and capillarity-the heat pipe effect. *Int. J. Heat Mass Transfer*, 28:485–495, 1985.

[107] J.S. Vrentas and D. Shin. Perturbation solutions of spherical moving boundary problems-I: Slow growth or dissolution rates. *Chem. Eng. Sci.*, 35:1687–1696, 1980.

[108] J.S. Vrentas and D. Shin. Perturbation solutions of spherical moving boundary problems-II: Rapid growth or dissolution rates. *Chem. Eng. Sci.*, 35:1697–1705, 1980.

[109] G.C. Wall and R.J.C. Brown. The determination of pore size distributions from sorption isotherms and mercury penetration in interconnected pores: The application of percolation theory. *J.Coll. Intf. Sci.*, 82:141–149, 1981.

[110] C.A. Ward, A. Balakrishnan, and F.C. Hooper. On the thermodynamics of nucleation in weak gas-liquid solutions. *Trans. ASME*, 92:695–704, 1970.

[111] C.A. Ward and T.W. Forest. On the relation between platelet adhesion and the roughness of a synthetic biomaterial. *Ann. Biomed. Eng.*, 4:184–207, 1976.

[112] C.A. Ward, W.R. Johnson, R.D. Venter, S. Ho, T.W. Forest, and W.D. Fraser. Heterogeneous bubble nucleation and conditions for growth in a liquid-gas system of constant mass and volume. *J. App. Phys.*, 54:1833–1843, 1983.

[113] D. E. White, L. J. Muffler, and A. H. Trusdell. Vapor-dominated hydrothermal systems compared with hot-water systems. *Econ. Geol.*, 66:75–97, 1971.

[114] G.B. Whitham. *Linear and Nonlinear Waves.* J. Wiley, New York, 1974.

[115] D.R. Wieland and H.T. Kennedy. Measurement of bubble frequency in cores. *Trans. AIME*, 210:122–125, 1957.

[116] D. Wilkinson and J.F. Willemsen. Invasion percolation: A new form of percolation theory. *J. Phys. A: Math. Gen.*, 16:3365–3376, 1983.

[117] G.P. Willhite and J.G. Dominguez. *Improved Oil Recovery by Surfactant and Polymer Flooding.* Academic Press Inc., New York, 1977. Editors D.O. Shah and R.S. Schechter.

[118] Y. C. Yortsos and M. Parlar. Phase change in porous media: Application to solution gas drive. *Paper SPE 19697 presented at the 64th Annual Technical Conference and Exhibition of SPE, San Antonio, TX Oct. 8-11*, 1989.

[119] Y.C. Yortsos. in preparation.

[120] Y.C. Yortsos and F.J. Hickernell. Linear stability analysis of immiscible displacement in porous media. *SIAM J. Appl. Math.*, 49:730–748, 1989.

[121] A. Zaitoun and N. Kohler. Two-phase flow through porous media: Effect of an adsorbed polymer layer. *Paper SPE 18085*, 1988.

[122] A.C. Zettlemoyer. *Nucleation.* Dekker, New York, 1969.

[123] V.P. Zhdanov, V.B. Fenelonov, and D.K. Efremov. Determination of pore size distribution from sorption isotherms: Application of percolation theory. *J. Coll. Intf. Sci.*, 120:218–223, 1987.

9 APPENDIX A

Consider the immiscible displacement of an incompressible liquid by the injection of an inviscid gas at variable volumetric rate Q and constant pressure P_G at a point source. At creeping flow conditions, the liquid pressure is typically taken to satisfy a Laplace equation

$$\nabla^2 P = 0, \tag{252}$$

$$P_L = P_i \text{ at } \underline{r} \to \infty. \tag{253}$$

Locally, at the advancing gas interface we have

$$P_G = P_L + 2\gamma H, \tag{254}$$

and a growth condition

$$u_s = -\frac{k}{\mu}\frac{\partial P_L}{\partial s}, \tag{255}$$

where $\underline{s}$ is the local outer normal and Darcy's law has been used to approximately relate velocity and pressure gradient. An overall balance for the gas phase growth reads

$$\frac{d}{dt}[\rho_G V] = \rho_G Q, \tag{256}$$

which, in case of not-too-large variations in pressure becomes

$$\frac{dV}{dt} = Q = \int_A u_s dA. \tag{257}$$

Note that the second equality in (257) is a direct consequence of Reynolds Transport Theorem.

We shall, next, reduce the problem into a dimensionless form by normalizing spatial distance by an initial gas phase radius R_o, time by $R_o^2\mu/(P_G - P_i)k$ and velocity by $(P_G - P_i)k/R_o\mu$, gas volume by R_o^3 and interfacial area by R_o^2, and interfacial curvature by H_o (again not necessarily related to R_o). Dimensionless liquid pressure is further defined by

$$T = \frac{P_G - P_L}{P_G - P_i}, \tag{258}$$

to yield

$$\nabla^2 T = 0, \tag{259}$$

$$T = 1 \text{ at } \underline{r} \to \infty, \tag{260}$$

while at the interface we get

$$\nu_s = \frac{\partial T}{\partial s}, \tag{261}$$

$$T = \Psi\eta, \tag{262}$$

where $\Psi = 2\gamma H_o/(P_G - P_i)$. The dimensionless volume Υ also satisfies the equation

$$\frac{d\Upsilon}{d\tau} = \int_{\mathcal{A}} \frac{\partial T}{\partial s} dA, \tag{263}$$

while the latter also equals $Q\mu/\Delta P R_o k$.

10 APPENDIX B

The dimensionless constants c, e, f are obtained by a straightforward analysis. We obtain

$$c = \frac{\beta R_p A_1 k_{rV}(S_{Lr})}{1 + k_{rV}(S_{Lr}) K R_m \frac{A_1}{\tau_1^2}} \tag{264}$$

$$e = \frac{R_v + K R_p R_h \frac{A_1}{\tau_1^2}}{R_p A_1 J'(S_{Lr})} \tag{265}$$

$$f = -\frac{nL}{\beta} J'(S_{Lr})\, e^2 \tag{266}$$

where A_1 and τ_1 pertain to conditions at ξ_1. For typical parameter values [18] and $k = 1$ d, we obtain the estimates

$$c = 2.469 * 10^{-4} \quad , \quad e = 80.5169 \quad , \quad f = 3.0981 * 10^6$$